Investigations into fracture and vein systems in Gale crater, Mars

A Dissertation Presented for the
Doctor of Philosophy
Degree
The University of Tennessee, Knoxville

Rachel Emily Kronyak
December 2019

Copyright © 2019 by Rachel E. Kronyak
All rights reserved.

DEDICATION

To my parents, for their unrivaled support of all my space adventures.

And to my late grandfathers, Ernest “Pa” Bergmueller and Nicholas Kronyak, for providing me with the greatest family and values a granddaughter could hope for.

ACKNOWLEDGEMENTS

This dissertation research was funded by NASA's Mars Science Laboratory mission. I am grateful to those who provide operational support to the Curiosity rover and its instruments and for the experience to participate in the mission. I would like to thank the IBEW Local 3 and the Geological Society of America for providing additional financial support along the way.

I would like to thank my adviser, Dr. Linda Kah for taking me on as her student and bringing me to Mars. I also want to thank Dr. Stephanie TerMaath and her lab group, especially Corey Arndt, Will Ferrell, and Cody Crusenberry, for engineering lab support and abundant patience. I would also like to acknowledge the rest of my committee members for insightful feedback and guidance every step of the way: Drs. Christopher Fedo, Bradley Thomson, and Robert Hatcher.

This dissertation would not have been possible without the support of many magnificent people. To my incredible family; to my awesome friends and lab group mates Jake Alexander and Agustin Kriscautzky; to my wonderful friends Mary Eibl, Laura Checki, Samantha Gwizd, Ashley Manning-Berg, Keenan Golder; to my exceptionally patient and kind boyfriend Dustin Smith; to my gym teammates in the CrossFit community; and to my rescue dog Sadie – thank you!

ABSTRACT

Rock fractures and veins are among the most common structural features in the Earth's crust and provide information regarding the stress and deformation of a geologic succession. Assessment of fracture morphology and host rock properties can inform the conditions under which fracturing occurred. The chapters in this dissertation investigate fractures within Gale crater, Mars, to understand the nature and timing of post-depositional fluid events and the formation mechanisms driving fracture formation.

Chapter 1 focuses on veins using the instruments of the Curiosity rover. Since 2012 Curiosity has been exploring sedimentary environments of Gale crater. Although veins have been observed since the early days of the mission, analysis of the Pahrump Hills site revealed an increase in the size, complexity, and range in composition of veins. Analysis of vein color, morphology, texture, and chemistry indicate at least three distinct events of post-depositional fluid flow. Observation of the relationships between veins and host rock, discrete mineral signatures, and mineral microtextures support hydrofracture as the primary formation mechanism.

Chapter 2 focuses on observations of an extensive polygonal fracture network that is visible in orbital images. Relatively young strata in Gale crater contain a regionally extensive network of erosionally resistant polygonal ridges. Polygonal fractures exhibit relatively uniform size and shape, indicating uniform stress fields during formation. Intersection angles of polygons further indicate that fractures formed during repetitive contraction-expansion events that were later modified by diagenetic fluids. The considerable amount of time between fracture and cementation indicates a protracted history of fluid stability near the surface in Gale crater.

Chapter 3 focuses on laboratory observation and analysis of Mars analog materials as a potential mechanism to better understand planetary surface materials. Information regarding mechanical rock properties are critical in informing the conditions required for fracture propagation. Utilizing a rock mechanics and engineering approach, analog rocks were selected to represent specific lithologies within Gale crater and experimentally tested to determine a variety of mechanical properties. Finite element models were then used to validate our understanding of, and ability to predict, rock properties.

TABLE OF CONTENTS

Introduction 1
Mars as a Target for Astrobiological Investigation 1
Fluids in the Martian Subsurface 2
Constraints on Mars 2
Overview of the Present Study 4
References 7
Chapter 1 Mineral-Filled Fractures as Indicators of Multigenerational Fluid Flow in the Pahrump Hills Member of the Murray Formation, Gale Crater, Mars 11
Abstract 12
Introduction 13
Geologic Context 15
Gale crater 15
Pahrump Hills field site, lower northern Mount Sharp 17
Methods 20
Mineral-filled Fractures (Veins) at Pahrump Hills 23
Gray veins at Pahrump Hills 23
White veins at Pahrump Hills 31
Dark-toned veins at Pahrump Hills 37
Garden City vein outcrop: a case study 40
Beyond Garden City: Salsberry Peak and Artist's Drive 53
Discussion 54
Evidence for hydrofracture at Pahrump Hills 54
Implications for burial depth 60
Source(s) of vein-forming fluids 61
Broader implications for water stability and astrobiology in Gale crater 63
Conclusions 64
Acknowledgements 66
References 67
Chapter 2 Extensive Polygonal Fracture Network in Siccar Point Group Strata: Fracture Mechanisms and Implications for Fluid Circulation in Gale Crater, Mars 77
Abstract 78
Introduction 79
Geology of Gale Crater 80
Bradbury group 82
Mount Sharp group 82
Siccar Point group 83
Methods 84
Data and Observations 85
Geology of Siccar Point group strata 85
Polygonal features in the Siccar Point group 98
Additional observations of the Siccar Point group 105
Discussion 113
Potential formation mechanisms of polygonal features 113

Lithification of fracture polygons and implications for fluid circulation 123
Conclusions 123
Acknowledgements 124
References 126
Chapter 3 Predicting the Mechanical and Fracture Properties of Sedimentary Lithologies in Gale Crater 136
Abstract 137
Introduction 137
Lithologies of Gale crater 139
Assessment of rock properties on Mars 139
Material properties of surface rocks in Gale crater 140
Selection of analog lithologies 142
Methods 146
Experimental determination of mechanical properties 148
Mechanical property correlation 152
Computational model development 153
Results 156
Mechanical properties 156
Mechanical property correlation 163
Computational modeling 167
Discussion 172
Variation in mechanical property data 172
Validated fracture model and property correlation 178
Application of property correlation to Gale crater lithologies 179
Conclusions 180
References 183
Conclusions 190
References 193
Vita 195

LIST OF TABLES

Table 1.1 Vein and bedrock targets analyzed by Curiosity's remote sensing instruments at the Garden city vein outcrop, shaded by vein type (white, white veins; light gray, gray veins; dark gray, dark-toned veins). Most targets analyzed by the APXS instrument represent a mixture of gray and white vein material; for these targets, the box color designates the intended primary component in the APXS FOV. 41
Table 2.1 Slope and thickness data for Siccar Point group regions. 90
Table 3.1 Correlation between mechanical properties of compressive and tensile strength, as well as between fracture toughness and tensile strength. UCS = unconfined compressive strength, TS = tensile strength, K_{IC} = fracture toughness. 154
Table 3.2 Unconfined compressive strength (UCS) test data. 157
Table 3.3 Tensile strength test data for disc specimens. 160
Table 3.4 Fracture toughness and fracture energy data for semi-circular disc three-point bend specimens 162
Table 3.5 Predicted TS values from measured UCS data and comparisons to measured TS for each rock type. 166
Table 3.6 Predicted K_{IC} values from measured TS data and comparisons to measured K_{IC} for each rock type 166
Table 3.7 Mean UCS values for analog lithologies and predicted properties of TS and KIC from correlation equations established by Nazir et al., (2013) and Whittaker et al. Values of elastic modulus were estimated based on the relative UCS of rock types. Predicted tensile elastic modulus reflect typical sandstone values from the literature (Zhang & Yu, 2019). 171
Table 3.8 Predicted TS (from Nazir et al., 2013) and K_{IC} values (from Whittaker et al., 1992 and Zhang, 2002) for Murray and Stimson formation rocks drilled by the Curiosity rover. 181

LIST OF FIGURES

Figure 1.1 Context overview of Curiosity's Gale crater field site. (a) Gale crater with white line indicating Curiosity's traverse from Bradbury Landing to the rover's Sol 2020 (1 September 2018) location on the Vera Rubin ridge. (b) Curiosity's traverse, with black dashed line distinguishing the approximate boundary between exposures of the Bradbury group (Aeolis Palus) and Mount Sharp group strata. The location of Pahrump Hills is indicated by a black dot. (c) Pahrump Hills field site, representing ~12 meters of Murray formation stratigraphy. (d) Composite stratigraphic column of lithologic units encountered by Curiosity, constructed as a function of elevation in meters, courtesy of the MSL Sedimentology and Stratigraphy group. The Pahrump Hills member is the lowermost exposure of the Murray formation (Mount Sharp group). The Mount Sharp and Bradbury groups show an interfingering relationship; the Stimson formation (Siccar Point group) is firmly established as overlying the Murray formation along an erosional unconformity. 16

Figure 1.2 The stratigraphic section at the Pahrump Hills locality. The stratigraphic column of facies exposed at Pahrump Hills is superimposed and includes planar laminated mudstone, cross-laminated sandstone, and thickly laminated sandstone (modified after Stack et al., 2018). Portion of Mastcam mosaic (mcam03370) of the Pahrump Hills locality acquired on Sol 778, showing the uppermost ~5 meters of section. 18

Figure 1.3 Gray veins in the lower Pahrump Hills section, expressing thin, positive-relief ridge morphology along fracture margins. Images are color-merge products that combine color from Mastcam-100 images with ChemCam RMI images following LIBS analyses. Red crosshairs indicate the location of LIBS observation points. Counterclockwise from the upper left, targets include (a) "Castlegate," analyzed on Sol 916, (b) "Keetley," analyzed on Sol 918, (c) "Elbert," analyzed on Sol 903, (d) "Marsden," analyzed on Sol 921, (e) "Ophir," analyzed on Sol 918. Scale bar applies for all images. 24

Figure 1.4 (a) Whale Rock outcrop, with cross-bedded sandstone overlying recessive laminated mudstone. Resistant veins are exposed underneath the sandstone lens. Mastcam mosaic mcam03476, taken on Sol 796. (b) White veins are present along cross bed boundaries as well as vertically crosscutting bedding (white arrows). (c) White arrows indicate thin gray veins that comprise the majority of boxwork veins at Whale Rock. (d-f) Preserved white vein material held up by resistant gray vein and (f, far right) sandwiched in between vertical thin gray veins. 26

Figure 1.5 Relationship between gray and white veins throughout Pahrump Hills. White veins commonly bisect gray veins, resulting in a gray-white-gray morphology at a variety of scales. Millimeter-thick white veins are bounded on both sides by resistant gray ridges near (a) ChemCam target "Cowhole Mountain," analyzed on Sol 837 (Mastcam image 0837MR0036750020500725E01), (b) and "Calico Mountain," taken on Sol 837 (Mastcam image 0837MR0036760020500763C00). (c) Centimeter-thick gray-white-gray vein (white arrows) near gray vein target "Keetley," indicated by black box (Mastcam image 0918MR0040330000501547E01)." (d-e) Gray-white-gray veins that make up the intersecting vein network at Garden City (Portion of Mastcam mosaic mcam04087 and Mastcam image 0946MR0041570010502002E01, respectively). 27

Figure 1.6 Fragmented gray vein material preserved within the matrix of white veins at the Garden City vein outcrop, suggesting a potential time relationship between vein episodes:

initial gray vein formation followed by reutilization of fractures and formation of white veins (0926MR00407002050173E01 and 0926ML0040730040402791E01, respectively). 28
Figure 1.7 White veins in the lower 10 meters of Pahrump Hills. Veins are mm-thick and crosscut Murray mudstone bedding and earlier diagenetic features. Images are Mastcam-100 frames acquired after ChemCam LIBS observations. (a) Target "Straight Cliffs," analyzed on Sol 766, an erosionally resistant vein (white arrow) crosscuts dendritic crystal cluster (Mastcam image 0766MR0032930000403839E01). (b) Target "Delta" analyzed on Sol 781 (Mastcam image 0781MR0034080000404106E01). The circular gray area to the right of the white arrow represents the area where the ChemCam laser shots hit the surface, clearing surface dust. (c) Target "San Gabriel," analyzed on Sol 789, with white vein material exposed obliquely along a fracture margin (Mastcam image 0789MR0034380000500044C00). (d) Target "Vaqueros (Sol 833)," where white vein material is observed at several orientations, both vertical and at a low angle to bedding (white arrows; Mastcam image 0833MR0036680000500719E01). 32
Figure 1.8 Texture of white veins in the lower 10 meters of Pahrump Hills as revealed by ChemCam RMI images. (a) ChemCam target "San Gabriel," which displays parallel interior lineations that appear roughly perpendicular to fracture edges. (b) Target "Crazy Hollow," analyzed on Sol 906, which contains a massive interior texture. Scale bar applies to both images. 34
Figure 1.9 Dark-toned gray veins at Pahrump Hills. (a) Dark-toned veins exhibit positive relief and intersect with sandwich veins at Garden City at roughly 90-degree angles (white arrows). ChemCam target "Hakatai," analyzed on Sol 935 is indicated by the inset RMI image and shows a layered texture near the dark-toned vein edges (portion of Mastcam mosaic mcam04087). (b) ChemCam target "Bishop," analyzed on Sol 946, is shown in the ChemCam RMI image and expresses an upright, flaky appearance (Mastcam image 0946MR0041560000502000E01). (c) Close-up view of "Bishop;" white arrows indicate the potential presence of thin, white veins bisecting layers of dark-toned vein material. (d) ChemCam target "Temblor," analyzed on Sol 948 which exhibits a smooth, shiny surface texture (Mastcam image 0948MR0041690000502040E01). (e) Float pieces of potential dark-toned vein material (white circles) along the west wall of the Artist's Drive valley (Sol 950; portion of Mastcam mosaic mcam04175). 38
Figure 1.10 Mastcam mosaic of Garden City vein complex (portion of Mastcam mosaic mcam04068) acquired on Sol 925 prior to the rover's approach to conduct remote and contact science observations. Circles indicate the locations of ChemCam (yellow) and APXS (red) targets on veins across the outcrop; black boxes indicate the locations of high-resolution MAHLI image mosaics 42
Figure 1.11 Mastcam-34 mosaic (mcam04150) of the Garden City vein complex acquired on Sol 944. Centimeter-thick sandwich veins comprise the positive-relief intersecting network. Sandwich veins that were imaged with the MAHLI camera are indicated by white boxes (Vein 1 (V1), see Fig. 1.12; V2, see Fig. 1.13; V3, see Fig. 1.14; V4, see Fig. 1.15). 43
Figure 1.12 Portion of MAHLI mosaic of Garden City Vein 1 (V1); vein target "Live Oak Canyon," imaged on Sol 937. (a) V1 is ~1 cm thick and contains fairly eroded white vein fill along the vein center. (b-c) Vein fabric exhibits roughly parallel lineations. MAHLI image 0937MH0004760050303426C00. 45

Figure 1.13 (a) Portion of MAHLI mosaic of Garden City Vein 2 (V2) imaged on Sol 948. Vein is ~1 cm thick and expresses a variety of interior textures, with significant eroded portions in the vein center. (b) White vein material growth likely originated along the fracture walls and proceeded inward towards the vein center, producing an elongate blocky, "toothy" crystal texture. (c) Boxes indicate the presence of sub-mm-thick veinlets parallel to the vein interior. Circles indicate gray material entrained within the white vein matrix. MAHLI images 0948MH0004920000404116R00, 0948MH0004920000404118R00, 0948MH0004920000404120R00, 0948MH0004920000404122R00, 0948MH0004920000404124R00, 0948MH0004920000404126R00, 0948MH0004920000404128R00. 46
Figure 1.14 Portion of MAHLI mosaic of Garden City Vein 3 (V3) acquired on Sol 946. The left side of the vein exhibits a smooth, massive texture, whereas white exhibits a faint linear fabric, oriented obliquely to the vein walls (black lines). A potential median line is observed (white arrow) along the vein center. MAHLI images 0946MH0004900000303878R00, 0946MH0004900000303880R00. 47
Figure 1.15 Portion of MAHLI mosaic of Garden City Vein 4 (V4) acquired on Sol 946. (a) White material in V4 exhibits a dominantly massive texture, with a few eroded and pockmarked regions. (b) Arrow indicates a potential median line, separating the white vein material into upper and lower segments. Veinlets are observed in adjacent gray vein material (white box). (c) Thinly laminated texture of gray vein material along the bottom fracture margin (white box). This lower portion of gray vein material is significantly thicker than the gray material on the opposite side of the vein. Gray material is permeated by sub-mm white veinlets. MAHLI images 0946MH0004900000303870R00, 0946MH0004900000303878R00, 0946MH0004900000303880R00, 0946MH0004900000303880R00, 0946MH0004900000303884R00, 0946MH0004900000303886R00. 47
Figure 1.16 Vein interactions at the Salsberry Peak caprock. (a) Portion of Mastcam mosaic acquired on Sol 938 (mcam04119). Salsberry Peak is a ~1-meter-thick thickly laminated sandstone lithology that caps the underlying laminated mudstone. (b) Parallel white veins penetrate the mudstone-sandstone contact. (c) Positive relief vein networks are present just beneath Salsberry Peak. The Garden City complex is located just out of frame beneath the bottom of the mosaic..... 55
Figure 1.17 Centimeter-thick veins imaged with the MAHLI camera beyond Pahrump Hills. Vein targets include: (a) "Tofte," imaged on Sol 2083, exhibits a finely laminated, linear texture parallel to vein walls along the left side of the vein, and at a high angle to vein walls on the right. MAHLI image 2083MH0007490000802265R00, (b) "Palmwag," imaged on Sol 1276, which contains potentially multigenerational white material, entrained gray fragments, and a distinct median line. MAHLI image 1276MH0004580000404503R00, (c) "Rona," imaged on Sol 1937, which shows a complex interior of multigenerational inward-facing white and gray vein material. MAHLI images 1937MH0001710000703855R00, 1937MH0001710000703855R00, 1937MH0001710000703861R00, 1937MH0001710000703863R00. 65
Figure 2.1 Geographic context of this study. (a) Gale crater, with Curiosity's traverse outlined in white. (b) Region of Curiosity's traverse (white line) and the geologic units within

northwest Gale crater. The thin dashed black line indicates the approximate boundary between exposures of the Bradbury group and the Mount Sharp group. In the region of the Siccar Point group, the Mount Sharp group consists predominantly of lacustrine mudstone of the Murray formation and contains a distinct topographic ridge that is designated as the Vera Rubin ridge. Exposures of the Siccar Point group, here in purple, unconformably overlie strata of lower the Murray formation. Strata of upper Mount Sharp (south of thick dashed line) are not yet named..... 81
Figure 2.2 Exposures of the Siccar Point group (SPg; outlined in white) examined for this study. (a) Regions of the SPg east and northeast of the Curiosity rover traverse (See Figure 2.1b), adjacent to the Bagnold dune field. (b) Regions of the SPg south and southwest of the Curiosity rover traverse, including the Greenheugh pediment (see Bryk et al., 2019). (c) Highly dissected portions of the SPg in the region of the Curiosity rover traverse (dashed black line). In this region, the SPg is informally designated as the Stimson formation. 87
Figure 2.3 Three primary surface morphologies of the Siccar Point group, including: (a) surficial E-W trending ridges, (b) rough crater-retentive surface, and (c) polygonal terrain. 89
Figure 2.4 Example of estimated thickness of Siccar Point group exposures. Here, the thickness of the ridged subunit is measured in the northeast SPg. The local slope is shown along the elevation profile as a dashed line. Slope is derived from multiple measurements of the regional slope, which here corresponds to the base of ridge troughs. The overlying thickness of strata is then measured along 20-meter increments (double-sided arrows); the maximum height of ridges is approximately 1 meter..... 89
Figure 2.5 Stratigraphic expression of polygonal features in the Siccar Point group. (a) Polygons (left of white dashed line) most commonly occur underlying regions of cratered surfaces of the SPg. (b) Polygons, however, also occur in topographic lows between erosional remnants of E-W trending parallel ridges (white dashed lines). 92
Figure 2.6 Features of the Greenheugh pediment capping unit. (a) Present-day fan-shaped exposure of the Greenheugh pediment capping unit; white boxes indicate the locations of b, c, and d. (b) Regions of the pediment capping unit near the Gediz Vallis ridge preserve evenly spaced WNW-ESE trending ridges, highlighted by white lines. (c) More distal portions of the pediment exhibit a rough surface texture that preserves numerous small craters; potential remnants of E-W trending ridges are highlighted in white. (d) Erosionally resistant polygons (within white boxes) are exposed primarily at the southwestern edge of the Greenheugh pediment capping unit, where erosion has revealed the contact between the Greenheugh pediment and the underlying Murray formation. 94
Figure 2.7 Portion of Mastcam mosaic acquired on Sol 2019 (mcam10651) pointed toward the eastern Greenheugh pediment. The pediment is overlain by a <1-meter-thick cap (white arrows) overlying the Murray formation mudstone; note lateral variation in color of underlying Murray mudstone..... 96
Figure 2.8 Cross-sectional elevation profile through polygons. Polygons consist of distinct, light-toned, erosionally resistant ridges; the difference in elevation of adjacent polygon centers reflects the local slope over which SPg strata was deposited. The stair-step pattern of the profile represents DEM pixel edges, not true topography. 100
Figure 2.9 Polygons in the SPg. (a-b) Polygons from two different regions within the northeastern exposures of the SPg. (c) Polygons from the southwestern exposures of the

SPg, separated from polygons shown in (a) and (b) by more than 20 km. (d) Distinctly elongate polygons in far northeastern exposures of the SPg. 101
Figure 2.10 Angles of intersection of polygonal ridges, measured from three regions of the Siccar Point group northeast of the Curiosity rover traverse. Each region consisted of approximately 140,000 m^2. All regions show discrete modes that reflects dominance of 90° T-junctions (~23% of all measured intersections) and a second mode that reflects 120° Y-junctions (~14% of all measured intersections). 102
Figure 2.11 Polygon diameter data for regions of the Siccar Point group. Polygons in all regions (main exposures of the SPg, Greenheugh pediment exposures, far northeastern exposures of the SPg, and regions near the Curiosity rover traverse) exhibit a lognormal distribution and an overall mean of 7.5 ± 3.0 meters (N=8714). 103
Figure 2.12 (a) Portion of Mastcam mosaic acquired on Sol 23 (mcam00114). The Siccar Point group is observed as a thin dark-toned unit overlying the Murray formation. Distinct white features (white arrows) extend from the Murray formation into the SPg. (b) Orbital context for Mastcam mosaic mcam00114, with the white box indicating the mosaic portion from (a). These features that crosscut the Murray formation and SPg (white arrows) exhibit a distinct morphology from the organized uniform polygonal fractures present in the SPg terrain in the right side of the image. 106
Figure 2.13 (a) Siccar Point group exposures in areas of the Curiosity rover traverse. In these areas, the Siccar Point group is designated as the Stimson formation, which was encountered in the Emerson plateau, the Naukluft plateau, and the Murray buttes region (white boxes). (b-c) Uniform polygonal fractures, similar in size and scale to other areas of the Siccar Point group, are observed within the Naukluft plateau and Murray butte terrain. The Curiosity rover traverse indicated by heavy white lines in all images. 108
Figure 2.14 Veins and alteration halos in the Stimson formation. (a) White calcium sulfate veins in the underlying Murray formation approach, but commonly do not cross, the Murray-Stimson contact. Dashed white lines trace several prominent veins that approach the contact. Portion of Mastcam mosaic acquired on Sol 1275 (mcam05976). (b) Alteration halos in the Stimson formation, where bedrock adjacent to fractures has been modified by diagenetic fluids. Portion of Navcam image acquired on Sol 1083. Approximate halo margins are indicated by dashed black lines. (c) Veins (dashed white lines) and halos (black arrows) in the vicinity of the Murray-Stimson contact. Portion of Mastcam mosaic acquired on Sol 1267 (mcam05931). 109
Figure 2.15 Polygonal fractures in the Naukluft plateau region. (a) Dashed white line indicates the areas imaged by Mastcam (viewshed) on Sol 1296 (mcam06154). Areas visible in mcam06154 are shown in brown, and non-visible portions in gray. (b) Portion of Mastcam mosaic mcam06154 showing several erosionally resistant polygons (dashed white lines). (c) Viewshed of Mastcam mosaic acquired on Sol 1296 (mcam06153) showing visible (brown) and non-visible (gray) portion of imaged region. (d) Portion of Mastcam mosaic mcam06153 showing resistant ridges that form rough polygons (dashed white lines). In the foreground, alteration halos may correspond with polygons. (e) Viewshed of Mastcam mosaic acquired on Sol 1312 (mcam06260). (f) Portion of Mastcam mosaic mcam06260 showing several polygon edges (dashed white lines). 111

Figure 2.16 Fracture vertices, intersection angles, and changed with repeated fracture events. (a) Fractures initially show random to rectilinear orientations and grow in the direction that maximizes energy release, resulting in curvature toward pre-existing fractures and intersection angles approaching 90°. (b) Change in fracture morphology during repeated events can result in migration of fracture vertices, resulting in a change in intersection angles toward 120° (modified after Goehring, 2013). (c) SPg strata showing common fracture morphologies, including curved fractures, T-junctions, and Y-junctions (dotted lines)..... 119
Figure 3.1 Grain size distribution of sandstone lithologies used in this study. Aeolian strata of the Cutler Formation consist of predominantly well-sorted medium to coarse silt. Marine sandstone of the Clinch and Chapman Ridge formations vary in both grain size and grain sorting. 143
Figure 3.2 Petrographic images of sandstone samples. (A) Cutler Formation siltstone; scale bar is 350 micrometers. (B) Cutler Formation siltstone with primary framework grains (Q=quartz, F=feldspar), detrital sheet silicates (M=mica), and an abundance of iron oxide grain coatings; scale bar is 100 micrometers. (C) Clinch Formation sandstone; scale bar is 350 micrometers. (D) Clinch Formation sandstone with primary framework grains (Q=quartz, F=feldspar); note abundant alteration of feldspar to clay minerals. Scale bar is 100 micrometers. (E) Chapman Ridge Sandstone; scale bar is 350 micrometers. (F) Chapman Ridge Sandstone showing iron oxide grain coatings and suturing of detrital quartz grains (white arrows); scale bar is 100 micrometers. 144
Figure 3.3 Flow chart of multi-step analytical approach. This study focuses on experimental testing and computational simulation, and future work aims to perform sensitivity analysis and uncertainty quantification..... 147
Figure 3.4 Geometry for experimental mechanical property testing of analog samples. Arrows indicate the orientation of applied force during testing. (a) Cylindrical core geometry used in compressive strength tests, with an example from the Cutler Formation. (b) Disc geometry used for tensile strength tests, with an example from the Chapman Ridge Formation. (c) Notched semi-circle geometry used for fracture toughness tests, with an example from the Clinch Formation; black circles indicate the approximate locations of support rollers. 149
Figure 3.5 Analog lithologies used for testing. (a) From left to right, Chapman Ridge Formation, Cutler Formation, and Clinch Formation sandstone cores. Cores are ~5 cm in diameter. (b) Missoula mudstone sample, showing failed drill attempts using a DeWalt hand drill..... 149
Figure 3.6 2D Abaqus model geometry used to demonstrate the XFEM crack growth through three-point bend tests. Model geometry matches experimental test geometry. The finest mesh was placed along the region of crack growth. Outside of this region, the specimen was partitioned and meshed more coarsely to reduce computational run time..... 157
Figure 3.7 Three-point bend test results on semi-circular disc specimens. (a) Test configuration with Clinch Formation sample loaded for testing; sample diameter = 50 mm, roller span = 35 mm. (b) Post-test photos for specimens Clinch3 (upper left), Clinch5 (upper right), Chapman Ridge4, Chapman Ridge5, and Cutler1. All specimens broke into discrete halves during testing. (c) Post-test specimens for Missoula mudstone specimens Missoula3 (top), Missoula4 (middle), and Missoula7 (bottom). To induce cracking from the sample notches,

a thin sheet of aluminum was placed along the top and bottom of semi-circular discs where the roller pins contacted the specimens. 164
Figure 3.8 Comparison of crack growth in three-point bend for (a) the Abaqus XFEM model and (b) experimental testing. Example shown is Chapman Ridge Formation specimen 4. 168
Figure 3.9 Abaqus XFEM model results for three-point bend rock specimens. Modeled results using experimental values (green solid lines) and predicted values based on UCS (red double solid lines) are shown alongside experimental test results (dotted lines). Model results include (a) Cutler Formation three-point bend (3PB), (b) Clinch Formation 3PB data, (c) Chapman Formation 3PB data, and (d) Missoula mudstone 3PB data. Missoula test results were below the resolution of the 100 kN test machine. Model results confirmed that test data were not valid for such weak materials. 169

INTRODUCTION

Mars as a Target for Astrobiological Investigation

Since the first telescopes pointed to the night sky, the planet Mars has been a primary target for extraterrestrial exploration. The earliest astronomers, performing telescopic investigations of the martian surface, documented vast dark, linear "canals" on the surface and interpreted them as constructs from intelligent civilizations (Lowell, 1906). It was not until NASA's Mariner flyby and orbiter missions in the 1960s that a clearer picture of the martian surface was revealed. The first images of Mars showed a heavily cratered surface containing large volcanic provinces, polar caps, and fluvial channels (e.g., Hartmann & Raper, 1974; Leighton et al., 1965; Masursky, 1973). Results from the landed Viking missions drastically enhanced our understanding of the current martian surface and showed a planet with extremely cold surface temperatures, intense diurnal temperature variations, low atmospheric pressure, oxidizing soil composition, and no clear evidence for life or the presence biotic organic molecules (Moore et al., 1987; Navarro-Gonzalez et al., 2011; Pollack et al., 1977).

Over the last two decades, a series of orbital and landed robotic missions have provided evidence for abundant water-derived features, (e.g., Gulick, 2001), hydrated minerals (e.g., Bibring et al., 2006; Carter et al., 2013; Ehlmann et al., 2008; Ehlmann & Edwards, 2015; Milliken & Bish, 2010; Mustard et al. 2008), and the chemical nutrients and the energy potential to harbor life (e.g., Grotzinger et al., 2014; Squyres & Knoll, 2005), suggesting that, in its ancient past, Mars may have mimicked more Earth-like environments. The present martian surface, however, as highlighted by Viking and corroborated by recent missions, remains cold, dry, and likely uninhabitable. Yet, even in this inhospitable world, high-resolution orbital images

provide evidence of intermittent surficial water in the form of recurring slope lineae, which have been interpreted as potential seasonal brine flows (McEwen et al., 2011, 2014; Ojha et al., 2015). While the origin and composition of such flows remain poorly understood, the potential for intermittent fluid recharge has raised a new set of questions about Mars' subsurface. At what point in martian history did surface waters disappear? Is there the possibility that surface fluids retreated into the subsurface, where they may continue to represent an active fluid reservoir? Might subsurface fluids provide a refuge for a potential subsurface biosphere on Mars?

Fluids in the Martian Subsurface

Rock fractures commonly serve as conduits for post-depositional fluid flow and may offer insight into the potential habitability of the martian subsurface. In particular, mineralized fractures formed by elevated fluid pressure in the subsurface (i.e., hydrofractures) represent direct indicators of post-depositional subsurface fluid flow. To generate hydrofractures, fluids pressure must exceed rock strength; this may occur at any depth within the subsurface (Long et al., 1996; Terzaghi, 1943). Under the correct pressure, temperature, and saturation conditions, mineral precipitation within hydrofractures may occur and form veins. Investigating such hydrofracture vein systems may shed light on the timing and conditions of fracture formation, fluid chemistry, and the potential number of post-depositional fluid events.

Constraints on Mars

Additional insight regarding fracture formation and timing on Mars may be gained by assessing fracture morphology, stratigraphic relationships, and lithologic boundaries and properties. Over the last several decades, visible cameras on orbiting satellites have provided

increasingly high-resolution images (up to 25 cm/pixel resolution on the HiRISE camera; McEwen et al., 2007) of the martian surface and allow us to make local to regional-scale interpretations about the origin of fracture systems. For example, extensive, radial fractures in the Tharsis (Carr, 1974; Mege & Masson, 1996b) and Valles Marineris (Mege & Masson, 1996a; Tanaka & Golombek, 1989) regions reflect regional tensional stresses associated with crustal forces. In addition, radial and concentric fractures reflect complex morphologies generated by hypervelocity impact processes (Kenkmann et al., 2018; Polansky & Ahrens, 1990; Rodriguez et al., 2005; Schultz et al., 1982). Finally, polygonal fractures observed from orbit have been interpreted to infer contractional, isotropic stress regimes associated with cycles of freeze-thaw, wetting-drying, and heating-cooling (El Maarry et al., 2014; Kerber et al., 2017; Mangold et al., 2004; Mangold, 2005; Siebach and Grotzinger, 2013). Similarly, from the rover scale, fractures and have been widely documented in Gale crater, the landing site of the Mars Science Laboratory Curiosity rover (Caswell & Milliken, 2017; Frydenvang et al., 2017; Nachon et al., 2014, 2016; Oehler et al., 2016; Stein et al., 2018; Yen et al., 2017).

Despite the availability of high-resolution orbital and rover images of the martian surface, it is often challenging to resolve the stratigraphic relationships critical for understanding the timing of fracture formation, and it is equally challenging to reconstruct the diagenetic history of rocks that contain observable fractures. From orbit, unit and formation boundaries are often unclear, and resolution commonly limits the scale of fractures that are identifiable. In addition, the ability of fluids to reutilize fractures at a later time requires the separation of fracture mechanism(s) and subsequent fill/alteration, thus complicating fracture mechanisms. From the rover perspective, lithologic contacts are commonly obscured by aeolian sand and dust, making

boundaries difficult to interpret. Additionally, differential erosion of complex stratigraphic relationships (e.g., unconformities) makes inferences regarding timing challenging to perform. Image viewing geometry and topographic relief of outcrops also contribute the difficulty in resolving fracture morphology.

Perhaps the most useful information regarding fracture formation can be inferred from rock mechanical property data, because these properties directly determine the conditions under which fractures form and propagate. Unfortunately, constraining such properties in an extraterrestrial environment is exceedingly difficult. Instrument payloads of landed missions to Mars have provided only a few constraints. For instance, the unconfined compressive strength (UCS) of surface materials has been estimated by utilizing motor currents and percussive energies of contact equipment and comparing these to laboratory testing of these instruments (Thomson et al., 2013; Peters et al., 2017). Until more direct means of measuring are available on mission payloads, our understanding of fracture formation will remain considerably limited.

Overview of the Present Study

The study outlined in the following chapters presents three case studies that explore rock fractures and veins in Gale crater, Mars to elucidate implications regarding post-depositional fluid flow and fracture formation conditions. I utilize multiple scales and datasets to provide a thorough, local to regional-scale assessment of mineralized fractures in the lithologies that comprise the stratigraphic section in Gale crater.

Chapter 1: Mineral-filled fractures as indicators of multigenerational fluid flow in the Pahrump Hills member of the Murray formation, Gale crater, Mars

This chapter utilizes local-scale image and chemical data from the Curiosity rover to describe a network of veins at the Pahrump Hills location in Gale crater. Here, veins are present in the Murray formation, the primary lacustrine deposits that comprise Lower Mount Sharp. In previous locations in Gale crater, mineralized fractures had been described (Nachon et al., 2014; Caswell & Milliken, 2017) and were interpreted as hydrofractures. These veins were primarily single generation, thin (mm-thick), and composed exclusively of calcium sulfate. The motivation for this chapter arose with Curiosity's arrival at Pahrump Hills, where veins exhibited increasing complexity within the ~12-meter-thick stratigraphic section. Using rectified, scaled Mastcam images I assess vein-host rock interactions and perform length and width measurements on veins to evaluate changes in vein size throughout Pahrump Hills. I also utilized high-resolution MAHLI images to investigate vein microtextures. Finally, I used ChemCam and APXS data to explore potential compositions of vein-forming fluids. Through these ground-based observations, I determine the number and nature of post-depositional fluid events at Pahrump Hills, compare the nature of veins to those observed earlier in the mission, and interpret potential vein formation mechanisms.

Chapter 2: Extensive polygonal fracture network in Siccar Point group strata, Gale crater, Mars: fracture mechanisms and implications for fluid circulation in Gale crater

This chapter investigates an extensive network of erosionally resistant polygonal fractures visible in orbital HiRISE images. Fractures were observed within Siccar Point group

(SPg) strata, which occupy a considerably younger stratigraphic position within the succession at Gale crater. Using digital elevation model (DEM) data, I perform a systematic characterization of polygons over the broadly exposed (20 km^2) Siccar Point group; this characterization includes measurements of polygon size, shape, morphology, and stratigraphic position within SPg strata. With these data, and in the absence of corroborating ground-based data, I interpret potential formation mechanisms for the extensive fracture network and provide implications for the nature and timing of fluid circulation in Gale crater.

Chapter 3: Predicting the mechanical and fracture properties of sedimentary lithologies in Gale crater

This chapter utilizes a rock mechanics and engineering method to better understand parameters that govern fracture growth on Mars. In this chapter, I report results from a multi-step approach that involves: (1) the measurement of mechanical rock properties in selected analog lithologies, (2) the simulation of fracture growth using finite-element computational modeling to validate laboratory measurements, (3) determination of whether there are computational relationships that can be accurately used to predict rock mechanical properties from limited measurements, and (4) the estimation of rock mechanical properties for lithologies encountered in Gale crater. These investigations will be followed with sensitivity analyses to identify the most influential parameters on fracture growth. From this work I demonstrate the value of obtaining such mechanical properties with future landed missions to Mars.

References

Bibring, J.-P., Langevin, Y., Mustard, J. F., Poulet, F., Arvidson, R., Gendrin, A., et al. (2006). Global mineralogical and aqueous Mars history derived from OMEGA/Mars Express data. *Science,* 312, 400-404.

Carr, M. H. (1974). Tectonism and volcanism of the Tharsis Region of Mars. *Journal of Geophysical Research*, *79*(26), 3943–3949. http://doi.org/10.1029/JB079i026p03943

Carter, J., Poulet, F., Bibring, J. -P., Mangold, N., & Murchie, S. (2013). Hydrous minerals on Mars as seen by the CRISM and OMEGA imaging spectrometers: updated global view. *Journal of Geophysical Research: Planets*, 118, 831-858. doi:10.1029/2012JE004145

Caswell, T. E., & Milliken, R. E. (2017). Evidence for hydraulic fracturing at Gale crater, Mars: Implications for burial depth of the Yellowknife Bay formation. *Earth and Planetary Science Letters*, 468, 72–84. https://doi.org/10.1016/j.epsl.2017.03.033

El Maarry, M. R., Watters, W., McKeown, N. K., Carter, J., Noe Dobrea, E., Bishop, J. L., et al. (2014). Potential desiccation cracks on Mars: a synthesis from modeling, analogue-field studies, and global observations. *Icarus* 241, 248-268. http://dx.doi.org/10.1016/j.icarus.2014.06.033

Frydenvang, J., Gasda, P. J., Hurowitz, J. A., Grotzinger, J. P., Wiens, R. C., Newsom, H. E., et al. (2017). Diagenetic silica enrichment and late-stage groundwater activity in Gale crater, Mars. *Geophysical Research Letters*, 44, 4716–4724. https://doi.org/10.1002/2017GL073323

Grotzinger, J. P., Sumner, D. Y., Kah, L. C., Stack, K., Gupta, S., Edgar, L., et al. (2014). A habitable fluvio-lacustrine environment at Yellowknife Bay, Gale crater, Mars. *Science*, 343, doi: 10.1126/science.1242777

Gulick, V. C. (2001). Origin of the valley networks on Mars: a hydrological perspective. Geomorphology, 37(3-4), 241-268. https://doi.org/10.1016/S0169-555X(00)00086-6

Ehlmann, B. L. & Edwards, C. S. (2015). Mineralogy of the martian surface. *Annual Reviews of Earth and Planetary* Sciences, 42, 291-315. doi: 10.1146/annurev-earth-060313-055024

Ehlmann, B. L., Mustard, J. F., Fassett, C. I., Schon, S. C., Head III, J. W., Des Marais, D. J., Grant, J. A., et al. (2008). Clay minerals in delta deposits and organic preservation potential on Mars. *Nature Geoscience*, 1, 355-358. doi:10.1038/ngeo207

Hartmann, W. K. & Raper, O. (1974). The new Mars: The discoveries of Mariner 9. NASA Technical Report, 19750005657, 193 p.

Kenkmann, T., Sundell. K. A., & Cook, D. (2018). Evidence for a large Paleozoic impact crater strewn field in the Rocky Mountains. *Scientific Reports*, 8. doi:10.1038/s41598-018-31655-4

Kerber, L., Dickson, J. L., Head, J. W., & Grosfils, E. B. (2017). Polygonal ridge networks on Mars: Diversity of morphologies and the special case of the eastern Medusae Fossae Formation. *Icarus*, 281, 200–219. https://doi.org/10.1016/j.icarus.2016.08.020

Leighton, R. B., Murray, B. C., Sharp, R. P., Allen, J. D., & Sloan, R. K. (1965). Mariner IV photography of Mars: initial results. *Science Reports*, 149 (3684), 627-630. doi: 10.1126/science.149.3684.627

Long, J. C. S., Aydin, A., Brown, S. R., Einstein, H. H., Hestir, K., Hsieh, P. A., et al. (1996). *Rock fractures and fluid flow: Contemporary understanding and applications*. Washington DC: National Academy Press

Lowell, P. (1906). *Mars and its canals*. Norwood Press: Norwood, MA.

Mangold, N., Maurice, S., Feldman, W. C., Costard, F., & Forget, F. (2004). Spatial relationships between patterned ground and ground ice detected by the Neutron Spectrometer on Mars. *Journal of Geophysical Research*, 109. doi:10.1029/2004JE002235

Mangold, N. (2005). High latitude patterned grounds on Mars: Classification, distribution, and climatic control. *Icarus*, 174, 336-359. doi:10.1016/j.icarus.2004.07.030

Masursky, H. (1973). An overview of geological results from Mariner 9. *Journal of Geophysical Research*, 78(20), 4009-4030.

McEwen, A. S., Eliason, E. M., Bergstrom, J. W., Bridges, N. T., Hansen, C.J., Delamere, W. A., et al. (2007). Mars Reconnaissance Orbiter's High-Resolution Imaging Science Experiment (HiRISE). *Journal of Geophysical Research: Planets,* 112. doi:10.1029/2005JE002

McEwen, A. S., Ojha, L., Dundas, C. M., Mattson, S. S., Bryne, S., Wray, J. J., et al. (2011). Seasonal flows on warm martian slopes. *Science*, 333, 740-743. doi: 10.1126/science.1204816

McEwen, A. S., Dundas, C. M., Mattson, S. S., Toigo, A. D., Ojha, L., Wray, J. J., et al. (2014). Recurring slope lineae in equatorial regions of Mars. *Nature Geoscience*, 7, 53-58. https://doi.org/10.1038/ngeo2014

Mege, D. & Masson, P. (1996a). Amounts of crustal stretching in Valles Marineris, Mars. *Planetary and Space Science*, 44(8), 749-781. https://doi.org/10.1016/0032-0633(96)00013-X.

Mege, D. & Masson, P. (1996b). Stress models for Tharsis formation, Mars. *Planetary and Space Science*, 144(12), 1471-1497. https://doi.org/10.1016/S0032-0633(96)00112-2

Milliken, R. E. & Bish, D. L. (2010) Sources and sinks of clay minerals on Mars. *Philosophical Magazine*, 90 (17-18), 2293-2308. https://doi.org/10.1080/14786430903575132

Moore, H. J., Hutton, R. E., Clow, G. D. & Spitzer, C. R. (1987). Physical properties of the surface materials at the Viking landing sites on Mars. USGS Professional Paper, https://doi.org/10.3133/pp1389

Mustard, J. F., Murchie, S. L., Pelkey, S. M., Ehlmann, B. L., Milliken, R. E., Grant, J. A., et al. (2008). Hydrated silicate minerals on Mars observed by the Mars Reconnaissance Orbiter CRISM instrument. *Nature*, 454, 305-309.

Nachon, M., Clegg, S. M., Mangold, N., Schröder, S., Kah, L. C., Dromart, G., et al. (2014). Calcium sulfate veins characterized by ChemCam/Curiosity at Gale crater, Mars. *Journal of Geophysical Research: Planets*, 119, 1991–2016. https://doi.org/10.1002/2013JE004588

Nachon, M., Mangold, N., Forni, O., Kah, L. C., Cousin, A., Wiens, R. C., et al. (2016). Chemistry of diagenetic features analyzed by ChemCam at Pahrump Hills, Gale crater, Mars. *Icarus*, 281, 121–136. https://doi.org/10.1016/j.icarus.2016.08.026

Navarro-Gonzalez, R., Vargas, E., de la Rosa, J., Raga, A. C., & McKay, C. P. (2011). Reanalysis of the Viking results suggests perchlorate and organics at midlatitudes on Mars. *Journal of Geophysical Research: Planets*, 115(E8). https://doi.org/10.1029/2010JE003599

Oehler, D. Z., Mangold, N., Hallet, B., Fairen, A. G., Le Deit, L., Williams, A. J., et al. (2016).Origin and significance of decameter-scale polygons in the lower Peace Vallis fan of Gale crater, Mars. *Icarus*, 277, 56-72. http://dx.doi.org/10.1016/j.icarus.2016.04.038

Ojha, L., Wilhelm, M. B., Murchie, S. L., McEwen, A. S., Wray, J. J., Hanley, J., et al. (2015) Spectral evidence for hydrated salts in recurring slope lineae on Mars. *Nature Geoscience*, 8, 829-832. doi: 10.1038/NGEO2546

Polansky, C. A. & Ahrens, T. J. (1990). Impact spallation experiments: Fracture patterns and spall velocities. *Icarus*, 87, 140-155. https://doi.org/10.1016/0019-1035(90)90025-5

Pollack, J. B., Colburn, D., Kahn, R., Hunter, J., Van Camp, W., Carlston, C. E., et al. (1977). Properties of aerosols in the martian atmosphere, as inferred from Viking lander imaging data. *Journal of Geophysical Research*, 4479-4496. https://doi.org/10.1029/JS082i028p04479

Rodriguez, J. A. P., Sasaki, S., Dohm, J. M., Tanaka, K. L., Strom, B., Kargel, J., et al. (2005). Control of impact crater fracture systems on subsurface hydrology, ground subsidence, and collapse, Mars. *Journal of Geophysical Research: Planets*, *110*(6), 1–22. http://doi.org/10.1029/2004JE002365

Schultz, P. H., Schultz, R. A., & Rogers, J. (1982). The structure and evolution of ancient impact basins on Mars. *Journal of Geophysical Research*, 87(B12), 9803. http://doi.org/10.1029/JB087iB12p09803

Siebach, K. L., & Grotzinger, J. P. (2013). Volumetric estimates of ancient water on Mount Sharp based on boxwork deposits, Gale crater, Mars. *Journal of Geophysical Research: Planets*, 119, 189–198. https://doi.org/10.1002/2013JE004508

Squyres, S. W. & Knoll, A. H. (2005). Sedimentary rocks at Meridiani Planum: origin, diagenesis, and implications for life on Mars. *Earth and Planetary Science Letters*, 240, 1-10. doi: 10.1016/j.epsl.2005.09.038

Stein, N., Grotzinger, J. P., Schieber, J., Mangold, N., Hallet, B., Newsom, H., et al. (2018). Desiccation cracks provide evidence of lake drying on Mars, Sutton Island member, Murray formation, Gale crater. *Geology*, 46(6), 515–518. https://doi.org/10.1130/G40005

Terzaghi, K. (1943). *Theoretical soil mechanics*. New York: John Wiley.

Tanaka, K. L., & Golombek, M. P. (1989). Martian tension fractures and the formation of grabens and collapse features at Valles Marineris. *Proceedings of the 19th Lunar and Planetary Science Conference*, 383–396.

Yen, A. S., Ming, D. W., Vaniman, D. T., Gellert, R., Blake, D. F., Morris, R. V., et al. (2017). Multiple stages of aqueous alteration along fractures in mudstone and sandstone strata in Gale Crater, Mars. *Earth and Planetary Science Letters*, 471, 186–198. https://doi.org/10.1016/j.epsl.2017.04.033

CHAPTER 1
MINERAL-FILLED FRACTURES AS INDICATORS OF MULTIGENERATIONAL FLUID FLOW IN THE PAHRUMP HILLS MEMBER OF THE MURRAY FORMATION, GALE CRATER, MARS

A version of this chapter was originally published by Rachel E. Kronyak et al.:
Kronyak, R. E., Kah, L. C., Edgett, K.S., VanBommel, S. J., Thompson, L. M., R.C. Wiens, R. C., Sun, V. Z., & Nachon, M. (2019) Mineral-filled fractures as indicators of multigenerational fluid flow in the Pahrump Hills member of the Murray formation, Gale crater, Mars. *Earth and Space Sciences,* 6, 238-265.

The article was written by R.E. Kronyak based on image and chemical data collected by the Mars Science Laboratory rover. Co-authors S. J. VanBommel, L. M. Thompson, and R. C. Wiens contributed to specific rover instrument details and assisted with interpretations for APXS and ChemCam data. Co-authors L. C. Kah, K. S. Edgett, and V. Z. Sun assisted in editing of the article prior to submission. The article was assessed by the MSL science team prior to submission and was reviewed by Kirsten Siebach and Paul Bons. After two rounds of reviews, the article was accepted for publication in February 2019.

Abstract

Mineral-filled fractures (veins) are valuable indicators of deformation and fluid flow within a sedimentary package. Information obtained from vein morphology, texture, and chemistry may elucidate the sequence and nature of post-depositional fluid events. Additional information from vein patterns and the interactions between veins and host rock provides insight into fracture formation mechanism(s). The widespread occurrence of veins and other diagenetic features in the sedimentary rock record preserved in Gale crater, Mars, indicates that post-depositional fluids were regionally active considerably later in time than the primary fluvio-lacustrine environments responsible for the deposition of Mount Sharp strata. Here I report on a suite of veins within the Murray formation at the Pahrump Hills locality using the scientific payload of the Mars Science Laboratory (MSL) Curiosity rover. Based on an analysis of vein color, morphology, and texture, and corroborated by vein chemistry, I interpret three distinct vein types at Pahrump Hills: gray veins, white veins, and dark-toned veins. These veins represent distinct, separate episodes of post-depositional fluid flow, suggesting a protracted history of fluid stability in Gale crater. Additionally, I utilize vein patterns across multiple lithologies at the Pahrump Hills field site to indicate hydrofracture as the primary mechanism of fracture formation.

Introduction

Rock fractures are among the most common structural features of the Earth's crust and occur on scales from sub-millimeter microcracks to kilometer-scale extensional fractures and faults (Jaeger et al., 2007; Gudmundsson 2011). Fractures are important indicators of deformation; they provide information about stress conditions at the time of formation. Fluids play a major role in both the formation and preservation of fractures; fractures driven open by elevated fluid pressure are hydrofractures (Long, 1996; Gudmundsson, 2011). Fluids (e.g. meteoric, hydrothermal, diagenetic) commonly utilize fractures for transport and leave behind their signatures in the form of mineral veins. Veins are direct indicators of fluid flow and are crucial in elucidating the diagenetic history of a stratigraphic section. Vein textures can be used to infer the number and timing of fluid events as well as information regarding mineral growth and vein formation. Additionally, veins provide valuable information regarding diagenetic fluid chemistry and provenance, both of which are useful in reconstructing the geochemical conditions of fluids transported through fractures (Bons et al., 2012; Oliver and Bons, 2001).

Observations of Mars acquired from orbital and landed instrumentation reveal heavily fractured surface terrains. The widespread nature of fractured bedrock across the martian surface requires an understanding of sources of stress. Primary sources of stress responsible for fracture initiation include changes in overburden, fluid pressure, thermal cycling, and impacts (e.g. Long, 1996; Engelder, 1993). Diurnal and seasonal temperature variations on Mars induce thermal stresses, resulting in contraction and tension fractures; these are commonly observed as polygonal networks within bedrock and ice-rich terrains (Mellon, 1997; Chan et al., 2007; Eppes et al., 2015). Impact-generated fractures are also common across the martian surface across

broad time scales (Schultz et al., 1982). Additionally, stresses associated with burial, exhumation, and elevated fluid pressure likely play additional roles in the origin and propagation of fractures on Mars.

Evidence for water-rock interactions has been well documented across Mars, at both orbiter and lander/rover scales (cf. Grotzinger and Milliken, 2012; McLennan et al., 2005; Elhmann and Edwards, 2014; Thomas et al., 2007). At the scale of rover observations, diagenetic features provide unambiguous evidence for post-depositional fluid flow and, in Gale crater, include concretions (Stack et al, 2014; Sun et al., 2018), dendritic crystal clusters (Nachon et al., 2016; Kah et al., 2015), crystal pseudomorphs (Kah et al., 2018), veins (Nachon et al., 2014; Nachon et al., 2016; Grotzinger et al., 2014), and fracture-associated alteration halos (Frydenvang et al., 2017; Yen et al., 2017). Despite the pervasiveness of diagenetic features within the rocks of Gale crater, the relative timing of post-depositional fluid events is poorly constrained, as are their formation mechanisms. Here I utilize a suite of veins observed at the Pahrump Hills locality of the Murray formation to infer the number and relative timing of post-depositional fluid events that interacted with the strata of lower Mount Sharp. I use additional information on vein morphology and patterns across various lithologies at Pahrump Hills to inform relationships between fracture mechanism and mineral infill and provide implications for the broader burial and exhumation of Gale crater.

Geologic Context

Gale crater

Gale crater is a 154 km-diameter impact basin located on the martian global dichotomy boundary, a roughly equatorial divide that separates the ancient, heavily cratered southern highlands from the relatively crater-free northern lowlands (Thomson et al., 2011). Gale contains a ~5 km-thick sedimentary package expressed as a mound near the crater center called Aeolis Mons, or informally Mount Sharp (Fig. 1.1) (Wray, 2013; Anderson and Bell, 2010). Through spectroscopic observations, the layers that comprise lower Mount Sharp contain a range of hydrated mineral phases that suggest substantial water interaction (Milliken et al., 2010). Mineral phases are arranged in a distinct package that transitions from phyllosilicate-bearing to sulfate-bearing (Fraeman et al., 2016; Thomson et al., 2011; Ehlmann and Edwards, 2014). This sequence is hypothesized to represent a climate shift on Mars from fluvial-lacustrine to drier, more arid environments (Hurowitz et al., 2017; Thomson et al., 2011). The presence of such aqueous environments in Gale crater led to its selection as the landing site for NASA's Mars Science Laboratory (MSL) Curiosity rover based on its potential to have hosted past habitable conditions (Grotzinger et al., 2012; Wray et al., 2010).

In addition to strata that comprise Mount Sharp, Gale crater preserves extensive sedimentary deposits at and beneath the plains that surround the mountain. The relatively flat-lying regions to the north of Mount Sharp, including the MSL landing site (Bradbury Landing), are referred to as Aeolis Palus; outcrops investigated along Aeolis Palus collectively make up the Bradbury Group (Fig. 1.1).

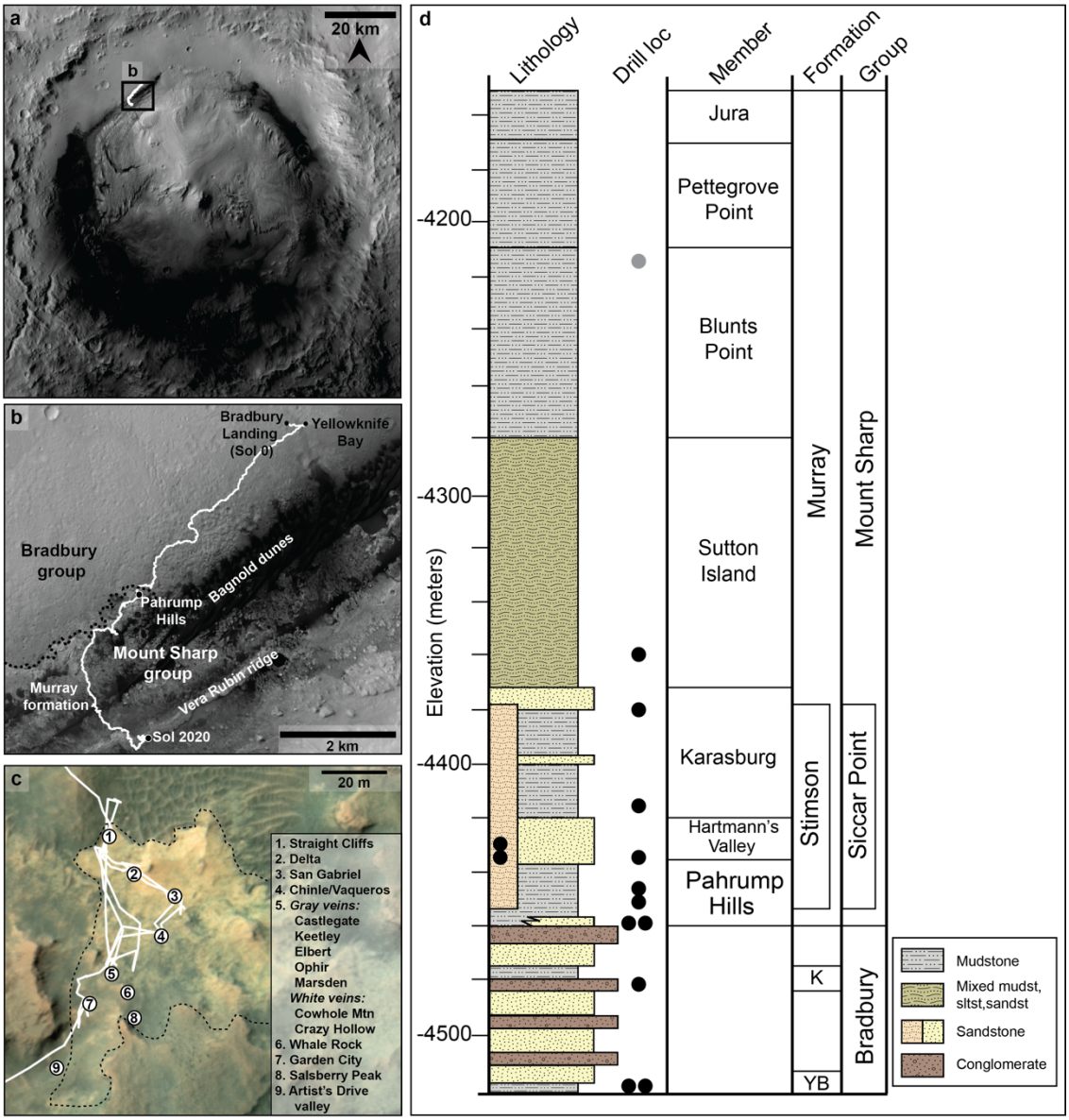


Figure 1.1 Context overview of Curiosity's Gale crater field site. (a) Gale crater with white line indicating Curiosity's traverse from Bradbury Landing to the rover's Sol 2020 (1 September 2018) location on the Vera Rubin ridge. (b) Curiosity's traverse, with black dashed line distinguishing the approximate boundary between exposures of the Bradbury group (Aeolis Palus) and Mount Sharp group strata. The location of Pahrump Hills is indicated by a black dot. (c) Pahrump Hills field site, representing ~12 meters of Murray formation stratigraphy. (d) Composite stratigraphic column of lithologic units encountered by Curiosity, constructed as a function of elevation in meters, courtesy of the MSL Sedimentology and Stratigraphy group. The Pahrump Hills member is the lowermost exposure of the Murray formation (Mount Sharp group). The Mount Sharp and Bradbury groups show an interfingering relationship; the Stimson formation (Siccar Point group) is firmly established as overlying the Murray formation along an erosional unconformity.

The Bradbury Landing site is located near the distal edge of the Peace Vallis fan, an alluvial fan deposit formed through fluvial incision of Gale crater's northern rim (Palucis et al., 2014). Fine-grained mudstones and sandstones observed at Yellowknife Bay indicate suspension settling in a relatively low-energy lake environment (Grotzinger et al., 2013). Beyond Yellowknife Bay, the dominant sedimentary facies of the Bradbury group include stratified to cross-stratified sandstones, conglomerates, and clinoform sandstones, interpreted to represent sedimentation during fluvial and deltaic processes (Williams et al., 2018; Edgar et al., 2018; Rice et al., 2017; Grotzinger et al., 2015). Together, these erosional windows through the surface of Aeolis Palus reveal a long history of deposition defined by interfingered fluvial, deltaic, and lacustrine environments.

Pahrump Hills field site, lower northern Mount Sharp

Strata comprising the lower portion Gale crater's central mound are known as the Mount Sharp group. The dominant component of the Mount Sharp group is the Murray formation, a 300+ meter thick assemblage consistent with fluvial, deltaic, lacustrine, and intermittent aeolian depositional environments. This assemblage is represented by a variety of lithological units and includes cross-stratified siltstone, fine-grained sandstone, and flat-laminated mudstone (Fedo et al., 2017).

The Pahrump Hills member is the lowermost exposed member of the Murray formation and is interpreted based on strata exposed at the Pahrump Hills locality (Fig. 1.2). The Pahrump Hills field site contains approximately 12 meters of sedimentary rock and is divided into several distinct sedimentary facies, including (1) finely laminated mudstone, (2) thickly laminated mudstone-sandstone, and (3) cross-stratified sandstone (Stack et al., 2018; Grotzinger et al.,

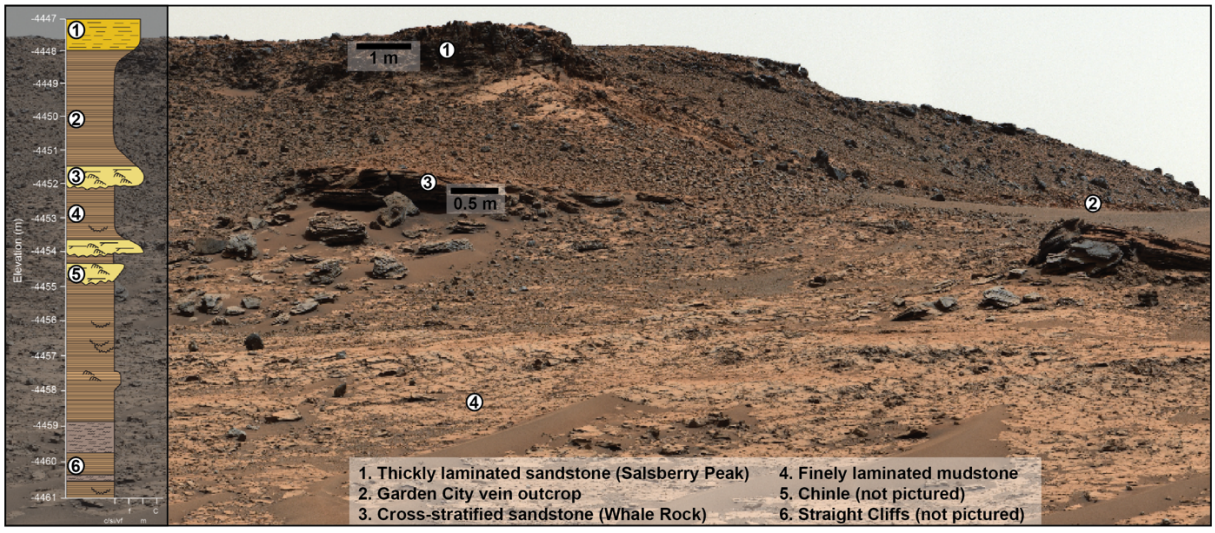


Figure 1.2 The stratigraphic section at the Pahrump Hills locality. The stratigraphic column of facies exposed at Pahrump Hills is superimposed and includes planar laminated mudstone, cross-laminated sandstone, and thickly laminated sandstone (modified after Stack et al., 2018). Portion of Mastcam mosaic (mcam03370) of the Pahrump Hills locality acquired on Sol 778, showing the uppermost ~5 meters of section.

2015). The dominant lithology consists of mudstone that contains abundant sub-mm to mm-thick planar laminations and silt or finer grain sizes (Stack et al., 2018). Two lenses of cross-stratified sandstones named Whale Rock and Newspaper Rock are located at an elevation of -4451 m (Fig. 1.2). These sandstones exhibit fine to very fine grain sizes and are both well-sorted and well-rounded (Stack et al., 2018). The section is capped by the meter-thick laminated fine-grained sandstone called Salsberry Peak. Salsberry Peak is distinctly dark gray and exhibits laminations on the order of several millimeters thick. Laminae are difficult to trace laterally along Salsberry Peak due to the blocky, fractured nature of the outcrop. Together, the facies investigated at Pahrump Hills are interpreted to represent subaqueous lacustrine deposition with episodic fluvial-deltaic progradation (Grotzinger et al., 2015; Stack et al., 2018).

Beyond the Pahrump Hills site, the Murray formation (Mount Sharp group) is unconformably overlain by a younger unit called the Siccar Point group, which exhibits high thermal inertia and truncates the Murray formation along the slopes of lower Mount Sharp (Fraeman et al., 2016; Anderson and Bell, 2010). As viewed in images acquired from orbit, exposures of the Siccar Point group to the east of the Bagnold dunes contain dense networks of mineralized fractures (Kronyak et al., 2018). A portion of the notional Siccar Point group was encountered by MSL just beyond Pahrump Hills and was designated the Stimson formation. The Stimson formation consists of meter-scale cross-bedded sandstones interpreted to represent deposition in an aeolian environment (Banham et al., 2018; Watkins et al., 2016). Thin white Ca-sulfate veins are present within the Stimson formation, indicating Ca-sulfate fluid stability late in Gale crater's history (Watkins et al., 2016; Banham et al., 2018). Additionally, detailed investigations of veins along the Murray-Stimson contact suggest the potential for multiple fluid

events across significant time scales (Newsom et al., 2016; Kronyak et al., 2018). Alteration halos surrounding fractures crosscut both the Murray and Stimson formations, indicating interaction with groundwater following the deposition of the aeolian Stimson formation (Frydenvang et al., 2017; Yen et al., 2017).

These observations made using the instruments of the Curiosity rover indicate that mineral-filled fractures are prevalent features in the rocks of Gale crater and are consistently observed in Bradbury group, Mount Sharp group, and Siccar Point group strata (Nachon et al., 2014, 2016; Banham et al., 2018). Here I perform a detailed investigation of veins observed at the Pahrump Hills locality and associated outcrops (Fig. 1.1b-c). I utilize image data to classify vein types based on color, morphology, and texture. These data are used to infer distinct vein generations and discuss potential formation mechanisms. Additionally, I use geochemical data to corroborate the multigenerational nature of veins at Pahrump Hills.

Methods

Veins were identified and characterized using images acquired by the Curiosity rover's Mastcam, MAHLI, and ChemCam instruments. Mastcam consists of two cameras with different fixed focal lengths; the left Mastcam (M-34) has a 34 mm focal length and f/8 lens, creating a 15° field of view (FOV), and the right Mastcam (M-100) has a 100 mm focal length and f/10 lens, with a 5° FOV (Malin et al., 2017; Bell et al., 2017). Mastcam images were rectified and scaled to allow vein length and width measurements to be performed. Single frame M-100 images acquired following chemical analyses by the ChemCam instrument (see below) were preferred in this study, since most observations on veins were performed <3 meters from the rover. This proximity to the rover helped limit foreshortening and viewing angle distortions in

rectified images. Measurement of vein parameters was completed using ImageJ software. Measurements of exposed vein lengths were made along the apparent center of preserved vein material. Apparent thickness (aperture) was measured across preserved vein material perpendicular to fracture edges. Most veins appear steeply dipping across exposed bedrock, so measured widths likely resemble true vein thickness. If possible, at least 10 width measurements were made on each vein to determine potential variation in vein width.

Detailed information regarding vein texture was obtained using images from the Mars Hand Lens Imager (MAHLI). The MAHLI is a color camera located on the turret of Curiosity's robotic arm and is capable of taking images at scales comparable to a geologist's common hand lens. MAHLI can be placed as close as 21 mm from a surface of interest, resulting in image resolutions of 14 μm/pixel (Edgett et al., 2012; Ghaemi, 2009). Unfortunately, for this study, MAHLI images are limited due to the relief of many veins of interest. Only when Mastcam images indicated robotic arm access to potential internal vein textures were MAHLI images planned and acquired.

Chemical composition of vein-filling material was collected primarily by the ChemCam instrument, which is located on Curiosity's mast, just above Mastcam. ChemCam was designed as a fine-scale probe for elemental compositions (Wiens et al., 2015). It uses Laser-Induced Breakdown Spectroscopy (LIBS), which focuses a pulsed 1067 nm laser beam on a target, creating a plasma from the ablated surface. ChemCam's spectrometer analyzes the plasma for emission lines characteristic of specific major, minor, and trace elements (Maurice et al., 2012; Wiens et al., 2012). ChemCam data are acquired as either a linear or gridded array of laser points with a typical spacing of 1-2 mrad that spans approximately 20 mrad (Wiens et al., 2015). The

fine-scale nature of ChemCam laser shots is ideal for analyzing mm-scale veins around the rover. Vein targets of limited size may only be analyzed by isolated observation points, permitting chemical comparison between veins and adjacent host rock. ChemCam also contains a Remote Micro Imager (RMI) that acquires grayscale images before and after LIBS observations. The RMI field of view is 20 mrad, providing a resolution of ~40 μm/pixel from a distance of 2 meters from the rover mast (Maurice et al., 2012). These images provide geologic context for chemical data and provide the exact position of each LIBS observation point which is critical for distinguishing vein material from adjacent bedrock. RMI images were also used for textural information on targets for which MAHLI images were not acquired.

When possible, additional geochemical information was collected using Curiosity's Alpha Particle X-Ray Spectrometer (APXS). The APXS instrument determines elemental chemistry through Particle-Induced X-ray Emission and X-Ray fluorescence, with data reported in elemental oxide weight percent for major elements and in ppm for trace elements (Campbell et al., 2012). The sample area measured by APXS is 1.5 cm when the sensor is in contact with the target. This field of view is larger than most veins, and surface relief commonly places limitations on the placement of the rover's robotic arm and APXS sensor (VanBommel et al., 2017). As a result, APXS measurements on veins reflect a mixture of both vein and bedrock compositions. However, efforts are made to mitigate geometric constraints and sample heterogeneity (cf. VanBommel et al., 2017, 2016). These efforts are particularly useful at the Garden City vein outcrop, where complex mixtures of vein materials are observed.

Mineral-filled Fractures (Veins) at Pahrump Hills

The bedrock exposures over which Curiosity has traversed in Gale crater are strongly fractured. While most fractures within exposed bedrock remain unfilled, others contain distinct fracture-filling (vein) material. At the Pahrump Hills site, veins are present throughout the ~12 meters of stratigraphic section and display a range of fill materials. I characterize the veins at Pahrump Hills into three endmember types. These endmembers were identified as having distinct patterns of fill and chemical composition and include gray veins, white veins, and dark-toned veins.

Gray veins at Pahrump Hills

Observations

In the lowermost 10 meters of stratigraphy exposed at the Pahrump Hills site, gray veins are observed on exposed bedding planes and rock surfaces, where they occur as primarily positive-relief, nearly vertical ridges along fracture margins. These positive relief ridges contain less aeolian dust than the adjacent host rock surfaces. They appear darker, with a distinct grayer tone than both host rock and white vein fills. Gray veins are rather subtle features; ridges are thin (<1.5 mm in thickness) and, when exposed across patches of bedrock, exhibit heights of 7 mm or less (Fig 1.3). Gray veins display consistent textures; they are characteristically pitted, with pits observed as small, sub-mm depressions that are evenly distributed throughout the ridges. Areas between pits are relatively smooth. While gray veins exhibit fairly uniform textures, their heights are uneven and jagged along the length of the fracture, likely a result of differential erosion of vein material. Individual crystals or crystal growth lines are not resolvable. In some places (e.g.

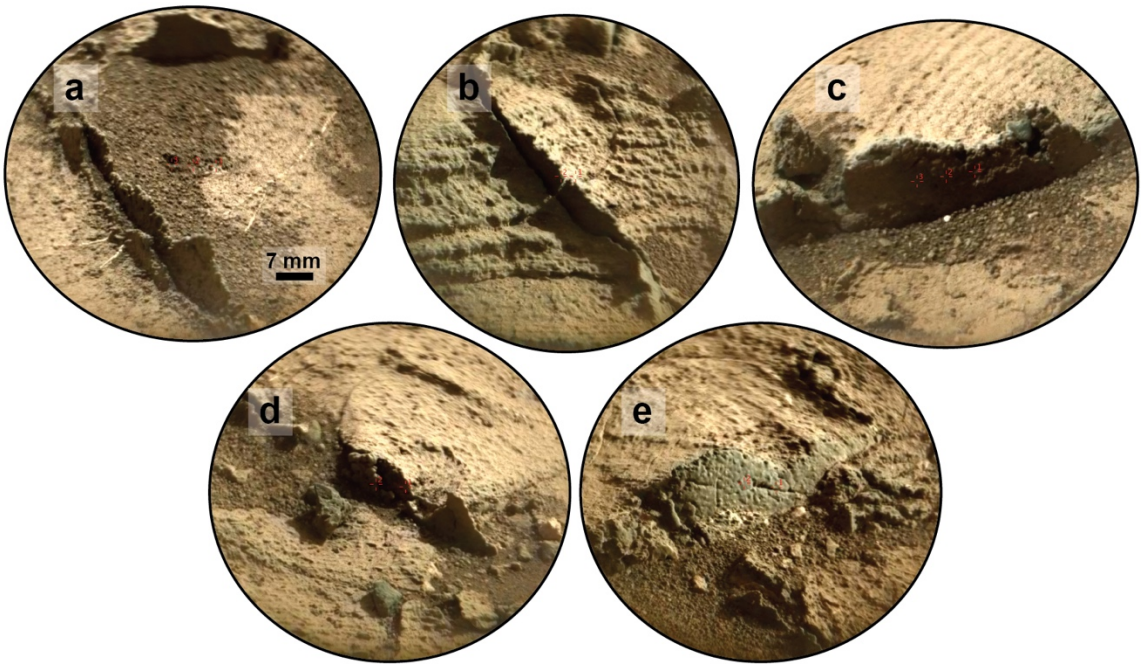


Figure 1.3 Gray veins in the lower Pahrump Hills section, expressing thin, positive-relief ridge morphology along fracture margins. Images are color-merge products that combine color from Mastcam-100 images with ChemCam RMI images following LIBS analyses. Red crosshairs indicate the location of LIBS observation points. Counterclockwise from the upper left, targets include (a) "Castlegate," analyzed on Sol 916, (b) "Keetley," analyzed on Sol 918, (c) "Elbert," analyzed on Sol 903, (d) "Marsden," analyzed on Sol 921, (e) "Ophir," analyzed on Sol 918. Scale bar applies for all images.

ChemCam target “Keetley,” Fig. 1.3b), the laminations of adjacent mudstone appear to curve up into the vertical gray ridge.

Gray veins are also exposed underneath a prominent lens of cross-bedded sandstone called Whale Rock (Fig. 1.4). Here, erosion has removed much of the underlying Murray mudstone, leaving behind an erosion-resistant network of thin vein. Unlike the more isolated and linear expression of gray vein material in the lower 10 meters of Pahrump Hills, gray veins exposed at Whale Rock display a boxwork-like structure, with near-vertical veins intersecting at a variety of angles. Gray veins beneath Whale Rock are also associated with a white vein component. At Whale Rock, white vein material is sandwiched between thin gray veins or exposed as partial remnants (Fig. 1.4). This “sandwich” relationship is commonly observed throughout Pahrump Hills, where gray vein material along fracture margins is bisected by white material along the center, resulting in a gray-white-gray pattern (Fig. 1.5). At Whale Rock, these “sandwich” veins are millimeter-thick but increase to centimeter-thick at the Garden City vein outcrop (elevation -4450 m) and in the few meters below the Salsberry Peak cap rock.

An additional relationship between gray and white veins at Pahrump Hills is observed exclusively at the Garden City vein outcrop, where veins express centimeter-scale thicknesses. Here, gray fragments are observed within the matrix of thicker white veins, suggesting that gray vein material was sufficiently lithified prior to the emplacement of white veins, allowing fragments to be incorporated as coherent pieces (Fig. 1.6).

The chemical composition of gray vein material shows variability within ChemCam LIBS observations (Nachon et al., 2016). Generally, thin gray ridges exhibit elevated magnesium and calcium, although calcium enrichments may represent mixing with or contamination from

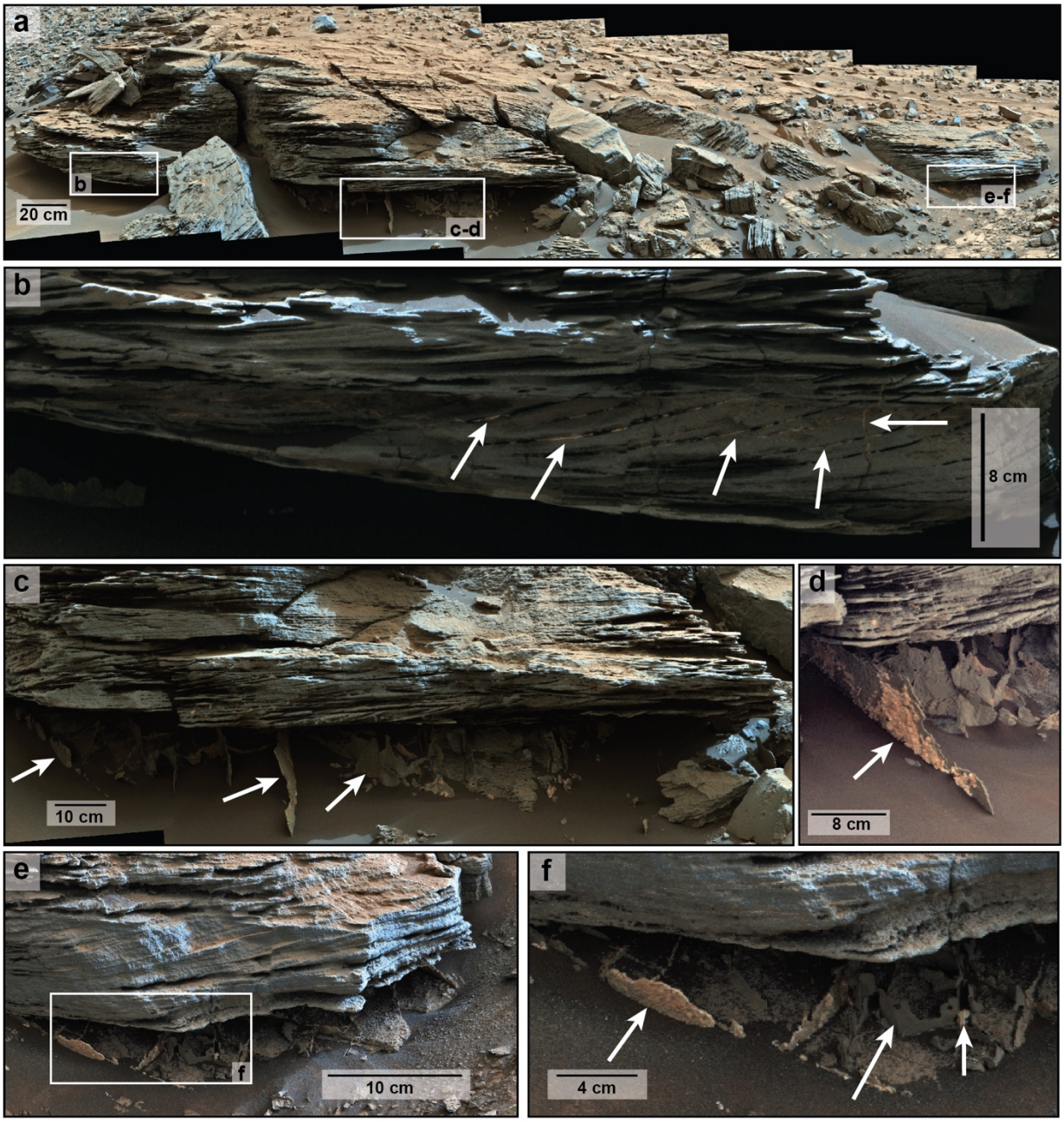


Figure 1.4 (a) Whale Rock outcrop, with cross-bedded sandstone overlying recessive laminated mudstone. Resistant veins are exposed underneath the sandstone lens. Mastcam mosaic mcam03476, taken on Sol 796. (b) White veins are present along cross bed boundaries as well as vertically crosscutting bedding (white arrows). (c) White arrows indicate thin gray veins that comprise the majority of boxwork veins at Whale Rock. (d-f) Preserved white vein material held up by resistant gray vein and (f, far right) sandwiched in between vertical thin gray veins.

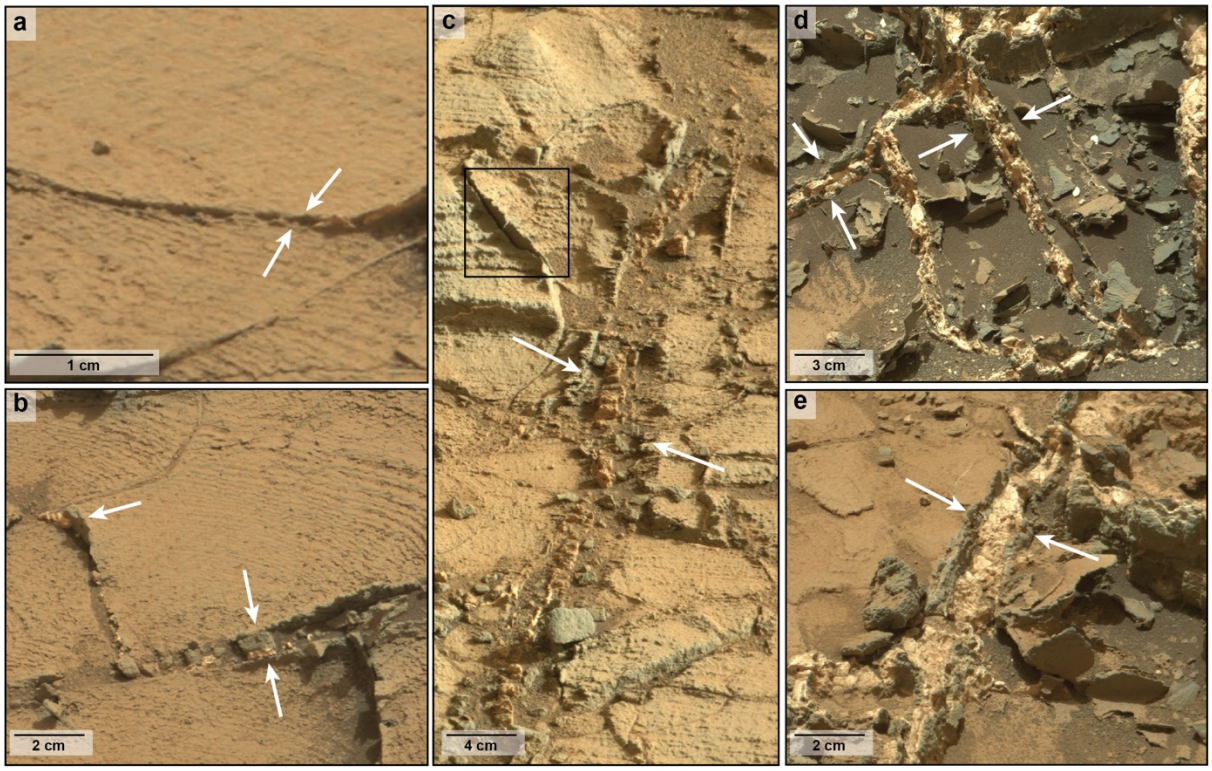


Figure 1.5 Relationship between gray and white veins throughout Pahrump Hills. White veins commonly bisect gray veins, resulting in a gray-white-gray morphology at a variety of scales. Millimeter-thick white veins are bounded on both sides by resistant gray ridges near (a) ChemCam target "Cowhole Mountain," analyzed on Sol 837 (Mastcam image 0837MR0036750020500725E01), (b) and "Calico Mountain," taken on Sol 837 (Mastcam image 0837MR0036760020500763C00). (c) Centimeter-thick gray-white-gray vein (white arrows) near gray vein target "Keetley," indicated by black box (Mastcam image 0918MR0040330000501547E01)." (d-e) Gray-white-gray veins that make up the intersecting vein network at Garden City (Portion of Mastcam mosaic mcam04087 and Mastcam image 0946MR0041570010502002E01, respectively).

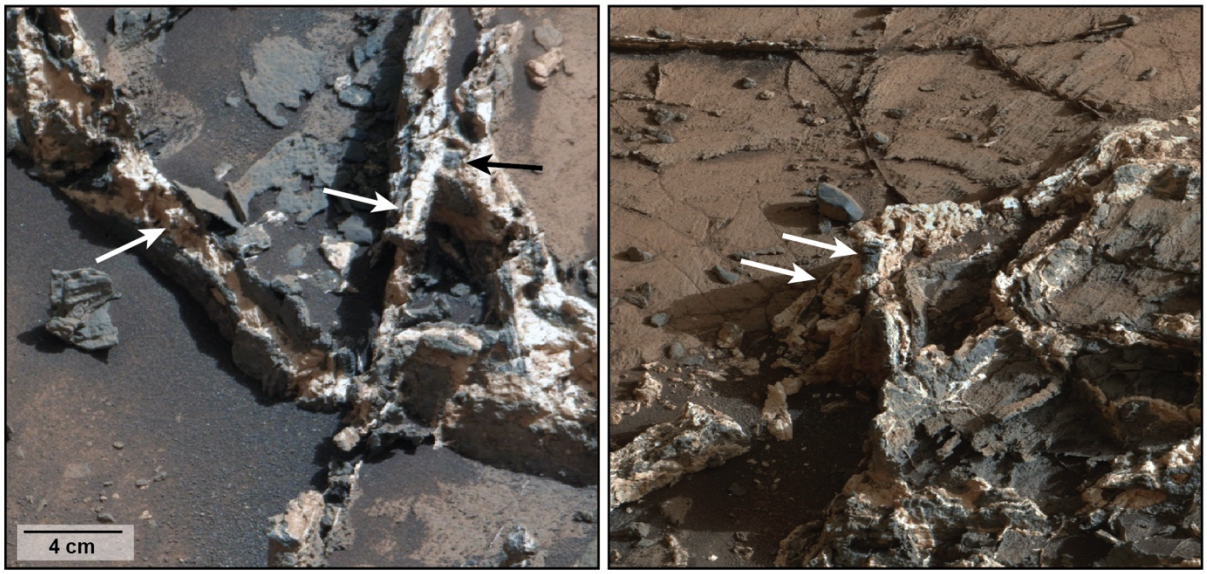


Figure 1.6 Fragmented gray vein material preserved within the matrix of white veins at the Garden City vein outcrop, suggesting a potential time relationship between vein episodes: initial gray vein formation followed by reutilization of fractures and formation of white veins (0926MR00407002050173E01 and 0926ML0040730040402791E01, respectively).

associated white veins. Additionally, ChemCam measured notable but inconsistent enrichments in minor elements manganese, fluorine, strontium, chromium, and rubidium in these gray vein materials (Nachon et al., 2016). During a portion of the Pahrump Hills campaign (Sols 800-980), ChemCam operations were reduced due to the loss of the autofocus capability (Maurice et al., 2016). As a result, most ChemCam sequences during this time consisted of rasters of only up to three observation points.

APXS measurements on gray veins were primarily acquired at the Garden City locality. Unfortunately, outcrop relief prevented APXS from measuring the gray ridges analyzed by ChemCam. Most APXS measurements of gray veins at Garden City (e.g. targets "Coalville," "Alvord Mountain," and "Amboy") contain both gray and white vein fill material within the sensor FOV. Although measurements contain mixtures of gray and white vein material, deconvolution methods confirm the chemical distinction between these two vein phases. APXS analyses indicated that the "Coalville"/ "Alvord Mountain" gray veins are primarily composed of silicon, calcium, iron, sulfur, and magnesium. The amount of calcium present is far in excess of the concentration required to account for all the sulfur as $CaSO_4$. APXS also indicates significant enrichments in minor elements manganese, chlorine, zinc, germanium, and copper, relative to the Murray host rock and surrounding white veins (VanBommel et al., 2017). In contrast, the "Amboy" gray vein material does not exhibit the same excess calcium after accounting for $CaSO_4$, and has significantly higher iron, magnesium, chromium, potassium, and phosphorus, and lower manganese, chlorine, and zinc concentrations than the "Alvord Mountain" gray material. It does exhibit similarly elevated copper and germanium, but with notable enrichments in selenium and gallium also detected. This suggests the possibility of more than one phase of

gray vein material. The germanium levels in both gray vein targets "Amboy" and "Alvord Mountain" represent the highest germanium measurements made by APXS in Gale crater (Berger et al., 2017; Yen et al., 2017).

Interpretations

The occurrence of gray vein material exclusively along fracture margins and its common association with a second white vein phase suggests several possible scenarios to interpret its origin and relationship to white vein fill. First, I must address the initial deposition of gray material. In one scenario, gray material could represent preferential cementation of host rock. This hypothesis is consistent with the observation that gray ridges commonly appear to curve into surrounding mudstone laminations (Fig. 1.3). However, the distinct chemical signature of gray material as well as its concentration along fracture edges suggest that at least some of the gray vein material represents fracture fill not associated with host rock. As a result, I favor the hypothesis that gray material likely represents a distinct episode of fluid flow that resulted in mineral precipitation within fractures and with minor permeation of host rock. The APXS signatures of two gray vein targets in particular ("Amboy" and "Alvord Mountain") also support the possibility of more than one phase of gray vein material. Second, I must address the relationship between gray and white vein material. In one scenario, white mineral fill reflects the chemical evolution of a single fluid event. Although this scenario cannot be discounted, discrete differences in chemistry between gray and white phases would necessitate an abrupt, rather than gradual, shift in fluid chemistry. Rather, I favor an interpretation that gray and white mineralized material reflects distinct fluid flow events.

If gray material represents mineral precipitation during a discrete fluid episode, could such a fluid event be related to other diagenetic features observed at Pahrump Hills? Similar gray material is observed in the lower portions of the Pahrump Hills stratigraphic column, particularly around the Chinle outcrop, where resistant ridges along vertical fractures grade into adjacent bedding planes and laminations (Kah et al., 2018). Gray ridges also share a chemical similarity to other diagenetic features near the base of Pahrump Hills such as dendritic crystal clusters that are enriched in magnesium (Kah et al., 2018; Nachon et al., 2016; Sun et al., 2018). Such spatial and chemical similarity to other diagenetic features supports an interpretation that gray material was deposited relatively early in the diagenetic sequence, prior to complete lithification and loss of porosity in the Murray host rock. Its primary concentration along fractures solidifies its interpretation as a distinct, early phase of pore and fracture filling that pre-dates white veins in the Murray formation.

White veins at Pahrump Hills

Observations

The most abundant fracture-filling material in the exposed Pahrump Hills section is represented by white veins. White veins are recognized by their distinct white infills within fractures. In general, veins are often obscured within the strongly fractured bedrock by poor lighting conditions and sediment infill of low relief areas. However, when visible, white veins crosscut bedding and are oriented vertical to sub vertical. In the lower 10 meters of Pahrump Hills, white veins average ~2.2 mm (n=75) in thickness and occur primarily as isolated fracture fills that dissect exposed bedrock (Fig. 1.7). Additionally, veins crosscut other diagenetic features such as crystal clusters, dendrites, and areas of enhanced relief that are present on

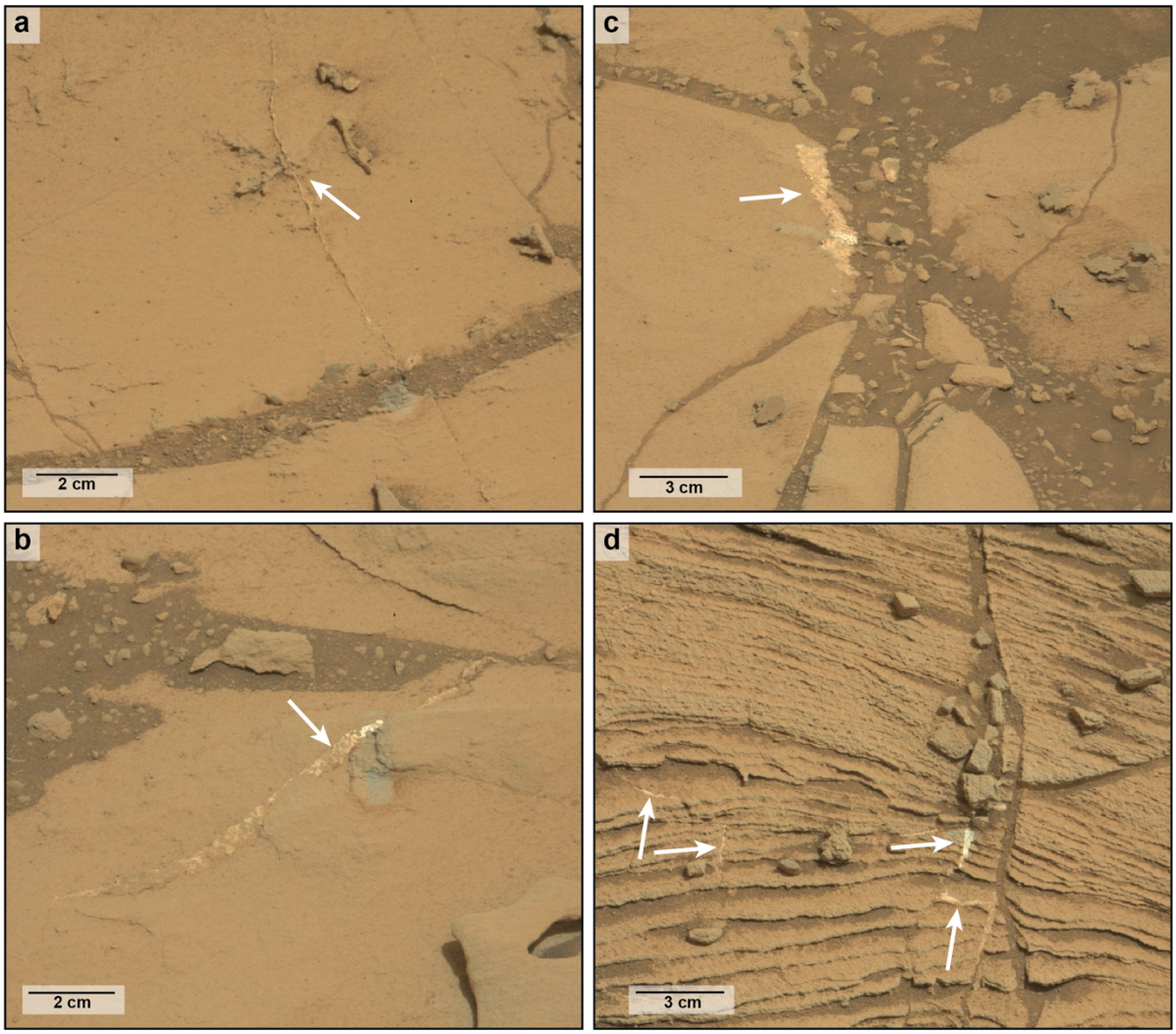


Figure 1.7 White veins in the lower 10 meters of Pahrump Hills. Veins are mm-thick and crosscut Murray mudstone bedding and earlier diagenetic features. Images are Mastcam-100 frames acquired after ChemCam LIBS observations. (a) Target "Straight Cliffs," analyzed on Sol 766, an erosionally resistant vein (white arrow) crosscuts dendritic crystal cluster (Mastcam image 0766MR0032930000403839E01). (b) Target "Delta" analyzed on Sol 781 (Mastcam image 0781MR0034080000404106E01). The circular gray area to the right of the white arrow represents the area where the ChemCam laser shots hit the surface, clearing surface dust. (c) Target "San Gabriel," analyzed on Sol 789, with white vein material exposed obliquely along a fracture margin (Mastcam image 0789MR0034380000500044C00). (d) Target "Vaqueros (Sol 833)," where white vein material is observed at several orientations, both vertical and at a low angle to bedding (white arrows; Mastcam image 0833MR0036680000500719E01).

bedrock surfaces (Fig. 1.7a; Sun et al., 2018). The erosional relief of white veins varies. Most occur flush with, or slightly indented into, surrounding Murray bedrock; less commonly, white veins exhibit slight raised relief (Fig 1.7a). In other locations, white vein material is poorly persevered within fractures and only portions of the vein remain (Fig 1.7c-d).

Less frequently at Pahrump Hills, veins occur at low angles to or concordant with bedding; these bedding-concordant veins appear more common in stratigraphically higher members of the Murray formation (Fedo et al., 2017). However, low-angle veins are evident at the Whale Rock outcrop, where white veins occur in multiple orientations: (1) beneath the sand lens as part of the vertical vein network (Fig. 1.4), (2) concordant with primary laminae within cross beds (Fig. 1.4b), and (3) vertically crosscuting stratigraphy (Fig. 1.4b).

In the lower 10 meters of the Pahrump Hills section, the thickest white veins exhibit a variety of interior textures, as recorded in ChemCam RMI and Mastcam-100 images acquired after LIBS analyses. White veins that that have apertures thicker than 5 mm are ideal candidates for revealing interior textures; however, veins this thick are rare in the lower 10 meters of Pahrump Hills. The vein target “San Gabriel” (maximum aperture ~5 mm) contains distinct parallel lineations. Laminations appear roughly perpendicular to the fracture edge; however, viewing geometry prevents accurate crystal orientations from being made (Fig. 1.7c, Fig. 1.8a). Target “Crazy Hollow” has a maximum aperture of ~7 mm and displays a more massive, pitted texture but also contains as well as a faintly linear fabric approximately perpendicular to fracture walls (Fig. 1.8b).

As noted previously, white veins commonly exhibit a close association with gray veins throughout the Pahrump Hills section. Primarily, white veins exhibit a bisecting relationship,

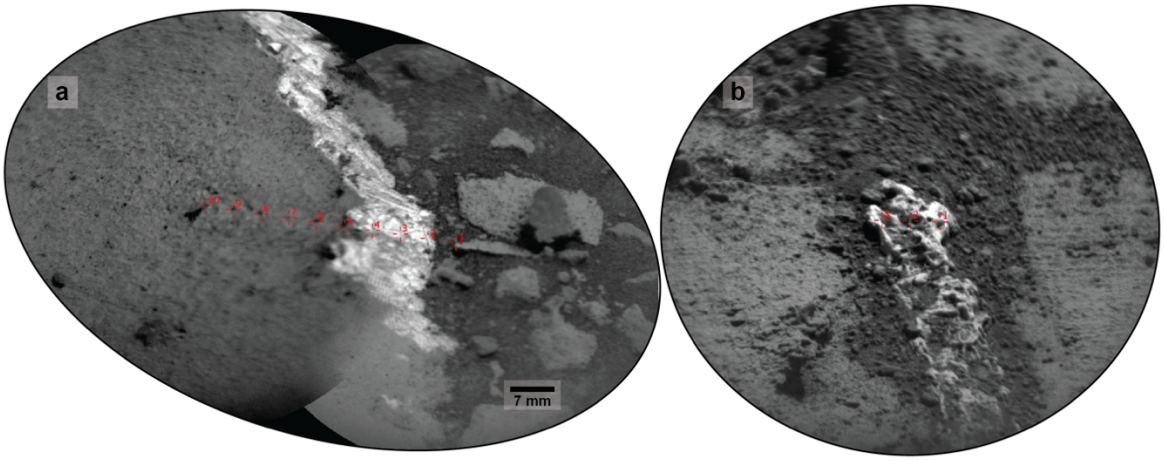


Figure 1.8 Texture of white veins in the lower 10 meters of Pahrump Hills as revealed by ChemCam RMI images. (a) ChemCam target "San Gabriel," which displays parallel interior lineations that appear roughly perpendicular to fracture edges. (b) Target "Crazy Hollow," analyzed on Sol 906, which contains a massive interior texture. Scale bar applies to both images.

with gray material present along fracture edges and white material filling the center of the fracture (Fig. 1.5). Gray vein material is consistently more resistant to erosion than bisecting white material, resulting in inconsistent preservation. This "sandwich" relationship is consistently observed throughout Pahrump Hills, although veins in the lower 10 meters of section are characteristically smaller and more challenging to recognize, especially where white vein material is partially eroded.

Although "sandwich" veins are common throughout Pahrump Hills, both gray and white veins are also observed independent of one another. More commonly, thin white veins occur that show no evidence of gray material along their margins, and occasionally crosscut sandwich veins. Gray veins undissected by white material are less common. The largest veins at Pahrump Hills are located in the uppermost 2 meters of section and occur as positive-relief vein networks at the Garden City outcrop and along the slopes approaching the Salsberry Peak caprock; these thicker-aperture veins always display gray-white-gray patterns.

In ChemCam LIBS observations, all white vein fills exhibit unambiguous enrichments in calcium and sulfur with respect to surrounding host rock and are consistently depleted in all other major elements, indicating a nearly pure phase of $CaSO_4$ (cf. Nachon et al., 2012; Nachon et al., 2014). Strontium is consistently present at low abundances in these veins, likely a result of strontium substitution in minerals containing calcium. Analyses detect, as well, the presence of hydrogen, suggesting the potential presence of a hydrated $CaSO_4$ phase, likely bassanite (Rapin et al., 2016). The "San Gabriel" target shows a slight increase in hydrogen detection levels with ChemCam shot depth, suggesting the possibility of exposure-related dehydration of a hydrated sulfate phase (Ming et al., 2014; Rapin et al., 2016). APXS measurements on white veins (cf.

Yen et al., 2017; VanBommel et al., 2017) corroborate calcium and sulfur concentrations consistent with $CaSO_4$.

Interpretations

White veins are interpreted to have been emplaced relatively late in the diagenetic history of the Murray formation. Crosscutting relationships indicate that white veins occurred after the deposition of other diagenetic features (clusters, dendrites, gray veins), and that all diagenetic phases occurred after Murray formation lithification. At Pahrump Hills, white veins occur as both thin, isolated fracture fills and as bisecting components of gray-white-gray (sandwich) vein patterns. The presence of both isolated and sandwich vein expressions indicates at least one or multiple fluid events; the latter is favored, as fluids at least partially reutilized fractures during the formation of sandwich veins. Sandwich veins crosscut by isolated white veins suggests at least two distinct episodes of fluid flow. Beyond Pahrump Hills, the continued persistence of white veins throughout the broader Mount Sharp and Siccar Point groups implies that calcium sulfate-rich fluids were regionally active following the deposition and lithification of Gale crater sediments (Nachon et al., 2018; Watkins et al., 2016). Additionally, the presence of white calcium-rich clasts along the Murray-Stimson contact and within the lowermost Stimson sandstones suggests the formation of veins prior to the deposition of the Stimson formation (Newsom et al., 2016). These veins, together with those present within the Stimson formation, suggest an extended history of fluid stability within in Gale crater.

Dark-toned veins at Pahrump Hills

Observations

In addition to gray-toned and white-toned vein-filling material, a third vein-filling material is present in isolated regions of Pahrump Hills. This subset of veins is marked by thin (sub mm- to mm-scale) erosionally resistant intersecting veins composed of dark-toned material. Dark-toned veins commonly exhibit high positive relief and a platy, fin-like fabric, suggesting the vein-filling material is substantially hard relative to surrounding vein and host rock material. The surface texture of dark-toned veins is smooth and relatively dust-free; RMI images show an almost specular reflective appearance of dark-toned vein material (Fig. 1.9c). Also, RMI images show that dark-toned material exhibits a layered, chipped appearance (Fig.1.9a-b). While most dark-toned veins are observed upright and vertically oriented, some are also observed as broken pieces of float (Fig. 1.9d-e).

Dark-toned veins are primarily preserved at the Garden City site (elevation -4450 m), where they cross-cut patches of bedrock in between the thick, positive-relief sandwich veins throughout the outcrop. Dark-toned veins intersect sandwich veins at approximate right angles but do not completely crosscut them (Fig. 1.9a-c). The ChemCam target “Bishop” (Fig. 1.9b-c) shows a layered texture along its edges; these edges appear to be bisected by thin, mm-thick white vein material, suggesting a time relationship between dark-toned and thin white veins. Potential float fragments of dark-toned vein material are also observed along the walls of the Artist’s Drive valley beyond Garden City (Fig. 1.9).

ChemCam observations of dark-toned veins at Garden City show consistent enrichments in iron and potassium relative to local Murray host rock; several analyses also indicated

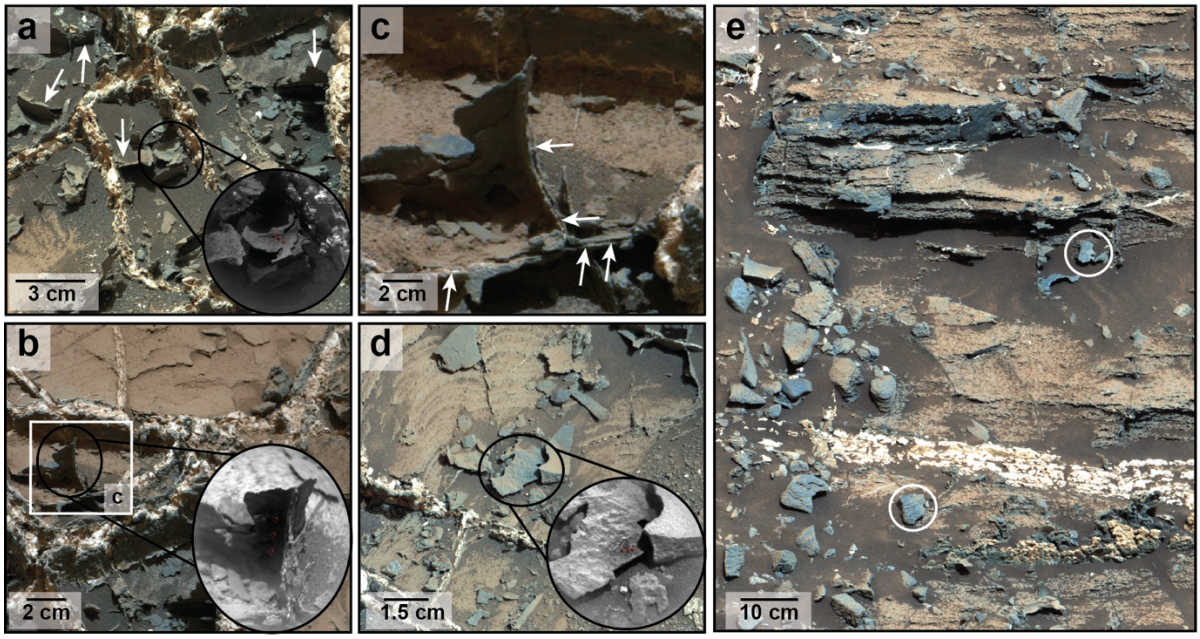


Figure 1.9 Dark-toned gray veins at Pahrump Hills. (a) Dark-toned veins exhibit positive relief and intersect with sandwich veins at Garden City at roughly 90-degree angles (white arrows). ChemCam target "Hakatai," analyzed on Sol 935 is indicated by the inset RMI image and shows a layered texture near the dark-toned vein edges (portion of Mastcam mosaic mcam04087). (b) ChemCam target "Bishop," analyzed on Sol 946, is shown in the ChemCam RMI image and expresses an upright, flaky appearance (Mastcam image 0946MR0041560000502000E01). (c) Close-up view of "Bishop;" white arrows indicate the potential presence of thin, white veins bisecting layers of dark-toned vein material. (d) ChemCam target "Temblor," analyzed on Sol 948 which exhibits a smooth, shiny surface texture (Mastcam image 0948MR0041690000502040E01). (e) Float pieces of potential dark-toned vein material (white circles) along the west wall of the Artist's Drive valley (Sol 950; portion of Mastcam mosaic mcam04175).

elevations in strontium and phosphorous. Especially noteworthy are high abundances (up to >5 weight %) of fluorine, suggesting the presence of fluorite (Nachon et al., 2016; Forni et al., 2015a,b, 2016).

APXS measurements on dark-toned target "Kern Peak" indicated elevated levels of silicon, iron, chromium, potassium, phosphorus, germanium, and lead relative to nearby Murray bedrock. "Kern Peak" also exhibited enhanced gallium and strontium (highest concentration detected at Gale crater by APXS), as well as arsenic levels just above detection limits.

Interpretations

The texture, color, and geochemistry of dark-toned vein material suggest that it is the product of a distinct episode of fluid flow, separate from the events that produced both gray- and white veins in the Pahrump Hills section. The limited spatial distribution of dark-toned veins (Garden City and adjacent areas of Artist's Drive) suggests that the diagenetic fluid event responsible for their formation was relatively localized, or that its distribution was constrained by a pre-existing concentration of fractures. The presence of germanium and other trace elements in dark-toned veins may indicate that hydrothermal and/or mildly acidic fluids were responsible for this vein-forming event (Yen et al., 2017). The occurrence of dark-toned veins in between sandwich veins and the lack of cross-cutting at Garden City suggests that sandwich veins were already in place and potentially acted as fluid barriers and constraining the spatial distribution of dark-toned veins. This suggests that dark-toned veins may represent one of the most recent diagenetic fluid events to interact with the Murray bedrock at Pahrump Hills. However, the occurrence of dissecting white veins suggests that at least one fluid episode of Ca-sulfate followed the formation of dark-toned veins.

Garden City vein outcrop: a case study

The uppermost 2 meters of the Pahrump Hills section record a dramatic change in the overall character and complexity of veins. Thin, sub-mm white veins continue to be present throughout the section. However, in these upper 2 meters of section, which occur between Whale Rock and Salsberry Peak, veins show substantially thicker apertures. For example, along the slopes approaching Salsberry Peak, veins reach up to 5 centimeters thick and exhibit exposed lengths in excess of 4 meters. Vein complexity is best displayed at Garden City, a vein-rich outcrop located along the east wall of the Artist's Drive Valley two meters beneath Salsberry Peak (Fig. 1.10). At Garden City, veins protrude from Murray formation host rock in an exposure covering ~10 m^2. The Curiosity science team investigated Garden City for approximately 20 sols (first approach on Sols 926-939; second approach from Sols 944-949), collecting extensive Mastcam, MAHLI, ChemCam, and APXS data (Fig. 1.10). Although veins are abundant features in the Murray formation as a whole (Nachon et al., 2016; Nachon et al., 2018), the Garden City outcrop represents the most extensive analysis of vein materials carried out by the MSL science team to date. Analysis of Garden City included 14 ChemCam targets, 7 APXS targets, and high-resolution MAHLI image mosaics of several discrete target areas (Table 1.1; Fig. 1.10).

The veins that comprise the Garden City outcrop exhibit diversity in size and texture. All three types of vein-filling materials (gray, white, and dark-toned) occur together at Garden City. Centimeter-thick sandwich veins, made up of both gray and white vein material, crosscut the local Murray mudstone host rock and comprise the erosionally resistant network of intersecting veins (Fig. 1.11). These sandwich veins show substantial positive relief, exhibiting heights up to

Table 1.1 Vein and bedrock targets analyzed by Curiosity's remote sensing instruments at the Garden city vein outcrop, shaded by vein type (white, white veins; light gray, gray veins; dark gray, dark-toned veins). Most targets analyzed by the APXS instrument represent a mixture of gray and white vein material; for these targets, the box color designates the intended primary component in the APXS FOV.

Sol	Target Name	Target Type	Data Acquired
928	"Ouray"	Gray vein	ChemCam
	"Hoskinnini"	White vein	ChemCam
	"Swasey"	Bedrock	ChemCam
935	"Aneth"	Gray vein	ChemCam
	"Hakatai"	Dark-toned vein	ChemCam
937	"Coalville"/ "Alvord Mountain"	Mixed gray/white vein	ChemCam, APXS, MAHLI
	"Indianola"	Mixed white/gray vein	ChemCam, APXS, MAHLI
	"Hyrum"	Bedrock	ChemCam, APXS
939	"Live Oak Canyon"	White vein	ChemCam, APXS, MAHLI
	"Idyllwild"	Gray vein	ChemCam
	"Blanco Mountain"	White vein	ChemCam, APXS, MAHLI
946	"Elsinore"	Dark-toned vein	ChemCam
	"Bishop"	Dark-toned vein	ChemCam
	"White Mountain"	White vein	ChemCam
	"Kern Peak"	Dark-toned vein	MAHLI, APXS
948	"Temblor"	Dark-toned vein	ChemCam
	"Lindavista"	White vein	ChemCam
	"Amboy"	Mixed gray/white vein	APXS, MAHLI

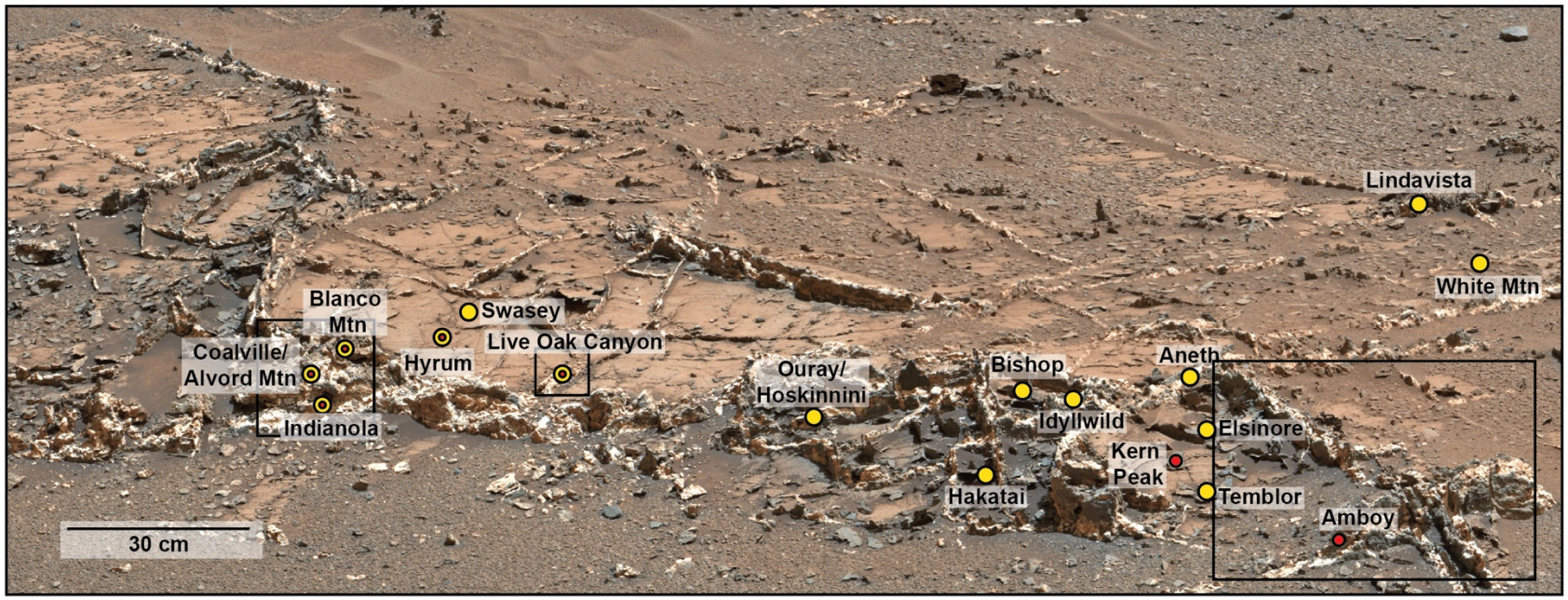


Figure 1.10 Mastcam mosaic of Garden City vein complex (portion of Mastcam mosaic mcam04068) acquired on Sol 925 prior to the rover's approach to conduct remote and contact science observations. Circles indicate the locations of ChemCam (yellow) and APXS (red) targets on veins across the outcrop; black boxes indicate the locations of high-resolution MAHLI image mosaics

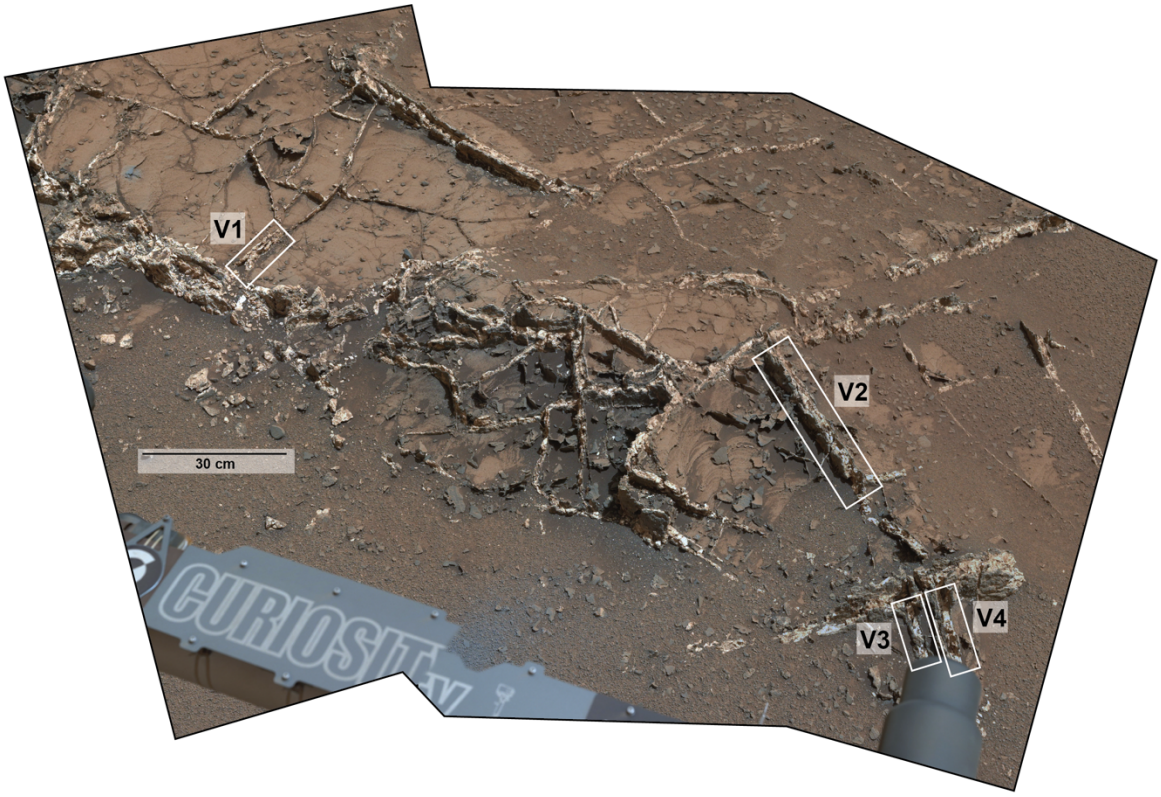


Figure 1.11 Mastcam-34 mosaic (mcam04150) of the Garden City vein complex acquired on Sol 944. Centimeter-thick sandwich veins comprise the positive-relief intersecting network. Sandwich veins that were imaged with the MAHLI camera are indicated by white boxes (Vein 1 (V1), see Fig. 1.12; V2, see Fig. 1.13; V3, see Fig. 1.14; V4, see Fig. 1.15).

~5 cm above the adjacent host rock. Dark-toned veins are present both upright in between sandwich veins at Garden City and as fragments of float scattered across the outcrop. Additionally, vein strike and dip measurements show significant variability across Garden City (see Barnes et al., 2018).

White veins at Garden City

White material is the dominant vein fill at Garden City and includes veins that vary in thickness from 1.2 mm to 2.9 cm. Four thicker aperture (>1 cm) white veins were imaged using MAHLI; these contain a diversity of interior textures. These veins are designated V1-V4 (Fig. 1.11; for corresponding MAHLI mosaics see Figs. 1.12-15). White material most commonly displays a smooth, massive texture that is continuous across the width of the vein (Figs. 1.14-15). In V1 and V3, white vein material exhibits distinct lineations roughly perpendicular to fracture edges (Fig. 1.12b-c; Fig. 14). Although faint and commonly obscured by dust, lineations are roughly parallel to one another.

White veins contain significant eroded portions, commonly concentrated near vein centers (Fig. 1.12a; Fig. 1.13a-b); V3 contains an apparent eroded line along the vein center (Fig. 1.14). Small eroded pits are also observed within white material (Fig. 1.15b). Erosion of the central region of V2 emphasizes a unique texture of the residual white vein material (Fig. 1.13). Remaining vein material in V2 exhibits an elongate blocky, almost bladelike form, with rounded terminations facing the fracture center.

Also associated with cm-thick sandwich veins at Garden City are extremely thin (sub-mm) white veinlets. These veinlets are observed within sandwich veins along marginal gray vein

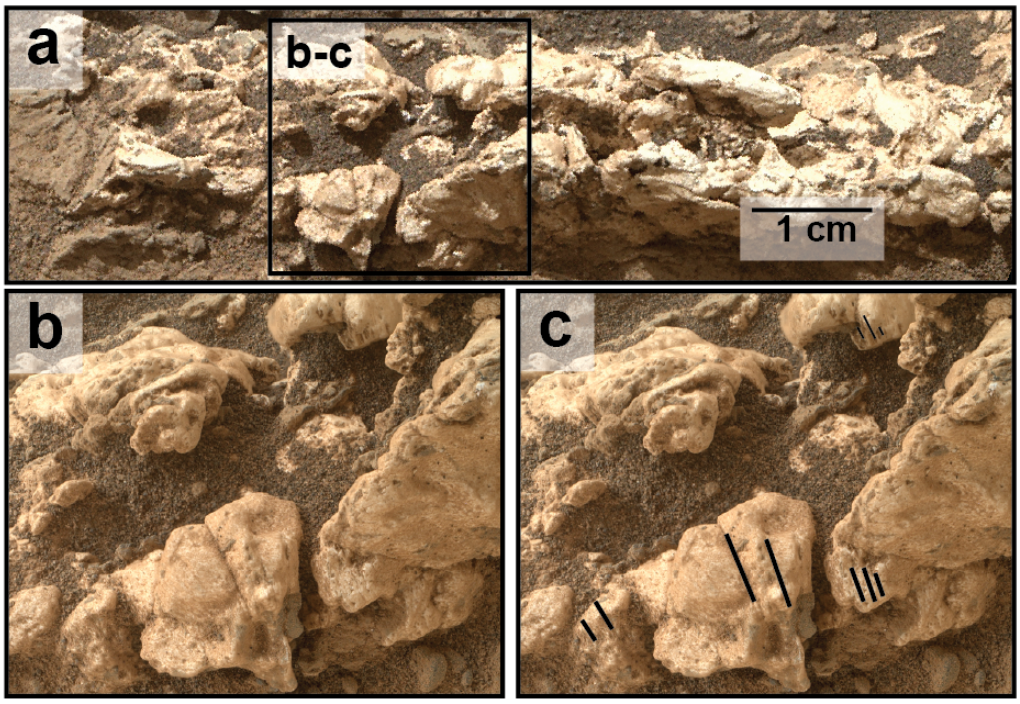


Figure 1.12 Portion of MAHLI mosaic of Garden City Vein 1 (V1); vein target "Live Oak Canyon," imaged on Sol 937. (a) V1 is ~1 cm thick and contains fairly eroded white vein fill along the vein center. (b-c) Vein fabric exhibits roughly parallel lineations. MAHLI image 0937MH0004760050303426C00.

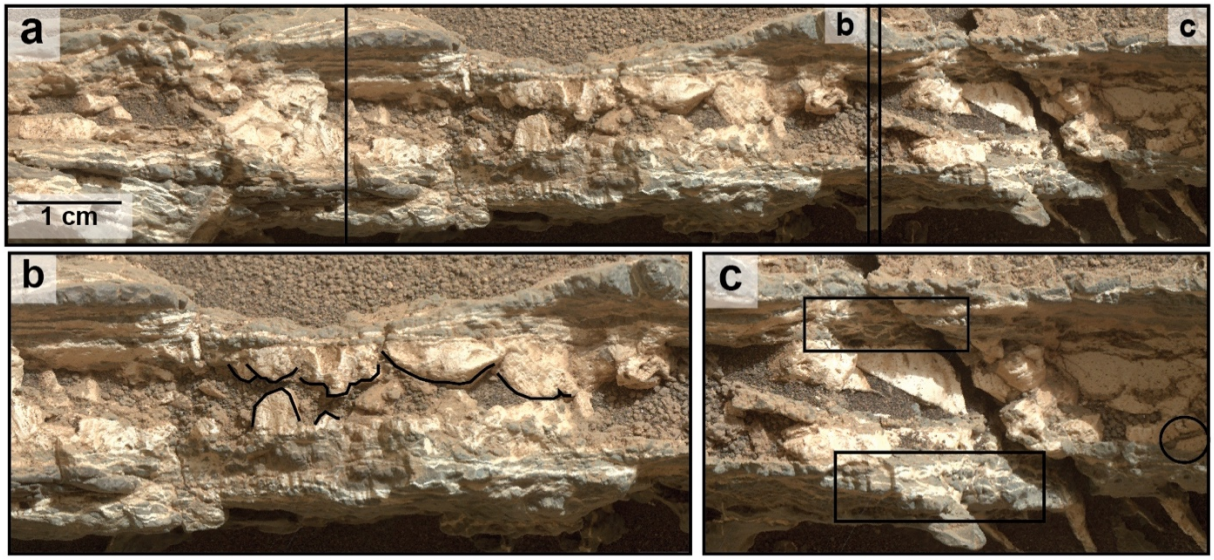


Figure 1.13 (a) Portion of MAHLI mosaic of Garden City Vein 2 (V2) imaged on Sol 948. Vein is ~1 cm thick and expresses a variety of interior textures, with significant eroded portions in the vein center. (b) White vein material growth likely originated along the fracture walls and proceeded inward towards the vein center, producing an elongate blocky, "toothy" crystal texture. (c) Boxes indicate the presence of sub-mm-thick veinlets parallel to the vein interior. Circles indicate gray material entrained within the white vein matrix. MAHLI images 0948MH0004920000404116R00, 0948MH0004920000404118R00, 0948MH0004920000404120R00, 0948MH0004920000404122R00, 0948MH0004920000404124R00, 0948MH0004920000404126R00, 0948MH0004920000404128R00.

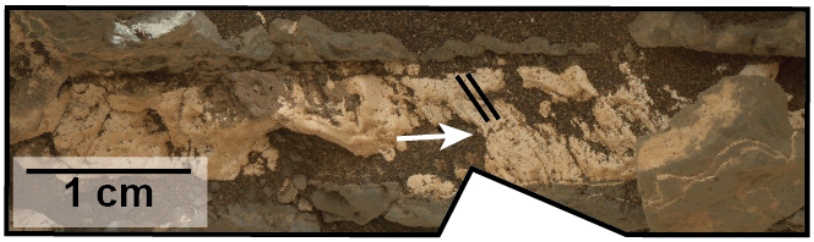


Figure 1.14 Portion of MAHLI mosaic of Garden City Vein 3 (V3) acquired on Sol 946. The left side of the vein exhibits a smooth, massive texture, whereas white exhibits a faint linear fabric, oriented obliquely to the vein walls (black lines). A potential median line is observed (white arrow) along the vein center. MAHLI images 0946MH0004900000303878R00, 0946MH0004900000303880R00.

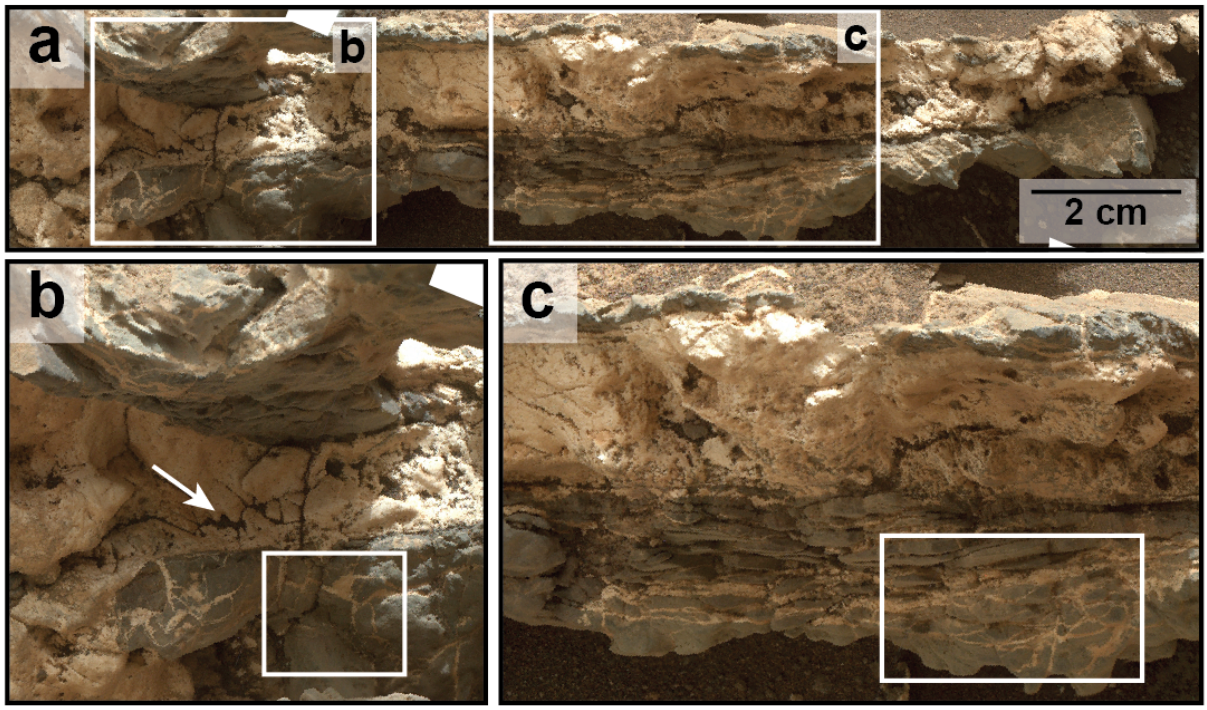


Figure 1.15 Portion of MAHLI mosaic of Garden City Vein 4 (V4) acquired on Sol 946. (a) White material in V4 exhibits a dominantly massive texture, with a few eroded and pockmarked regions. (b) Arrow indicates a potential median line, separating the white vein material into upper and lower segments. Veinlets are observed in adjacent gray vein material (white box). (c) Thinly laminated texture of gray vein material along the bottom fracture margin (white box). This lower portion of gray vein material is significantly thicker than the gray material on the opposite side of the vein. Gray material is permeated by sub-mm white veinlets. MAHLI images 0946MH0004900000303870R00, 0946MH0004900000303878R00, 0946MH0004900000303880R00, 0946MH0004900000303880R00, 0946MH0004900000303884R00, 0946MH0004900000303886R00.

material (Fig. 1.13c; Fig. 1.15c). Veinlets are primarily oriented parallel to central white vein material, although V4 veinlets merge into the thick white vein center (Fig. 1.15b).

Gray veins at Garden City

Gray vein material is also abundant at Garden City and is only observed along the margins of white veins. Similar to gray veins lower at Pahrump Hills, gray material at Garden City is commonly symmetrical on either side of the fracture; however, some exhibit variable thickness. When this asymmetry is present, gray vein material shows a thinly layered texture (Fig. 1.15c). This laminated fabric is highlighted by the presence of small white veinlets that penetrate gray material along lamination boundaries (Fig. 1.15c).

In addition to along fracture margins, gray material also occurs as fragments within the interior of thick sandwich veins at Garden City (Fig. 1.6). These fragments give many of the thick veins at Garden City a chaotic, brecciated texture.

Interpretation of Garden City veins

The thickness and accessibility of veins at Garden City permitted a detailed investigation of interior vein textures. Such textures are useful in determining formation mechanism(s) as well as crystal growth history (Bons et al., 2012; Philipp, 2008). Many of the centimeter-thick sandwich veins at Garden City indicate the potential for multigenerational formation. In the lower Pahrump Hills section, gray vein material is uniformly thin. However, at Garden City, gray vein material commonly displays a laminated texture, indicating fracture along zones of weakness; these layers may be the result of gray vein material deposited from multiple fluid injections. In addition, the presence of sandwich veins throughout Pahrump Hills, and primarily at Garden City, indicates that fractures were commonly re-utilized by multiple generations of

fluid of substantially different origins and/or chemistry. The consistent sandwich vein morphology, with resistant gray fracture edges bisected by white Ca-sulfate, implies that the fluid(s) responsible for the deposition of gray material likely occurred first, followed by later vein deposition from Ca-sulfate-saturated fluids.

On Earth, episodes of enhanced fluid pressure are commonly intermittent, with repetitive cycles of high pressure and fracturing followed by subsequent pressure lowering (due to fluid expulsion) and mineral precipitation (Cosgrove, 2001; Barker, 2006). While veins may form in a single event, the process of fracture opening and filling is commonly a repetitive process, with each event leading to the incremental deposition of vein material. This process is commonly referred to as "crack-seal" growth and reflects the sequential addition of vein material within a fracture (Ramsay 1980; Cox, 1987). The inability to resolve veins at the micron scale prevents a true estimation for the number of crack-seal events that resulted in the largest veins at Pahrump Hills. Terrestrial vein studies indicate that the addition of vein material is on the order of tens to hundreds of microns for individual crack-seal events (Dabi et al., 2011; Bons et al., 2012). Although vein textures indicate that crack-seal growth mechanisms likely operated at Garden City, the estimated number of fluid events is likely underestimated.

During crack-seal events, crystal growth can occur on both sides of opening fracture. Commonly associated with crack-seal veins are median lines. A median line is recognized as a discontinuity along the central region of the vein fabric (Hilgers and Urai, 2002). Inward-growing (syntaxial) veins are commonly asymmetric and have off-centered median lines. Growth can also occur from one side of fracture only (unitaxial) and lack a median line. In some cases, small mineral grains or host rock fragments comprise the median zone of a fibrous vein (Bons et

al., 2012; Ramsay 1980). In these scenarios, the median line serves as the site of mineral nucleation and growth occurs outward towards the fracture walls. Known as antitaxial veins, crystal fabrics are commonly fibrous and symmetrical (Wiltschko and Morse, 2001; Bons et al., 2007). The mechanism of fluid flow and precipitation of antitaxial veins is poorly understood. The predominantly symmetrical nature of antitaxial vein fibers is unexpected for repetitive crack-seal events. Additionally, antitaxial growth requires two planes of crystal growth, on either side of the median zone; this scenario is difficult to model mechanically (Bons et al., 2012; Barker 2006). Other mechanisms have been proposed to describe antitaxial growth; for example, the force of crystallization may be sufficient in driving wall rock apart and forming a vein (Wilschko and Morse, 2001; Bons and Montenari, 2005; Passchier and Trouw, 2005). In this case, elevated fluid pressure and fluid flow are not strictly required. Instead, dissolved material diffuses to and precipitates at an opportunistic site (usually a pre-existing crack or other surface), where the pressure from crystal growth maintains host rock displacement and addition of vein material (Barker, 2006; Wiltschko and Morse, 2001).

At a smaller scale, vein microstructures can be used to infer conditions during vein growth, such as fracture opening history and crystal growth direction (Passchier and Trouw, 2005; Hilgers and Urai, 2002). Thick white veins at Garden City encompass a variety of textures, including massive, laminated, and elongate blocky. Common vein-forming minerals on Earth include quartz, carbonates, sulfates, and fluorite, and often exhibit elongate blocky crystal morphologies (Wendler et al., 2016; Bons and Montenari, 2005; Cobbold et al., 2013). These patterns are the result of growth competition; neighboring seed crystals grow on a fresh fracture surface and proceed inward towards the fracture center (Ramsay, 1980; Wiltschko and Morse,

2001). As inward growth occurs, some crystals outgrow one another and become wider and/or elongate along the growth direction (Bons et al., 2012). The V2 vein at Garden City is reminiscent of this texture and suggests that crystal growth initiated along the fracture walls and proceeded inward; the resulting texture is inward-facing crystals (Fig. 1.13).

Several of the largest veins at Garden City exhibit suspect median zones, observed as eroded, roughly linear gaps near vein centers. In these cases, Ca-sulfate material exhibits a primarily elongate morphology, reminiscent of syntaxial growth that originated at the fracture margins and proceeded inward. In addition, the absence of material within these median zones suggests that crystal growth likely did not proceed in an antitaxial fashion. As a result, I interpret the majority of relatively undeformed veins at Garden City to be the result of multigenerational fluid flow and dominantly syntaxial crystal growth.

The laminated nature of several thick Ca-sulfate veins at Garden City indicates that the host mudstone may have exhibited repetitive opening. Growing vein crystals commonly reflect and record changing states of stress within host rock material during mineral precipitation (Gudmundsson 2011; Gudmundsson and Brenner, 2001). For example, vein lineations may be oriented obliquely to fracture edges or exhibit a curved morphology; this indicates either a change in fracture opening direction, some form shear motion of wall rock, or incremental crack-seal growth reflecting varying stress fields (Mandl, 2005). Curved vein fibers reflect changing stress fields during formation and may be valuable in tracking the deformation history of a vein or vein set (Passchier and Trouw, 2005). In other cases, curves may reflect later deformation of originally straight, orthogonally oriented vein fibers (Gudmundsson 2011; Passchier and Trouw, 2005).

Laminations that are parallel to vein walls are generally good indicators for incremental growth of crack-seal veins. Alternatively, laminated textures may reflect the crystal orientation of large, singular vein-forming crystals. In this scenario, weathering of large anhydrite/gypsum crystals may reveal the crystallographic orientation, visible as apparent laminations on the vein surface. Depending on the orientation of these crystal facets, they may be confused with increments of crack-seal layers. Unfortunately, image resolution of even the largest veins at Garden City prevents us from definitively interpreting vein laminations as crack-seal increments or as crystallographically controlled lineations. I therefore utilize additional lines of evidence to support incremental and repetitive fracture and vein growth at Pahrump Hills.

A complex fracture opening history is additionally supported at Garden City by the chaotic, brecciated nature of the majority of veins at Garden City. The thickest regions of Ca-sulfate veins at Garden City contain gray inclusions; most appear rounded and likely derive from wall rock and/or precursor gray vein material. Wall rock inclusions are common in terrestrial veins at the micron scale and are interpreted to be the result of crack-seal processes along fracture edges (Ramsay 1980; Cox 1987).

Based on vein morphology, fabric, and cross-cutting relationships at Garden City, I interpret that at least 3 distinct events of post-depositional fluid flow occurred. Relatively early in the diagenetic sequence, magnesium-rich fluids permeated the Murray formation, depositing material along fractures (gray veins) and within pore space as clusters and dendrites (Kah et al., 2018; Sun et al., 2018). The bisecting nature of white veins indicates that calcium sulfate fluids entered the system later in time than gray veins. Crack-seal textures indicate that the injection of calcium sulfate fluids was episodic. The brecciated nature and thick aperture of many white

veins at Garden City suggest that fluid pressure was elevated at the time of vein formation, relative to the mm-scale nature of previously described veins throughout Gale crater and Pahrump Hills. White veins observed within the Siccar Point group (i.e. Stimson formation), which sits unconformably atop the Murray formation beyond Pahrump Hills (Banham et al., 2018), suggests that fluid flow involving calcium sulfate occurred over a relatively prolonged timespan within Gale crater. A third, iron-, potassium-, and fluorine-rich fluid resulted in the deposition of dark-toned veins at Garden City and Artist's Drive; however, the timing of this event is poorly constrained. Bisection of dark-toned veins by thin, sub-mm white veins indicates that an even later episode of Ca-sulfate fluid flow occurred at Pahrump Hills.

Beyond Garden City: Salsberry Peak and Artist's Drive

In addition to localized exposures of intersecting vein networks (i.e. Garden City), thick, long veins are present in the ~2 meters above Garden City; these veins are exposed along the valley walls that comprise the Artist's Drive valley. Along Artist's Drive, veins are centimeter-thick, can be traced up to ~4.2 m long, and contain dominantly white fill material. Although many are flush with surrounding host rock, several exhibit positive relief and stand several centimeters above the surface, particularly those along the east wall of Artist's Drive. These vertical, erosionally resistant veins are white along their centers and contain gray material along their edges, similar to, but larger in scale than the sandwich veins at Garden City and lower in the Pahrump Hills section. Other thick veins appear to contain gray material mixed within their white matrix. Unfortunately, abundant debris on the Artist's Drive slopes make vein edges difficult to resolve.

The stratigraphic section at Pahrump Hills is capped by the Salsberry Peak sandstone, best exposed along the east wall of Artist's Drive. Although most of the dense, intersecting vein networks are present in the underlying mudstone, veins are also observed within this well-cemented capping unit (Fig. 1.16). Several white veins can be traced from underlying mudstone upwards into the Salsberry Peak sandstone without any apparent change in thickness. However, veins do not penetrate through the entire thickness of Salsberry Peak. It is unclear whether veins arrest at a sharp boundary within the Salsberry Peak sandstone or dissipate upward; their ends are not clearly visible within the outcrop. Despite similarity in color, gray veins clearly penetrate the base of Salsberry Peak.

Discussion

Evidence for hydrofracture at Pahrump Hills

Mineralized fracture networks are conspicuous features on the surface of Mars across rover and orbital scales. In Gale crater alone, networks of cemented fractures have been described from HiRISE images and are present in several locations within the material that comprises Mount Sharp (Siebach and Grotzinger, 2013; Kerber et al., 2017, Milliken et al., 2014, Kronyak et al., 2018). For instance, decameter-long resistant ridges that intersect to form a dense boxwork network occur at a discrete stratigraphic level of the Mount Sharp group (Siebach and Grotzinger, 2013). Within the topographically lower, yet younger Siccar Point group, similar cemented fractures are present that form a highly ordered polygonal networks exposed over >10 km^2 (Kronyak et al., 2018).

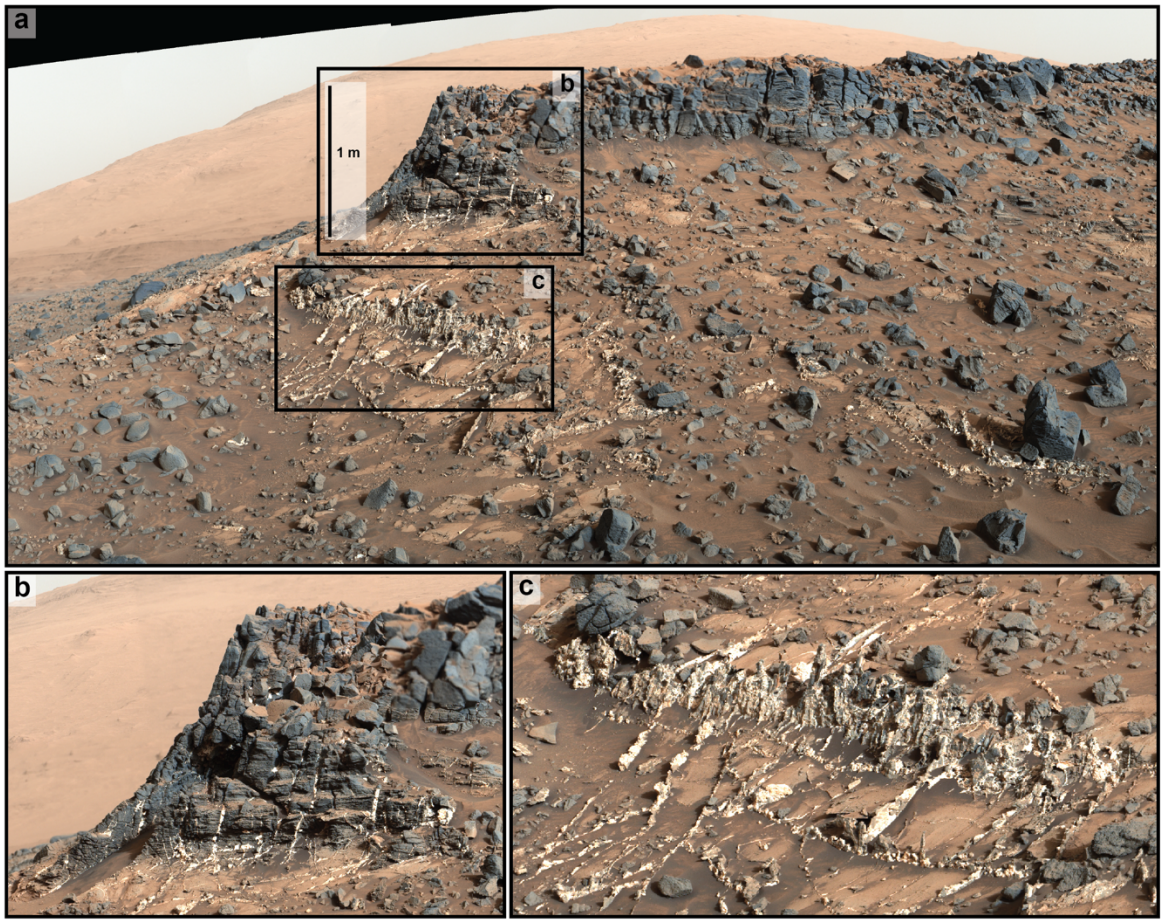


Figure 1.16 Vein interactions at the Salsberry Peak caprock. (a) Portion of Mastcam mosaic acquired on Sol 938 (mcam04119). Salsberry Peak is a ~1-meter-thick thickly laminated sandstone lithology that caps the underlying laminated mudstone. (b) Parallel white veins penetrate the mudstone-sandstone contact. (c) Positive relief vein networks are present just beneath Salsberry Peak. The Garden City complex is located just out of frame beneath the bottom of the mosaic.

At the rover scale, calcium sulfate veins have been described in nearly all rock units encountered by Curiosity (Nachon et al., 2014; Nachon et al., 2016; Nachon et al., in prep.). Millimeter-thick calcium sulfate veins crosscut all three members of the Yellowknife Bay formation (Bradbury group) of Aeolis Palus (Nachon et al., 2014; Grotzinger et al., 2014). Throughout Curiosity's traverse across the Bradbury group, Ca-sulfate veins remain mm-scale in aperture (Kronyak et al., 2015).

Elucidating the mechanisms responsible for producing the veins at Pahrump Hills and the broader Gale system requires an understanding of the mechanics and stresses involved during fracture formation. Fractures propagate through rock bodies when applied stresses exceed rock strength (Gudmundsson 2011; Jaeger et al., 2007). In a sedimentary basin, there are numerous potential mechanisms to increase pressure; these stresses may be lithostatic, tectonic, thermal, or impact, or fluid-induced (Long et al., 1996; Gudmundsson 2011; Mandl 2010). Lithostatic stresses include those induced by changes in overburden, either by burial (compaction) or exhumation and erosion. Tectonic stresses include processes associated with plate motion such as folding and faulting (Long et al., 1996). Thermal stresses occur as rocks cool and/or contract, which commonly occurs in igneous regimes and in desiccating environments. Impact-induced stresses occur following collisions with extraterrestrial objects.

Finally, stresses may form from increased fluid pressures within a sedimentary package, resulting in the formation of hydrofractures. Aside from increasing burial depth, fluid pressures may build up within a sedimentary basin during fluid volume changes, which may be induced by a variety of mechanisms including temperature increase, hydrocarbon generation, and any chemical reactions that involve the release of volatiles (Cosgrove 2001; Long et al., 1996). These

volume changes are especially important in reactions involving the hydration and dehydration of calcium sulfate minerals. The hydration of anhydrite to gypsum involves complex dissolution and precipitation reactions, resulting in a significant volume increase of ~60% and subsequent swelling pressure (Schieber et al., 2017; Philipp 2008). Fluid pressure may also become elevated during disequilibrium compaction and in or below rocks with low permeabilities that act as impermeable seals (Philipp 2008; Hart et al., 1995).

In the Earth's crust, most fractures in sedimentary rock are the result of natural hydrofracturing - the direct result of overburden and elevated fluid pressure (Gudmundsson 2011; Cosgrove 2001). Hydrofractures are extensional fractures driven open by overpressurized fluids within a succession (Mandl 2010; Gudmundsson 2011). Although burial depth and overburden pressure play significant roles in the overall stress state in a basin, hydrofractures can occur at any depth within the crust as long as fluid pressures are high enough (Long et al., 1996). In order to generate a hydrofracture, fluid pressure must exceed the sum of the tensile strength and minimum compressive stress of the rock body (Terzaghi, 1943). The propagation direction, length, and overall organization of hydrofractures are strongly affected by both the orientation of stress axes as well as the mechanical properties of the host rock, including rock strength, grain size, porosity and permeability, layering, and the potential presence of pre-existing fractures (Passchier and Trouw, 2005; Jaeger et al., 2007).

A hydrofracture origin has previously been suggested to explain vein formation in Gale crater (Schieber et al., 2017; Caswell and Milliken, 2017; Nachon et al., 2014). Veins at Yellowknife Bay (Bradbury group) exhibit similar mm-scale thicknesses as the Ca-sulfate veins observed throughout the Pahrump Hills section. Veins are dominantly vertical (i.e. crosscut

bedding planes) and exhibit random strike dimensions (orientations) and intersection angles, suggesting the maximum principal stress direction was primarily vertical and that veins formed as extension fractures (Schieber et al., 2017; Caswell and Milliken, 2013). The high density of horizonal veins at the Sheepbed mudstone-Gillespie sandstone is interpreted as additional support for hydrofracture, as fluid deflection along contacts is a common phenomenon for hydrofractures propagating through layered rock bodies with differing mechanical properties (Weertman, 1980). I use these previous studies on veins at Yellowknife Bay as a basis on which to build a model for hydrofracturing at Pahrump Hills. While I recognize that in reality, extensional fractures fall within a range of fracture formation end members, here I present further evidence to show that elevated fluid pressures and hydrofracturing played a role in the formation of veins at Pahrump Hills.

Primary lines of evidence in support of hydrofracture are observed as vein-host rock interactions and vein behavior at lithologic boundaries (Whale Rock and Salsberry Peak). Layer boundaries play a significant role in the behavior of propagating hydrofractures. Orientations may change across bed boundaries as stress fields rotate upon encountering lithologies with different mechanical properties (Gale et al., 2014; Philipp et al., 2013). The majority of veins in the Pahrump Hills section are oriented at high angles to bedding. However, veins around the cross bedded Whale Rock outcrop exhibit multiple behaviors (Fig. 1.4). First, veins that comprise the boxwork network underneath Whale Rock arrest at the sandstone lens. While it cannot be observed directly whether veins arrest or change directions at the mudstone-sandstone contact, the shift in host rock lithology and associated contrast in mechanical properties likely played a role in vein propagation. Hydrofractures commonly arrest at contacts between stiff and

soft layers; this may be the case at Whale Rock, where the well-cemented sandstone lens served as an effective barrier to fluid flow for veins propagating through the underlying softer mudstone (Gudmundsson and Brenner, 2001). Second, veins are observed oriented along bedding planes within the Whale Rock cross-bedded sandstone. Assuming a similarly oriented stress field, hydrofractures commonly utilize planes of weakness as pathways for fluid flow, such as bedding planes or other discontinuities (Hayashi 1997; Gale et al., 2014). These veins therefore suggest that propagating cracks exploited pre-existing discontinuities within the host rock as paths for fluid flow. Third, vertically oriented veins are observed crosscutting the laminations of the Whale Rock sand lens, suggesting the maximum stress direction was vertical. These three distinct vein patterns suggest the potential for up to 3 different hydrofracture events: one during which fluids followed along planes of weakness (sandstone cross beds); one with fluid pressures insufficient to penetrate the mudstone-sandstone contact; one with fluid pressures high enough to penetrate and crosscut the sand lens.

By contrast, veins in the vicinity of the Salsberry Peak caprock exhibit drastically different behaviors. I refer to Salsberry Peak as a "caprock" for several reasons. First, the Salsberry sandstone physically caps the Murray mudstone at the Pahrump Hills site; its elevation marks the top of the ~12-meter-thick stratigraphic section at the Pahrump Hills locality. Second, its designation as a cap suggests that it may have served as an impermeable seal underneath which pressures built up. Veins exhibit a drastic increase in thickness in the uppermost 2 meters of Pahrump Hills strata approaching Salsberry Peak. Vein thickness is roughly proportional to fluid overpressure; higher fluid pressures typically result in veins with thicker apertures (Gudmundsson 2012; Philipp 2012). Lithology also plays a role in the resulting thickness of a

vein; in general, weaker rocks have a tendency to develop fractures and veins with wider apertures than stronger rocks (Gudmundsson 2011; Gudmundsson and Brenner 2001). This may contribute to why the largest, most complex veins are observed within the weaker Murray mudstone rather than other stronger lithologies at Pahrump Hills. Although fluid pressure and lithology are important components, the final shape and thickness of a vein are the result of complex and accumulated fracturing events over time.

Unlike the veins underneath Whale Rock, several veins at the mudstone-sandstone contact at Salsberry Peak unquestionably penetrate the contact and continue into the overlying sandstone unit. Although arrest is common for fractures that encounter layer boundaries, hydrofractures may also penetrate a contact if fluid pressure is sufficiently maintained behind the advancing crack tip. After penetrating a contact, fractures will commonly taper off as a reflection of dissipating fluid pressure (Gudmundsson 2012; Gudmundsson and Brenner, 2001). At Salsberry Peak, several white veins (inferred to consist of Ca-sulfate) advance from the underlying mudstone into the capping sandstone with little to no visible change in direction or vein thickness. Although mechanical data for the Salsberry Peak sandstone are unavailable, it exhibits a higher resistance to erosion relative to the underlying Murray mudstone and comprises the mesas that form the Artist's Drive valley walls. The presence of veins crossing the boundary between materials with contrasting mechanical properties suggests that fluid pressure was high enough for hydrofractures to penetrate the contact.

Implications for burial depth

A hydrofracture origin for the veins at Pahrump Hills has implications for elucidating the overall burial and exhumation history of the units that comprise Mount Sharp. Vertical stresses

associated with burial and hydrofracturing are a function of sediment density, burial depth, and fluid pressure. Modeling efforts estimate a range of possible burial depths (1.2 km to 4.5 km) to form the millimeter-thick calcium sulfate veins observed at Yellowknife Bay, based on input parameters of rock strength (Caswell and Milliken, 2017). However, models that account for overburden pressure alone are insufficient in resolving the conditions under which hydrofracturing may have occurred. Hydrofracturing can occur at any depth, provided fluid pressures are high enough to exceed rock strength (Long et al., 1996). Episodic events, such as heat input from impacts, may sufficiently increase pore fluid pressure to initiate fluid migration and hydrofracture. The multigenerational nature of veins at Pahrump Hills supports episodic fluid injection. Large, chaotic vein networks and the penetration of veins across lithologic boundaries indicate that fluid pressure was elevated and high enough for hydrofracturing to occur. Additionally, local capping lithologies such as Salsberry Peak likely played an important role in constraining fluid flow, resulting in a build up of fluid pressure and emplacement of veins with large apertures (e.g. Garden City). The high fluid pressure induced by an impermeable caprock may suggest that the veins within the Murray formation might not have required extensive burial depths to form.

Source(s) of vein-forming fluids

Determining the source of fluids responsible for the deposition of veins at Pahrump Hills is a difficult task. In general, the formation of a vein involves a number of steps, including dissolution, fluid transport, and precipitation of vein minerals (Fisher and Brantley, 1992). Material deposited in veins can be transported via advective or diffusive processes (Dabi et al., 2011; Bons et al., 2012; Barker 2006). During advective processes, fluids are derived externally

and are transported along fracture networks or host rock void space. Advectively transported fluids may travel over long distances and flow commonly occurs through fractures and/or pore space. Alternatively, material may be transported by diffusion, where fluids derive from the local host rock and flow is driven by gradients in chemical potential (Barker 2006). Fluid flow within a basin is affected and driven by a number of factors including compaction, convection, topography, osmosis, potential gradients (hydraulic and/or chemical), and porosity.

Lacustrine environments contain a variety of chemical constituents primarily depending on fluvial input. Common lake cations include sodium, calcium, potassium, and magnesium, whereas anions tend to be more variable. Sulfates are typically produced as a result of sulfide mineral oxidation (i.e. pyrite) or by the weathering of previously deposited evaporitic minerals (James and Dalrymple, 2010). In general, evaporite deposits are common constituents of lake depositional environments, as lake water chemistry and volume are subject to rapid changes such as solute input, precipitation, and evaporation rates. Hydrothermal fluids may introduce additional solutes and further alter lake chemistry (James and Dalrymple 2010).

Interpretations of depositional environments within the Murray formation include a range of progradationally stacked lake facies consistent with an overfilled lake basin model (Fedo et al., 2017; James and Dalrymple, 2010). Facies range from lacustrine to lacustrine-margin to aeolian and reflect a variety of wet to likely intermittently dry environments (Stein et al., 2018). As a result, periods of intermittently dry conditions in the Gale lake system likely favored the deposition of evaporitic minerals. Facies containing sulfates include mudflats, where wet-dry conditions result in significant subaerial exposure and growth of evaporite crystals (Kah et al., 2018). Sulfates may also derive from shallow-water facies, where evaporite minerals precipitate

from saturated brines. While such brines and/or evaporite horizons have not been observed in situ in Mount Sharp strata, the consistent abundance of sulfate minerals in veins indicates that evaporite minerals in the subsurface were likely mobilized by circulating groundwater and became the fluid source for the veins at Pahrump Hills. In particular, the widespread nature of Ca-sulfate veins requires a broad, regional source of subsurface sulfate.

The interpretation of hydrofracturing as the primary mechanism of vein formation at Pahrump suggests that sulfate minerals were sourced from a subsurface reservoir and were brought upward during fracturing to relieve excess fluid pressures. Groundwater hydration of subsurface evaporitic minerals and the corresponding volume increase may have provided an additional source of enhanced fluid pressure that helped drive fractures open. Fluids moving upward through fractures will lose heat into fracture walls; this cooling may be sufficient to initiate precipitation of veins within open fractures. Rising fluids and subsequent decompression may also contribute to mineral precipitation.

Broader implications for water stability and astrobiology in Gale crater

The widespread nature of mineralized veins indicate that extensive fluids were stable and active for an extended period following the deposition and lithification of the Gale crater strata. Generally, individual veins require a relatively large volume of water to form constituent mineral fill, with a water-rock ratio on the order of ~10^3-10^4 (Philipp 2012). While the absolute timing of fluid interaction cannot be resolved, the pulsed, multigenerational nature of veins at Pahrump Hills suggests that water activity was intermittently stable over a long period of time.

The fluid interactions inferred from veins provide important constraints on the chemical composition of post-depositional water and implications for depositional environments in Gale

crater. Over the past several decades, veins have also become areas of interest for astrobiological studies. Shallow water to evaporitic environments contain an abundance of microbial communities. The growth of primary sulfate phases in such evaporitic environments has been observed to encounter, invade, and potentially incorporate material from microbial mat communities (James and Dalrymple 2010). In recent studies, several authors report on the preservation of microfossils that were transported and trapped in vein-forming fluids (Trewin and Knoll 1999; Hofman and Farmer 2000; Kirkland et al., 1999; Bons et al., 2007; Bons and Montenari, 2005; Elburg et al., 2002; Pederson et al., 1997; Schopf et al., 2012; Zhou et al., 2015).

Beyond Pahrump Hills, Curiosity has encountered sporadically thick veins on a similar scale as those observed at Garden City, with interior structures and textures resolvable in MAHLI and RMI imaging (Fig. 1.17). These cm-thick veins offer relatively easily accessible targets that represent environments suitable for the potential preservation of microfossils within vein crystals. To date, clear biosignatures have not yet been identified within vein materials.

Conclusions

Veins observed by the Curiosity rover at the Pahrump Hills locality indicate a protracted history of post-depositional fluid stability in Gale crater. Veins at Pahrump Hills exhibit characteristically thicker, more complex morphologies than those previously observed by the Curiosity rover. Chemical evidence from the ChemCam and APXS instruments indicate chemically distinct batches of fluid were responsible for the deposition of at least 3 vein types at Pahrump Hills: Mg-rich gray veins, Ca-sulfate white veins, and Fe-, K-, and F-rich dark-toned veins. Chemical similarities between gray veins and other diagenetic features at Pahrump Hills,

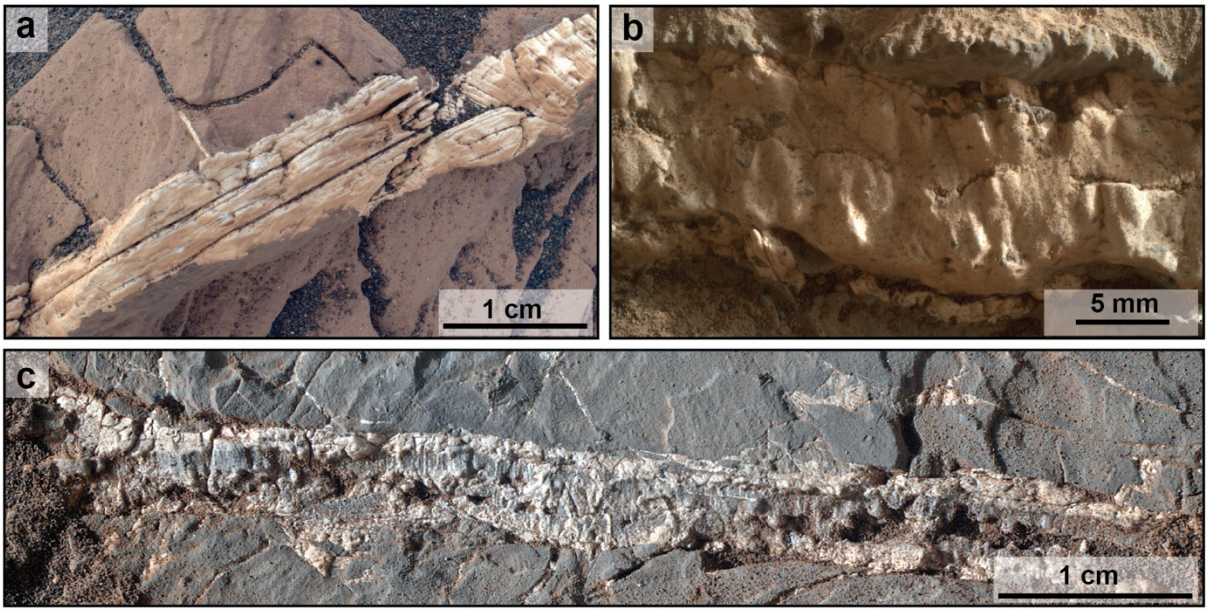


Figure 1.17 Centimeter-thick veins imaged with the MAHLI camera beyond Pahrump Hills. Vein targets include: (a) "Tofte," imaged on Sol 2083, exhibits a finely laminated, linear texture parallel to vein walls along the left side of the vein, and at a high angle to vein walls on the right. MAHLI image 2083MH0007490000802265R00, (b) "Palmwag," imaged on Sol 1276, which contains potentially multigenerational white material, entrained gray fragments, and a distinct median line. MAHLI image 1276MH0004580000404503R00, (c) "Rona," imaged on Sol 1937, which shows a complex interior of multigenerational inward-facing white and gray vein material. MAHLI images 1937MH0001710000703855R00, 1937MH0001710000703855R00, 1937MH0001710000703861R00, 1937MH0001710000703863R00.

including crystal clusters and dendrites, suggest that they were deposited relatively early in the diagenetic sequence and preceded the formation of white Ca-sulfate veins (Kah et al., 2018; Sun et al., 2018). White veins that bisect gray veins indicate that fluids commonly utilized preexisting planes of weakness for transport through the Murray formation. Thicker, more complex white veins suggest the possibility for multiple pulses of Ca-sulfate fluid flow and mineralization through crack-seal microtextures. The presence of complex networks of thick, intersecting veins near the top of the Pahrump Hills section, and vein behavior across lithologic boundaries, indicate localized enhancements of fluid pressure during burial, implying hydrofracturing as the primary mode of vein formation.

Acknowledgements

This work was supported by NASA's Mars Science Laboratory program. I graciously thank the many individuals who provide operational support to the Curiosity rover and its instruments. I thank Jim Bell and his research team at Arizona State University for producing the rectified Mastcam images used in this study. Images acquired by MSL through Sol 2003 are available through the PDS Geosciences Node. I thank reviewers Kirsten Siebach and Paul Bons for incredibly helpful feedback that greatly improved the content and clarity of the manuscript.

References

Anderson, R.B. and Bell III, J.F. (2010) Geologic mapping and characterization of Gale crater and implications for its potential as a Mars Science Laboratory landing site. *The International Journal of Mars Science and Exploration* 5, 76-128. doi:10.1555/mars.2010.0004

Bell, J.F. III, Godber, A., McNair, S., Caplinger, M.A., Maki, J.N., Lemmon, M.T., Van Beek, J., et al., (2017) The Mars Science Laboratory Curiosity rover Mastcam instruments: Preflight and in-flight calibration, validation, and data archiving. *Earth and Space Science 4, 396-452.* doi:10.1002/2016EA000219

Barker, S.L.L., Cox, S.F., Eggins, S., Gagan, M.K. (2006) Microchemical evidence for episodic growth of antitaxial veins during fracture-controlled fluid flow. *Earth and Planetary Science Letters* 250, 331-344. doi: 10.1016/j.epsl.2006.07.051

Barnes, R., Gupta, S., Traxler, C., Ortner, T., Bauer, A., Hesina, G., Paar, G., et al. (2018) Geological analysis of Martian rover-derived Digital Outcrop Models using the 3-D visualization tool, Planetary Robotics 3-D Viewer—Pro3D. *Earth and Space Science*, *5*, 285–307. https://doi.org/10.1002/2018EA000374

Banham, S.G., Gupta, S., Rubin, D.M., Watkins, J.A., Sumner, D.Y. Edgett, K.S., Grotzinger, J.P., et al. (2018) Ancient Martian aeolian processes and palaeomorphology reconstructed from the Stimson formation on the lower slope of Aeolis Mons, Gale crater, Mars. *Sedimentology*, 65(4), 993-1042. https://doi.org/10.1111/sed.12469

Berger, J.A., Schmidt, M.E., Gellert, R., Boyd, N., Desouza, E., Flemming, R.L., Izawa, M.R.M., et al. (2017) Zinc and germanium in the sedimentary rocks of Gale crater on Mars indicate hydrothermal enrichment followed by diagenetic fractionation. *Journal of Geophysical Research: Planets*, 122, https:doi.org/10.1002/2017JE005290

Bons, P.D., Elburg, M.A., Gomez-Rivas, E. (2012) A review of the formation of tectonic veins and their microstructures. *Journal of Structural Geology*, 43, 33-62. http://dx.doi.org/10.1016/j.jsg.2012.07.005

Bons, P.D., Montenari, M., Bakker, R.J., Elburg, M.A. (2007) Potential evidence of fossilized Neoproterozoic deep life: SEM observations on calcite veins from Oppaminda Creek, Arkaroola, South Australia. *International Journal of Earth Science*, doi: 10.1007/s00531-007-0245-4.

Bons, P.D. and Montenari, M. (2005) The formation of antitaxial calcite veins with well-developed fibers, Oppaminda Creek, South Australia. *Journal of Structural Geology*, 27, 231-248. doi:10.1016/j.jsg.2004.08.009

Campbell, J.L., Perrett, G.M., Gellert, R., Andrushenko, S.M., Boyd, N.I., Maxwell, J.A., King, P.L., Schofield, C.D.M. (2012) Calibration of the Mars Science Laboratory Alpha Particle X-ray Spectrometer. *Space Sciences Reviews*, 170, 319-340. https://doi.org/10.1139/cjes-2012-0164

Caswell, T.E., Milliken, R.E. (2017) Evidence for hydraulic fracturing at Gale crater, Mars: implications for burial depth of the Yellowknife Bay formation. *Earth and Planetary Science Letters*, 468, 72-84. http://dx.doi.org/10.1016/j.epsl.2017.03.033

Chan, M.A., Yonkee, W.A., Netoff, D.I., Seiler, W.M., Ford, R.L. (2008) Polygonal cracks in bedrock on Earth and Mars: implications for weathering. *Icarus*, 194, 65-7. doi:10.1016/j.icarus.2007.09.026

Cobbold, P.R., Zanella, A., Rodrigues, N., Loseth, H. (2013) Bedding-parallel fibrous veins (beef and cone-in-cone): worldwide occurrences and possible significance in terms of fluid overpressure, hydrocarbon generation and mineralization. *Marine and Petroleum Geology*, 43, 1-20. http://dx.doi.org/10.1016/j.marpetgeo.2013.01.010

Cosgrove, J.W. (2001) Hydraulic fracturing during the formation and deformation of a basin: a factor in the dewatering of low-permeability sediments. *AAPG Bulletin*, 85, 737-748.

Cox, S.F. (1987) Antitaxial crack-seal vein microstructures and their relationship to displacement paths. *Journal of Structural Geology*, 9(7), 779-787, https://doi.org/10.1016/0191-8141(87)90079-4

Edgar, L.A., Gupta, S., Rubin, D.M., Lewis, K.M., Kocurek, G.A, Anderson, R.B., Bell, J.F. III, et al. (2018) Shaler: in situ analysis of a fluvial sedimentary deposit on Mars. *Sedimentology*, 65, https://doi.org/10.1111/sed.12370

Edgett, K.S., Yingst, R.A., Ravine, M.A., Caplinger, M.A., Maki, J. N., Ghaemi, F.T., Schaffner, J.A., et al. (2012) Curiosity's Mars Hand Lens Imager (MAHLI) Investigation. *Space Science Reviews*, 170, 259-317. https://doi.org/10.1007/s11214-012-9910-4

Ehlmann, B.L., Edwards, C.S. (2014) Mineralogy of the Martian surface. *Annual Review of Earth and Planetary Sciences*, 42, 291-315. doi: 10.1146/annurev-earth-060313-055024

Elburg, M.A., Bons, P.D., Foden, J., Passchier, C.W. (2002) The origin of fibrous veins: constraints from geochemistry. *Geological Society, London, Special Publications*, 200, 103-118. doi: 10.1144/GSL.SP.2001.200.01.07

Engelder, T. (1993) *Stress regimes in the lithosphere*. Princeton University Press, Princeton, NJ.

Eppes, M., Willis, A., Molaro, J., Abernathy, S., Zhou, B. (2015) Cracks in Martian boulders exhibit preferred orientations that point to solar-induced thermal stress. *Nature Communications*, 6, doi:10.1038/ncomms7712

Fedo, C.M., Grotzinger, J., Gupta, S., Stein, N.T., Watkins, J., Banham, S., Edgett, K.S., et al. (2017) Facies analysis and basin architecture of the upper part of the Murray formation, Gale crater, Mars, *LPS XLVIII* #1689.

Fisher, D.M., Brantley, S.J. (1992) Models of quartz overgrowth and vein formation: deformation and episodic fluid flow in an ancient subduction zone. *Journal of Geophysical Research*, 97(20), 20,043-20,061, doi:10.1029/92JB01582.

Forni O., M. Nachon, N. Mangold, D. L. Blaney, R.C. Wiens, S. M. Clegg, P.-Y. Meslin, et al. (2016) Fluorine in the Pahrump outcrop, Gale crater: Implications for fluid circulation and alteration. *LPS XLVII*, Abstract #1990.

Forni O., Gaft, M., Toplis M., Clegg S.M., Sautter V., Maurice S., Wiens R.C., et al. (2015) First detection of fluorine on mars: Implications on Gale crater's geochemistry. *Geophysical Research Letters*. 42, doi:10.1002/2014GL062742.

Forni, O., Vaniman, D.T., Le Deit, L., Clegg, S.M., Lanza, N.L., Lasue, J., Bish, D.L. (2015) Fluorine and lithium at the Kimberley outcrop, Gale crater. *LPS XLVI*, Abstract #2099.

Fraeman, A. A., Ehlmann, B.L., Arvidson, R.E., Edwards, C.S., Grotzinger, J.P., Milliken, R. E., Quinn, D.P., Rice, M.S. (2016), The stratigraphy and evolution of lower Mount Sharp from spectral, morphological, and thermophysical orbital data sets. *Journal of Geophysical Research*: *Planets*, 121, 1713–1736, doi:10.1002/2016JE005095.

Frydenvang J., Gasda P.J., Hurowitz J.A., Grotzinger J.P., Wiens R.C., Newsom H.E., Bridges J., et al. (2017) Diagenetic silica enrichment and late-stage groundwater activity in Gale crater, Mars. *Geophysical Research Letters,* 44, 4716-4724. doi: 10.1002/2017GL073323.

Gale, J.F., Laubach, S.E., Olson, J.E., Eichhubl, P., Fall, A. (2014) Natural fractures in shale: a review and new observations. *AAPG Bulletin*, 98, 2165-2216. doi: 10.1306/08121413151

Ghaemi, F. T. (2009) Design and fabrication of lenses for the color science cameras aboard the Mars Science Laboratory rover. *Optical Engineering*, 48(10), 103002, doi:10.1117/1.3251343

Grotzinger, J.P., Gupta, S., Malin, M.C., Rubin, D.M., Schieber, J., Siebach, K., Sumner, D.Y., et al. (2015) Deposition, exhumation, and paleoclimate of an ancient lake deposit, Gale crater, Mars. *Science*, 350, doi:10.1126/science.aac.7575.

Grotzinger, J.P., Sumner, D.Y., Kah, L.C., Stack, K., Gupta, S., Edgar, L., Rubin, D., et al., Lewis, K., (2014) A habitable fluvio lacustrine environment at Yellowknife Bay, Gale crater, Mars. *Science*, 343, doi:10.1126/science.1242777

Grotzinger, J.P., and Milliken, R. (2012) The sedimentary rock record of Mars: distribution, origins, and global stratigraphy. *SEPM Special Publication: Sedimentary Geology of Mars*, 102, 1-48. doi: 10.2110/pec.12.102.0001

Grotzinger, J.P., Crisp, J., Vasavada, A.R., Anderson, R.C., Baker, C.J., Barry, R., Blake, D.F., et al. (2012) Mars Science Laboratory Mission and Science Investigation. *Space Science Reviews,* 170, 5-56. doi:10.1007/s11214-012-9892-2

Gudmundsson, A., Kusumoto, S., Simmenes, T.H., Philipp, S.L., Larsen, B., Lotveit, I.F. (2012) Effects of overpressure variations on fracture apertures and fluid transport. *Tectonophysics*, 581, 220-230. doi: 10.1016/j.tecto.2012.05.003

Gudmundsson, A. (2011) *Rock Fractures in Geological Processes*. Cambridge University Press, New York.

Gudmundsson, A., Fjeldskaar, I., Brenner, S.L. (2002) Propagation pathways and fluid transport of hydrofractures in jointed and layered rocks in geothermal fields. *Journal of Volcanology and Geothermal Research 116*, 257-278. https://doi.org/10.1016/S0377-0273(02)00225-1

Gudmundsson, A. and Brenner, S.L. (2001) How hydrofractures become arrested. *Terra Nova*, 13, 456-462. https://doi.org/10.1046/j.1365-3121.2001.00380.x

Hart, B.S., Flemings, P.B., Deshpande, A. (1995) Porosity and pressure: Role of compaction disequilibrium in the development of geopressures in a Gulf Coast Pleistocene basin. *Geology*, 23(1), 45-48. https://doi.org/10.1130/0091-7613(1995)023<0045:PAPROC>2.3.CO;2

Hilgers, C., and Urai, J. (2002) Microstructural observations on natural syntectonic fibrous veins: implications for the growth process. *Tectonophysic*s, 352, 257-274. doi: 10.1016/S0040-1951(02)00185-3

Hofmann, B.A., and Farmer, J.D. (2000) Filamentous fabrics in low-temperature mineral assemblages: are they fossil biomarkers? Implications for the search for a subsurface fossil record on the early Earth and Mars. *Planetary and Space Science*, 48, 1077-1086. doi: 10.1016/S0032-0633(00)00081-7

Hurowitz, J.A., Grotzinger, J.P., Fischer, W.W., McLennan, S.M., Milliken, R.E., Stein, N., Vasavada, A.R., et al. (2017) Redox stratification of an ancient lake in Gale crater, Mars. *Science*, 356, doi: 10.1126/science.aah6849

Jaeger, J., Cook, N.G. W., Zimmerman, R. (2007) *Fundamentals of rock mechanics*. Blackwell Publishing, MA.

James, N.P. and Dalrymple, R.W. (2010) *Facies Models 4*. Geological Association of Canada.

Kah, L.C., Stack, K.M., Eigenbrode, J.L., Yingst, R.A., Edgett, K.S. (2018) Syndepositional precipitation of calcium sulfate in Gale crater, Mars. *Terra Nova*, 1-9. doi: 10.1111/ter.12359.

Kah, L.C., Kronyak, R.E., Van Beek, J., Nachon, M., Mangold, N., Thompson, L., Wiens, R., et al. (2015) Diagenetic crystal clusters and dendrites, Lower Mt. Sharp, Gale crater. *LPS XLVI* #1901.

Kerber, L., Dickson, J.L., Head, J.W., Grosfils, E.B. (2017) Polygonal ridge networks on Mars: diversity of morphologies and the special case of the Eastern Medusae Fossae Formation. *Icarus*, 281, 200-219. http://dx.doi.org/10.1016/j.icarus.2016.08.020

Kirkland, B.L., Lynch, F.L., Rahnis, M.A., Folk, R.L., Molineux, I.J., McLean, R.J.C. (1999) Alternative origins for nannobacteria-like objects in calcite. *Geology*, 27, 4, 347-350. doi: 10.1073pnas.0832464100

Kronyak, R.E., Miklusicak, N.B., Kah, L.C., Edgett, K.S., Nachon, M., Fedo, C.M. (2018) Formation of fracture networks in the Siccar Point Group: Implications for timing of post-depositional fluid flow in Gale crater, Mars. *LPS XLIX*, #1371.

Kronyak, R.E., Kah, L.C., Nachon, M., Mangold, N., Wiens, R.C., Williams, R., Schieber, J., Grotzinger, J. (2015) Distribution of mineralized veins from Yellowknife Bay to Mount Sharp, Gale crater: insight from textural and compositional variation. *LPS XLVI* #1903.

Long, C.S., National Research Council chair (1996) *Rock fractures and fluid flow: contemporary understanding and applications.* National Academy Press, Washington DC.

Malin, M. C., Ravine, M.A., Caplinger, M.A., Ghaemi, F.T., Schaffner, J.A., Maki, J.N., Bell, J.F. III, et al. (2017), The Mars Science Laboratory (MSL) Mast cameras and Descent imager: Investigation and instrument descriptions, *Earth and Space Science*, 4, doi:10.1002/2016EA000252.

Malin, M.C., Edgett, K.S. (2000) Sedimentary rocks of early Mars. *Science*, 290, 1927-1937. doi: 10.1126/science.290.5498.1927

Mandl, G. (2005) *Rock Joints: The Mechanical Genesis*. Springer, NY.

Maurice S., Clegg S., Wiens R.C., Gasnult O., Rapin W., Forni O., Cousin A., et al. (2016) ChemCam activities and discoveries during the Mars Science Laboratory nominal mission in Gale crater, Mars. *Journal of Analytical Atomic Spectrometry*. DOI: 10.1039/c5ja00417a.

Maurice, S., Wiens, R.C., Saccoccio, M., Barraclough, B., Gasnault, O., Forni, O., Mangold, N., et al. (2012) The ChemCam instrument suite on the Mars Science Laboratory (MSL) Rover: science objectives and mast unit description. *Space Science Reviews*, 170, 95-166. https://doi.org/10.1007/s11214-012-9912-2

McLennan, S. M., Bell, J.F. III, Calvin, W.M., Christensen, P.R., Clark, B.C., de Souza, P.A., Farmer, J., et al. (2005), Provenance and diagenesis of the evaporite-bearing Burns formation, Meridiani Planum, Mars. *Earth and Planetary Science Letters*, 240(1), 95–121, doi:10.1016/j.epsl.2005.09.041.

Mellon, M.T. (1997) Small-scale polygonal features on Mars: seasonal thermal contraction cracks in permafrost. *Journal of Geophysical Research: Planets*, 102, https://doi.org/10.1029/97JE02582

Milliken, R.E., Ewing, R.C., Fischer, W.W., & Hurowitz, J (2014) Wind-blown sandstones cemented by sulfate and clay minerals in Gale Crater, Mars. *Geophysical Research Letters*, 41, 1149–1154, doi:10.1002/2013GL059097.

Milliken, R.E., Grotzinger, J.P., Thomson, B.J. (2010) Paleoclimate of Mars as captured by the stratigraphic record in Gale crater. *Geophysical Research Letters*, 37, doi:10.1029/2009GL041870.

Ming, D.W., Archer, P.D. Jr., Glavin, D.P., Eigenbrode, J.L., Franz, H.B., Sutter, B., Brunner, A.E. et al. (2014) Volatile and organic compositions of sedimentary rocks in Yellowknife Bay, Gale crater, Mars. *Science*, 343, doi:10.1126/science.1245267

Nachon, M., Mangold, N., Forni, O., Kah, L.C., Cousin, A., Wiens, R.C., Anderson, R., et al. (2016) Chemistry of diagenetic features analyzed by ChemCam at Pahrump Hills, Gale crater, Mars. *Icarus*, 218, 121-136. https://doi.org/10.1016/j.icarus.2016.08.026

Nachon, M., Clegg, S.M., Mangold, N., Schröder, S., Kah, L.C., Dromart, G., Ollila, A., et al. (2014) Calcium sulfate veins characterized by ChemCam/Curiosity at Gale crater, Mars. *Journal of Geophysical Research: Planets*, 119, 1-26. https://doi.org/10.1002/2013JE004588

Newsom, H.E., Belgacem, I., Jackson, R., Ha, B., Vaci, Z., Wiens, R.C., Frydenvang, J., et al. (2016) The materials at an unconformity between the Murray and Stimson formations at Marias Pass, Gale crater, Mars. *LPS XLVII*, #2397.

Oliver, N.H. and Bons, P.D. (2001) Mechanisms of fluid flow and fluid-rock interaction in fossil metamorphic hydrothermal systems inferred from vein-wall rock patterns, geometry and microstructure. *Geofluids*, 1, 137-162. https://doi.org/10.1046/j.1468-8123.2001.00013.x

Passchier, C.W. and Trouw, R.A.J. (2005) *Micro-tectonics*. Springer, Berlin.

Pederson, K., Ekendahl, S., Tullborg, E., Furnes, H., Thorseth, I., Tumyr, O. (1997) Evidence of ancient life at 207 m depth in a granitic aquifer. *Geology*, 25, 9, 827-830. doi: 10.1130/0091-7613(1997)025<0827:EOALAM>2.3.CO;2

Philipp, S.L., Asfar, F., Gudmundsson, A. (2013) Effects of mechanical layering on hydrofracture emplacement and fluid transport in reservoirs. *Frontiers in Earth Science*, 1(4). doi: 10.3389/feart.2013.0004.

Philipp, S.L. (2012) Fluid overpressure estimates from the aspect ratio of mineral veins. *Tectonophysics*, 581, 35-47. doi:10.1016/j.tecto.2012.01.015

Philipp, S.L. (2008) Geometry and formation of gypsum veins in mudstones at Watchet, Somerset, SW England. *Geological Magazine*, 145(6), 831-844. doi:10.1017/S0016756808005451.

Ramsay, J.G. (1980) The crack-seal mechanism of rock deformation. *Nature*, 284, 135-139. https://doi.org/10.1038/284135a0

Rapin, W., Meslin, P.-Y., Maurice, S., Vaniman, D., Nachon, M., Mangold, N., Schroder, S., et al. (2016) Hydration state of calcium sulfates in Gale crater, Mars: identification of basanite veins. *Earth and Planetary Science Letters*, 452, 197-205. 10.1016/j.epsl.2016.07.045

Rice, M.S., Gupta, S., Treiman, A.H., Stack, K.M., Calef, F., Edgar, L.A., Grotzinger, J.P., et al. (2017) Geologic overview of the Mars Science Laboratory rover mission at the Kimberley, Gale crater, Mars. *Journal of Geophysical Research: Planets*, 122, 2-20. https://doi.org/10.1002/2016JE005200.

Schieber, J., Bish, D., Coleman, M., Reed, M., Hausrath, E.M., Cosgrove, J., Gupta, S., et al., (2017) Encounters with an unearthly mudstone: Understanding the first mudstone found on Mars. *Sedimentology*, 64, 311–358. https://doi.org/10.1111/sed.12318

Schopf, J.W. and Kudryavtsev, A.B. (2012) Biogenicity of Earth's earliest fossils: A resolution of the controversy. *Gondwana Research*, 22, 761-771. https://doi.org/10.1016/j.gr.2012.07.003

Siebach, K. L., J. P. Grotzinger, L. C. Kah, K. M. Stack, M. Malin, R. Léveillé, and D. Y. Sumner (2014) Subaqueous shrinkage cracks in the Sheepbed mudstone: Implications for

early fluid diagenesis, Gale crater, Mars. *Journal of Geophysical Research: Planets*, 119, 1597–1613, doi:10.1002/2014JE004623.

Siebach, K.L., Grotzinger, J.P. (2013) Volumetric estimates of ancient water on Mount Sharp based on boxwork deposits, Gale crater, Mars. *Journal of Geophysical Research: Planets*, 119, 189-198. https://doi.org/10.1002/2013JE004508

Stack, K.M., Grotzinger, J.P., Lamb, M.P., Gupta, S., Rubin, D.M., Kah, L.C., Edgar, L.A., et al., (2018) Evidence for plunging river plume deposits in the Pahrump Hills member of the Murray formation, Gale crater, Mars. *Submitted for publication.*

Stack, K. M., Grotzinger, J.P., Kah, L.C., Schmidt, M.E., Mangold, N., Edgett, K.S., Sumner, D.Y., et al. (2014) Diagenetic origin of nodules in the Sheepbed member, Yellowknife Bay formation, Gale crater, Mars. *Journal of Geophysical Research: Planets*, 119, 1637–1664, doi:10.1002/ 2014JE004617.

Stein, N., Grotzinger, J.P., Schieber, J., Mangold, N., Hallet, B., Newsom, H., Stack, K.M., et al. (2018) Desiccation cracks provide evidence of lake drying on Mars, Sutton Island member, Murray formation, Gale crater. *Geology*, 46, 515-518. https://doi.org/10.1130/G40005.

Sun, V.Z., Stack, K.M., Kah, L.C., Thompson, L., Fischer, W., Williams, A., Johnson, S.S., House, C.H., et al., (2018) Late-stage concretions in the Murray formation, Gale crater, Mars. *Icarus*, 321, 866-890.

Terzaghi, K. (1943) *Theoretical Soil Mechanics*. John Wiley and Sons, New York.

Thomas, M., Clarke, J.D.A., Pain, C.F. (2007) Weathering, erosion, and landscape processes on Mars identified from recent rover imagery, and possible Earth analogues. *Australian Journal of Earth Sciences*, 52, 365-378. https://doi.org/10.1080/08120090500134597

Thomson, B.J., Bridges, N.T., Milliken, R., Baldridge, A., Hook, S.J., Crowley, J.K., Marion, G.M., et al., (2011) Constraints on the origin and evolution of the layered mound in Gale crater, Mars using Mars Reconnaissance Orbiter data. *Icarus*, 214, 413-432. https://doi.org/10.1016/j.icarus.2011.05.002

Trewin, N.H., and Knoll, A.H. (1999) Preservation of Devonian chemotrophic filamentous bacteria in calcite veins. *Palaios*, 14, 288-294. doi: 10.2307/3515441

VanBommel, S.J., Gellert, R., Berger, J.A., Thompson, L.M., Edgett, K.S., McBride, M.J., Minitti, M.E., et al. (2017) Modeling and mitigation of sample relief effects applied to chemistry measurements by the Mars Science Laboratory Alpha Particle X-ray Spectrometer. *X-ray Spectrometry*, 46, 229-236. https://doi.org/10/1002/xrs.2755.

VanBommel, S.J., Gellert, R., Berger, J.A., Campbell, J.L., Thompson, L.M., Edgett, K.S., McBride, M.J., et al. (2016) Deconvolution of distinct lithology chemistry through oversampling with the Mars Science Laboratory Alpha Particle X-ray Spectrometer. *X-ray Spectrometry*, 45, 155-161. https://doi.org/10/1002/xrs.2681.

Watkins, J. A., J. Grotzinger, N. Stein, S. G. Banham, S. Gupta, D. Rubin, K. Stack, and K. Edgett (2016) Paleotopography of erosional unconformity, base of Stimson formation, Gale crater, Mars. *LPS XLVII* #2939.

Weertman, J. (1980) The stopping of a rising liquid-filled crack in the Earth's crust by a freely slipping horizontal joint. *Journal of Geophysical Research: Solid Earth*, 85, 967-976. https://doi-org.proxy.lib.utk.edu/10.1029/JB085iB02p00967.

Wendler, F., Okamoto, A., Blum, P., et al. (2016) Phase-field modeling of epitaxial growth of polycrystalline quartz veins in hydrothermal experiments. *Geofluids* 16, 211-230. https://doi.org/10.1111/gfl.12144

Wiens R.C., Maurice S., and the ChemCam and MSL Science Teams (2015) ChemCam: Chemostratigraphy by the first Mars microprobe. *Elements*, 11, 33-38. https://doi.org/10.2113/gselements.11.1.33

Wiens R.C., Maurice S., Barraclough B., Saccoccio M., Barkley W.C, Bell J.F. III, Bender S., et al. (2012) The ChemCam Instruments on the Mars Science Laboratory (MSL) Rover: Body Unit and Combined System Performance. *Space Science Reviews*, 170, 167-227. doi 10.1007/S11214-012-9902-4.

Williams, R.M.E., Malin, M.C., Stack, K.M., Rubin, D.M. (2018) Assessment of Aeolis Palus stratigraphic relationships based on bench-forming strata in the Kylie and the Kimberley regions of Gale crater, Mars. *Icarus*, 309, 84-104. https://doi.org/10.1016/j.icarus.2018.02.028

Williams, R.M.E., Grotzinger, J.P., Dietrich, W.E., Gupta, S., Sumner, D.Y., Wiens, R.C., Mangold, N., et al., (2013) Martian fluvial conglomerates at Gale crater. *Science*, 340, 1068-1072. doi: 10.1126/science.1237317

Wiltschko, D.V., Morse, J.W. (2001) Crystallization pressure versus "crack-seal" as the mechanism for banded veins. *Geology*, 29 (1), 79-82. https://doi.org/10.1130/0091-7613(2001)029<0079:CPVCSA>2.0.CO;2

Wray, J. J. (2013), Gale Crater: The Mars Science Laboratory/Curiosity rover landing site. *International Journal of Astrobiology*, 12, 25–38. https://doi.org/10.1017/S1473550412000328

Yen, A.S., Ming, D.W., Vaniman, D.T., Gellert, R., Blake, D.F., Morris, R.V., Morrison, S.M., et al. (2017) Multiple stages of aqueous alteration along fractures in mudstone and sandstone strata in Gale Crater, Mars. *Earth and Planetary Science Letters*, 471, 186-198. https://doi.org/10.1016/j.epsl.2017.04.033

Zhou, X., Chen, D., Tang, D., Dong, S., Guo, C., Guo, Z., Zhang, Y. (2015) Biogenic iron-rich filaments in the quartz veins in the uppermost Ediacaran Qigebulake formation, Aksu area, northwestern Tarim Basin, China: Implications for iron oxidizers in subseafloor hydrothermal systems. *Astrobiology*, 15, 7. doi:10.1089/ast.2014.1234

CHAPTER 2
EXTENSIVE POLYGONAL FRACTURE NETWORK IN SICCAR POINT GROUP STRATA: FRACTURE MECHANISMS AND IMPLICATIONS FOR FLUID CIRCULATION IN GALE CRATER, MARS

A version of this chapter has been submitted for publication and is in review in the *Journal of Geophysical Research: Planets* by R. E. Kronyak et al.:

Kronyak, R. E., Kah, L. C., Miklusicak, N. B., Edgett, K. S., Sun, V. Z., Bryk, A. B., & Williams, R. M. E. Extensive polygonal fracture network in Siccar Point group strata: fracture mechanisms and implications for fluid circulation in Gale crater, Mars.

The article was written by R. E. Kronyak based on HiRISE orbital images and rover images collected by the Mars Science Laboratory rover. Co-authors L. C. Kah and N. B. Miklusicak assisted in mapping efforts and article editing. MSL co-authors K. S. Edgett, V. Z Sun, A. B. Bryk, and R. M. E. Williams, and committee member B. J. Thomson provided helpful feedback and edits that improved the clarity of the article prior to submission.

Abstract

Rock fractures are indicators of stress release within geologic systems, and fracture morphologies can commonly be used to infer formation conditions. Polygonal fractures are common in isotropic, contractional stress regimes such as in rocks exposed at the surface of a planet undergoing thermal cycling or in sedimentary substrates undergoing repeated wetting and drying. Such polygonal fracture systems – on centimeter to decameter scales – have been widely documented on Mars. Utilizing a combination of orbital- and ground-based images, I report a laterally extensive polygonal fracture network that occurs within siliciclastic rocks of the lowermost Siccar Point group, Gale crater, Mars. The Siccar Point group is exposed over approximately 20 km^2 in northwest Gale crater, where it unconformably overlies eroded strata of Mount Sharp (Aeolis Mons) and reflects likely aeolian deposition along the lower flanks of Mount Sharp. Images reveal an extensive network of erosionally resistant polygons, approximately 7.5 meters across, that exhibit interior angles (i.e. fracture intersections) with modes at 90° and 120°. Polygon morphology indicates that fractures formed during multiple cycles of expansion and contraction, which is attributed to desiccation and subsequent recharge of near-surface groundwater. The erosional resistance of preserved fractures is inferred to reflect

post-fracture diagenetic fluid flow along the sub-Siccar Point group unconformity and cementation. Evidence for multiple fluid events in the relatively young strata of the Siccar Point group requires a protracted history of fluid stability in Gale crater.

Introduction

Linear features interpreted as fractures are widely observed on the martian surface, and their diverse morphologies are used to infer their formation mechanism. For example, a combination of concentric and radial orientations is generally assumed to reflect fracture generated by hypervelocity impacts (Kenkmann et al., 2018; Polansky & Ahrens, 1990; Rodriguez et al., 2005; Schultz et al., 1982). Regionally extensive fractures, such as radial fractures in the Tharsis region (Carr, 1974; Mege & Masson, 1996b), or linear fractures within the Valles Marineris region (Mege & Masson, 1996a; Tanaka & Golombek, 1989) reflect regional tensional stress associated with crustal forces. Finally, polygonal fracture patterns are inferred to reflect local contractional stresses within an otherwise isotropic stress field, associated with cyclic heating and cooling, wetting and drying, or freezing and thawing (e.g., Chan et al., 2008; El Maarry et al., 2014; Hiesinger & Head, 2000; Kerber et al., 2017; Levy et al., 2009; Mangold et al., 2004; Mangold, 2005; Mellon, 1997; Milazzo et al., 2009).

Several distinct fracture systems occur in Gale crater, Mars, within the field area of the Mars Science Laboratory Curiosity rover. Images from the Curiosity rover record a variety of fracture morphologies, mineral veins, and fracture-associated alteration halos (Frydenvang et al., 2017; Kronyak et al., 2019; Nachon et al., 2014, 2016; Yen et al., 2017). The majority of these features have been broadly attributed to hydrofracturing (Caswell & Milliken, 2017; Kronyak et al., 2019) during post-depositional fluid flow, and are interpreted to reflect circulation of deep

subsurface groundwater through the sediment package during burial. Polygonal fractures have also been described from elsewhere in Gale crater, including centimeter-scale features attributed to desiccation of surficial fluids (Stein et al., 2018) and decameter-scale polygons attributed to non-cyclic desiccation or thermal contraction events (i.e., boxwork structures; Siebach and Grotzinger, 2013).

Here I explore a locally extensive network of polygonal features that are exposed within aeolian siliciclastic strata of the Siccar Point group (SPg), the youngest stratigraphic unit examined by Curiosity in Gale crater, Mars. I use orbital images within previously mapped areas in northwest Gale crater to examine the distribution of polygonal features within the SPg and their position within the internal stratigraphy of the SPg. Measurement of polygon size and shape parameters permit comparison of polygons across the region of study and lead to inferences of their potential origin.

Geology of Gale Crater

Gale crater is a 154 km-diameter impact crater that spans the north-south dichotomous boundary near the martian equator (5°S, 138°E) (Figure 2.1a). Sedimentary strata within the field area of the Curiosity rover mission have been divided into three primary groups (Figure 2.1b): the Bradbury group (Grotzinger et al., 2015), which represents the intracrater plains that from the crater rim (Aeolis Palus); the Mount Sharp group (Grotzinger et al., 2015), which represents strata exposed within Mount Sharp (Aeolis Mons); and the Siccar Point group (Figure 1b;

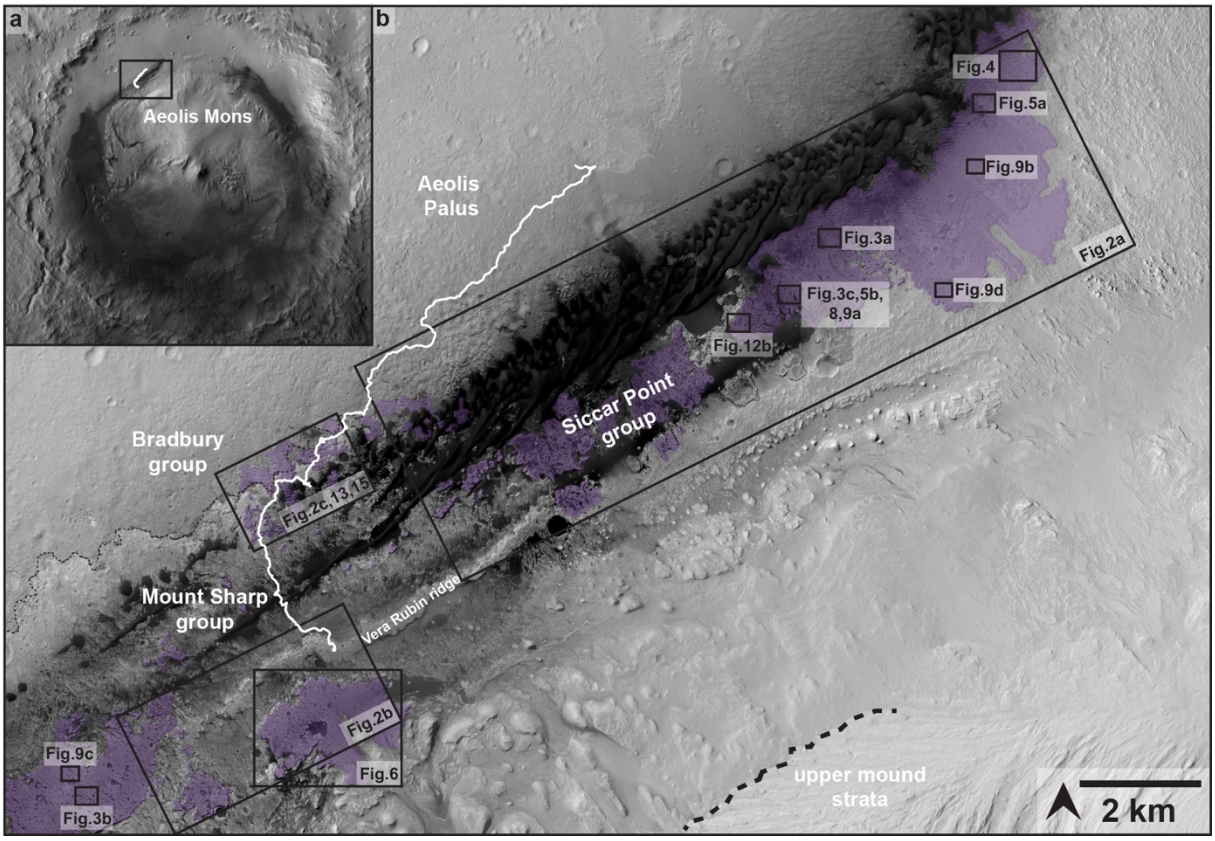


Figure 2.1 Geographic context of this study. (a) Gale crater, with Curiosity's traverse outlined in white. (b) Region of Curiosity's traverse (white line) and the geologic units within northwest Gale crater. The thin dashed black line indicates the approximate boundary between exposures of the Bradbury group and the Mount Sharp group. In the region of the Siccar Point group, the Mount Sharp group consists predominantly of lacustrine mudstone of the Murray formation and contains a distinct topographic ridge that is designated as the Vera Rubin ridge. Exposures of the Siccar Point group, here in purple, unconformably overlie strata of lower the Murray formation. Strata of upper Mount Sharp (south of thick dashed line) are not yet named.

Fraeman et al., 2016; Stack et al., 2017), which unconformably overlies strata of lower Mount Sharp. Dark-toned sand also occurs on the crater floor along the lowermost flanks of Mount Sharp, in the same region as exposures of the Siccar Point group. These sand deposits, called the Bagnold dunes, represent active aeolian dunes (e.g., Ewing et al., 2017) and mark the break in slope at the base of Mount Sharp (Bridges & Ehlmann, 2018).

Bradbury group

Within the study region, the Bradbury group consists of strata that compose the intracrater plains (Aeolis Palus) of Gale crater, north of Mount Sharp. Strata of the Bradbury group include lithologies exposed northwest of the Bagnold dunes, which lay roughly parallel to, and at times obscure, the contact with the Mount Sharp group (Figure 2.1b). Because dip observations within the Bradbury group are approximately horizontal, elevation is commonly used as a proxy for stratigraphic thickness (e.g., Grotzinger et al., 2015; Siebach et al., 2017). The Curiosity rover traversed ~60 meters of vertical stratigraphy within the Bradbury group and documented abundant evidence for past aqueous activity, including outcroppings of fluvial conglomerate (Williams et al., 2013) and cross-stratified fluvial sandstone (Edgar et al., 2018; Rice et al., 2017; Williams et al., 2018).

Mount Sharp group

The Mount Sharp group consists of strata that crop out southeast of the Bradbury group, along the flanks of Gale crater's central sedimentary mound, Aeolis Mons (Figure 2.1b). Data from orbiting near-infrared spectrometers suggest that strata of the Mount Sharp group contain hematite, hydrated silica, phyllosilicate minerals, and both mono- and poly-hydrated sulfate

minerals, all of which indicate a history of fluid interaction (Fraeman et al., 2016; Milliken et al., 2010). The major component of the lower Mount Sharp group is the Murray formation, a >300-meter-thick succession dominated by finely laminated lacustrine mudstone (Grotzinger et al., 2015), with intermittent fluvial (Stack et al., 2018) and aeolian sandstone (Fedo et al., 2017). Fluvial sandstone, in particular, is interpreted as potential interfingering between strata of the Mount Sharp and Bradbury groups (Grotzinger et al., 2015).

Siccar Point group

The Siccar Point group (SPg), which is the primary focus of this study, refers to regionally discontinuous, erosionally resistant strata that unconformably overlie the basal strata of the Mount Sharp group (Figure 2.2) (Fraeman et al., 2016; Watkins et al., 2016). The SPg occupies a topographic depression in northwest Gale crater, where it bridges the contact between strata of the Bradbury and Mount Sharp groups (Grotzinger et al., 2015), and is preserved at higher elevations as a fan-shaped pediment, "the Greenheugh pediment," at the base of a prominent valley (Gediz Vallis) that originates at the unconformity that separates strata of lower and upper Mount Sharp (Milliken et al., 2010). Strata associated with the Siccar Point group have previously been referred to as the "mound skirting" unit (Anderson & Bell, 2010), the "lower mound marginal" unit (Thomson et al., 2011), the "washboard" unit (Buz et al., 2017; Kah et al., 2013; Milliken et al., 2014; Rubin et al., 2014), the "crater floor" unit (Le Deit et al., 2013), and the "high thermal inertia" unit (Fraeman et al., 2016). The range of potential depositional environments represented by SPg strata is uncertain (cf. Kah et al., 2013; Rubin et al., 2014); although where encountered by the Curiosity rover, the SPg (Figure 2.2c) consists

predominantly of cross-bedded aeolian sandstone classified as the Stimson formation (Banham et al., 2018).

Methods

Exposures of the Siccar Point group (SPg) were identified and characterized using HiRISE images accessed through the Multi-Mission Geographic Information System (MMGIS). The MMGIS is a web-based platform that uses HiRISE 25 cm/pixel visible images (McEwen et al., 2007) as a base map and contains data overlays from a variety of orbital and rover instruments (Calef et al., 2017). Map overlays include a 1 m/pixel digital elevation model (derived from HiRISE base pairs; Calef & Parker, 2016), hyperspectral mineralogic data from CRISM (Compact Reconnaissance Imaging Spectrometer for Mars; Murchie et al., 2007), thermal inertia (Fergason et al., 2006). Data from targets analyzed by the Curiosity science team are also available, including context images from the primary navigation cameras (Navcam; Maki et al., 2012) and quick-look products of geochemistry from the ChemCam instrument (Wiens et al., 2015).

In this study, I utilize HiRISE images in the MMGIS to explore regions across which the SPg is exposed. Sub-units of the SPg were characterized by surface texture and morphology. Elevation profiles generated within the MMGIS were then used to estimate the thickness of individual SPg units. To do this, I derived the local slope from the average of three ~7 km-long elevation transects across each region of SPg exposure. These local slopes were applied to smaller, 200-meter-long elevation transects and the overlying thickness of strata was measured at 20-meter increments. In regions where polygonal features occur, I measured polygon size by defining the diameter of a circumscribing circle and recorded these values using ImageJ

software. Polygon shape was estimated by the number of sides, and intersection angles of polygon edges were measured to provide data on fracture mechanism. Statistical analyses were then applied to assess the relationships of polygon populations across exposures of the SPg.

For regions of the SPg traversed by the Curiosity rover, I used color Mastcam images to attempt to identify polygonal features that were observed from orbit. The Mastcam instrument consists of a pair of digital CCD cameras, located on the rover's mast ~2 meters above the ground (Malin et al., 2017). The left Mastcam has an f/8 lens with a 34 mm focal length, providing a 15° field of view, and the right Mastcam has an f/10 lens with a 100 mm focal length, providing a 5° field of view (Malin et al., 2017).

Data and Observations

Geology of Siccar Point group strata

Rover-based observations

Primary exposures of Siccar Point group strata (Figures 2.1 and 2.2) are observable only from orbit. A small portion of the SPg, however, was observed along the traverse of the Curiosity rover in a series of small E-W trending plateaus and designated as the Stimson formation (Figure 2.2c). Along the rover traverse, the Stimson formation consists of a thin (1-3-meter-thick), dark-toned, erosionally resistant package of fine-grained sandstone with abundant cross-beds (Banham et al., 2018). Where visible, the Murray-Stimson contact is sharp, with the Stimson formation unconformably overlying previously eroded strata Murray formation (Newsom et al., 2018; Watkins et al., 2016). Observations from the Mars Hand Lens Imager (MAHLI; Edgett et al., 2012) reveal that the Stimson formation consists of well-sorted, well-

rounded fine sandstone, with little evidence of a contribution from silt- or clay-sized particles, consistent with deposition via aeolian processes (Banham et al., 2018). On a larger scale, Mastcam images reveal that the Stimson formation consists predominantly of decimeter- to meter-scale cross-sets separated by sub-horizontal bounding surfaces, with a conspicuous lack of interdune deposits. Observed architectures are consistent with the migration of aeolian dunes across the lower flanks of Mount Sharp and accumulation under predominantly dry conditions, where regional groundwaters did not intersect the depositional surface (Banham et al., 2018).

Observations from orbital images

In this study, I focus on exposures of the Siccar Point group (SPg) along the northwest flank of Mount Sharp, south of the Bagnold dunes. Here, the SPg spans approximately 20 km^2 and is divided into three broad regions: SPg strata exposed northeast of Curiosity's traverse and south of the Bagnold dunes (Figure 2.2a); SPg strata exposed south and southwest of Curiosity's traverse, including strata of the Greenheugh pediment (Figure 2b); and SPg exposed around Curiosity's traverse during Sols ~750-1450, where SPg exposures were designated as the Stimson formation (Figure 2.2c). For most areas, the boundaries of the Siccar Point group are easily recognizable in orbital images: the SPg (1) has a characteristically lower albedo than surrounding strata of the Murray formation; (2) unconformably overlays strata Murray formation; and (3) commonly terminates as a discrete 1-3-meter-high escarpment. The dark sand of the Bagnold dunes, however, obscures much of the northern boundary of the SPg, making its stratigraphic relationship to the strata north of the dune field uncertain (Kah et al., 2013).

Three dominant surface textures are recognized across exposures of the Siccar Point group (Figure 2.3). The first, and most prominent, surface texture consists of parallel E-W

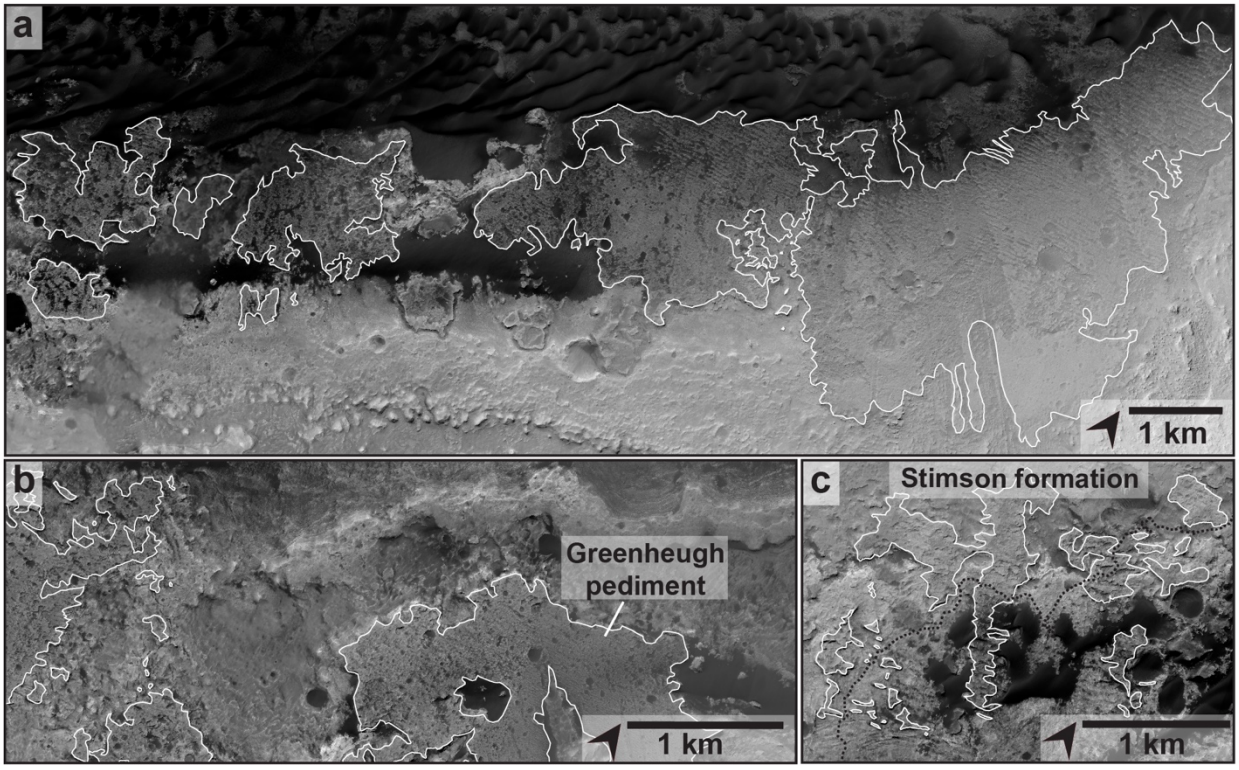


Figure 2.2 Exposures of the Siccar Point group (SPg; outlined in white) examined for this study. (a) Regions of the SPg east and northeast of the Curiosity rover traverse (See Figure 2.1b), adjacent to the Bagnold dune field. (b) Regions of the SPg south and southwest of the Curiosity rover traverse, including the Greenheugh pediment (see Bryk et al., 2019). (c) Highly dissected portions of the SPg in the region of the Curiosity rover traverse (dashed black line). In this region, the SPg is informally designated as the Stimson formation.

trending ridges (Figure 2.3a; cf. Kah et al., 2013; Milliken et al., 2014; Rubin et al., 2014). Ridges are most extensively preserved in SPg exposures northeast of Curiosity's traverse, along the margin of the Bagnold dunes (Figure 2.2a). Here, ridges are ~1 meter in height (Figure 2.4; Table 2.1) and exhibit ~25-40-meter wavelengths. Individual ridges can be traced laterally up to 1 kilometer. Troughs between ridges commonly contain dark aeolian sand emanating from the Bagnold dune field. In the region of the Curiosity traverse, a series of ~25-100-meter-long mesas (the Murray Buttes) and two ridged plateaus (Naukluft and Emerson) exhibit an E-W trend that may indicate an origin as erosional remnants of surficial ridges. Ridged morphologies are generally absent from the southwest SPg, where only highly eroded E-W trending remnants are observed.

The second surface texture of the SPg is a rough, erosionally resistant surface that preserves small (typically <75-meter diameter) craters (Figure 2.3b). Cratered surface textures are most laterally continuous in the southwestern exposures of the SPg and are patchy in the northeast SPg, where such textures are commonly associated with E-W trending ridges. Where remnants of E-W trending parallel ridges can be observed, elevation profiles demonstrate that parallel ridges overlie the surrounding cratered surface. The estimated thickness of strata was derived by measuring the difference in elevation from the cratered surfaces to the top of underlying polygonal ridges, providing an average thickness of ~1.2 meters (Table 2.1). Regions where strata defined by cratered surfaces are thinner than average may reflect either erosional loss or perhaps the occurrence of multiple, distinct cratered surfaces.

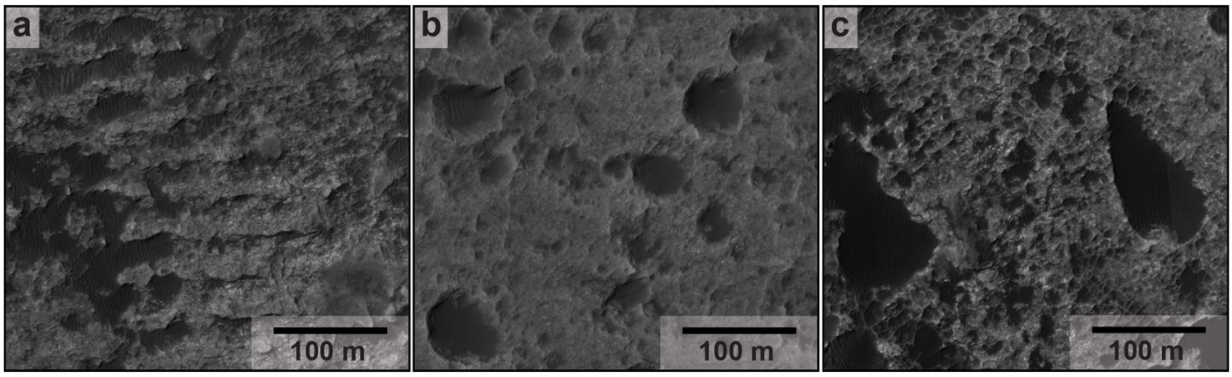


Figure 2.3 Three primary surface morphologies of the Siccar Point group, including: (a) surficial E-W trending ridges, (b) rough crater-retentive surface, and (c) polygonal terrain.

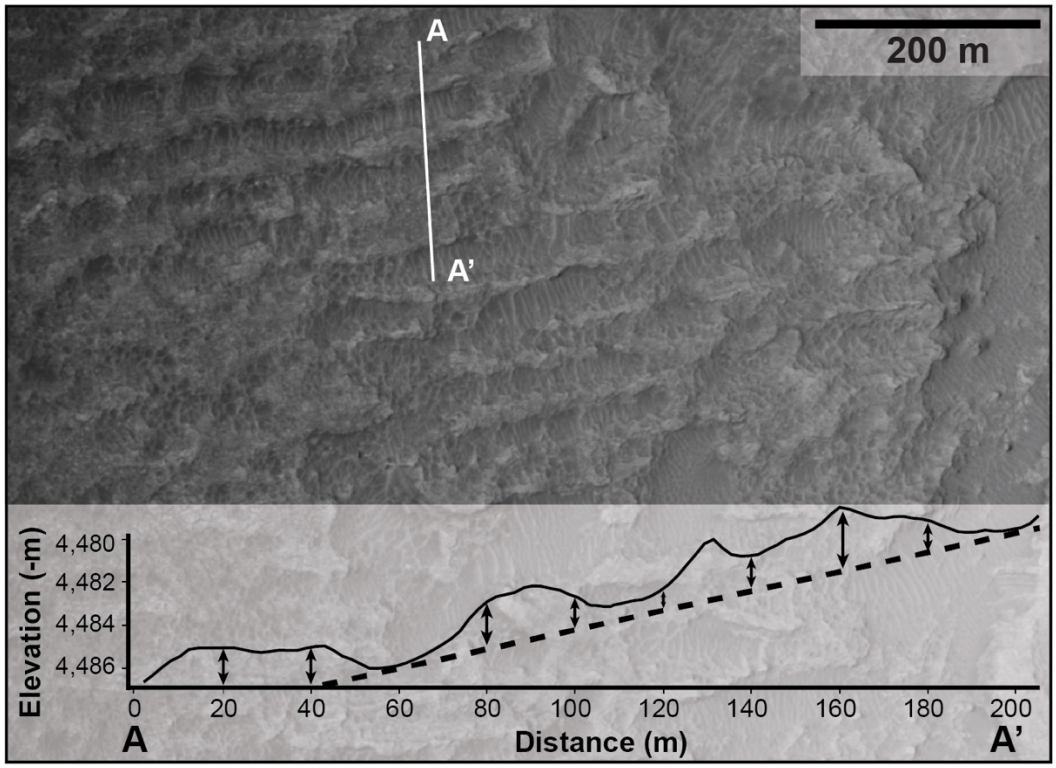


Figure 2.4 Example of estimated thickness of Siccar Point group exposures. Here, the thickness of the ridged subunit is measured in the northeast SPg. The local slope is shown along the elevation profile as a dashed line. Slope is derived from multiple measurements of the regional slope, which here corresponds to the base of ridge troughs. The overlying thickness of strata is then measured along 20-meter increments (double-sided arrows); the maximum height of ridges is approximately 1 meter.

Table 2.1 Slope and thickness data for Siccar Point group regions.

SPg region and local slope	**Siccar Point group sub-unit**	**Estimated thickness (m)**
NE Siccar Point group (slope=8.8 ± 2.9°, N=4)	Ridged SPg	1.2 ± 0.9
	Cratered SPg	1.1 ± 0.7
	Fractured SPg	0.6 ± 0.4
Greenheugh pediment (slope=7 ± 1.4°, N=3)	Lower cratered	2.4 ± 1.5
	Upper	2.1 ± 0.7
SW Siccar Point group (slope=7.1 ± 2.0°, N=3)	Cratered	1.2 ± 0.6

The third surface texture of the SPg is characterized by a laterally extensive network of multi-directional ridges that form discrete polygons (Figure 2.3c). Polygon edges are light-toned relative to the surrounding host rock and are erosionally resistant, resulting in exposure as topographically elevated ridges. Polygon interiors commonly contain dark sand. Although polygons are present within all exposed regions of the SPg, they are most common in northeastern exposures of the SPg. Polygons commonly underlie cratered surfaces (Figure 2.5a), although they also can directly underlie the erosional remnants of E-W trending ridges (Figure 2.5b), suggesting that cratered surfaces may not be laterally continuous through the SPg. In all cases, however, polygonal terrain occurs in the lowermost portions of the SPg., The thickness of polygonal SPg terrain was derived by measuring the difference in elevation between ridge tops and the underlying Murray formation, providing an average thickness of <1 meter (Table 2.1).

South of the main exposures of the SPg, the Greenheugh pediment capping unit is a present-day fan-shaped element that occurs at the terminus of Gediz Vallis (Figure 2.1b). The Greenheugh pediment capping unit is defined as part of the Siccar Point group because, like the lower-elevation exposures, it exhibits an unconformable relationship with the underlying Murray formation (Bryk et al., 2019; Fraeman et al., 2016). The pediment is also associated with the ~1.6 km long Gediz Vallis ridge deposit (Figure 2.6a), which is interpreted as terminal deposition from the Gediz Vallis channel (Bryk et al., 2019). The thickness of the Greenheugh pediment capping unit varies with elevation. Whereas lower elevation portions of the western pediment average ~2.4 meters thick, higher elevation portions of the eastern pediment average ~2.1 meters thick. The exposed surface morphology of the Greenheugh pediment capping unit mimics those

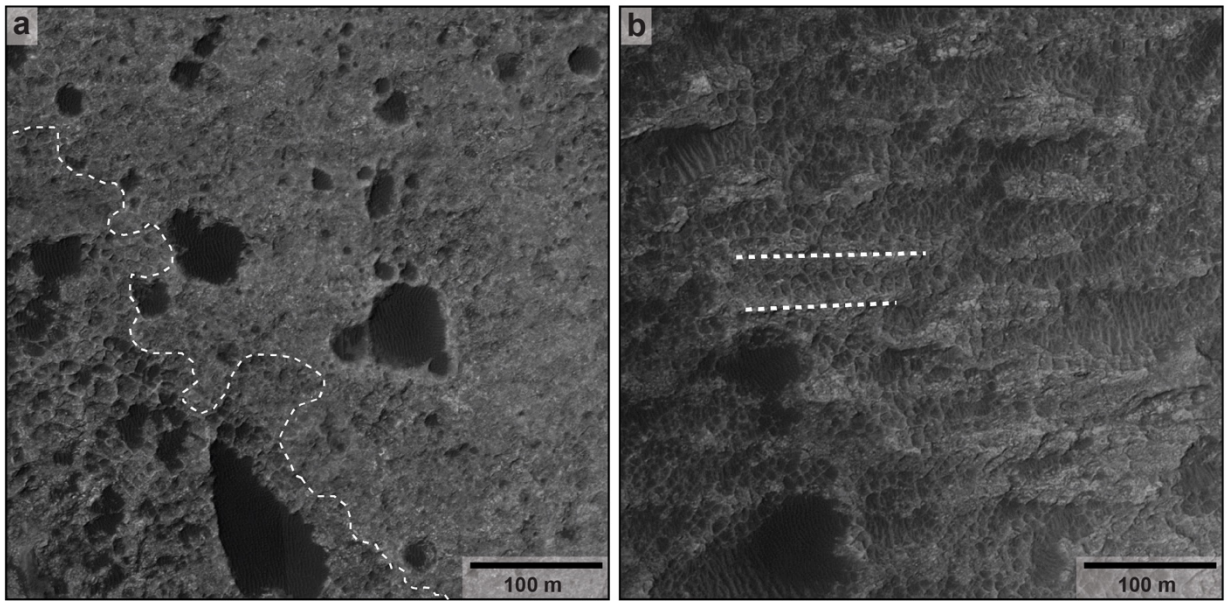


Figure 2.5 Stratigraphic expression of polygonal features in the Siccar Point group. (a) Polygons (left of white dashed line) most commonly occur underlying regions of cratered surfaces of the SPg. (b) Polygons, however, also occur in topographic lows between erosional remnants of E-W trending parallel ridges (white dashed lines).

observed elsewhere in the SPg. More proximal portions of the pediment, near the Gediz Vallis ridge, are characterized by evenly spaced, parallel ridges. Unlike elsewhere in the SPg, however, pediment ridges are oriented WNW-ESE and record shorter wavelengths (~10 meters) between ridge crests (Figure 2.6b). By contrast, the portions of the Greenheugh pediment capping unit more distal from the Gediz Vallis ridge are characterized by a regionally rough surface that is pockmarked by small craters and occasionally preserve remnant E-W trending parallel ridges, similar to those in the main SPg (Figure 2.6c). Polygonal terrain is sparse in the Greenheugh pediment capping unit and occurs primarily near the southwest boundary of the unit, where erosion reveals small patches of polygonal terrain at the interface between the pediment and the underlying Murray formation (Figure 2.6d).

Curiosity's Mastcam instrument acquired images of a portion of the northeast Greenheugh pediment capping unit from a location atop the nearby Vera Rubin ridge that highlights the unconformable relationship between the Greenheugh capping unit and the underlying Murray formation (Figure 2.7). At the terminus of the capping unit, strata occur as a thin (<1 meter), dark-toned, erosionally resistant, cross-bedded caprock, similar to that observed within the Stimson formation (Bryk et al., 2019). The underlying Murray bedrock shows distinct variation in color that has been interpreted to represent fluid alteration of Murray formation bedrock (Fraeman et al., 2019; Horgan et al., 2019). No through going mineralized fractures or polygonal features have been observed, thus far, in rover images of the Greenheugh pediment capping unit.

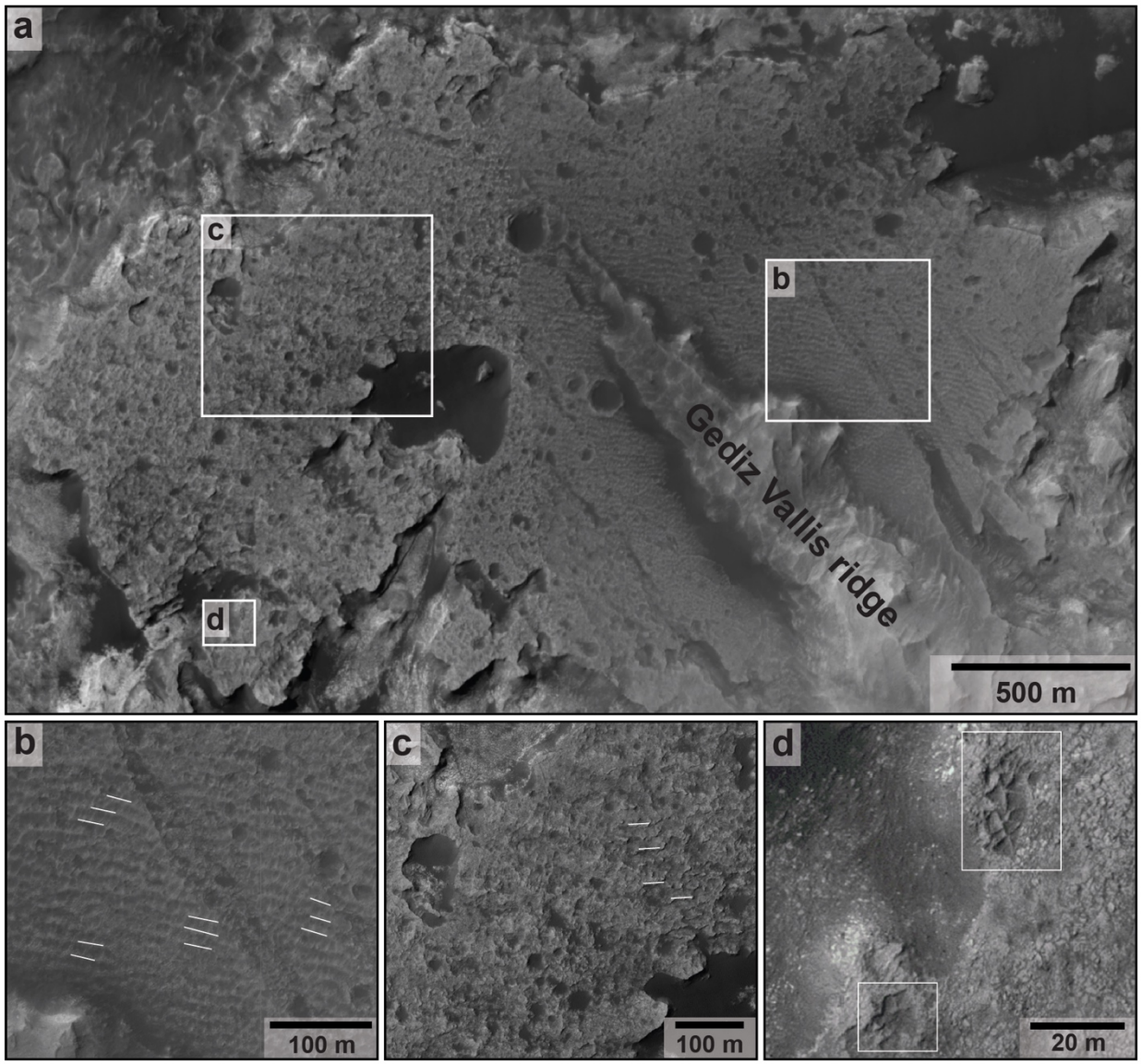


Figure 2.6 Features of the Greenheugh pediment capping unit. (a) Present-day fan-shaped exposure of the Greenheugh pediment capping unit; white boxes indicate the locations of b, c, and d. (b) Regions of the pediment capping unit near the Gediz Vallis ridge preserve evenly spaced WNW-ESE trending ridges, highlighted by white lines. (c) More distal portions of the pediment exhibit a rough surface texture that preserves numerous small craters; potential remnants of E-W trending ridges are highlighted in white. (d) Erosionally resistant polygons (within white boxes) are exposed primarily at the southwestern edge of the Greenheugh pediment capping unit, where erosion has revealed the contact between the Greenheugh pediment and the underlying Murray formation.

Interpretation of Siccar point group strata

Where imaged by instruments aboard the Curiosity rover, SPg strata contain abundant evidence for deposition via migration of an aeolian dune-field across the lower flanks of Mount Sharp, unconformably overlying previously eroded strata of the Murray formation (Banham et al., 2018). Although orbital images cannot provide a comparable scale of information, characteristics of SPg strata are broadly consistent with this interpretation. Throughout its extent, SPg strata unconformably overlie strata of the Murray formation along the lower flanks of Mount Sharp, and E-W trending ridges have previously been interpreted to originate from preferential cementation along the bounding surfaces that separate migrating aeolian dunes (Kah et al. 2013; Rubin et al., 2014).

Three distinct surface morphologies—ridged, heavily cratered, and polygonally ridged—observed in the SPg, however, suggest a potentially more complex depositional history across the region. Unfortunately, because the SPg drapes a previously eroded and irregular surface, is deposited along a local slope (spanning up to ~500 meters in elevation change), and is itself differentially eroded, it is difficult to resolve clear relationships between exposed surface morphologies. Based on local observations and superposition relationships (Figure 2.5), I infer that exposed surface morphologies represent distinct stratigraphic sub-units of the Siccar Point group (SPg). In all cases, polygonal features occur at the base of the SPg, and differentially eroded ridged facies occur at the top of the SPg. Polygons, however, can be overlain by either rough cratered surfaces or E-W trending ridged elements, suggesting that rough, cratered materials are inconsistently present across the SPg.

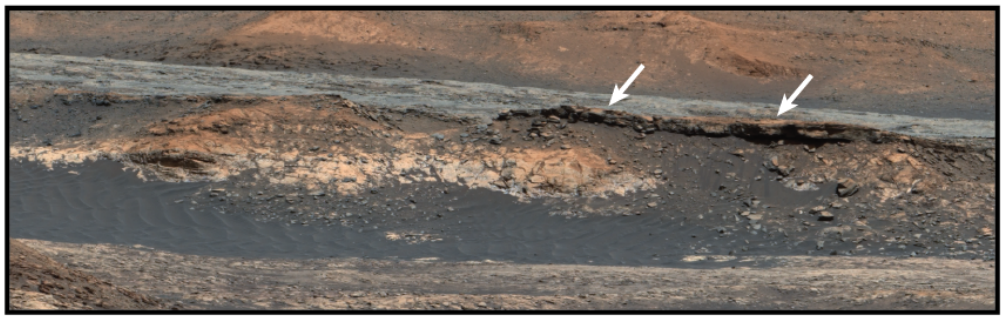


Figure 2.7 Portion of Mastcam mosaic acquired on Sol 2019 (mcam10651) pointed toward the eastern Greenheugh pediment. The pediment is overlain by a <1-meter-thick cap (white arrows) overlying the Murray formation mudstone; note lateral variation in color of underlying Murray mudstone.

Where rough, cratered surfaces are observed, measurements of stratal thickness (Table 2.1) show substantial variability between the top of the polygonal unit and the overlying cratered surface, suggesting that cratered materials may contain either single, or multiple, surfaces. In either case, the presence of numerous small craters, or secondary craters, suggest that these surfaces reflect an extended episode of exposure. Within aeolian systems, such surfaces would most likely result from dune migration interacting with a subsurface groundwater table, which would inhibit erosional denudation of the surface. Such groundwaters could represent either expansion of the groundwater reservoir, or the upward draw of fluids, via capillary flow through SPg strata, from the sub-Siccar Point unconformity. The presence of water-laden sediment is also consistent with erosional resistance and retention of small craters associated with rough, cratered surfaces. Collapse of pore-space associated with hypervelocity impacts, meteorite strewn fields, and associated sub-hypervelocity secondary craters, generates heat that can result in shock lithification when impacting water-bearing, poorly lithified materials (Kenkmann et al. 2018; Kieffer, 1971; Kieffer and Simonds, 1980).

In this scenario, regions where the basal polygonal unit occurs directly beneath E-W trending ridges, where extensive cratering is not apparent, may reflect regions where crater surfaces were entirely removed by erosion, or where erosional exposure times were insufficient to develop cratered surfaces. Once the groundwater table receded from the depositional surface, dry aeolian deposition (cf. Banham et al., 2018) could resume, resulting in formation of E-W trending parallel ridges.

Although classified as part of the Siccar Point group, the Greenheugh pediment capping unit occupies higher elevations and has steeper local slopes relative to other regions of SPg.

Surface textures, however, suggest a stratigraphy similar to that of the main outcrop of the SPg. Polygonal features, although rare in the Greenheugh pediment capping unit, occur only in the lowermost strata of the pediment, where modern erosion exposes the contact with the underlying Murray formation. The majority of the distal (lower elevation) regions of the pediment capping unit are characterized by a rough, cratered surface, that suggests interaction with local groundwater fluids. By contrast, parallel ridges of the Greenheugh pediment capping unit, likely represent an additional aeolian facies of the SPg.

Polygonal features in the Siccar Point group

Observations

A key observation within the Siccar Point Group is the presence of a network of polygonal features that is exposed across approximately 8 km^2 of the SPg. Polygons are present in all of the primary Siccar Point group exposures, although they are most abundant in SPg exposures northeast of the Curiosity rover traverse. Polygon edges are exposed as topographically elevated ridges. The composition of erosionally resistant ridges is impossible determine from orbital images. The erosional relief is typically <1 meter (Figure 2.8), and ridges appear light-toned relative to surrounding host rock, with the brightest regions concentrated at topographic highs and at the intersection of discrete ridges. The presence of dark-toned sand in the low-lying interiors of many polygons enhances their identification. Limitations in image resolution, as well, do not permit observation of central lines, such as those observed in larger-scale boxwork structures in Gale crater (Siebach & Grotzinger, 2013).

The shape of polygons in the SPg is variable (Figure 2.9). Polygons are dominantly four-sided; although, three-sided, five-sided, and more complex polygons are also observed. Polygon

edges can be straight or curved, with intersections commonly poorly defined. Polygons through most of the SPg show a similar range of shapes (Figure 2.9a-c), although a small region within the northeastern portion of the SPg displays distinctly elongate polygons with more laterally continuous edges (Figure 2.9d). Where image resolution permit clear determination of intersection angles, polygons show a range of angles from approximately 40° to 160° (N=642), with distinct modes at 90° and 120° (Figure 2.10).

Measurement of polygon size (i.e., the diameter of a circumscribed circle) reveal that, despite variation in shape and state of preservation, polygons exhibit relatively uniform diameters of approximately 7.5 ± 3.0 meters (N=8714). Polygons were separated into 4 regions to assess statistical similarity between populations. These regions include (Figure 2): the primary SPg strata both NE and SW of the Curiosity rover traverse, the Greenheugh pediment, areas traversed by the Curiosity rover, and regions in the far northeast that contain unusually elongate polygon shapes. Diameters of all polygon populations exhibit lognormal distributions as confirmed by Kolmogorov-Smirnov tests for normality (p value <0.01; Figure 2.11).

Non-parametric statistical analyses of population medians (i.e. Kruskal Wallis test) confirm that there is significant variance between populations; however, these tests do not indicate how populations differ. Tukey's Studentized Range test, however, is able to define regional variation between polygons and shows that the population of elongate polygons—present only in the far northeast SPg—is statistically different from other populations. Polygons within the main exposures of the SPg are statistically similar to both those observed in the region of the rover traverse and those in the Greenheugh pediment, but polygons observed near the rover traverse are statistically dissimilar to those in the Greenheugh pediment.

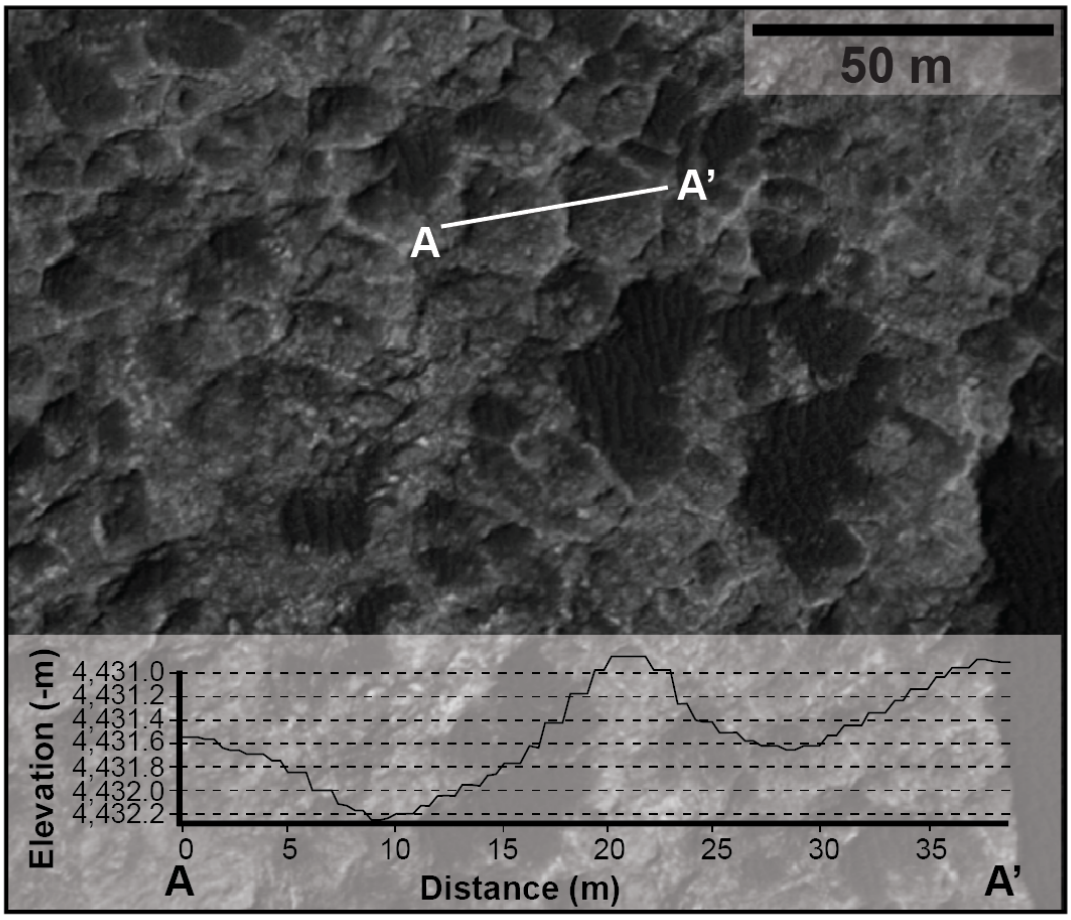


Figure 2.8 Cross-sectional elevation profile through polygons. Polygons consist of distinct, light-toned, erosionally resistant ridges; the difference in elevation of adjacent polygon centers reflects the local slope over which SPg strata was deposited. The stair-step pattern of the profile represents DEM pixel edges, not true topography.

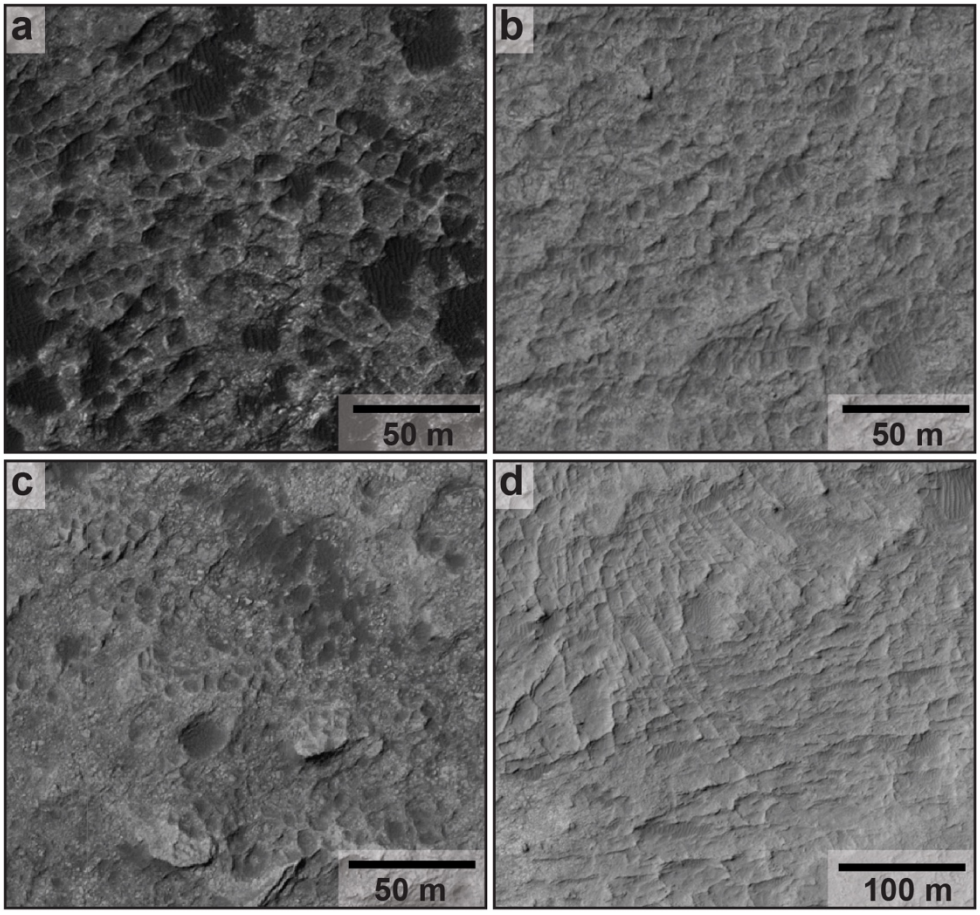


Figure 2.9 Polygons in the SPg. (a-b) Polygons from two different regions within the northeastern exposures of the SPg. (c) Polygons from the southwestern exposures of the SPg, separated from polygons shown in (a) and (b) by more than 20 km. (d) Distinctly elongate polygons in far northeastern exposures of the SPg.

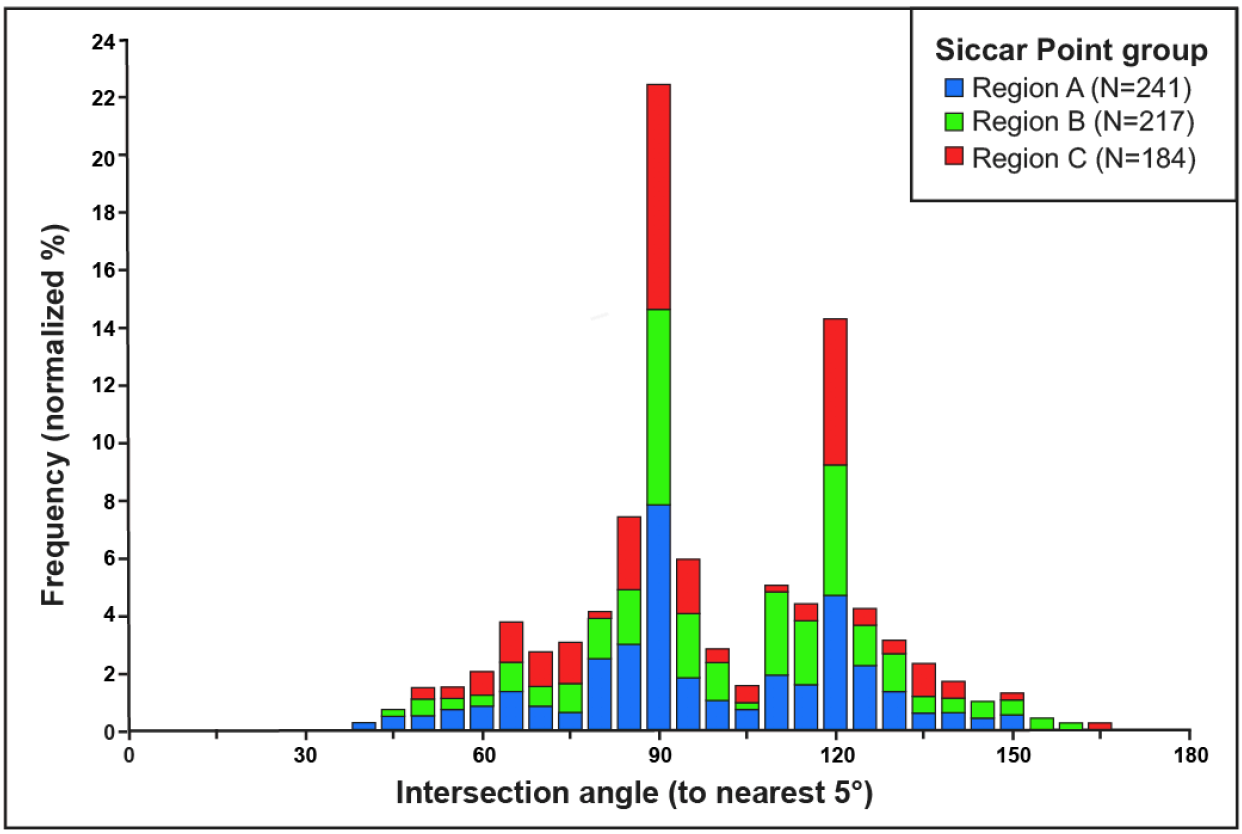


Figure 2.10 Angles of intersection of polygonal ridges, measured from three regions of the Siccar Point group northeast of the Curiosity rover traverse. Each region consisted of approximately 140,000 m^2. All regions show discrete modes that reflects dominance of 90° T-junctions (~23% of all measured intersections) and a second mode that reflects 120° Y-junctions (~14% of all measured intersections).

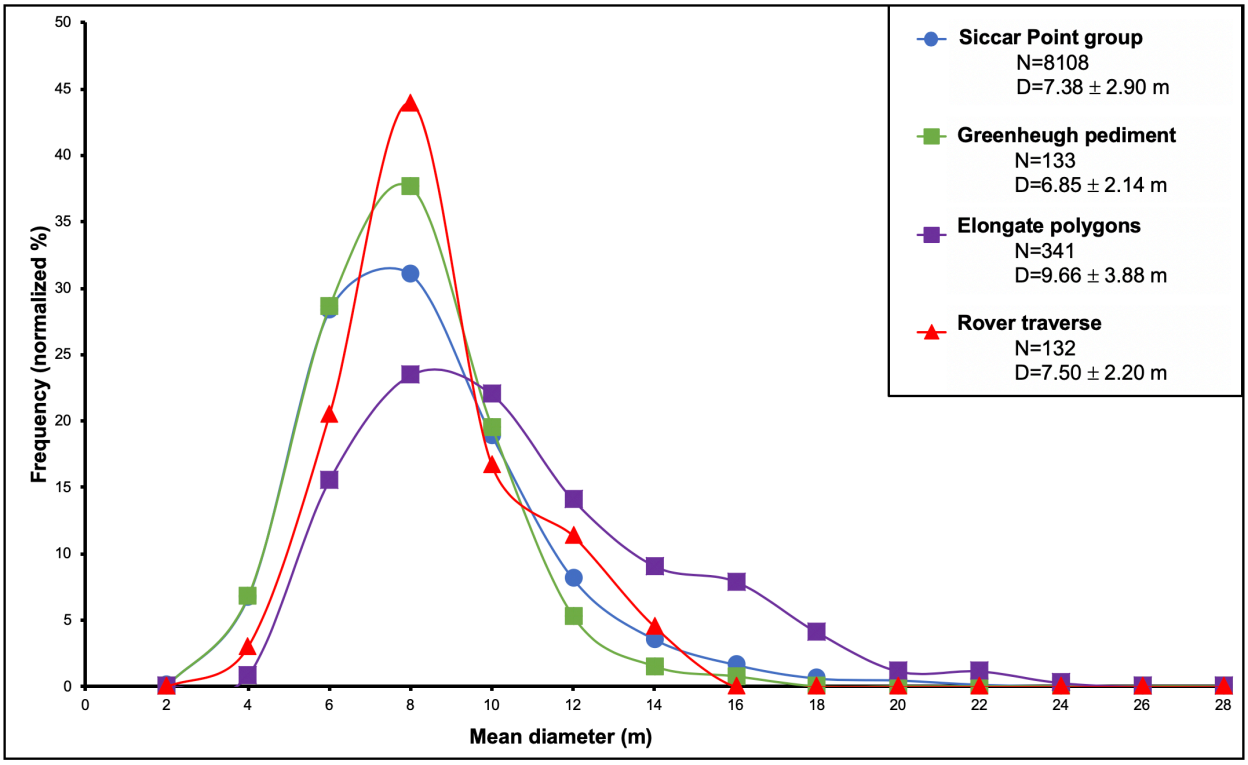


Figure 2.11 Polygon diameter data for regions of the Siccar Point group. Polygons in all regions (main exposures of the SPg, Greenheugh pediment exposures, far northeastern exposures of the SPg, and regions near the Curiosity rover traverse) exhibit a lognormal distribution and an overall mean of 7.5 ± 3.0 meters (N=8714).

Initial interpretation of polygonal features

Positive relief, polygonal features within the Siccar Point group (SPg) are interpreted to represent an extensive network of fluid-modified fractures. Fracturing of rock materials is the most common mechanism for forming linear features (Gudmundsson, 2011). In this scenario, the continuity and regional similarity in size of polygons suggests that fractures formed under relatively uniform, tensile stress conditions within a host rock or sediment that has generally homogeneous composition and material properties. Polygons are also stratigraphically constrained to the lowermost horizon of the SPg, implying a similar formation mechanism across the SPg. The positive relief of polygons additionally indicates syn- or postdepositional modification of fractures to provide greater erosional resistance than the surrounding host rock. Polygon boundaries are light-toned relative to surrounding host rock. Although lighter tone in images might, in part, reflect illumination on topographic highs, I suggest that the topographic relief supports the potential for either a secondary mineral phase within fractures, or fluid modification of bedrock adjacent to the fracture, as has been observed by the Curiosity rover (Kronyak et al., 2019; Nachon et al., 2014, 2016; Yen et al., 2017).

Statistical analysis verifies that there are differences in mean diameter within populations of polygons across the SPg. Most notably, the population of elongate polygons in the far northeastern exposures of the SPg is shown to be distinct by both parametric and non-parametric tests, suggesting that additional factors may have affected their development. Laterally continuous, curvilinear fractures in this region suggest a distinct episode of fracturing that occurred after primary lithification of the lower SPg, potentially driven by impact-related processes or localized crustal movement (e.g., mass wasting). The contrast of these fractures,

with respect to the regularly sized polygons in the rest of the SPg, suggests that multiple episodes of fracturing may have occurred. Statistical tests show that polygons within the higher elevation Greenheugh pediment are statistically different in size from those observed along the rover traverse and may reflect variation in formation conditions.

Additional observations of the Siccar Point group

Regional, ground-based observations

Additional observations regarding polygons in the lowermost SPg can be derived from ground-based images. Early in the Curiosity mission (Sol 23), a portion of the Siccar Point group (SPg) was imaged in a long-range mosaic of lower Mount Sharp. In both Mastcam (Figure 2.12a) and orbital (Figure 2.12b) images, discrete regions of white material ~0.5 m thick occur that cross-cut both the strata of the Murray formation and SPg. From orbit, these linear (and potentially planar) features are brighter-toned than surrounding strata of the SPg, but rarely exhibit the positive erosional relief observed in SPg polygons. These white features also show a variety of steeply dipping, yet non-vertical, orientations through strata and do not form consistent polygons in plan view (Figure 2.12b). By contrast, SPg polygonal ridges <50 meters to the east are thicker (~1 m), show a more regular size and shape, and exhibit consistent erosional relief.

Local, ground-based observations

Ground-based observations were also made as the Curiosity rover traversed remnant exposures of the SPg, locally designated as the Stimson formation (cf. Banham et al., 2018), in the area of the Emerson plateau, the Naukluft plateau, and the Murray buttes. From orbit,

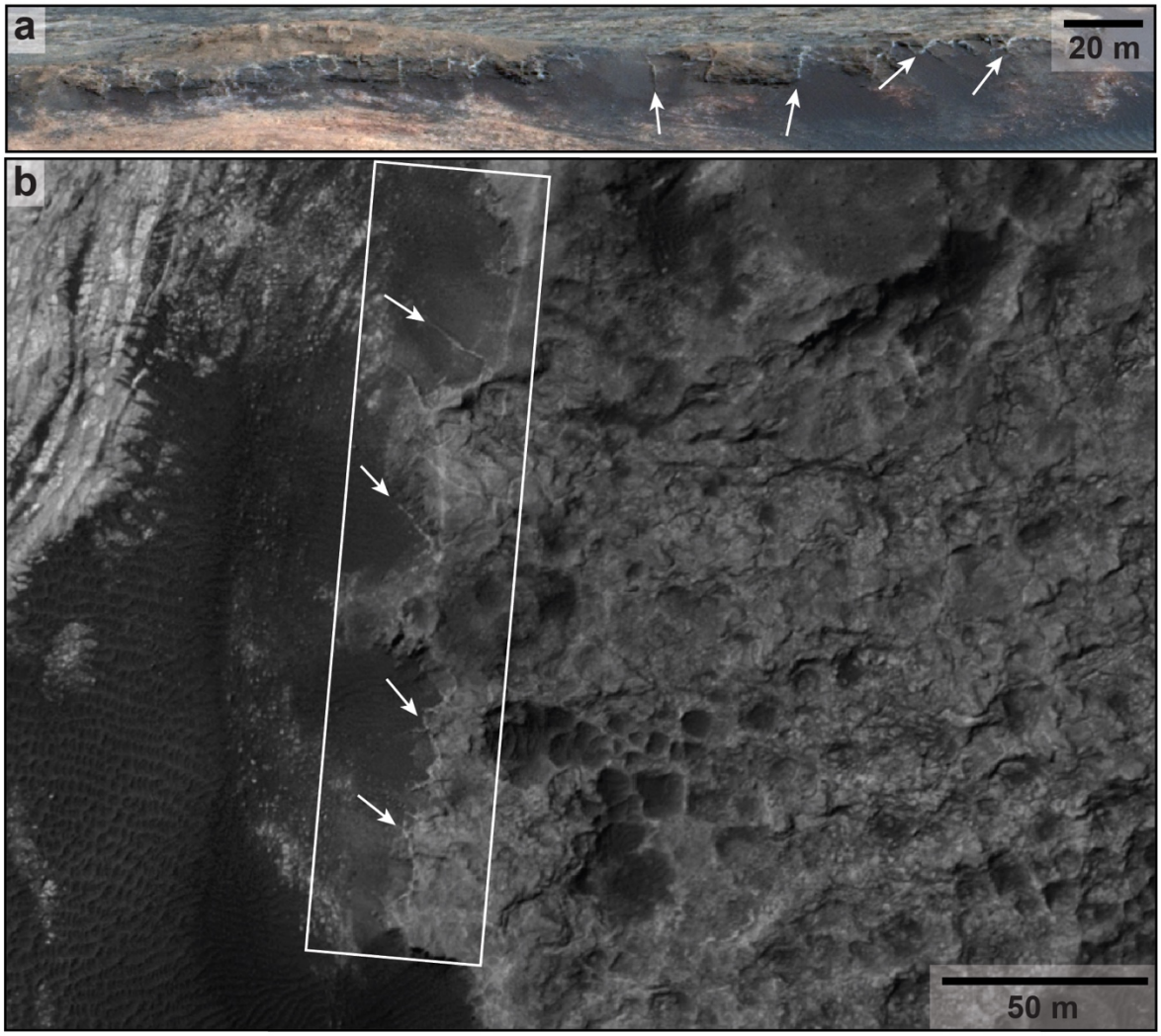


Figure 2.12 (a) Portion of Mastcam mosaic acquired on Sol 23 (mcam00114). The Siccar Point group is observed as a thin dark-toned unit overlying the Murray formation. Distinct white features (white arrows) extend from the Murray formation into the SPg. (b) Orbital context for Mastcam mosaic mcam00114, with the white box indicating the mosaic portion from (a). These features that crosscut the Murray formation and SPg (white arrows) exhibit a distinct morphology from the organized uniform polygonal fractures present in the SPg terrain in the right side of the image.

polygonal features are clearly visible in the Naukluft plateau and Murray buttes (Figure 2.13). Polygons occur in relative topographic lows along the Murray-Stimson unconformity and do not extend through the full thickness of the Stimson formation. From orbit, polygons show a similar morphology and scale as those observed in the primary outcrop exposures of the SPg (Figure 2.11).

The Stimson formation contains abundant evidence for postdepositional fluid flow along discrete fractures. Most prominently, calcium sulfate-filled hydrofracture veins occur in both the Stimson formation and underlying Murray formation (Nachon et al., 2019). Veins in the Stimson formation, however, are generally thinner and scarcer than those observed in the underlying Murray formation, and, in several locations, do not appear to cross the contact with the Stimson formation. It is unclear, in these cases, whether veins arrest or change directions at the contact (Figure 2.14a).

Fracture-associated alteration halos are also common in the Stimson formation. These occur as light-toned fracture-parallel alteration bands that reflect modification of host rock along fractures (Frydenvang et al., 2017; Yen et al., 2017; Figure 2.14b-c). The fractures themselves are commonly unmineralized and are, instead, filled with unlithified sand. Fractures associated with alteration halos cross-cut primary bedding at high angles, and commonly intersect one another in plan view. Zones of alteration reach up to ~20 centimeters on either side of fractures and reflect a complex diagenetic fluid history involving the enrichment of silica, sulfate, and other phases (Figure 14b-c; see Yen et al., 2017). Alteration halos commonly exhibit little to no positive relief and are dominantly lighter-toned than surrounding host rock (Figure 2.14b).

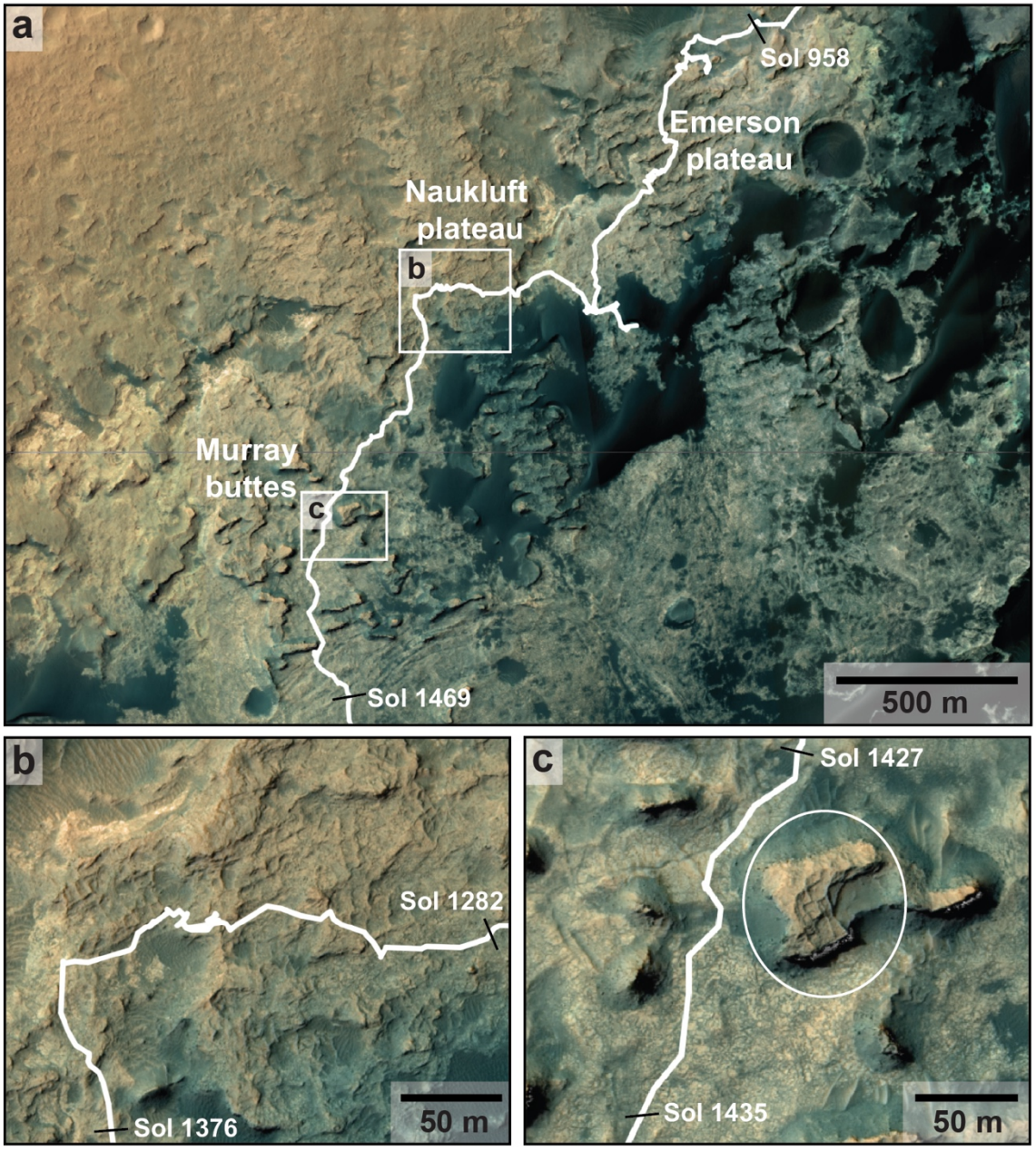


Figure 2.13 (a) Siccar Point group exposures in areas of the Curiosity rover traverse. In these areas, the Siccar Point group is designated as the Stimson formation, which was encountered in the Emerson plateau, the Naukluft plateau, and the Murray buttes region (white boxes). (b-c) Uniform polygonal fractures, similar in size and scale to other areas of the Siccar Point group, are observed within the Naukluft plateau and Murray butte terrain. The Curiosity rover traverse indicated by heavy white lines in all images.

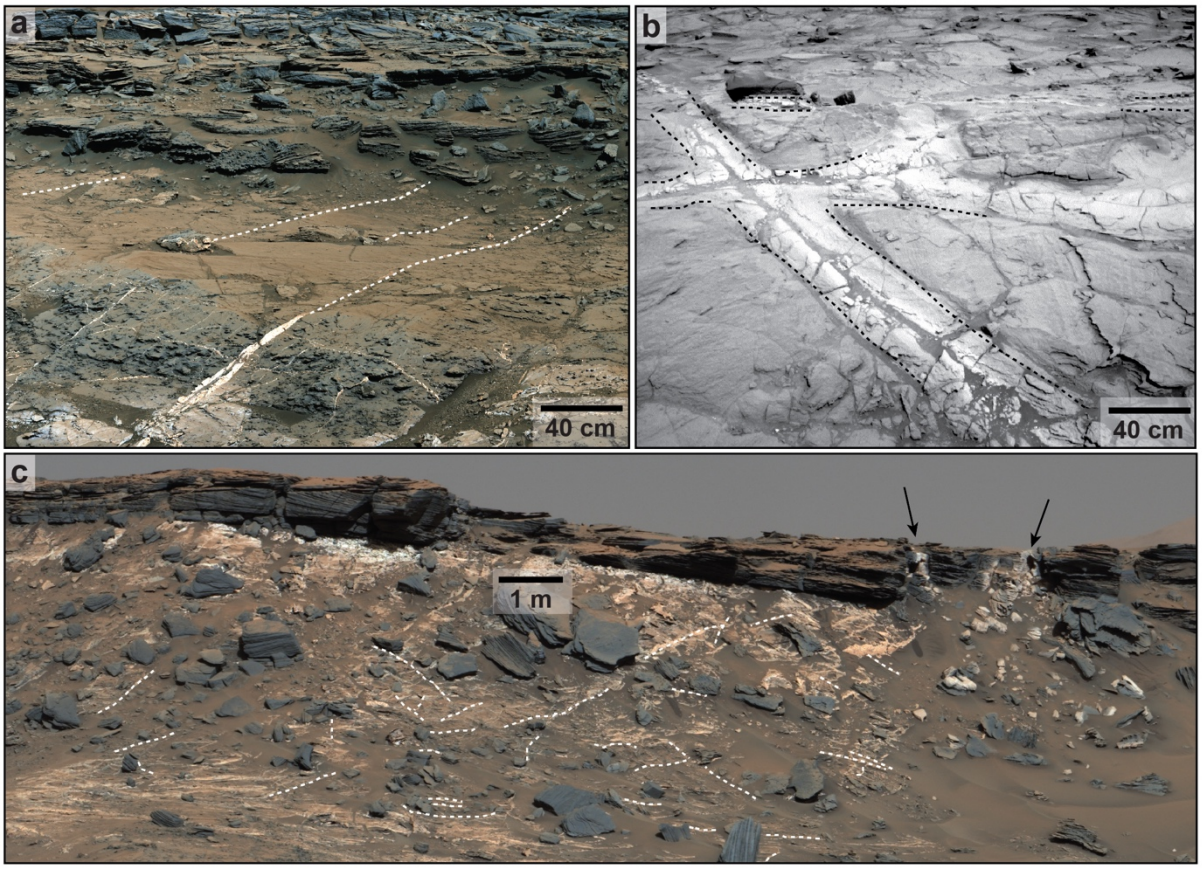


Figure 2.14 Veins and alteration halos in the Stimson formation. (a) White calcium sulfate veins in the underlying Murray formation approach, but commonly do not cross, the Murray-Stimson contact. Dashed white lines trace several prominent veins that approach the contact. Portion of Mastcam mosaic acquired on Sol 1275 (mcam05976). (b) Alteration halos in the Stimson formation, where bedrock adjacent to fractures has been modified by diagenetic fluids. Portion of Navcam image acquired on Sol 1083. Approximate halo margins are indicated by dashed black lines. (c) Veins (dashed white lines) and halos (black arrows) in the vicinity of the Murray-Stimson contact. Portion of Mastcam mosaic acquired on Sol 1267 (mcam05931).

However, in some locations, light-toned halos are bounded by darker-toned, erosionally resistant bands, giving the halos a ridged appearance.

The Mars Science Laboratory science team imaged the Stimson formation in the Naukluft plateau region where dense polygonal fractures are clearly visible from orbit (Figure 2.15). Polygonal structures are not observed in most Mastcam images because topographic relief obscures fractured regions from the camera view. Orbital viewsheds allow identification of Mastcam images that contain polygonal fractures (Figure 2.15a, c, d). However, in corresponding Mastcam images, polygons are subtle features, recognized only by small differences in erosional relief of the substrate and highlighted by the presence of aeolian sand in polygon centers (Figure 2.15b, d, f). The topographic expression of polygons varies; in some places (Figure 2.15b, f), polygon edges consist of erosionally resistant ridges; in other places (Figure 2.15d), polygon perimeters are nearly flush with surrounding host rock. Erosionally resistant polygon edges commonly expose layering within the host sandstone and can show hints of the cross-bedding that characterizes the Stimson formation in this region (Banham et al., 2018), but do not show any clear evidence of mechanical deformation. Locally, polygon edges correspond to alteration halos (Figure 2.15d). In most areas, however, there is insufficient evidence to clearly distinguish alteration of host rock associated with anything other than enhanced erosional resistance.

Interpretation of rover observations

The light-toned linear features that crosscut the Murray formation and Siccar Point group (SPg) (Figure 2.12), although close in proximity to erosionally resistant polygons, do not appear genetically related to SPg polygons because of their difference in size, color, erosional

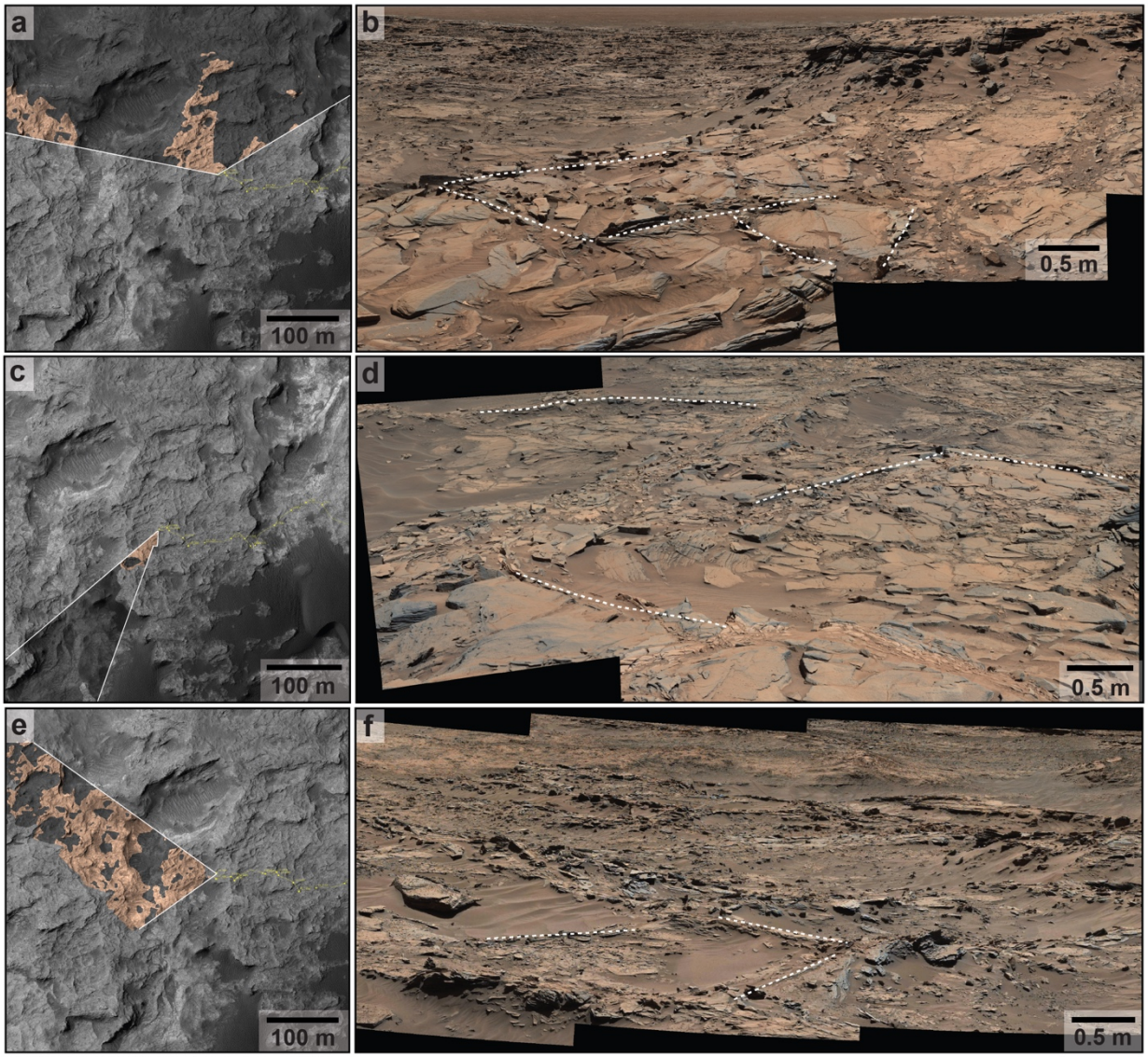


Figure 2.15 Polygonal fractures in the Naukluft plateau region. (a) Dashed white line indicates the areas imaged by Mastcam (viewshed) on Sol 1296 (mcam06154). Areas visible in mcam06154 are shown in brown, and non-visible portions in gray. (b) Portion of Mastcam mosaic mcam06154 showing several erosionally resistant polygons (dashed white lines). (c) Viewshed of Mastcam mosaic acquired on Sol 1296 (mcam06153) showing visible (brown) and non-visible (gray) portion of imaged region. (d) Portion of Mastcam mosaic mcam06153 showing resistant ridges that form rough polygons (dashed white lines). In the foreground, alteration halos may correspond with polygons. (e) Viewshed of Mastcam mosaic acquired on Sol 1312 (mcam06260). (f) Portion of Mastcam mosaic mcam06260 showing several polygon edges (dashed white lines).

resistance, and a distinct lack of consistent polygonal shape in plan view. Such features are through-going and bright-toned, suggesting that they represent fluid-altered fractures. With the available image resolution, it is difficult to infer whether these are mineralized hydrofractures or fracture-associated alteration halos; their thickness (~0.5 meter) is most consistent with a halo interpretation. These features are generally thinner than SPg polygonal ridges, which may suggest a lesser degree of fluid-host rock interaction.

Despite the abundance of polygonal fractures visible from orbit, rover images from the Naukluft plateau reveal that polygons can be subtle, commonly ambiguous, features from the ground. Oblique viewing geometry and topographic relief of outcrops, plus extensive sand coverage across areas of the Stimson formation, likely contribute to the difficulty in deciphering polygonal fractures from rover images. Processes responsible formation of polygonal features, and their enhanced erosional relief, cannot be uniquely determined from available images. The preservation of detailed lamination suggests that fracturing occurred after the primary deposition of basal aeolian strata and was not associated with additional mechanical deformation. Calcium sulfate veins are present within Mount Sharp and Siccar Point group strata, and many exhibit enhanced relief (cf. Kronyak et al., 2019; Nachon et al., 2016), yet there is no evidence that mineral veins are directly associated with polygons. Similarly, although alteration haloes are occasionally associated with polygons, this relationship is not uniquely linked to observed polygons. Alteration haloes, however, are likely analogous to polygon ridges as they represent the utilization of pre-existing fractures in the substrate by later-diagenetic fluids, which differentially affect host materials surrounding the fracture pathways. The presence of later-diagenetic fluid flow in the region of the Murray-Stimson unconformity is consistent, as well,

with observations of diagenetic concretions in the basal Stimson formation (Banham et al., 2018) and the color alteration of the Murray formation directly below the unconformity (Fraeman et al., 2019; Horgan et al., 2019). Together these observations emphasize the need to decouple the formation mechanism of polygonal fractures in the SPg from one or more potential fluid event that may have utilized pre-existing fractures and modified the host rock around the fractures.

Discussion

Potential formation mechanisms of polygonal features

The Siccar Point group (SPg) contains widespread, erosionally resistant polygonal features that are interpreted to represent fluid modification of a polygonal fracture system. Polygon size is relatively uniform over nearly 8 km^2 with minor variation at higher elevation. Polygon shapes vary, with most exhibiting three to six sides and internal angles that show strong modes at 90° and 120°.

Fracture networks—on centimeter to decameter scales—are widely documented on Mars (Chan et al., 2008; El Maarry et al., 2010, 2012, 2014; Kerber et al., 2017; Kronyak et al., 2019; Levy et al., 2009; Mangold et al., 2004; Mangold, 2005; McGill & Hills, 1992; Mellon, 1997; Nachon et al., 2014, 2016; Oehler et al., 2016; Seibert and Kargel, 2001; Siebach & Grotzinger, 2013; Sletten et al., 2003; Stein et al., 2018). Potential formation mechanisms for fractures include impact processes, hydrofracture, and contraction (i.e., desiccation and thermal-induced). Here I assess the viability of each formation mechanism and discuss the most parsimonious model for the origin of polygonal fractures in the SPg.

Impact processes generate characteristic radial and concentric fractures that commonly result in polygonal patterns (Ahrens & Rubin, 1993; Melosh, 1984, 1989). Radial fractures extend away from the impact basin up to several basin radii and exhibit straight to curvilinear patterns in plan view (e.g., Kumar & Kring, 2008; Ohman, 2009). These radial fractures form as initial stress waves from the impact propagate outward (Kumar & Kring, 2008; Polanskey & Ahrens, 1990). Concentric fractures then form distinctive rings that result from post-impact lithospheric rebound and inward contraction (Ahrens & Rubin, 1993). Despite the potential for polygonal fracture patterns to develop as radial and concentric patterns intersect, the apparent absence of fracture propagation into underlying strata of the Murray formation rules out impact as the primary mechanism of formation for SPg fractures. However, a small population of elongate polygons in the far northeast SPg (Figure 2.9d) exhibits curvilinear fractures in plan view that may indicate a differential stress field during fracture formation.

Hydrofractures are extensional fractures that form when fluid pressures within a rock body exceed rock strength. Mineral-filled fractures (veins) are commonly formed by this mechanism because depressurization and cooling of fluids can lead to mineral precipitation within fractures (Bons et al., 2012). Elevated fluid pressure may result from a variety of mechanisms, including overburden pressure, disequilibrium compaction, temperature increase, and chemical reactions that release volatiles or induce mineral swelling pressure (Cosgrove, 2001; Philipp, 2008; Schieber et al., 2017). Once rock strength is exceeded, the propagation direction and organization of hydrofractures depend strongly on the mechanical properties of the host rock, most prominently the tensile and compressive strength (themselves a function of porosity, grain size, and degree of cementation), and the degree of homogeneity or heterogeneity

of the host rock (Gudmundsson, 2011; Passchier & Trouw, 2005). A hydrofracture origin has been proposed to explain sparse to concentrated exposures of calcium sulfate-filled veins in the Bradbury and Mount Sharp groups in Gale crater (Caswell & Milliken, 2017; Kronyak et al., 2019; Schieber et al., 2017). These examples, however, often produce chaotic, unorganized fracture networks that reflect the potential for multiple generations of hydrofracture under different conditions of regional stress and the re-utilization of preexisting fractures (Kronyak et al., 2019). Although hydrofractures rarely form organized networks, such networks can hypothetically form under conditions of low differential stress (i.e., shallow burial), where fractures have a stronger tendency to connect and form polygonal intersections (Long et al., 1996) Under such conditions, an impermeable caprock is required to provide a sufficient barrier to fluid flow to permit the buildup of fluid pressure within a succession.

A hydrofracture origin for fractures in the SPg would require the relatively unusual scenario of hydrofracture under low differential stress. The SPg overlies previously eroded strata of Mount Sharp, which has been interpreted to reflect full or partial filling of Gale crater (Grotzinger et al., 2015), but SPg strata itself lacks indication of burial and exhumation. Therefore, fractures must have formed near the martian surface. In a hydrofracture scenario, the SPg would have had to have been well-lithified prior to fracturing, to serve as an effective caprock for increased fluid pressure. It is unlikely, however, that sufficient fluid pressures could be generated along the Murray-SPg unconformity; fractures would more likely propagate from the underlying units Murray formation, to ultimately arrest within the lower SPg. Potential hydrofracture veins observed in the Murray formation (Kronyak et al., 2019; Nachon et al., 2019) rarely cross the Murray-Stimson (SPg) contact, but instead end at the sub-Siccar Point

unconformity. Small pockets of breccia along the unconformity also contain fragments of light-toned material (Newsom et al., 2018), suggesting that hydrofractures in the Murray formation formed prior to erosional exhumation of Murray formation rocks and deposition of the SPg. A hydrofracture origin, therefore, is not the preferred mechanism to explain the formation of polygonal fractures in the SPg.

Perhaps the most common fracture-forming processes in near-surface environments reflect contractional processes associated with desiccation (e.g., mud cracks, tepee structures) or thermal cycling (e.g., patterned ground, surficial rock fracture, columnar jointing). In these cases, tensile stress develops in a surface undergoing volume reduction, resulting in extensional fractures (Allen, 1982; Chan et al., 2008; El Maarry et al., 2014; Lachenbrauch, 1962). In the case of columnar joints in a cooling lava, thermal contraction cracks incrementally propagate into the substrate, advancing perpendicular to the heat transfer front and away from areas of maximum cooling (tensile stress) (DeGraff & Aydin, 1987; Goehring & Morris, 2005). Similarly, during thermal expansion and contraction of rocks, internal stress develops as a function of the temperature gradient and associated thermal expansion (Chan et al., 2008; Goehring et al., 2013; Lachenbrauch, 1962). The presence of surface and ground waters can contribute to the formation and preservation of thermal cracking as fluids in cracks expand and contract during freeze-thaw cycles (Kerfoot, 1972; Lachenbrauch, 1962; Oehler et al., 2016).

Contractional polygons have been identified for many areas of the martian surface. Large-scale (i.e., hundreds of meters to kilometers in diameter) polygons (cf. El Maarry et al., 2012; McGill & Hills, 1992) are commonly restricted to surficial regolith at latitudes >50° and correlate with occurrences of ground ice, suggesting the potential for climatic control on polygon

formation (Mangold, 2005; Pina et al., 2008). In other cases, polygonal fracturing of lithified bedrock exposures has been attributed to a combination of thermal cycling and potential shrink-swell associated with wetting and drying of chemical weathering products (Chan et al., 2008). In a more recent example, centimeter-scale polygons preserved within Murray formation sedimentary strata has been attributed to desiccation in the environment of deposition (Stein et al., 2018).

Additional information on the origin of fracture systems can be reflected in the morphology of the preserved fractures. In a sedimentary substrate, shrinkage cracks form in response to tensile stresses within sediment that result from contraction (Shorlin et al., 2000). When stress exceeds local tensile strength, cracks open to relieve the buildup of tensile stress, usually along inhomogeneities in the substrate (i.e., pre-existing crack, bubble, or other defect), and grow in a direction that maximizes the release of energy (Goehring et al., 2012). Growth occurs until the crack hits a boundary or another crack. As initial cracks are influenced by any overarching contractional gradient, with long primary cracks indicating the direction of the gradient (Shorlin et al., 2000). Since the maximum energy release occurs perpendicular to a crack's edges, nearby cracks will commonly curve to intersect each other at roughly right angles. As cracks continue to form and intersect one another, they can form extensive polygonal networks. Common crack patterns include square to 4-sided, rectilinear, polygons that exhibit ~90° crack intersections, or T-junctions (Bohn et al., 2005; Goehring et al., 2010), and 5-6-sided polygons with intersections that trend toward ~120° intersections and Y-junctions.

Although the latter of these are typified by columnar basalts (DeGraff & Aydin, 1987; Goehring & Morris, 2005), polygon shapes reflect a complex the evolution of a crack system

through time (Goehring, 2013). A rectilinear pattern is favored during primary fracturing (Shorlin et al., 2000), and commonly records a single episode of shrinkage, but during repetitive fracture-forming events, each successive event alters the original crack positions and intersections. Old cracks, if not fully healed prior to the next cracking, commonly serve as planes of weakness and guide the propagation of newly forming cracks. Cracks approaching previous 90° junctions curve slightly because of asymmetric stress fields at intersection points, which causing junctions to shift and, over repeated cycles, results in T-junctions evolving into 120° Y-junctions (Goehring et al., 2010; Goehring, 2013; Goehring & Morris, 2014). Experiments in thin clay slurries demonstrate that crack patterns can evolve from 90°-dominated to 120°-dominated in as few as 10 contraction/expansion cycles (cf. Figure 4 in Goehring, et al., 2010). However, if sufficiently healing of the substrate occurs between cycles, new cracks may not have pre-existing pathways to guide their propagation and will again form rectilinear crack patterns. In this scenario, a network dominated by rectilinear (90° junctions) polygons would therefore be interpreted to reflect either an immature fracture system, or a fracture system that experienced sufficient healing between cycles (e.g., full wetting and homogenization of a muddy substrate) such that subsequent fracturing established new pathways (Figure 2.16).

Environmental factors can also influence the scale and nature of contractional crack patterns, including the rate of volume reduction, sediment thickness, and sediment composition (Allen, 1982). Slow rates of contraction favor the formation of fewer, longer, and potentially deeper cracks that produce polygons 10-100s of meters in diameter, whereas rapid rates favor the formation of relatively small polygons at the centimeter to meter-scale (Chan et al., 2008; El Maarry et al., 2014; Lachenbrauch, 1962).

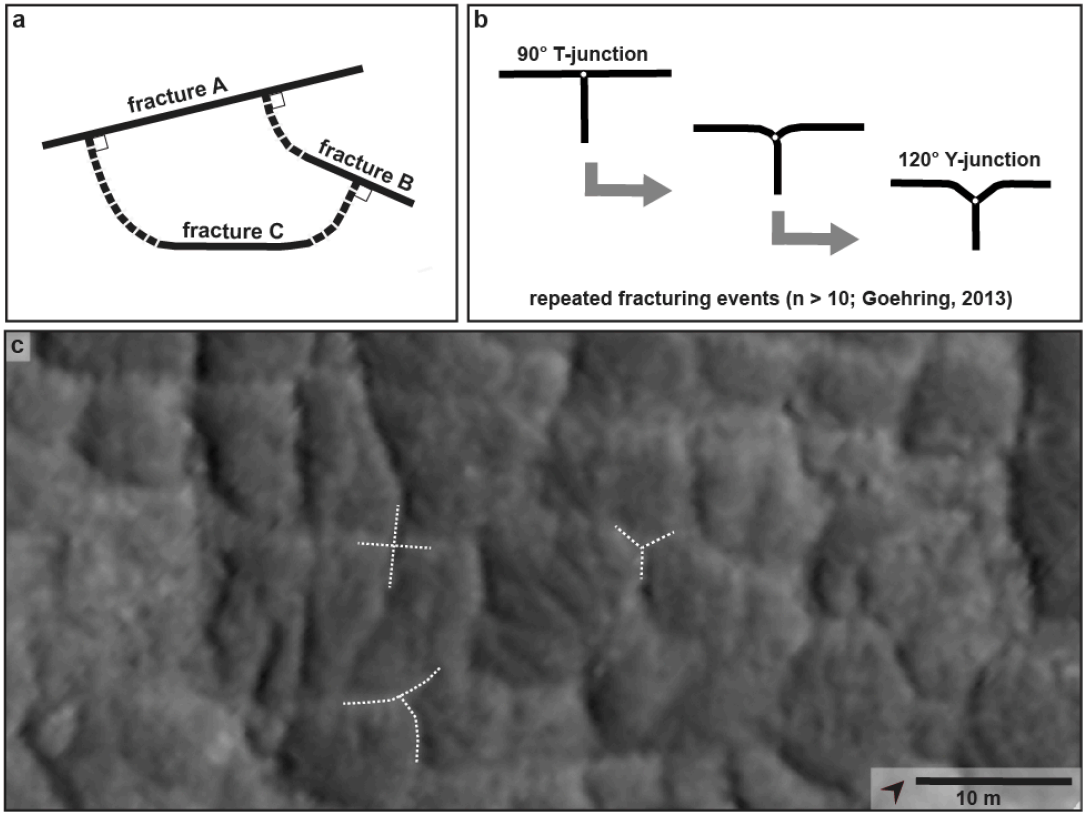


Figure 2.16 Fracture vertices, intersection angles, and changed with repeated fracture events. (a) Fractures initially show random to rectilinear orientations and grow in the direction that maximizes energy release, resulting in curvature toward pre-existing fractures and intersection angles approaching 90°. (b) Change in fracture morphology during repeated events can result in migration of fracture vertices, resulting in a change in intersection angles toward 120° (modified after Goehring, 2013). (c) SPg strata showing common fracture morphologies, including curved fractures, T-junctions, and Y-junctions (dotted lines).

Fracture depth and polygon size are also related to the thickness of the fractured substrate, with size-to-depth ratios of polygons ranging from 4:1 to 10:1 (El Maarry et al., 2010; Lachenbrauch, 1962; McGill & Hills, 1992). Despite such observations, experimental data show that fracture spacing (i.e., polygon size) is most strongly affected by layer thickness, as well as substrate composition and texture (Shorlin et al., 2000). For example, materials with a high content of shrink-swell clays, or the presence of salt and ice compounds can also contribute to a substrate susceptibility to expansion and contraction processes (Chan et al., 2008; Chavdarian & Sumner, 2006). The lithology of substrate materials also affects the overall morphology of fractures. Fractures formed dominantly by contraction (e.g., mud cracks, thermal fracturing) can remain devoid of crack fill, be filled from above by detrital material, or be filled at a much later stage by mineral precipitation from post-formation fluids. By contrast, the formation of ice or mineral salts can modify contractional (desiccation or thermal) fractures by increasing the volume of substrate materials. This can lead to deformation of either the interior or the perimeter of polygons, such as with ice-wedging (Levy et al., 2010; Matsuoka et al., 2018; Morse & Burn, 2013) or tepee structures (Assereto & Kendall, 1971; Burri et al., 1973). With such hybrid polygons, contraction forms original fractures that are then modified by compressional forces that result from the addition of material. Tepee structures are also commonly modified by post-fracture fluid migration that can result in precipitation of secondary minerals within fractures (Assereto & Kendall, 1977; Kendall & Warren, 1987; Warren, 1983). Post-fracture addition of mineral fills typically results in fracture-related phases that are more resistant to erosion than surrounding host rock surfaces (Havholm & Kocurek, 1994).

In Gale crater, polygonal fractures within the Siccar Point group are exposed across 8 km^2 and are statistically uniform in size. Polygons are restricted to a thin (meter-thick), lower horizon within the SPg and exhibit interior fracture angles with predominant modes at 90° and 120°. Together, these data suggest are consistent with fracture formation under contractional processes that occurred at the martian surface in a thin, regionally homogeneous substrate. Fractures occur at a variety of angles (Figure 2.10) and commonly curve to intersect at 90° T-junctions (23% of intersections). Although such behavior reflects the basic physics of fracture propagation (Bohn et al., 2005; Shorlin et al., 2000), a second dominant mode of 120° Y-junctions (14% of intersections) is indicative of time-wise evolution of fractures where repeated fracture events result in intersection migration and a shift in intersection angles from 90° to 120° (Goehring et al., 2010; Goehring 2013). Retention of a dominant mode at 90°, however, suggests either that: (1) reorganization of fractures was inhibited by the ability of the substrate to heal some fractures between contraction events, such as may occur with the deposition of detrital material (or ground ice) within cracks (Kerfoot, 1972; Lachenbrauch, 1962; Levy et al., 2009, 2010); or that (2) preserved fractures reflect a combination of the time-modification of some cracks and the complete healing of others, such as may occur with sufficient wetting to homogenize the host rock lithology.

Here I suggest that polygonal fractures in the SPg represent the interaction of aeolian strata with near-surface groundwaters. In this scenario, SPg strata were initially deposited by migrating aeolian dunes (Banham et al., 2018). Introduction of groundwaters—either through growth of a regional groundwater reservoir or capillary wicking of fluids (cf. Chavdarian & Sumner, 2006) into the lower SPg from the sub-Siccar Point unconformity, resulted in aeolian

denudation down to this fluid-adhered surface. Given sufficient cohesion of these aeolian sands, the evaporation of fluids and, in places, subsequent cycles of fluid recharge and evaporation, would then result in the formation of variably-evolved polygons.

Where observed by the Curiosity rover, the SPg consists of cross-bedded sandstone that is interpreted to have been deposited in a dry aeolian system (Banham et al., 2018). The widespread presence of polygonal fractures through the SPg, however, requires lateral variation in the lithologic properties across the SPg. Although such variation cannot be constrained from orbital data, even a minor contribution from clay minerals or evaporative salts may have provided sufficient sediment cohesion to support formation of contractional fractures.

The erosional relief on the sub-Siccar Point unconformity (Watkins et al. 2016) and potential ponding of fluids in erosional lows along the sub-Siccar Point unconformity could also have influenced the behavior of SPg during evaporation-recharge events by producing regions where fluid saturation may have been sufficient to heal earlier fractures. Local upwelling of groundwaters along the sub-Siccar Point unconformity may have even held fractures open, inhibiting fracture healing. On Earth, such fluid migration through open fractures plays a role in both the formation of tepee structures (Assereto & Kendall, 1971, 1977; Burri et al., 1973; Kendall & Warren, 1987) and the deposition of microbialites in ephemeral, desiccation-prone lakes (Vanden Berg, 2019; Warden et al., 2019). In drier areas of the SPg, perhaps only influenced by capillary flow of fluids through the SPg sandstone, repeated cycles of desiccation would have resulted in continuous evolution of fracture patterns. More persistent wetting of portions of the SPg, may have also led to the temporary decrease in aeolian sediment accumulation, driving development of cratered surfaces. The absence of fracturing associated

with the ridged sandstone in the upper SPg may then reflect deposition under climate conditions marked by reduction of groundwater flow and dominance of dry aeolian deposition (c.f. Banham et al., 2018).

Lithification of fracture polygons and implications for fluid circulation

Evidence for potentially repeated cycles of wetting and drying, and potential healing of fractures during this process, requires that fractures remain unfilled during their formation. Unfortunately, available image resolution does not permit identification of the process responsible for lithifying fractures and imparting increased resistance to erosion. Calcium sulfate-filled hydrofractures observed from the Curiosity rover's position appear to reflect late diagenetic mobilization of subsurface fluids (Kronyak et al., 2019; Nachon et al., 2019). Neither these calcium sulfate veins (Kronyak et al., 2019; Nachon et al., 2019) nor silica-enhanced fracture halos (Frydenvang et al., 2017; Yen et al., 2017) observed in the region of the Curiosity rover show evidence for detrital infill penecontemporaneous with fracture formation. The occurrence of halos in the Stimson formation, as well as pervasive alteration of mudstone directly beneath the Murray formation-Siccar Point group unconformity (Figure 2.7) suggests the potential for the protracted availability of fluids that may have migrated laterally at this geologic contact.

Conclusions

The Siccar Point group (SPg) unconformably overlies strata of lower Mount Sharp and is exposed over ~20 km^2 in northwest Gale crater. Based on observations in orbital images, several distinct surface textures characterize the SPg, including: (1) E-W trending parallel ridges; (2)

erosionally resistant, crater-retentive terrain; and (3) a laterally extensive network of resistant polygonal fractures, which is constrained to the lowermost horizon of the SPg. Across the SPg, fracture polygons exhibit relatively uniform sizes, approximately 7.5 ± 3.0 meters in diameter, a range of intersection angles with discrete modes at 90° and 120°. Morphology of polygons suggests that fractures formed as a result of repetitive contractional cycles, likely during desiccation and recharge of local groundwater, which concentrated at the boundary between the underlying Murray formation and initial deposits of the SPg. The erosional resistance of polygons indicates cementation by later diagenetic fluid flow. Timing relationships suggest the following sequence of events in Gale crater: (1) Deposition of Mount Sharp group strata and emplacement of syndepositional to early diagenetic features (Kah et al., 2018; Stein et al., 2018; Sun et al., 2019); (2) burial of Mount Sharp strata and multiple events of hydrofracture and fracture-filling mineralization (Kronyak et al., 2019); (3) erosional exhumation of lower Mount Sharp strata; (4) deposition of lower Siccar Point group strata, formation of polygonal fractures, and formation of cratered surface; (5) deposition of upper Siccar Point group strata (i.e., ridged unit) under hydrologically drier conditions; (6) post-depositional modification of SPg fractures by migrating fluids. The cementation of such relatively young structures within the SPg indicate a protracted history of fluid stability.

Acknowledgements

This work was supported by the Mars Science Laboratory (MSL) Curiosity rover mission; I thank all those who provide operational support to the rover and its instruments, with particular thanks to Fred Calef (NASA/JPL) for his work on the MMGIS system. I thank Ed Perfect (University of Tennessee) for assistance in statistical analyses and Bradley Thomson (University

of Tennessee) for helpful manuscript feedback. I thank reviewers two anonymous reviewers for comments and feedback that improved the clarity of this manuscript. MSL rover images acquired through Sol 2223 may be accessed through the NASA Planetary Data System.

References

Ahrens, T. J. & Rubin, A. M. (1993). Impact-induced tensional failure in rock. *Journal of Geophysical Research*, 98, 1185-1203 https://doi.org/10.1029/92JE02679

Allen, J. R. L. (1982). *Sedimentary Structures: Their character and physical basis*. Elsevier, New York.

Anderson, R. & Bell III, J. F. (2010). Geologic mapping and characterization of Gale Crater and implications for its potential as a Mars Science Laboratory landing site. *The Mars Journal*, *5*, 76–128. http://doi.org/10.1555/mars.2010.0004

Assereto, R.L. & Kendall, C. G. St. C. (1971). Megapolygons in Ladinian limestones of Triassic of southern Alps: evidence of deformation by penecontemporaneous desiccation and cementation. *Journal of Sedimentary Petrology*, 41(3), 715-723.

Assereto, R.L. & Kendall, C. G. St. C. (1977). Nature, origin, and classification of peritidal tepee structures and related breccias. *Sedimentology* 24, 153-210.

Banham, S. G., Gupta, S., Rubin, D. M., Watkins, J. A., Sumner, D. Y., Edgett, K. S., et al. (2018). Ancient Martian aeolian processes and palaeomorphology reconstructed from the Stimson formation on the lower slope of Aeolis Mons, Gale crater, Mars. *Sedimentology*, *65*(4), 993–1042. http://doi.org/10.1111/sed.12469

Bohn, S., Pauchard, L. & Couder, Y. (2005). Hierarchical crack pattern as formed by successive domain divisions. I. Temporal and geometrical hierarchy. *Physical Review E*, 71. doi: 10.1103/PhysRevE.71.046214

Bons, P. D., Elburg, M. A., & Gomez-Rivas, E. (2012). A review of the formation of tectonic veins and their microstructures. *Journal of Structural Geology*, 43, 33-62. http://dx.doi.org/10.1016/j.jsg.2012.07.005

Bridges, N. T. & Ehlmann, B. L. (2018). The Mars Science Laboratory (MSL) Bagnold Dunes Campaign, Phase I: Overview and introduction to the special issue. *Journal of Geophysical Research Planets*, 123, 3-19. doi:10.1002/2017JE005401

Bryk, A. B., Dietrich, W. E., Lamb, M. P., Grotzinger, J. P., Vasavada, A. R., Stack, K. M., et al. (2019). In Curiosity's path: the geomorphology and stratigraphy of the Greenheugh pediment and Gediz Vallis ridge Gale crater. *LPS L*, Abstract 2263.

Burri, P., du Dresnay, R., & Wagner, C. W. (1973). Tepee structures and associated diagenetic features in intertital carbonate sands (Lower Jurassic, Morocco). Sedimentary Geology, 9, 221-228. https://doi.org/10.1016/0037-0738(73)90046-8

Buz, J., B. L. Ehlmann, L. Pan, and J. P. Grotzinger (2017). Mineralogy and stratigraphy of the

Gale crater rim, wall, and floor units. *Journal of Geophysical Research Planets*, 122, 1090–1118, doi:10.1002/ 2016JE005163

Calef III, F. J. & Parker, T. (2016). MSL Gale Merged Orthophoto Mosaic, Publisher: PDS Annex, U.S. Geological Survey, URL: http://bit.ly/MSL_Basemap.

Calef III, F. J., Gengl, H. E., Soliman, T., Abercrombie, S. P., & Powell, M. W. (2017). MMGIS: A multi-mission geographic information system for insitu Mars operations. *LPS XLIC*, Abstract 2541.

Carr, M. H. (1974). Tectonism and volcanism of the Tharsis Region of Mars. *Journal of Geophysical Research*, *79*(26), 3943–3949. http://doi.org/10.1029/JB079i026p03943

Caswell, T. E., & Milliken, R. E. (2017). Evidence for hydraulic fracturing at Gale crater, Mars: Implications for burial depth of the Yellowknife Bay formation. *Earth and Planetary Science Letters*, 468, 72–84. https://doi.org/10.1016/j.epsl.2017.03.033

Chan, M. A., Yonkee, W. A., Netoff, D. I., Seiler, W. M., Ford, R. L. (2008). Polygonal cracks in bedrock on Earth and Mars: implications for weathering. *Icarus*, 194, 65-71. doi:10.1016/j.icarus.2007.09.026

Chavdarian, G.V. & Sumner, D.Y. (2006). Cracks and fins in sulfate sand: Evidence for recent mineral-atmospheric water cycling in Meridiani outcrops? *Geology*, 34, 229-232. https://doi.org/10.1130/G22101.1

Cosgrove, J. W. (2001). Hydraulic fracturing during the formation and deformation of a basin: a factor in the dewatering of low-permeability sediments. *AAPG Bulletin*, 85, 737-748.

DeGraff, J. M. & Aydin, A. (1987). Surface morphology of columnar joints and its significance to mechanics and direction of joint growth. *Geological Society of America*, 99, 605-617. doi: 10.1130/0016-7606(1987)992.0.CO;2

Edgar, L. A., Gupta, S., Rubin, D. M., Lewis, K. M., Kocurek, G. A, Anderson, R. B., & Bell, J. F. III, et al. (2018). Shaler: in situ analysis of a fluvial sedimentary deposit on Mars. *Sedimentology*, 65, https://doi.org/10.1111/sed.12370

Edgett, K. S., Yingst, R. A., Ravine, M. A., Caplinger, M. A., Maki, J. M., Ghaemi, T, et al. (2012) Curiosity's Mars Hand Lens Imager (MAHLI) Investigation. *Space Science Reviews*, 170, 259-317. doi 10.1007/s11214-012-9910-4

El Maarry, M. R., Markiewicz, W. J., Mellon, M. T., Goetz, W., Dohm, J. M., & Pack, A. (2010). Crater floor polygons: Desiccation patterns of ancient lakes on Mars? *Journal of Geophysical Research*, 115. doi:10.1029/2010JE003609.

El Maarry, M. R., Kodikara, J., Wijessoriya, S., Markiewicz, W. J., & Thomas, N. (2012). Desiccation mechanism for formation of giant polygons on Earth and intermediate-sized polygons on Mars: Results form a pre-fracture model. *Earth and Planetary Science Letters*, 323-324, 19-26. doi:10.1016/j.epsl.2012.01.016

El Maarry, M. R., Watters, W., McKeown, N. K., Carter, J., Noe Dobrea, E., Bishop, J. L., et al. (2014). Potential desiccation cracks on Mars: a synthesis from modeling, analogue-field studies, and global observations. *Icarus* 241, 248-268. http://dx.doi.org/10.1016/j.icarus.2014.06.033

Ewing, R.C., Lapotre, M. G. A., Lewis, K. W., Day, M., Stein, N., Rubin, D. M. et al. (2017). Sedimentary processes of the Bagnold Dunes: the eolian rock record of Mars. *Journal of Geophysical Research: Planets*, 122(12), 2544-2573. https://doi.org/10.1002/2017JE005324

Fedo, C. M., Grotzinger, J. P., Gupta, S., Stein, N. T., Watkins, J., Banham, S., et al. (2017). Facies analysis and basin architecture of the upper part of the Murray formation, Gale crater, Mars. *LPS XLVIII*, Abstract 1689.

Fergason, R. L., Christensen, P. R. & Kieffer, H. (2006). High-resolution thermal inertia derived from the Thermal Emission Imaging System (THEMIS): Thermal model and applications. *Journal of Geophysical Research*, 11. https://doi.org/10.1029/2006JE002735

Fraeman, A. A., Ehlmann, B. L., Arvidson, R. E., Edwards, C. S., Grotzinger, J. P., Milliken, R. E., et al. (2016). The stratigraphy and evolution of lower Mount Sharp from spectral, morphological, and thermophysical orbital data sets. *Journal of Geophysical Research: Planets*, 121, 1713–1736. https://doi.org/10.1002/2016JE005095

Fraeman, A. A., Arvidson, R. E., Horgan, B. H., Jacob, S. R., Johnson, J. R., Morris, R. V., et al. (2019). Synergistic orbital and in situ observations at Vera Rubin ridge: comparing CRISM and Curiosity observations. *LPS L*, Abstract 2118.

Frydenvang, J., Gasda, P. J., Hurowitz, J. A., Grotzinger, J. P., Wiens, R. C., Newsom, H. E., et al. (2017). Diagenetic silica enrichment and late-stage groundwater activity in Gale crater, Mars. *Geophysical Research Letters*, 44, 4716–4724. https://doi.org/10.1002/2017GL073323

Goehring, L. & Morris, S.W. (2005). Order and disorder in columnar joints. *Europhysics Letters*, 69(5), 739-745. doi: 10.1209/epl/i2004-10408-x

Goehring, L., Conroy, R., Akhter, A., Clegg, W. J., & Routh, A. F. (2010). Evolution of mud-crack patterns during repeated drying cycles. *Soft Matter*, 6, 3562-3567.

Goehring, L. (2013). Evolving fracture patterns: columnar joints, mud cracks, and polygonal terrain. *Philosophical Transactions of The Royal Society*, 371. http://dx.doi.org/10.1098/rsta.2012.0353

Goehring, L. & Morris, S.W. (2014). Cracking mud, freezing dirt, and breaking rocks. *Physics Today*, 67, 39-44. https://doi.org/10.1063/PT.3.2584

Grotzinger, J. P., & Milliken, R. (2012). The sedimentary rock record of Mars: Distribution, origins, and global stratigraphy. *SEPM Special Publication: Sedimentary Geology of Mars*, 102, 1–48. https://doi.org/10.2110/pec.12.102.0001

Grotzinger, J. P., Sumner, D. Y., Kah, L. C., Stack, K., Gupta, S., Edgar, L., et al. (2014). A habitable fluvio lacustrine environment at Yellowknife Bay, Gale crater, Mars. *Science*, 343(6169). https://doi.org/10.1126/science.1242777

Grotzinger, J. P., Gupta, S., Malin, M. C., Rubin, D. M., Schieber, J., Siebach, K., et al. (2015). Deposition, exhumation, and paleoclimate of an ancient lake deposit, Gale crater, Mars. *Science*, 350(6257), aac7575. https://doi.org/10.1126/science.aac.7575

Gudmundsson, A. (2011). *Rock Fractures in Geological Processes*. Cambridge University Press, New York.

Havholm, K. G. & Kocurek, G. (1994). Factors controlling aeolian sequence stratigraphy: clues from super bounding surface features in the Middle Jurassic Page Sandstone. *Sedimentology*, 41, 913-934. https://doi.org/10.1111/j.1365-3091.1994.tb01432.x

Hiesinger, H. & Head, J. W. III (2000) Characteristics and origin of polygonal terrain in southern Utopia Planitia, Mars: Results from Mars Orbiter Laser Altimeter and Mars Orbiter Camera data. Journal of Geophysical Research, 105, 11999-12022. https://doi.org/10.1029/1999JE001193

Horgan, B., Fraeman, A., Johnson, J. R., Thompson, L., Jacob, S., Wellington, D., et al. (2019). Redox conditions during diagenesis in the Vera Rubin ridge, Gale crater, Mars, from Mastcam multispectral images. *LPS L,* Abstract 1424.

Kah, L.C., Rubin, D.M., Gupta, S., Lewis, K.W., Kocurek, G.A., Grotzinger, J.P. (2013) Origin of the low-albedo mound skirting unit in the region of the MSL landing ellipse and implications for the relative age of Glenelg strata. *LPS XLIV*, Abstract 1121.

Kah, L. C., Stack, K. M., Eigenbrode, J. L., Yingst, R. A., & Edgett, K. S. (2018). Syndepositional precipitation of calcium sulfate in Gale crater, Mars. *Terra Nova*, 1-9. doi: 10.1111/ter.12359.

Kendall, C. G. St. C. & Warren, J. (1987). A review of the origin and setting of tepees and their associated fabrics. *Sedimentology*, 34, 1007-1027.

Kenkmann, T., Sundell. K. A., & Cook, D. (2018). Evidence for a large Paleozoic impact crater strewn field in the Rocky Mountains. *Scientific Reports*, 8. doi:10.1038/s41598-018-31655-4

Kerber, L., Dickson, J. L., Head, J. W., & Grosfils, E. B. (2017). Polygonal ridge networks on Mars: Diversity of morphologies and the special case of the eastern Medusae Fossae Formation. *Icarus*, 281, 200–219. https://doi.org/10.1016/j.icarus.2016.08.020

Kerfoot, D.E. (1972) Thermal contraction cracks in an Arctic tundra environment. *Arctic Institute of North America*, 25(2), https://doi.org/10.14430/arctic2953

Kieffer, S. W. (1971). Shock metamorphism of the Coconino Sandstone at Meteor Crater, Arizona. *Journal of Geophysical Research*, 76(23), 5449-5473. https://doi.org/10.1029/JB076i023p05449

Kieffer, S. W. & Simonds, C. H. (1980) The role of volatiles and lithology in the impact cratering process. Reviews of Geophysics and Space Physics, 18(1), 143-181. doi: 10.1029/RG018i001p00143.

Kronyak, R. E., Kah, L. C., Edgett, K. S., VanBommel, S. J., Thompson, L. M., Wiens, R. C., et al. (2019). Mineral-filled fractures as indicators of multigenerational fluid flow in the Pahrump Hills member of the Murray formation, Gale crater, Mars. *Earth and Space Science*, 6, 238-265. https://doi.org/10.1029/2018EA000482

Kumar, P. S. & Kring, D. A. (2008). Impact fracturing and structural modification of sedimentary rocks at Meteor Crater, Arizona. *Journal of Geophysical Research*, 113. doi:10.1029/2008JE003115,

Lachenbrauch, A.H. (1962). Mechanics of thermal contraction cracks and ice wedge polygons in pemafrost. *Geological Society of America Special Paper*, 70, 1-69.

Le Deit, L., Hauber, E., Fueten, F., Pondrelli, M., Rossi, A.P., & Jaumann, R. (2013). Sequence of infilling events in Gale Crater, Mars: Results from morphology, stratigraphy, and mineralogy. *Journal of Geophysical Research: Planets*, 118, 2439–2473, doi:10.1002/2012JE004322.

Levy, J., Head, J., & Marchant, D. (2009). Thermal contraction crack polygons on Mars: Classification, distribution, and climate implications from HiRISE observations. *Journal of Geophysical Research: Planets*, *114*(1), 1–19. http://doi.org/10.1029/2008JE003273

Levy, J. S., Marchant, D. R., & Head, J. W. (2010). Thermal contraction crack polygons on Mars: A synthesis from HiRISE, Phoenix, and terrestrial analog studies. *Icarus*, 206, 229-252. doi:10.1016/j.icarus.2009.09.005

Long, J. C. S., Aydin, A., Brown, S. R., Einstein, H. H., Hestir, K., Hsieh, P. A., et al. (1996). *Rock fractures and fluid flow: Contemporary understanding and applications*. National Academy Press: Washington DC.

Maki, J., Thiessen, D., Pourangi, A., Kobzeff, P., Litwin, T., Scherr, L., et al. (2012). The Mars Science Laboratory engineering cameras. *Space Science Reviews*, 170, 77-93. doi 10.1007/s11214-012-9882-4

Malin, M. C., Ravine, M. A., Caplinger, M. A., Ghaemi, F. T., Schaffner, J. A., Maki, J. N., et al. (2017). The Mars Science Laboratory (MSL) Mast cameras and Descent imager: Investigation and instrument descriptions. *Earth and Space Science*, 4, 506-539. doi:10.1002/2016EA000252

Mangold, N., Maurice, S., Feldman, W. C., Costard, F., & Forget, F. (2004). Spatial relationships between patterned ground and ground ice detected by the Neutron Spectrometer on Mars. *Journal of Geophysical Research*, 109. doi:10.1029/2004JE002235

Mangold, N. (2005). High latitude patterned grounds on Mars: Classification, distribution, and climatic control. *Icarus*, 174, 336-359. doi:10.1016/j.icarus.2004.07.030

Matsuoka, N., Christiansen, H. H., & Watanabe, T. (2018). Ice-wedge polygon dynamics in Svalbard: Lessons from a decade of automated multi-sensor monitoring. *Permafrost and Periglacial Processes*, 29, 210-217. doi: 10.1002/ppp.1985

McEwen, A. S., Eliason, E. M., Bergstrom, J. W., Bridges, N. T., Hansen, C.J., Delamere, W. A., et al. (2007). Mars Reconnaissance Orbiter's High Resolution Imaging Science Experiment (HiRISE). *Journal of Geophysical Research: Planets,* 112. doi:10.1029/2005JE002605

McGill, G. E. & Hills, L. S. (1992). Origin of giant martian polygons. *Journal of Geophysical Research*, 97(E2), 2633-2647. https://doi.org/10.1029/91JE02863

Mege, D. & Masson, P. (1996a). Amounts of crustal stretching in Valles Marineris, Mars. *Planetary and Space Science*, 44(8), 749-781. https://doi.org/10.1016/0032-0633(96)00013-X

Mege, D. & Masson, P. (1996b). Stress models for Tharsis formation, Mars. *Planetary and Space Science*, 144(12), 1471-1497. https://doi.org/10.1016/S0032-0633(96)00112-2

Mellon, M. T. (1997). Small-scale polygonal features on Mars: Seasonal thermal contraction cracks in permafrost. *Journal of Geophysical Research: Planets*, 102 (E11), 25617-25628. https://doi.org/10.1029/97JE02582

Melosh, H. J. (1984). Impact ejection, spallation, and the origin of meteorites. *Icarus*, 59(2), 234-260. https://doi.org/10.1016/0019-1035(84)90026-5

Melosh, (1989). *Impact cratering: A geological process.* Oxford University Press, New York.

Milliken, R. E., Grotzinger, J. P., & Thomson, B. J. (2010). Paleoclimate of Mars as captured by the stratigraphic record in Gale crater. *Geophysical Research Letters*, 37, doi:10.1029/2009GL041870.

Milazzo, M. P., Keszthelyi, L. P., Jaeger, W. L., Rosiek, M., Mattson, S., Verba, C., et al. (2009). Discovery of columnar jointing on Mars. *Geology*, 37(2), 171-174. doi: 10.1130/G25187A.1

Milliken, R. E., Ewing, R. C., Fischer, W. W., & Hurowitz, J. (2014). Wind-blown sandstones cemented by sulfate and clay minerals in Gale Crater, Mars. *Geophysical Research Letters*, 41, 1149–1154. https://doi.org/10.1002/2013GL059097

Morse, P. D. & Burn, C. R. (2010). Field observations of syngenetic ice wedge polygons, outer Mackenzie Delta, western Arctic coast, Canada. *Journal of Geophysical Research: Earth Surface*, 118, 1320-1332. doi:10.1002/jgrf.20086, 2013

Murchie, S., Arvidson, R., Bedini, P., Beisser, K., Bibring, J. -P., Bishop, J., et al. (2007). Compact Reconnaissance Imaging Spectrometer for Mars (CRISM) on Mars Reconnaissance Orbiter (MRO). *Journal of Geophysical Research: Planets*, 112. https://doi.org/10.1029/2006JE002682

Nachon, M., Clegg, S. M., Mangold, N., Schröder, S., Kah, L. C., Dromart, G., et al. (2014). Calcium sulfate veins characterized by ChemCam/Curiosity at Gale crater, Mars. *Journal of Geophysical Research: Planets*, 119, 1991–2016. https://doi.org/10.1002/2013JE004588

Nachon, M., Mangold, N., Forni, O., Kah, L. C., Cousin, A., Wiens, R. C., et al. (2016). Chemistry of diagenetic features analyzed by ChemCam at Pahrump Hills, Gale crater, Mars. *Icarus*, 281, 121–136. https://doi.org/10.1016/j.icarus.2016.08.026

Nachon, M., Sumner, D. Y., Grotzinger, J. P., Edgett, K. S., Wiens, R. C., Schwenzer, S. P., et al., (2019). Stratigraphic distribution of veins within the lacustrine Murray and the aeolian Stimson formations at Gale crater: Implications for groundwater circulation on Mars. *Sedimentology*, In review.

Newsom, H. E., Edgett, K. S., Fey, D. M., Wiens, R. C., Frydenvang, J., Banham, S. G., et al. (2018). A buried aeolian lag deposit at an unconformity between the Murray and Stimson formations at Marias Pass, Gale crater, Mars. *LPS XLIX*, Abstract 2263.

Oehler, D. Z., Mangold, N., Hallet, B., Fairen, A. G., Le Deit, L., Williams, A. J., et al. (2016).Origin and significance of decameter-scale polygons in the lower Peace Vallis fan of Gale crater, Mars. *Icarus*, 277, 56-72. http://dx.doi.org/10.1016/j.icarus.2016.04.038

Ohman, T. (2009). *The structural control of polygonal impact craters*, (Doctoral dissertation). Oulu, Finland: University of Oulu.

Passchier, C. W. & Trouw, R. A. J. (2005) *Micro-tectonics*. Springer, Berlin.

Philipp, S. L. (2008). Geometry and formation of gypsum veins in mudstones at Watchet, Somerset, SW England. *Geological Magazine*, 145(6), 831-844. doi:10.1017/S0016756808005451.

Pina, P., Saraiva, J., Bandeira, L., & Antunes, J. (2008). Polygonal terrains on Mars: A contribution to their geometric and topological characterization. *Planetary and Space Science*, 56(15), 1919-1924. doi: 10.1016/j.pss.2008.09.020

Polansky, C. A. & Ahrens, T. J. (1990). Impact spallation experiments: Fracture patterns and spall velocities. *Icarus*, 87, 140-155. https://doi.org/10.1016/0019-1035(90)90025-5

Rice, M. S., Gupta, S., Treiman, A. H., Stack, K. M., Calef, F., Edgar, L. A., et al. (2017). Geologic overview of the Mars Science Laboratory rover mission at the Kimberley, Gale crater, Mars. *Journal of Geophysical Research: Planets*, 122, 2–20. https://doi.org/10.1002/2016JE005200

Rodriguez, J. A. P., Sasaki, S., Dohm, J. M., Tanaka, K. L., Strom, B., Kargel, J., et al. (2005). Control of impact crater fracture systems on subsurface hydrology, ground subsidence, and collapse, Mars. *Journal of Geophysical Research: Planets*, *110*(6), 1–22. http://doi.org/10.1029/2004JE002365

Rubin, D. M., Edgar, L., & Lewis, K. W. (2014). Physical sedimentology in Gale crater, Mars. *AAPG Annual Convention and Exhibition,* Article 50991.

Schieber, J., Bish, D., Coleman, M., Reed, M., Hausrath, E. M., Cosgrove, J., Gupta, S., et al., (2017). Encounters with an unearthly mudstone: Understanding the first mudstone found on Mars. *Sedimentology*, 64, 311–358. https://doi.org/10.1111/sed.12318

Schultz, P. H., Schultz, R. A., & Rogers, J. (1982). The structure and evolution of ancient impact basins on Mars. *Journal of Geophysical Research*, 87(B12), 9803. http://doi.org/10.1029/JB087iB12p09803

Seibert, N. M. & Kargel, J. S. (2001). Small-scale martian polygonal terrain: Implications for liquid surface water. *Geophysical Research Letters*, 28(5), 899-902. https://doi.org/10.1029/2000GL012093

Shorlin, K. A., de Bruyn, J. R., Graham, M., & Morris, S. W. (2000). Development and geometry of isotropic and directional shrinkage-crack patterns. *Physical Review*, 61(6), 6950-6957. doi: 10.1103/PhysRevE61.6950.

Siebach, K. L., & Grotzinger, J. P. (2013). Volumetric estimates of ancient water on Mount Sharp based on boxwork deposits, Gale crater, Mars. *Journal of Geophysical Research: Planets*, 119, 189–198. https://doi.org/10.1002/2013JE004508

Siebach, K. L., Baker, M. B., Grotzinger, J. P., McLennan, S. M., Gellert, R., Thompson, L. M., & Hurowitz, J. A. (2017). Sorting out compositional trends in sedimentary rocks of the Bradbury group (Aeolis Palus), Gale crater, Mars. *Journal of Geophysical Research: Planets*, 122, 295-328. doi:10.1002/2016JE005195.

Sletten, R. S., Hallet, B., & Fletcher, R. C. (2003). Resurfacing time of terrestrial surfaces by the formation and maturation of polygonal patterned ground. *Journal of Geophysical Research*, 108(E4). doi:10.1029/2002JE001914

Stack, K.M., Cofield, S.M., & Fraeman, A.A. (2017). Geologic map of the MSL Curiosity rover extended missiont traverse of Aeolis Mons, Gale crater, Mars. *LPS XLVIII*, Abstract 1889.

Stack, K. M., Grotzinger, J. P., Lamb, M. P., Gupta, S., Rubin, D. M., Kah, L. C., et al. (2018). Evidence for plunging river plume deposits in the Pahrump Hills member of the Murray formation, Gale crater, Mars. *Sedimentology*. https://doi.org/10.1111/sed.12558

Stein, N., Grotzinger, J. P., Schieber, J., Mangold, N., Hallet, B., Newsom, H., et al. (2018). Desiccation cracks provide evidence of lake drying on Mars, Sutton Island member, Murray formation, Gale crater. *Geology*, 46(6), 515–518. https://doi.org/10.1130/G40005

Sun, V. Z., Stack, K. M., Kah, L. C., Thompson, L., Fischer, W., Williams, A., et al. (2018). Late-stage concretions in the Murray formation, Gale crater, Mars. *Icarus,* 321, 866-890. https://doi.org/10.1016/j.icarus.2018.12.030

Tanaka, K. L., & Golombek, M. P. (1989). Martian tension fractures and the formation of grabens and collapse features at Valles Marineris. *Proceedings of the 19th Lunar and Planetary Science Conference*, 383–396.

Thomson, B. J., Bridges, N. T., Milliken, R., Baldridge, A., Hook, S. J., Crowley, J. K., et al. (2011). Constraints on the origin and evolution of the layered mound in Gale crater, Mars using Mars Reconnaissance Orbiter data. *Icarus*, 214(2), 413–432. https://doi.org/10.1016/j.icarus.2011.05.002

Vanden Berg, M. D. (2019). Domes, rings, ridges, and polygons: Characteristics of microbialites from Utah's Great Salt Lake. *The Sedimentary Record*, 17(1), 4-10. doi: 10.2110/sedred.2019.1

Warden, J. G., Coshell, L., Rosen, M. R., Breecker, D. O., Ruthrof, K. X., & Omelon, C. R. (2019). The importance of groundwater flow to the formation of modern thrombolitic microbialites. *Geobiology*. https://doi.org/10.1111/gbi.12344

Warren, J. K. (1983). Tepees, modern (southern Australia) and ancient (Permian - Texas and New Mexico) - a comparison. *Sedimentary Geology*, 34, 1-19. https://doi.org/10.1016/0037-0738(83)90032-5

Watkins, J. A., Grotzinger, J., Stein, N., Banham, S. G., Gupta, S., Rubin, D., Stack, K., et al. (2016). Paleotopography of erosional unconformity, base of Stimson formation, Gale crater, Mars. *LPS XLVII,* Abstract 2939.

Wiens, R. C., Maurice, S., Barraclough, B., Saccoccio, M., Barkley, W. C., Bell, J. F. III, et al. (2012). The ChemCam instruments on the Mars Science Laboratory (MSL) rover: Body unit and combined system performance. *Space Science Reviews*, 170(1-4), 167–227. https://doi.org/10.1007/S11214-012-9902-4

Williams, R. M. E., Grotzinger, J. P., Dietrich, W. E., Gupta, S., Sumner, D. Y., Wiens, R. C., et al. (2013). Martian fluvial conglomerates at Gale crater. *Science*, 340, 1068. doi: 10.1126/science.1237317

Williams, R. M. E., Malin, M. C., Stack, K. M., & Rubin, D. M. (2018). Assessment of Aeolis Palus stratigraphic relationships based on bench-forming strata in the Kylie and the Kimberley regions of Gale crater, Mars. *Icarus*, 309, 84–104. https://doi.org/10.1016/j.icarus.2018.02.028

Yen, A. S., Ming, D. W., Vaniman, D. T., Gellert, R., Blake, D. F., Morris, R. V., et al. (2017). Multiple stages of aqueous alteration along fractures in mudstone and sandstone strata in Gale Crater, Mars. *Earth and Planetary Science Letters*, 471, 186–198. https://doi.org/10.1016/j.epsl.2017.04.033

CHAPTER 3
PREDICTING THE MECHANICAL AND FRACTURE PROPERTIES OF SEDIMENTARY LITHOLOGIES IN GALE CRATER

Abstract

Rock fractures and veins are well-documented in the lithologies within Gale crater, Mars, and an understanding of rock mechanical properties may help constrain fracture formation conditions (i.e. burial depth, influence of fluids, etc.). Data collected by the Curiosity rover's drill allow estimation of unconfined compressive strength, but only for rocks that have been successfully sampled by the drill. These estimates reveal that drilled rock types in Gale crater are considerably weaker than comparative lithologies on Earth. Qualitative assessments on rock that were not drilled, however, suggest that substantially stronger lithologies also exist within Gale crater. Here I utilize a variety of experimental test methods to determine the mechanical properties of Gale analog lithologies, specifically iron-cemented silt and sandstone and poorly lithified mudstone. The range of properties determined from analog testing of sand and siltstone is consistent with similar, previously tested terrestrial materials; poorly lithified mudstone proved to be extremely weak and requires additional testing to validate experimental methods. Here I explore the utility of established correlation between measured properties and demonstrate the ability to accurately predict fracture using limited strength data. In addition, finite element modeling efforts confirm the ability to predict fracture conditions using limited data.

Introduction

Recent landed missions to Mars have employed sophisticated payloads capable of identifying potential biosignatures and determining the composition and environmental context of surface materials that may house biosignatures. At present, assessing the potential for ancient habitability is driven primarily by interpretations of past water-rock interactions, both during the

deposition of ancient sedimentary rocks (e.g., fluvial sandstones, lacustrine mudstones) and during post-depositional or subsurface modification (e.g., hydrofracture). Rock fractures formed by hydrofracturing are well-documented on Mars (Caswell & Milliken, 2017; Kronyak et al., 2019; Nachon et al., 2014, 2017; Schieber et al., 2017) and preserve a primary line of evidence for the interaction between vein-forming fluids and host rock. Because such veins preserve direct evidence for post-depositional fluid flow through the martian subsurface, they have the potential to serve as critical targets of astrobiological interest. Unfortunately, the formation conditions (e.g., fluid pressure, burial depth) for such fractures remain poorly constrained.

On Earth, the mechanical properties of rock play a critical role in the initiation and propagation of fractures (Gale et al., 2014; Gudmundsson et al., 2002; Philipp, 2008; Philipp et al., 2013). On Mars, however, our understanding of rock properties is restricted by a poor understanding of rock composition, limited access to samples for contact science, and a paucity of quantitative mechanical property characterization. In order to better assess the formation of rock fractures on Mars, it is therefore an essential goal to develop technology for future missions capable of providing essential rock property data and to evaluate the potential for data processing to predict a full suite of mechanical properties needed to evaluate the formation of observed fractures and veins. To advance the implementation of such technology on future rovers, here I: (1) investigate potential Mars analog rock types and present an approach to determine their mechanical properties from unconfined compressive strength (UCS) values, and (2) quantify the certainty in this predictive method using a finite element (FE) models to predict fracture growth and propagation through these analog lithologies.

Lithologies of Gale crater

Assessment of rock properties on Mars

The sedimentary rocks in northwest Gale crater, the landing site of the Mars Science Laboratory Curiosity rover, consist of a variety of conglomerate, sandstone, and mudstone lithologies. It is expected, as well, that these varied materials would show a variety of material behaviors, although such assessments are difficult in extraterrestrial environments. For instance, the relative strength of surface materials on Mars is qualitatively evaluated by examining the relative erosional resistance between material types and by examining the interaction between exposed rocks and rover hardware. In Gale crater, mineralized fractures (veins) commonly exhibit enhanced erosional resistance relative to host rock when observed in mudstone facies (Kronyak et al., 2019). The primary composition of these veins (Nachon et al., 2014, 2016) is calcium sulfate (i.e. gypsum) with a Mohs hardness of 2. The Mohs hardness scale is used to assess the relative resistance of mineral phases to scratching, and a Mohs hardness of 2 is typically understood to be very soft, and highly susceptible to mechanical erosion. The enhanced erosional resistance of these veins therefore indicates that mudstone lithologies are likely to be exceedingly weak, and therefore susceptible to greater aeolian erosion. In another example, notable punctures and cracks in the Curiosity rover's aluminum wheels, sustained while driving across regions containing iron-cemented sandstone lithologies—particularly in the absence of damage to the surface rocks—suggests that these materials have substantially greater strength (Arvidson et al., 2017).

There are currently no direct methods to quantitively determine the mechanical properties of rocks on Mars. The unconfined compressive strength of martian rocks in Gale crater has been

estimated by correlating data from rover instruments with corresponding data from terrestrial samples of known strength (Peters et al., 2018). For example, the Curiosity rover contains a drill that uses a combination of rotary and percussive movement to collect powdered rock samples directly from martian outcrops for analysis by Curiosity's geochemical payload (Anderson et al., 2012). Using the percussive energy of the drill to penetrate into the surface of Gale crater target lithologies and making direct comparison to identical analyses on terrestrial analogs of known strength, Peters et al. (2018) have estimated the unconfined compressive strength of rocks successfully drilled by Curiosity. Similarly, compressive strengths of rocks encountered by the Mars Exploration Rovers (MERs) have been estimated using the Rock Abrasion Tool (RAT), which grinds rock surfaces to reveal fresh interior surfaces (Gorevan et al., 2003). Thomson et al. (2013) utilized current data from the RAT motor to estimate the unconfined compressive strength (as well as the hardness) of samples on Mars by comparison with terrestrial rocks for which these mechanical properties had been experimentally determined.

Material properties of surface rocks in Gale crater

Sedimentary lithologies on Earth exhibit a range of mechanical properties that depend strongly on variables such as mineral composition, grain size, degree of cementation, and porosity (Bernabe et al., 1992; Dunn et al., 1973; Villenueve et al., 2012). Typical values for the compressive strength of sandstone lithologies range from ~6 to >200 MPa and ~25 to 50 MPa for mudstone (Cargill & Shakoor, 1990; Gudmundsson, 2001; Jaeger & Cook, 1979; Johnson & DeGraff, 1988).

Estimation of rock compressive strength using Curiosity rover data, however, is limited to rocks that have been drilled by the rover. Drilled samples include laminated, lacustrine

mudstone of the Murray formation (Grotzinger et al., 2015) and aeolian sandstone of the Stimson formation (Banham et al., 2018). Identification the Murray formation as a mudstone – a term that denotes an unknown mixture of clay- (<4 μm) and silt-sized (4-63 μm) particles – is confirmed by grain sizes below the resolution of images (Stack et al., 2018) taken with Curiosity's MAHLI camera (Edgett et al., 2012). The estimated unconfined compressive strength of Murray mudstone samples drilled in Gale crater ranges from <8 to 18 MPa (Peters et al., 2018), which is substantially less than expected for a mudstone that has been lithified, buried, and exhumed (Grotzinger et al., 2015).

Similarly, identification of the Stimson formation as a sandstone deposit results from observations of increased resistance to erosion relative to underlying mudstone of the Murray formation, direct observations of grains in images taken with the MAHLI camera that show an average grain size of medium sand (250-500 μm), and by the presence of abundant cross-beds whose formation requires transport of sand-sized particles in traction (Banham et al., 2018). The estimated strength of Stimson formation sandstone samples also ranges from <8.5 to 18 MPa (Peters et all., 2018), which is identical to strength estimates for substantially finer-grained Murray mudstone lithologies, and far less than that measured for terrestrial sandstone lithologies.

Other lithologies observed in Gale crater have not been drilled. With conglomerate facies, which consist of various-sized clasts of a variety of different lithologies (Mangold et al., 2016), the primary concern is that differences in strength between adjacent clasts could compromise drill performance. Similarly, a variety of sandstone lithologies – some of which are iron-rich and potentially iron-cemented (Kronyak et al., 2017) – have not been drilled because damage to rover wheels raises concerns that the potentially high strength of these lithologies may compromise

drill safety. MAHLI images of several sandstone outcrops reveal compositions that range from well-sorted to moderately sorted, and from fine (125-250 μm) to coarse (500-1000 μm) sand (Stack et al., 2018).

Selection of analog lithologies

In order to better understand the mechanical properties of rocks observed in Gale crater, I evaluated samples with grain size and qualitative strength characteristics similar to those observed in Gale crater, and specifically targeted a weak mudstone and three fine- to medium-grained silt and sandstone samples.

For comparison to the variety of sandstone deposits the occur in Gale crater, I selected three silt and sandstone units including the Permian Cutler Formation of the Paradox basin, Utah, and the Silurian Clinch Sandstone and Ordovician Chapman Ridge Sandstone of the Appalachian fold and thrust belt, east Tennessee. Cutler Formation samples selected for this study consist of massively bedded, pink to red aeolian siltstone (cf. Langford and Chan, 1988; Soreghan et al., 2002). Cutler Formation samples are well-sorted, coarse siltstones (Figure 3.1) with up to 3% porosity. Framework grains (Figure 3.2A, B) are composed of 65% detrital network silicate components (40% quartz, 60% feldspar), and up to 8% detrital mica. Carbonate (as cement and diagenetic dolomite rhombs) comprises up to 7% of the sample, and iron oxide (predominantly as grain coatings) comprises up to 15% of the sampled material.

Samples of the Clinch Sandstone (and the laterally equivalent Rockwood Formation; Dennison and Boucot, 1974) selected for this study are part of a widespread blanket of shallow marine quartz arenite deposited in the foreland basin of the Taconic Orogeny (Dorsch and Driese, 1995). Clinch samples used in this study are well-sorted, coarse silt to fine sand

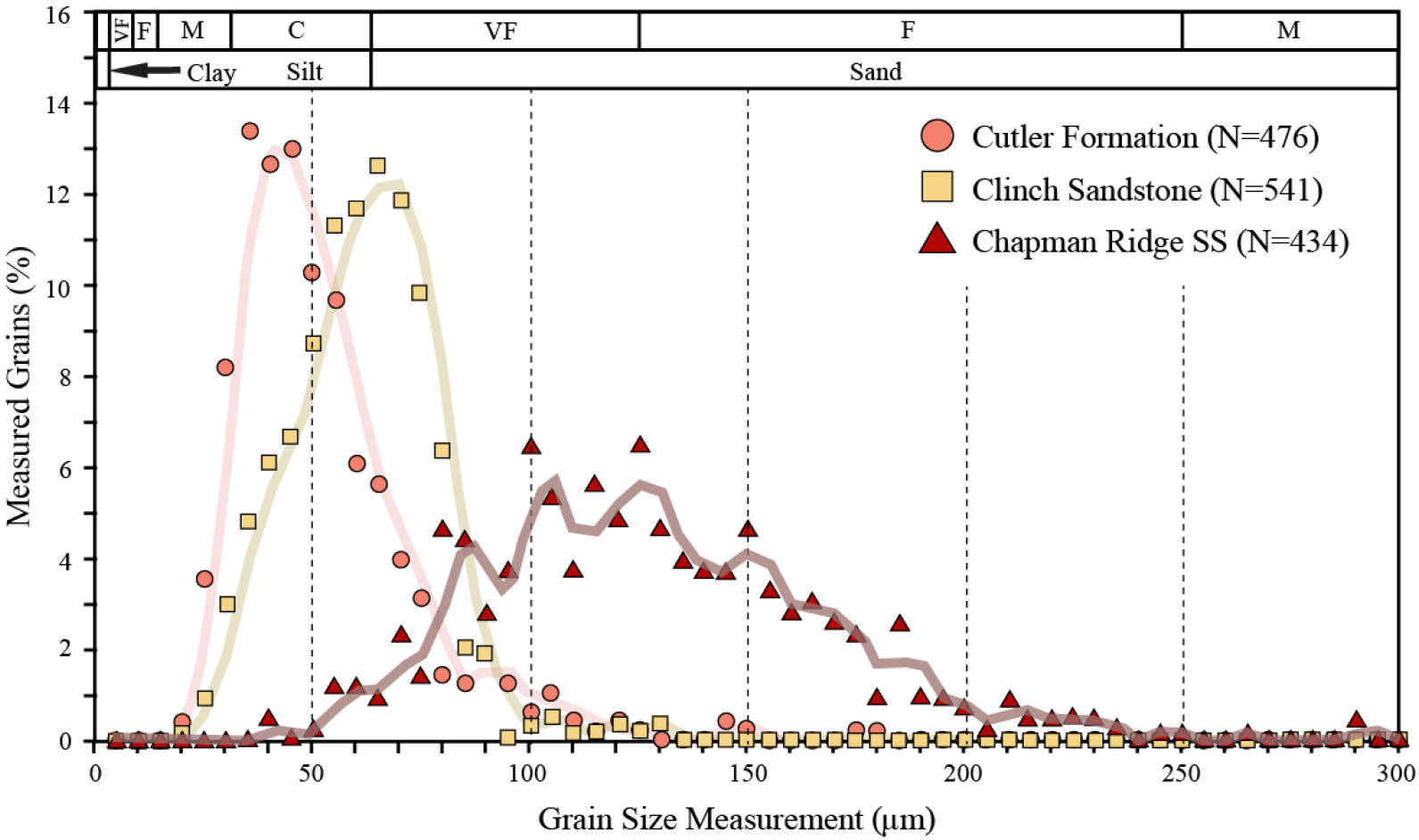


Figure 3.1 Grain size distribution of sandstone lithologies used in this study. Aeolian strata of the Cutler Formation consist of predominantly well-sorted medium to coarse silt. Marine sandstone of the Clinch and Chapman Ridge formations vary in both grain size and grain sorting.

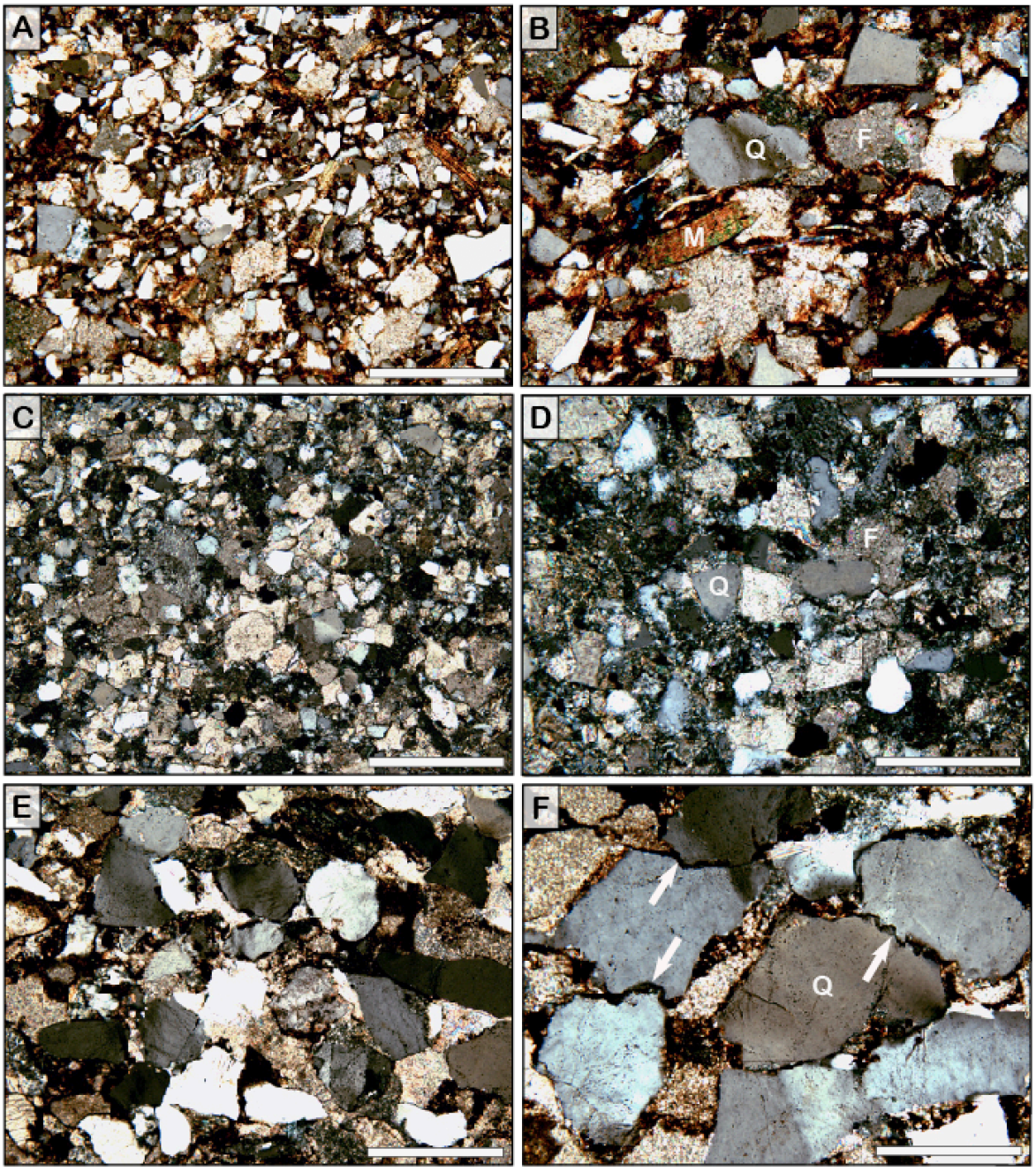


Figure 3.2 Petrographic images of sandstone samples. (A) Cutler Formation siltstone; scale bar is 350 micrometers. (B) Cutler Formation siltstone with primary framework grains (Q=quartz, F=feldspar), detrital sheet silicates (M=mica), and an abundance of iron oxide grain coatings; scale bar is 100 micrometers. (C) Clinch Formation sandstone; scale bar is 350 micrometers. (D) Clinch Formation sandstone with primary framework grains (Q=quartz, F=feldspar); note abundant alteration of feldspar to clay minerals. Scale bar is 100 micrometers. (E) Chapman Ridge Sandstone; scale bar is 350 micrometers. (F) Chapman Ridge Sandstone showing iron oxide grain coatings and suturing of detrital quartz grains (white arrows); scale bar is 100 micrometers.

(Figure 1) with no visible porosity in thin section. Framework grains (Figure 3.2C, D) are composed of 50% detrital silicate components (50% quartz, 50% feldspar). Carbonate occurs as a micritic matrix component and as diagenetic dolomite and comprises up to 35% of the sample. Remaining components include up to 10% clay (largely from weathered feldspar), and 2% opaque minerals.

The Chapman Ridge Sandstone (previously referred to as the Tellico Sandstone; Cattermole, 1955) consists of a red-brown weathering, hematite-rich, calcareous marine sandstone that was deposited in the evolving Appalachian foreland basin from deformed continental strata of the Taconic fold-and-thrust belt (Anderson, 1995; Walker et al., 1983; Whisner, 2005). Chapman Ridge samples used in this study are poorly-sorted, very fine to fine sand (Figure 3.1) with no visible porosity in thin section. Framework grains (Figure 3.2E, F) are composed of 50% detrital silicate components (60% quartz, 40% feldspar). Carbonate occurs as detrital grains (ooids, skeletal fragments), as crystalline cement, and as diagenetic dolomite rhombs, and comprises up to 40% of the sample. Remaining phases consist predominantly of iron oxide, which comprises 10% of the sample as grain coatings and as replaced carbonate grains.

Finally, for comparison to mudstone of the Murray formation, I selected unlithified mudstone (i.e. clay-rich siltstone) deposits of Pleistocene Glacial Lake Missoula (cf. Chambers, 1985; Hanson et al., 2012, 2015) near Missoula, Montana. Lacustrine deposits of Glacial Lake Missoula consist of stacked packages showing a basal erosional surface, a fining-upward succession of coarse- to medium-grained sand that grades into fine-grained rippled sand, followed by a succession of well-laminated silt and clay varves (Hanson et al., 2015). Between

these two successions there occasionally occurs 10-40 cm thick beds of a massive, featureless to vaguely laminated, clayey siltstone (i.e. mudstone) that has been interpreted to have been deposited in slack-water conditions as glacial flood waters ponded upstream from a drainage constriction (Baker and Bunker, 1985). For this study, I sampled the massive, featureless to poorly laminated, mudstone facies.

Methods

In this study I demonstrate the ability to estimate the mechanical properties of Mars lithologies from limited quantitative data from the Curiosity rover. My approach to develop and evaluate this method involves several components (Figure 3.3) including both experimental testing and computational modeling. First, experimental testing was performed to determine the mechanical properties of analog lithologies; such information was needed to investigate fracture behavior in modeling efforts described below. Correlation between UCS and the experimental test data for tensile strength and fracture energy were derived and used to calculate a set of predicted properties for each analog rock type. Second, a computational model was created and validated with the experimental test data to assess fracture propagation through analog lithologies. I also utilized computational models to predict fracture conditions using predicted property values to demonstrate the ability to demonstrate fracture with only limited mechanical data. Finally, correlation equations were used to estimate the fracture properties of drilled rock samples in Gale crater.

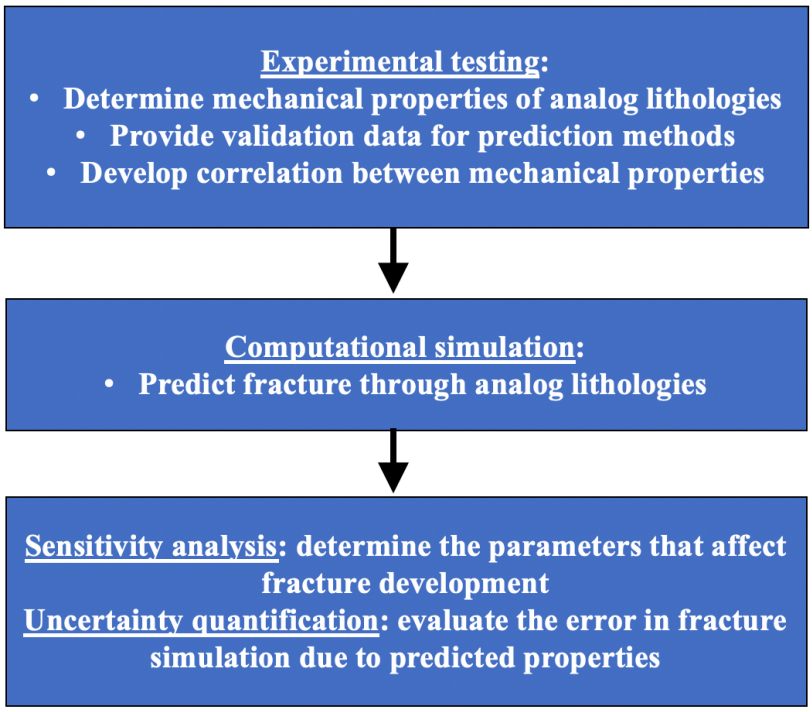


Figure 3.3 Flow chart of multi-step analytical approach. This study focuses on experimental testing and computational simulation, and future work aims to perform sensitivity analysis and uncertainty quantification.

Experimental determination of mechanical properties

To characterize the mechanical properties needed to predict fracture in my analog lithologies (Missoula mudstone, and silt and sandstone of the Cutler, Clinch, Chapman Ridge formations), three types of experimental testing were performed. These tests determined unconfined compressive strength (UCS), tensile strength (TS), and fracture toughness (K_{IC}) testing (Figure 3.4). Compressive elastic modulus (E) and fracture energy (J) were then, respectively, derived via standard relationships (ASTM 7012, 2014; Zhang & Yu, 2019) from compressive strength and fracture toughness test results. Additional properties, including tensile elastic modulus and Poisson's ratio, were estimated from data obtained from the literature.

Rock samples were prepared for testing by extracting cylindrical cores perpendicular to bedding (Figure 3.5a). Core ends were trimmed with a diamond-tipped grinding saw to achieve flat, parallel surfaces. Friable behavior of the Missoula mudstone specimens inhibited us from being able to extract coherent cores using a drill (Figure 3.5b). Instead, Missoula specimens were shaped into cores using sandpaper. Prior to mechanical testing, all samples all were dried at 120°C overnight to ascertain dryness.

Unconfined compressive strength testing

For unconfined compressive strength (UCS) testing (ASTM D2938, 1995), cylindrical core specimens were subjected to constant compressive loading until failure occurred (Figure 3.4a). ASTM standards require cylindrical core dimensions with a length to diameter ratio (L/D)

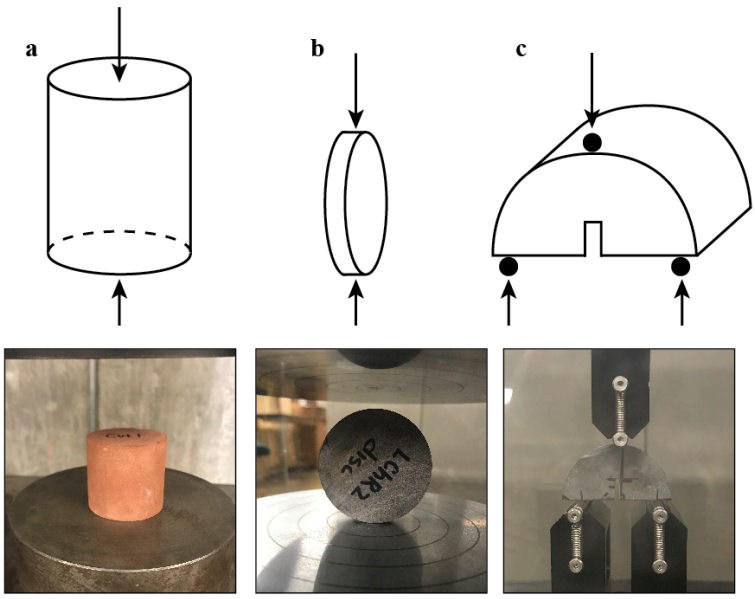


Figure 3.4 Geometry for experimental mechanical property testing of analog samples. Arrows indicate the orientation of applied force during testing. (a) Cylindrical core geometry used in compressive strength tests, with an example from the Cutler Formation. (b) Disc geometry used for tensile strength tests, with an example from the Chapman Ridge Formation. (c) Notched semi-circle geometry used for fracture toughness tests, with an example from the Clinch Formation; black circles indicate the approximate locations of support rollers.

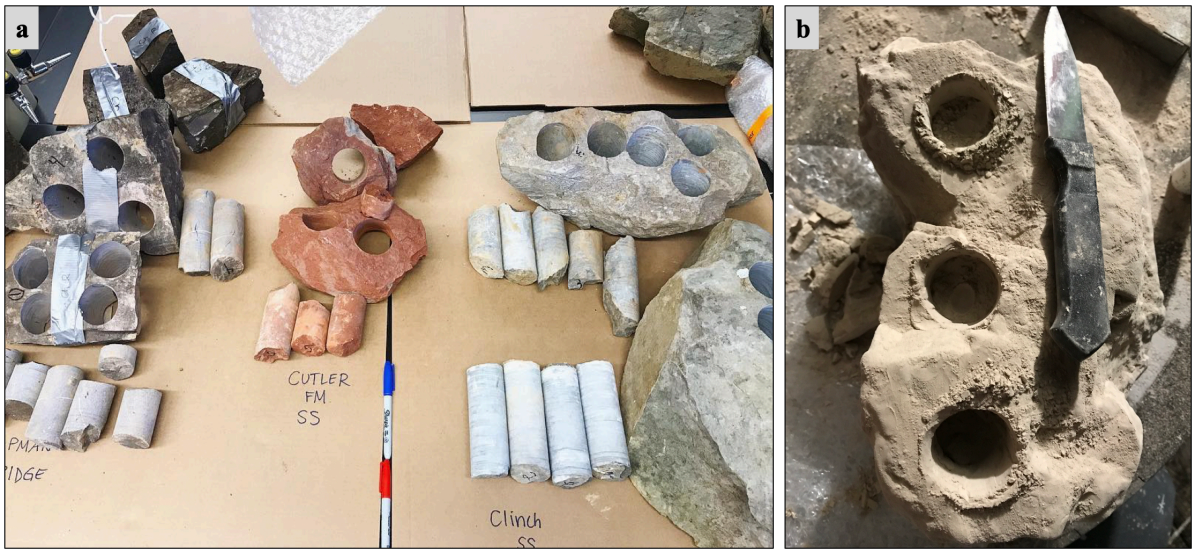


Figure 3.5 Analog lithologies used for testing. (a) From left to right, Chapman Ridge Formation, Cutler Formation, and Clinch Formation sandstone cores. Cores are ~5 cm in diameter. (b) Missoula mudstone sample, showing failed drill attempts using a DeWalt hand drill.

of 2.0-2.5. However, sample coring limitations resulted in variation in core length, preventing several specimens from achieving the desired L/D ratio of 2.0. In these cases, a strength correction factor was applied for UCS calculations (ASTM C42, 2003). All tests were performed with a continuous loading rate of 0.0025 mm/s until failure occurred. Force and crosshead displacement were continuously measured throughout testing. The UCS was calculated by:

$$\text{UCS (MPa)} = \frac{P}{A}, \tag{1}$$

where P is the maximum force sustained prior to failure and A is the specimen cross-sectional area (ASTM D2938, 1995). Displacement was converted to strain by dividing displacement by the original specimen length. The compressive elastic modulus (E) for compression was derived from the slope of the elastic portion of the stress-strain curve for each specimen test, given by:

$$\text{E (GPa)} = \frac{\sigma}{\varepsilon}, \tag{2}$$

where σ is stress and ε is strain (ASTM 7012, 2014).

Tensile strength testing

The tensile strength of rock specimens was determined by performing compression tests on disc specimens (i.e. splitting tensile strength; Figure 3.4b, ASTM D3967, 1996), a common alternative to performing true tensile tests that require application of extensional forces on test specimens. Tests on sandstones were performed using circular discs cut from untested, UCS core specimens. Discs were cut such that thickness to diameter (L/D) ratios were between 0.2-0.75 to meet ASTM standards (D3967, 1996). For the Missoula mudstone, discs were extracted from rock slabs using a Dewalt electric hand drill and shaped into the final dimensions using sandpaper. All specimens were tested in a 100 kN MTS load frame at a test rate of 0.00025 mm/s

until failure occurred. Tensile strength (TS) was then calculated from the maximum load applied before failure and the original dimensions of length and diameter, given by:

$$\text{TS (MPa)} = \frac{2P}{\pi LD}, \quad (3)$$

where P is the maximum force applied, L is specimen thickness, and D is specimen diameter (ASTM D3967, 1996).

Fracture toughness testing

To derive fracture toughness, three-point bend tests were performed on notched semi-circular disc specimens (Figure 3.4c; Kuruppu et al., 2014). To prepare silt and sandstone specimens for three-point bending, discs identical to those used for tensile strength testing were cut in half to produce semi-circular discs. Straight notches ~3 mm thick were cut into the flat edges of the semi-circular discs using a diamond-tipped grinding saw. The length of the notch was cut such that the ratio of its length (a) to the semi-circle radius (R) was between 0.4-0.6 (Kuruppu et al., 2014). To prepare the Missoula mudstone for three-point bend tests, discs were sanded into semi-circles and notches were cut using a single-edge steel razor blade. Initial tests of Missoula specimens failed because support rollers directly indented the poorly lithified mudstone. To achieve cracking along the specimen notch, a thin sheet of strip aluminum was placed along the rounded top and flat bottom of the semi-circular disc specimens. This material distributed the stress where the three-point bend loading rollers came in contact with the soft specimens preventing specimen failure resulting from stress concentration at the rollers. For all rock specimens, three-point bend tests were performed in a 100 kN MTS load frame with two bottom support rollers and one top loading roller (Figure 3.5c). The bottom rollers were positioned at a distance such that the ratio of the roller distance (s) to the semi-circular diameter

(D) was between 0.5-0.8 (Kuruppu et al., 2014). The load rate used for testing was 0.00025 mm/s and was applied until failure occurred. Specimen dimensions and the peak load observed during testing were used to derive plane strain fracture toughness (K_{IC}), given by:

$$K_{IC}\ (MPa*m^{1/2}) = Y' \frac{P_{max}\sqrt{\pi a}}{2RB}, \quad (4)$$

where P_{max} is the maximum load, a is the notch length, R is the specimen radius, and B is the specimen thickness (Kuruppu et al., 2014). Y' is the non-dimensional stress intensity factor, defined by:

$$Y' = -1.297+9.516\left(\frac{s}{2R}\right) - \left(0.47+16.457\left(\frac{s}{2R}\right)\right)\beta + \left(1.071+34.401\left(\frac{s}{2R}\right)\right)\beta^2, \quad (5)$$

where s is the distance between bottom rollers and β is equal to a/R.

Fracture toughness and tensile elastic modulus values were used to calculate fracture energy (J), given by:

$$J\ (Pa*m) = \frac{K^2}{E}, \quad (6)$$

where K is the fracture toughness and E is tensile elastic modulus. Since the tensile elastic modulus was not available from our test data, I utilized values reported in the literature for sandstone (Zhang & Yu, 2019).

Mechanical property correlation

The ability to perform computational fracture simulations on Mars-specific lithologies and scenarios depends on the availability of relevant mechanical property data. Our experimental testing on analog lithologies provides us with mechanical properties that include unconfined compressive strength, tensile strength, and fracture toughness. With available Mars rover data, however, we are only able to estimate unconfined compressive strength (cf. Peters et al., 2018).

Therefore, methods to estimate the mechanical properties needed for fracture prediction are required. In light of the limited available data regarding material properties on Mars, I investigated the relationships between existing rock properties. For instance, the correlation between the unconfined compressive strength and tensile strength of sedimentary rocks is well-documented in the literature (see Table 3.1; Altindag & Guney, 2010; Farah, 2011; Kahraman et al., 2012; Nazir et al., 2013). Additionally, correlations between tensile strength and fracture toughness have been demonstrated (Table 3.1; Whittaker et al., 1992; Zhang, 2002; Zhang et al., 1998). I explored the ability of these correlations to predict tensile strength and fracture toughness from the UCS from analog lithologies be comparing results with measured experimental data. I then utilized correlation equations to estimate the tensile strength and fracture toughness of Gale lithologies, based on estimated UCS from Peters et al. (2018).

Computational model development

Finite element (FE) models were created in Abaqus/CAE (Abaqus Software 6.13, 2013). I used an FE model to validate our three-point bend experimental results in order to corroborate crack propagation using experimentally derived mechanical and fracture properties. The finite element method (FEM) is a common numerical tool utilized to solve problems in fracture mechanics and engineering. The classic FEM method discretizes a physical structure using finite elements that can model the behavior of a wide range of structural geometries by solving partial differential equations (Khoei, 2014). Elements represent a distinct, finite portion of the structure

Table 3.1 Correlation between mechanical properties of compressive and tensile strength, as well as between fracture toughness and tensile strength. UCS = unconfined compressive strength, TS = tensile strength, K_{IC} = fracture toughness.

Correlation	Rock type(s) assessed	Reference
UCS (MPa) = $9.25*TS^{0.947}$	Limestone	Nazir et al., 2013
UCS (MPa) = 10.61*TS	Multiple rock types (including sandstone)	Kahraman et al., 2012
UCS (psi) = 5.11*TS – 133.86	Limestone	Farah, 2011
UCS (MPa) = $12.38*TS^{1.0725}$	Multiple rock types (including sandstone and siltstone)	Altindag & Guney, 2010
TS (MPa) = 9.35 K_{IC} – 2.53	Multiple rock types (including sandstone)	Whittaker et al., 1992
TS = 8.88 $K_{IC}^{0.62}$	Marble and granite	Zhang et al., 1998
TS = 6.88 K_{IC}	Multiple rock types (including sandstone)	Zhang, 2002

and are joined together by nodes; together these components create a mesh over the structure geometry. Using these elements, the propagation of a crack can be modeled. In traditional FEM approaches, however, regions surrounding the crack trip must be frequently remeshed to accommodate crack growth. The extended finite element method (XFEM) technique was designed to avoid this repetitive remeshing process. Using partition of unity enrichment functions, XFEM allows the crack to propagate independently of the mesh (Belytschko and Black, 1999; Khoei, 2014; Moes et al., 1999; Zi and Belytschko, 2003). I utilized the XFEM technique to help constrain the role of material properties (e.g., tensile strength, Young's modulus, and fracture energy) in the propagation of fractures through analog lithologies.

I tested the utility of the XFEM method by reconstructing our experimental testing methods. I created a notched semi-circular bend 2D XFEM model in Abaqus with two support pins along the bottom of the semi-circular disc and a loading pin on the top of the disc. I utilized the same boundary and loading conditions as the three-point bend testing procedure. Boundary conditions pinned the bottom supports and constrained the top pin from moving in the x-direction. Crack initiation was controlled by the max principle stress of the material. In this case, the maximum tensile strength of the material was used and was calculated by experimental testing (splitting tensile strength tests, ASTM D3967). The fracture energy was used to define the crack growth following crack initiation; the fracture energy was calculated by three-point bend testing (ISRM standard, cf. Kuruppu, 2014). The XFEM model requires that the crack be located within a crack domain; so, for this model, the crack domain was set to be the section above the notch of the specimen. A finer mesh was used in this region to obtain a higher resolution that permitted a more precise capture of crack growth. The mesh type was set to four-node bilinear

plane strain quadrilateral (CPE4R) with reduced integration and hourglass control. The number of elements necessary for convergence was 3760. The element size outside of the crack domain was coarser, which permitted a less resource-intensive computation. The meshing is shown in Figure 3.6. For XFEM to initiate crack growth, a pre-existing flaw must be present in the model. This was done by placing a small 0.25 mm long wire above the notch. The analysis was performed using the general implicit procedure within Abaqus.

To simulate the scenario in which only UCS values would be available from Curiosity rover data, we utilized correlation equations (Table 3.1) to predict properties of tensile strength, fracture toughness, fracture energy, and Young's modulus from UCS values for Chapman Ridge, Clinch, Cutler, and Missoula specimens. Using these predicted property values, we simulate hypothetical three-point experiments and compare to actual model results. With these comparisons we demonstrate the valuable information that can be inferred from only minimal rover mechanical property data.

Results

Mechanical properties

Compressive strength testing

A summary of unconfined compressive strength test data is listed in Table 3.2. In several cases, where the size of coherent sample material was limited, the L/D ratio of samples varied from the recommended standards. In these cases, Cutler, Clinch, and Chapman Ridge samples

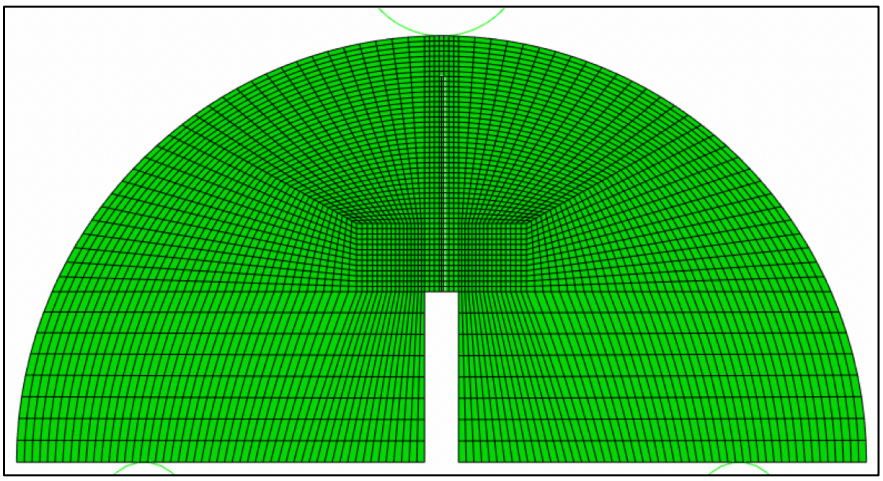


Figure 3.6 2D Abaqus model geometry used to demonstrate the XFEM crack growth through three-point bend tests. Model geometry matches experimental test geometry. The finest mesh was placed along the region of crack growth. Outside of this region, the specimen was partitioned and meshed more coarsely to reduce computational run time.

Table 3.2 Unconfined compressive strength (UCS) test data.

Sample	Specimen name	Diameter (mm)	Length (mm)	Pmax (N)	Strength correction factor (if L/D <2.0)	UCS (MPa)	Mean UCS (MPa)	E (GPa)	Mean E (GPa)	Test Machine
Cutler Fm	Cut1	50.64	47.1	215436.19	0.86	91.99	106.63 +/- 20.7	3.88	6.21 +/- 3.29	600 kN Instron
	Cut2	50.67	79.22	252045.04	0.97	121.27		8.54		600 kN Instron
Clinch Fm	sC3	50.75	55.27	179317.65	0.90	79.78	103.57 +/- 24.22	6.93	6.22 +/- 1.66	600 kN Instron
	LC3	50.71	105.29	178987.48	-	88.64		8.45		600 kN Instron
	skC1a	24.75	48.9	62730.72	-	130.44		5.98		100 kN MTS
	skC1b	24.69	50.62	43599.93	-	91.07		4.97		100 kN MTS
	skC2a	24.92	50.77	61444.2	-	126.02		5.68		100 kN MTS
	skC3a	24.87	50.7	38982.46	-	80.25		5.62		100 kN MTS
	skC3b	24.91	51.58	66280.5	-	136.06		6.56		100 kN MTS
	skC4b	24.87	50.67	69386.89	-	142.83		6.76		100 kN MTS
	skC5b	25.15	52.16	59198.94	-	119.59		6.34		100 kN MTS
	skC6a	24.78	51.09	56689.04	-	117.59		6.66		100 kN MTS
	skC6b	24.74	48.79	31717.3	-	66		5.56		100 kN MTS
	skC9a	24.95	50.75	31609.05	-	64.65		2.02		600 kN Instron
	skC11b	24.83	49.21	43094.36	-	89.03		8.84		600 kN Instron
Chapman Ridge Fm	LChR1	50.67	53.23	275011.2	0.90	122.77	100.48 +/- 49.59	6.29	7.24 +/- 3.69	600 kN Instron
	LChR2	50.69	97.3	263105.14	0.92	120.06		8.02		600 kN Instron
	LChR4	50.65	104.59	289566.75	-	143.74		11.93		600 kN Instron
	LChR5	50.65	115	120124.18	-	59.76		4.35		600 kN Instron
	LChR6	50.61	102.28	112682.31	-	56.06		5.02		600 kN Instron
Missoula mudstone	Mis1	21	21.5	122.53	0.87	0.31	0.37 +/- 0.2	0.0031	0.05 +/- 0.04	100 kN MTS
	Mis2	27	31	428.11	0.90	0.67		0.13		100 kN MTS
	Mis3	20	26.5	87.64	0.93	0.26		0.030		100 kN MTS
	Mis4	27	32	326.3	0.92	0.52		0.090		100 kN MTS
	Mis5	34.5	26.5	344.56	0.83	0.31		0.029		100 kN MTS
	Mis6	33	22	134.74	0.8	0.13		0.040		100 kN MTS

were 50 mm in diameter and exhibited lengths that ranged from 47 to 97 mm. Missoula samples ranged in diameter from 20 to 35 and ranged in length from 21.5 to 31 mm (Table 3.2). For these cases, a strength correction factor was applied when calculating unconfined compressive strength, according to ASTM C42 (2003).

Two machines with different sized load cells were used for cylindrical core compressive strength testing. A 100 kN capacity MTS was used to test the 25-mm-diameter specimens. However, the 100kN load cell was insufficient in inducing failure for larger, 50-mm diameter specimens. To obtain the UCS of these larger specimens, a 600 kN capacity Instron Model 5590 was used. To compare data from 100 kN and 600 kN capacity machines, 25-mm core samples of the Clinch Formation were tested on both machines. Compressive strength values acquired from the 600 kN load cell fell within the range of strength values obtained from the 100 kN machine (Table 3.2). In addition, for the Clinch Formation, I also tested specimens with different diameters, including 25-mm and 50-mm samples (Table 3.2). Larger diameter specimens fell within the range of UCS values for smaller-sized specimens.

The Cutler Formation represents the finest grained material tested. Cutler Formation siltstone exhibited strength values of 92-121 MPa, with a mean value of 106.63 ± 20.7 MPa. Upon failure, specimens were considerably shattered but intact. Young's modulus values for the Cutler Formation range from 3.88-8.54 GPa, with a mean of 6.21 ± 3.29 GPa.

The Clinch Formation samples are represented by grain sizes ranging from coarsest silt to very fine sand. These samples exhibited failure by axial splitting in the direction of applied force. Several core specimens were intact after failure; most, however, exhibited explosive failure and only small remnants of core were recovered. Compressive strength values range from 64-142.8

MPa, with a mean strength of 103.57 ± 24.22 MPa. Mean strength reported here includes specimens tested on the 600 kN Instron, which exhibited strength values between 64-89 MPa, and specimens tested on the 100 kN MTS, which exhibited strength values between 66-142 MPa. Young's modulus (E) values for Clinch Formation sandstone range from 2-8.45 GPa, with a mean of 6.22 ± 1.66 GPa.

Our coarsest grained materials from the Chapman Ridge Formation exhibited compressive strength values between 56-143 MPa, with a mean strength of 100.48 ± 49.59 MPa. All homogeneous specimens failed instantaneously and catastrophically. One specimen failed along a pre-existing oblique vein; this specimen was removed from the reported dataset. Young's modulus values range from 4.35-11.93 GPa, with a mean of 7.24 ± 3.69 GPa.

By contrast, Missoula mudstone samples exhibited compressive strength values from 0.13-0.67 MPa, with a mean of 0.37 ± 0.2 MPa. Specimens were considerably damaged at the conclusion of compression testing; samples showed extensive fragmentation along the core edges. Young's modulus values for Missoula mudstone specimens range from 0.0031-0.13 GPa, with a mean of 0.05 ± 0.04 GPa.

Tensile strength testing

Tensile strength (TS) data from disc specimens are listed in Table 3.3. Cutler Formation specimens exhibited a mean tensile strength of 4.83 ± 0.26 MPa; specimens failed cleanly along relatively straight single fractures. Clinch Formation specimens exhibited a mean tensile strength of 14.5 ± 3.5 MPa. Specimens consistency failed along a single fracture with some additional chipping during testing. Chapman Ridge Formation specimens exhibited a mean tensile strength

Table 3.3 Tensile strength test data for disc specimens.

Sample	Sample name	L/D ratio	Pmax (N)	TS (MPa)	Mean TS (MPa)
Cutler Fm	Cut1	0.2	3807.4	4.58	4.83 +/- 0.26
	Cut2	0.2	3739.46	4.8	
	Cut3	0.2	4463.6	5.1	
Clinch Fm	skC1a	0.4	6168.28	16.4	14.5 +/- 3.5
	skC2a	0.4	6712.14	19.9	
	skC3a	0.3	4255.03	12.9	
	skC4a	0.3	4721.03	13.8	
	skC4b	0.6	5175.44	9.6	
	skC6	0.4	5392.77	14.4	
Chapman Ridge Fm	skChR1	0.3	1770.27	7	10.57 +/- 3.87
	skChR2	0.2	5220.69	13.5	
	LChR1	0.2	10911.44	15.9	
	LChR2	0.2	3799.91	5.6	
	LChR3	0.2	7720.23	11.2	
	LChR4	0.2	8477.54	10.2	
Missoula mudstone	Mis4	0.3	15.19	0.03	0.063 +/- 0.027
	Mis5	0.2	31.48	0.08	
	Mis7	0.2	26.23	0.09	
	Mis8	0.3	24.38	0.05	

of 10.57 ± 3.87 MPa and similarly failed along single primary fractures with some chipping. By contrast, Missoula mudstone specimens exhibited a mean tensile strength of 0.058 ± 0.026 MPa. Failure of Missoula specimens occurred along through-going fractures but underwent considerable fragmentation during testing.

Fracture toughness testing

Fracture toughness data and fracture energy results are listed in Table 3.4. The standard requirements for the determination of fracture toughness from Kuruppu et al. (2014) assumes adequate specimen thickness and plane strain conditions. The size of available samples prevented construction of standard thickness discs (i.e. a minimum of 30-mm thickness for 50-mm diameter specimens). For most samples, I was only able to make discs 5-15-mm thick. In order to assess the effect of less-than-optimal disc thickness, I compared the difference in fracture toughness values for samples of the Clinch Formation of different thickness. Fracture toughness values for 30-mm thick specimens fell within the range of fracture toughness values measured in <30-mm thick specimens. These results are corroborated by data from the literature, where other authors have suggested that fracture toughness is independent of specimen thickness (Kataoka & Obara, 2015; Lim et al., 1994; Schmidt & Lutz, 1979). As a result, I assume plane strain conditions were met in our three-point bend testing.

Table 3.4 Fracture toughness and fracture energy data for semi-circular disc three-point bend specimens

Sample	Sample name	Radius, R (mm)	Notch length, a (mm)	Thickness, B (mm)	Beta (a/R)	Pmax (N)	Y'	Fracture toughness, KIC (MPa*m^1/2)	Mean KIC (MPa*m^1/2)	Fracture Energy, J (Pa*m)	Mean J (Pa*m)
Cutler Fm	Cut1	25.27	9.6	11.7	0.38	433.33	4.44	0.56	0.48 +/- 0.12	106.39	78.41 +/- 39.57
	Cut2	25	10.6	11.7	0.42	259.66	4.8	0.39		50.43	
Clinch Fm	C2	25.29	9.68	10.6	0.38	1108.86	4.4	1.55	1.35 +/- 0.23	837.94	649.34 +/- 181.23
	C3	25.2	9.49	10.46	0.38	1015.94	4.37	1.53		704.92	
	C4	25.22	10.2	9.27	0.4	796.34	4.58	1.24		649.83	
	C5	25.16	9.84	10.73	0.39	754.42	4.48	1.08		404.66	
Chapman Ridge Fm	ChR1	25.21	8.5	15.31	0.34	1397.92	4.14	1.22	1.31 +/- 0.21	499.71	565.87 +/- 172.57
	ChR2	25.3	9.4	15.3	0.37	1609.95	4.31	1.58		792.18	
	ChR4	25.3	9.5	14.7	0.38	1317.61	4.34	1.34		588.1	
	ChR5	25.1	9.65	11.8	0.38	820.2	4.45	1.08		383.51	
Missoula mudstone	Mis3	28	7	11	0.25	62.83	3.37	0.051	0.042 +/- 0.018	0.67	1.06 +/- 0.66
	Mis4	29	10	5	0.34	38.22	3.45	0.081		1.82	
	Mis7	29	8	11	0.28	59.61	3.24	0.048		0.67	

The determination of fracture energy, a critical parameter required for fracture modeling, depends on fracture toughness and elastic modulus. Three-point bend testing allowed us to derive fracture toughness and the compressive elastic modulus was determined from UCS testing. In computational fracture models, however, the use of the compressive elastic modulus alone is invalid, as specimens exhibit tensile failure under three-point bend conditions. It has been demonstrated that elastic moduli of rock may differ considerably in compression versus tension (Zhang & Yu, 2019). I was unable to derive the tensile elastic modulus of rock specimens from our experimental test efforts, so I utilized values from the literature in fracture energy determinations, with the recognition that doing so introduced a layer of error in our analysis.

Cutler Formation values for fracture toughness and energy were 0.48 ± 0.12 MPa*$m^{1/2}$ and ~78 Pa*m, respectively. Clinch Formation specimens exhibited the highest fracture toughness and energy values, 1.35 ± 0.23 MPa*$m^{1/2}$ and ~650 Pa*m, respectively. Chapman Ridge Formation fracture toughness and energy values were 1.305 ± 0.21 MPa*$m^{1/2}$ and ~565 Pa*m, respectively. During three-point bend testing, all specimens exhibited failure along a single relatively straight crack that originated at the notch (Figure 3.7). Missoula mudstone specimens exhibited fracture toughness and energy values of 0.042 ± 0.018 MPa*$m^{1/2}$ and ~1 Pa*m, respectively.

Mechanical property correlation

Correlation of compressive to tensile strength were evaluated based on the previously derived equations listed in Table 3.2. Values were then compared to actual measurements of

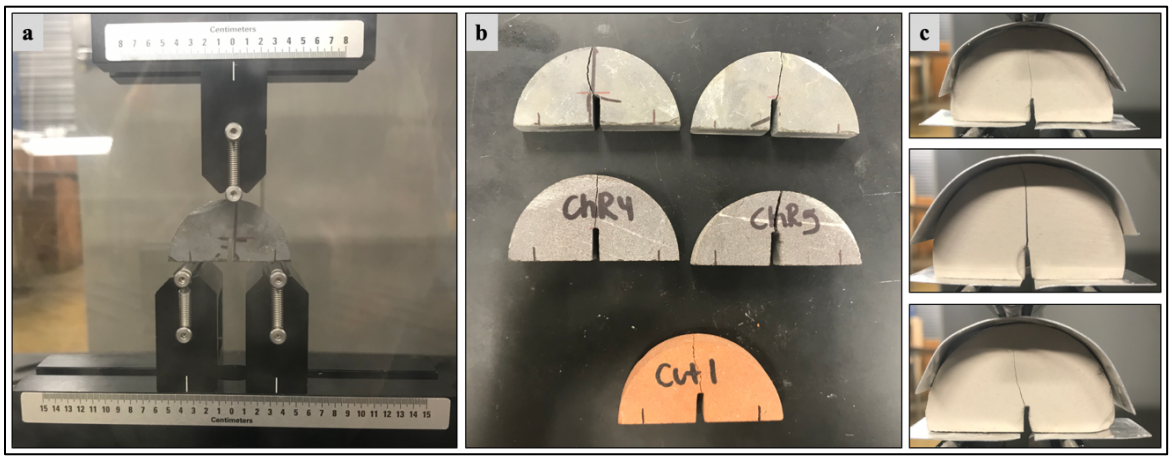


Figure 3.7 Three-point bend test results on semi-circular disc specimens. (a) Test configuration with Clinch Formation sample loaded for testing; sample diameter = 50 mm, roller span = 35 mm. (b) Post-test photos for specimens Clinch3 (upper left), Clinch5 (upper right), Chapman Ridge4, Chapman Ridge5, and Cutler1. All specimens broke into discrete halves during testing. (c) Post-test specimens for Missoula mudstone specimens Missoula3 (top), Missoula4 (middle), and Missoula7 (bottom). To induce cracking from the sample notches, a thin sheet of aluminum was placed along the top and bottom of semi-circular discs where the roller pins contacted the specimens.

tensile strength made during tensile strength testing to assess the applicability of each correlation method. The results are listed in Table 3.5. Based on comparisons to the mean measured tensile strength of each rock type, with an exception of the Cutler formation, the correlation method described by Nazir et al., 2013 provided predictability within ~20% for the two sandstonench Formation the most accurate correlations. The Nazir et al. (2013) correlation was also the most accurate method for the Missoula mudstone; this approximation, however, still provided approximations ~40% different from measured values. For the Cutler Formation, the Altindag & Guney (2010) method provided the closest approximation of tensile strength from UCS, but only provided predictions within 25% of measured values. By contrast, the Nazir et al. (2013) correlation for the Cutler samples provided particularly poor estimations of TS (>100% difference from measured values).

I performed additional correlations between tensile strength and fracture toughness and made comparisons to measured fracture toughness from three-point bend testing (Table 3.6). Based on comparisons to measured values, the correlation of Whittaker et al. (1992) was most applicable for predicting K_{IC} values for Clinch and Chapman Ridge sandstone samples and provided estimations within ~30% and ~7% of measured values, respectively. Correlations for silt and mudstone samples, by contrast, were most closely approximated by the Zhang (2002) correlation. Estimation of fracture toughness for Missoula mudstone samples, however, still exhibited differences greater than 100% from measured values (Table 3.6).

Table 3.5 Predicted TS values from measured UCS data and comparisons to measured TS for each rock type.

Sample	Measured UCS (MPa)	Measured Mean TS (MPa)	Predicted Mean TS (MPa) (Nazir et al., 2013)	% difference from measured TS	Predicted Mean TS (MPa) (Kahraman et al., 2012)	% difference from measured TS	Predicted Mean TS (MPa) (Altindag & Guney, 2010)	% difference from measured TS	Predicted Mean TS (MPa) (Farah, 2011)	% difference from measured TS
Cutler Fm	106.63 +/- 20.7	4.83 +/- 0.26	14.98 +/- 3.07	102.47	10.05 +/- 1.95	70.16	6.28 +/- 1.14	26.1	21.05 +/- 4.04	125.35
Clinch Fm	103.57 +/- 24.22	14.5 +/- 3.5	15.03 +/-4.57	3.59	10.06 +/- 2.9	36.16	6.28 +/- 1.69	79.11	21.08 +/- 6.03	36.99
Chapman Ridge Fm	100.48 +/- 49.59	10.57 +/- 3.87	13.08 +/- 5.8	21.23	8.81 +/- 3.72	18.16	5.53 +/- 2.19	62.61	18.47 +/- 7.72	54.41
Missoula mudstone	0.37 +/- 0.2	0.06 +/- 0.027	0.04 +/- 0.02	40	0.03 +/- 0.02	66.67	0.03 +/- 0.02	66.67	0.25 +/- 0.04	122.58

Table 3.6 Predicted K_{IC} values from measured TS data and comparisons to measured K_{IC} for each rock type

Sample	Measured Mean TS (MPa)	Measured Mean KIC (MPa*m^1/2)	Predicted KIC (MPa*m^1/2) (Whittaker et al., 1992)	% difference from measured KIC	Predicted KIC (MPa*m^1/2) (Zhang et al., 1998)	% difference from measured KIC	Predicted KIC (MPa*m^1/2) (Zhang, 2002)	% difference from measured KIC
Cutler Fm	4.83 +/- 0.26	0.48 +/- 0.12	0.79 +/- 0.03	48.8	1.43 +/- 0.13	99.00	0.70 +/- 0.04	37.3
Clinch Fm	14.5 +/- 3.5	1.35 +/- 0.23	1.82 +/- 0.37	29.6	8.61 +/- 3.28	145.78	2.11 +/- 0.50	43.93
Chapman Ridge Fm	10.57 +/- 3.87	1.31 +/- 0.21	1.40 +/- 0.41	6.64	5.33 +/- 2.98	121.08	1.54 +/- 0.56	16.14
Missoula mudstone	0.06 +/- 0.027	0.042 +/- 0.02	0.28 +/- 0.003	147.83	0.001 +/- 0.0008	190.70	0.008 +/- 0.003	136

Computational modeling

XFEM and validated fracture model

To validate the XFEM model, derived analog rock properties were used to simulate three-point bend tests for all four rock types. The XFEM model illustrated crack growth through the specimens. Cracks propagated in a stable, linear path parallel to the notch placed in the specimen, similar to experimental testing (Figure 3.8).

Model efforts to validate experimental results provided estimation of both the forces and displacements observed during experimental tests. The most accurate simulations were encountered in the coarser-grained, siltstone and sandstone lithologies of the Cutler, Clinch, and Chapman Ridge formations, yet modeled maximum forces deviated from experimental values (Figure 3.9). The maximum force of the modeled Cutler Formation (Figure 3.9a) fell within range of experimental values; however, failure was exhibited at a lower displacement. The stiffness (i.e. the slope of the Force-Displacement graph) of modeled versus experimental results are relatively comparable for the Chapman Ridge and Clinch formations. However, the modeled Cutler formation exhibited considerably stiffer behavior prior to failure than was observed during experimental testing. The maximum modeled force for the Clinch Formation (Figure 3.9b) was ~100 N higher than the maximum force exhibited during testing. Similarly, maximum forces obtained for the Chapman Ridge Formation (Figure 3.9c) in validation models were ~1000 N, whereas experimental forces ranged from ~800-1600 N.

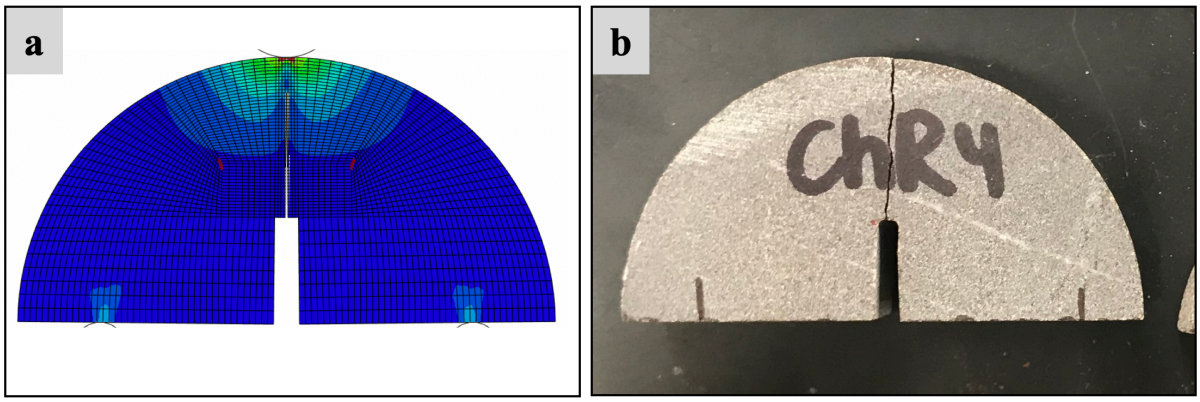


Figure 3.8 Comparison of crack growth in three-point bend for (a) the Abaqus XFEM model and (b) experimental testing. Example shown is Chapman Ridge Formation specimen 4.

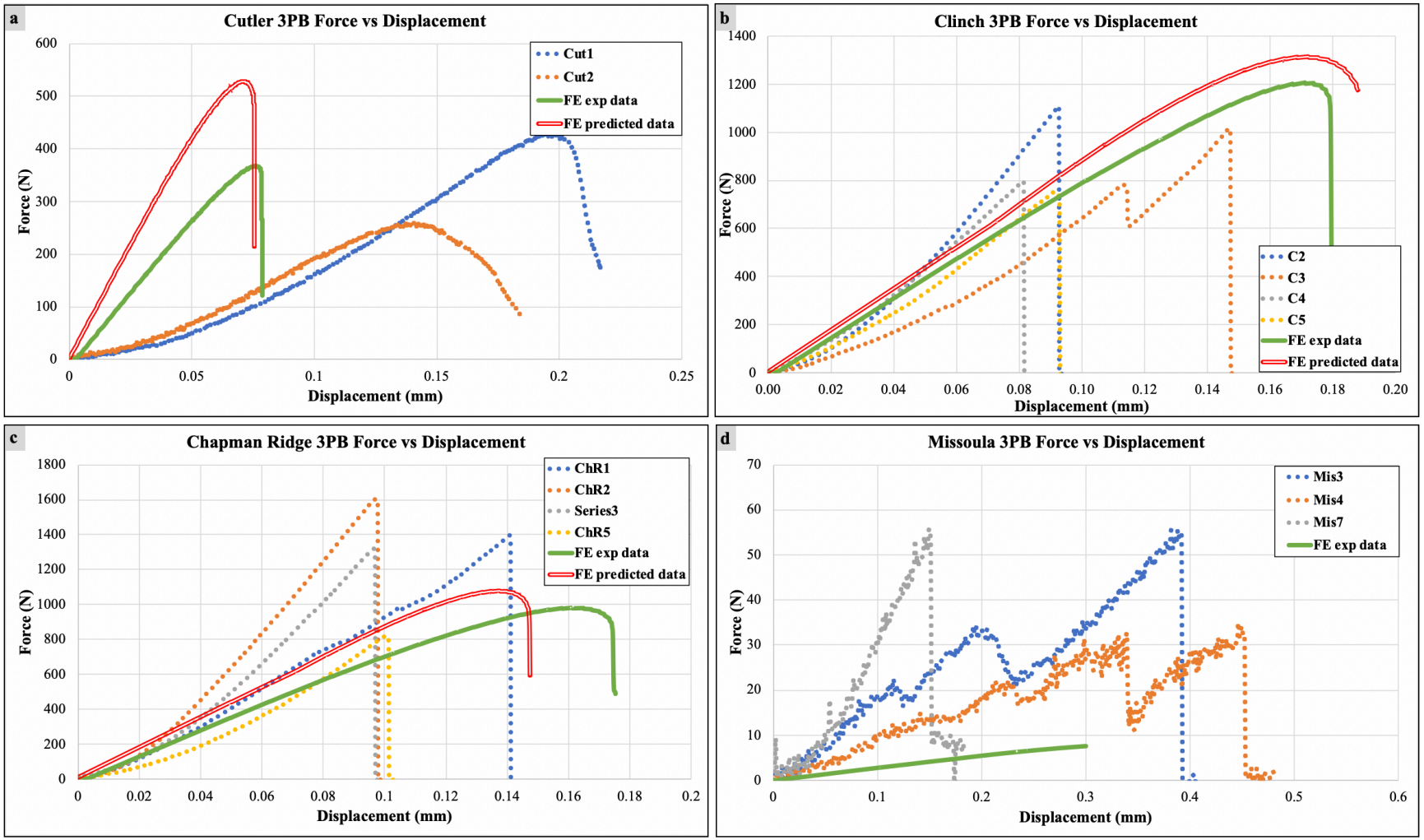


Figure 3.9 Abaqus XFEM model results for three-point bend rock specimens. Modeled results using experimental values (green solid lines) and predicted values based on UCS (red double solid lines) are shown alongside experimental test results (dotted lines). Model results include (a) Cutler Formation three-point bend (3PB), (b) Clinch Formation 3PB data, (c) Chapman Formation 3PB data, and (d) Missoula mudstone 3PB data. Missoula test results were below the resolution of the 100 kN test machine. Model results confirmed that test data were not valid for such weak materials.

With samples of the Missoula mudstone, I encountered considerable variation in experimental test data (Figure 3.9d). In particular, the force at which specimens underwent failure (between approximately 30-55 N) was within the error of the 100 kN load cell used during testing, deeming experimental data invalid. As a result, our modeling efforts were unable to validate the experimental three-point bend results of the Missoula mudstone. Efforts to increase the modeled displacement and induce cracking, despite being geologically unrealistic, were unsuccessful, and the modeled Missoula specimen did not exhibit failure.

Figure 3.9 also shows the results of modeling efforts using predicted property values. In this case, I utilized UCS values from experimental testing, and, using applicable correlation equations, predicted the properties of tensile strength and fracture toughness (Table 3.7). Average values for sandstone in the literature were used for the compressive and tensile elastic moduli (Zhang & Yu, 2019). Fracture energy was derived using the predicted values of fracture toughness and tensile elastic modulus. I excluded the Missoula mudstone from predicted modeling efforts because I was unable to validate the experimental test data.

In all cases, predicted values for tensile strength, fracture toughness, and fracture energy were slightly overpredicted. As a result, the modeled maximum forces using these predicted values were also higher than the original models that used experimental values. However, for the Chapman Ridge and Clinch Formation models (Figure 9a-b), these maximum forces were only

Table 3.7 Mean UCS values for analog lithologies and predicted properties of TS and KIC from correlation equations established by Nazir et al., (2013) and Whittaker et al. Values of elastic modulus were estimated based on the relative UCS of rock types. Predicted tensile elastic modulus reflect typical sandstone values from the literature (Zhang & Yu, 2019).

	Measured UCS (MPa)	Predicted TS (MPa)	Predicted KIC (MPa*m^1/2)	Predicted Compressive Elastic Modulus (GPa)	Predicted Tensile Elastic Modulus (GPa)	Predicted Fracture Energy (Pa*m)
Clinch Fm	103.57	15.03	1.82	6.5	3	1104.13
Chapman Ridge Fm	100.48	13.08	1.4	6.5	3	655.33
Cutler Fm	106.64	6.28	0.7	6.5	3	163.33

~100 N higher than expected and the displacements at failure were fairly accurate. The Cutler Formation model using predicted values exhibited a failure force ~200 N higher than expected.

Discussion

Variation in mechanical property data

With natural sedimentary samples, inhomogeneities imparted during deposition (e.g., differences in bedding thickness, lamination, and potential compositional variation), as well as those imparted during diagenesis and potential tectonic deformation (e.g., dissolution, grain suturing, cleavage and fracture) affect the mechanical behavior of samples. In this study, our ability to collect homogeneous samples of sufficient size prevented us from making all experimental test specimens of the dimensions recommended by standard practices. Efforts were made, however, to ensure our experimental test data were valid. For example, during UCS tests, specimens often did not meet the required L/D dimensions (>2.0; ASTM D2938, 1995). To circumvent this difficulty, I applied strength correction factors to specimens that exhibited L/D <2.0 (ASTM C42, 2003). I also tested multiple samples of the Clinch Formation sandstone with different diameters and using test machines with different load capacities; data from these efforts fell within the range of UCS values determined for the Clinch Formation from cores of standard size. Although results of these tests were similar, there is greater variation in test results from less-than standard core sizes, suggesting that the scale of natural heterogeneities are not necessarily recognizable within larger cores, but may affect the behavior of smaller core sizes.

Similarly, three-point bend specimens were commonly thinner than that recommended by standard practice (Kuruppu et al., 2014). To ensure that our assumption of plane strain conditions

under three-point bend was valid, I tested Clinch Formation samples of standard and less-than-standard thickness and observed the same values of fracture toughness. These results are consistent with other studies that were unable to establish a clear dependence between fracture toughness and specimen thickness (Kataoka & Obara, 2015; Lim et al., 1994; Schmidt & Lutz, 1979).

Values acquired during compressive strength testing for Clinch Formation sandstone range from 64.7 to 142.8 MPa. Similar scales of variation were observed among specimens for other mechanical tests. I attribute this variation to the presence of inhomogeneities within these natural rock specimens. In particular, the Clinch Formation and Chapman Ridge Formation sandstones, both of which occur within the fold-and-thrust belt of the Appalachian orogeny, contained abundant pre-existing veins that may have served as planes of weakness and induced premature failure. Although I collected the visually most homogeneous samples, one Chapman Ridge core specimen was tested that exhibited a visible vein. Failure occurred along this vein and, as a result, yielded a compressive strength value considerably lower than other Chapman Ridge cores; this specimen was removed from the Chapman Ridge compressive strength dataset. No other specimens exhibited failure along obvious heterogeneities; but I expect the presence of pre-existing flaws in rock specimens (e.g., bedding planes, microcracks, voids, etc.) to contribute to mechanical property variation.

With these variations in mind, I assess the trends of each rock type observed across testing methods. Similar trends were observed during compressive and tensile strength testing. Typical compressive strength values for sandstone range from approximately 6 to >200 MPa (Gudmundsson, 2001; Jaeger & Cook, 1979; Johnson & DeGraff, 1988). In this study, Clinch,

Chapman Ridge, and Cutler Formation specimens all exhibited compressive strengths near 100 MPa, placing them in the category of strong to very strong materials (Hoek & Brown, 1997; NRCS, 2012). Missoula mudstone specimens, by contrast, exhibited compressive strength values <1 MPa and were thus classified as extremely weak. For tensile strength measurements of silt and sandstones, expected values are in the range of 1-25 MPa (Gudmundsson, 2001; Jaeger & Cook, 1970). From experimental testing, Clinch Formation specimens exhibited the highest tensile strength (14.5 MPa), followed by Chapman Ridge (10.57 MPa), Cutler Formation siltstone (4.83 MPa), and Missoula mudstone (0.058 MPa) specimens.

Values of Young's modulus (modulus of elasticity) represent the stiffness of lithologies during compressive strength testing; typical values for sandstones range from <1-80 GPa (Gudmundsson, 2001; Jaeger & Cook, 1979). Since deviations in the stress-strain curves for compressive strength testing affect the resulting estimations of Young's modulus, heterogeneities from stable crack growth and/or specimen core chipping likely played a role in the stiffness variation. In general, the Cutler Formation and most Clinch Formation compressive test specimens exhibited uniform elastic behavior prior to failure, resulting in estimates of Young's modulus of ~6 GPa. Chapman Ridge specimens exhibited considerably greater variation in behavior, yielding a mean Young's modulus of 8.27 GPa; these specimens, however, contained a distinctly higher number of heterogeneities (i.e. cracks and veins) than other sample suites. Missoula stress-strain curves exhibited the highest degree of ancillary crack growth and

chipping, making estimates of elasticity difficult to perform. However, as expected, Missoula specimens exhibited the lowest Young's modulus values (~0.06 GPa).

Fracture toughness describes a material's resistance to fracture. A general range for typical sedimentary rocks (with compressive strength in the range of 40-120 MPa) is between 0.2 and 2 MPa*$m^{1/2}$ (Ashby, 1992). Trends in fracture toughness for analog lithologies in this study values mimicked those determined from compressive and tensile strength tests. Clinch and Chapman Ridge Formation specimens exhibited similar toughness values of approximately 1.3 MPa*$m^{1/2}$, Cutler Formation toughness values averaged 0.48 MPa*$m^{1/2}$, and Missoula toughness values averaged 0.04 MPa*$m^{1/2}$. Values of Clinch, Chapman Ridge, and Cutler lithologies matched expected values for relatively strong sandstone-like materials; however, Missoula values were roughly equivalent to the toughness of polymer and foam materials, making these specimens extremely prone to fracture (Ashby, 1992). Interestingly, the Cutler Formation exhibited a unique behavior before during failure of three-point bend specimens (Figure 3.7c); whereas other lithologies exhibited uniformly elastic behavior and an instantaneous drop-off in force upon fracture. Both Cutler test specimens exhibited broad decreasing slopes after reaching the maximum applied force.

Fracture energy describes the energy required to maintain fracture propagation in a specimen; it may also be described by the area under the curve for three-point bend testing. As with other test methods, Clinch Formation and Chapman Ridge Formation specimens exhibited the highest fracture energy values (649 and 565 Pa*m, respectively), followed by Cutler Formation (78 Pa*m) and Missoula (1 Pa*m) specimens. For Clinch and Chapman Ridge specimens, force-displacement curves from three-point bend testing confirmed that these well-

cemented sandstones exhibited elastic behavior until a maximum force was reached, which was followed by a sharp decrease as the crack quickly propagated through the specimen. In some cases, secondary crack growth was observed as abrupt dips in force-displacement curves, as in . specimens Clinch3 and Chapman Ridge1 (Figure 3.9b).

Two of the properties that I evaluated in terms of mechanical testing behavior are the porosity and the petrographic make-up of samples. It has been demonstrated that with increasing porosity, rock strength decreases (Hatzor et al., 1997; Heidari et al., 2014; Palchik, 1999). Ahren et al. (2019) quantitatively determined the porosity of all four analog rocks and observed porosity values of: Chapman Ridge (0.02), Clinch (0.062), Cutler (0.092), and Missoula (0.473). The relatively low porosity of these Clinch and Chapman Ridge sandstone samples (<0.10) reflect the abundance of the cement phase observed in thin section (clay and carbonate, and carbonate cements, respectively), and support the high strength values obtained from experimental testing. I note, as well that strength parameters of these carbonate-containing samples are best represented by the correlation of Nazir et al. (2013), who derived equations based on the testing of limestone samples. This suggests that the calcite cement may play a primary role in controlling the strength of these samples. Similarly, the relatively high porosity of the Cutler Formation siltstone and the unlithified Missoula mudstone is consistent with the extremely low values of strength and fracture properties observed from experimental testing.

The compositional makeup of analog lithologies may further constrain trends in mechanical property data. For example, the presence of abundant grain suturing in the Chapman Ridge Formation (Figure 3.2f) may serve as a mechanism to both decrease porosity and an increase in grain-to-grain contact, resulting in high UCS values. In addition, the failure behavior

of Cutler Formation samples under three-point bend may be explained by the relatively high abundance (~8%) of mica in thin section (Figure 3.2b). Mica has been shown to deform readily by slip (dislocation glide) along weakly bonded basal cleavage planes (Baños et al., 1983; Kronenberg et al., 1990; Mares & Kronenberg, 1993). This behavior, however, would not be captured in computational modeling. Since our FE models do not account for specific mineralogical phases in the rock specimens, I would expect the model to demonstrate more standard, elastic behavior similar to other sandstone lithologies, which is the case shown in Figure 3.7c.

The Missoula mudstone, originally selected to represent an analog for potentially weak Murray formation mudstone lithologies, exhibited extremely low strength and fracture properties in all experimental tests. In a specific case, three-point bend results were invalidated because the applied forces were below the resolution of the testing machine. The combined difficulty in preparing specimens for testing, and the extremely low forces required to induce fracture, demonstrate the need for additional testing and characterization. Weak rocks are known to be difficult to prepare for standard mechanical tests, especially tests that require specific specimen geometries, and data are commonly disparate and unreliable (Haberfield & Johnston, 1990). Extremely weak lithologies (<10 MPa), including the Missoula mudstone, are so commonly poorly consolidated that standard drilling with water circulation causes specimens to completely disintegrate (Durmekova et al., 2003; Kanji, 2014). Future testing might utilize smaller load cells; for example, tests conducted by Agustawijaya (2007) achieved success in determining UCS using a 5 kN load cell. Additionally, other test methods might be considered, including those that do not require cylindrical specimens. Such methods include point load strength index

testing (ASTM D5731, 1995), which may be conducted on irregularly shaped and sized specimens. Conversion factors may be applied to these strength index tests to easily estimate unconfined compressive strength (Agustawijaya, 2007).

Validated fracture model and property correlation

Computational models for Cutler, Clinch, and Chapman Ridge Formation samples adequately predicted the maximum force exhibited by specimens prior to failure. Discrepancies in the stiffness behavior exhibited during modeling of Cutler Formation siltstone versus the coarser-grained sandstone lithologies can likely be explained by porosity and mineralogical differences that the models cannot currently constrain. In addition, once unvalidated Missoula samples were rejected, correlation efforts demonstrated the ability to estimate relevant rock properties from UCS data and accurately predict fracture using the XFEM technique in Abaqus (Figure 3.7). For estimation of tensile strength from UCS data, the correlation method described by Nazir et al. (2013) provided the best corroboration of tensile strength for most rock types tested. Correlations made by other authors commonly utilized ranges of rock types including igneous and metamorphic specimens, whereas Nazir et al. (2013) solely utilized dry limestone specimens and achieved a correlation coefficient (R^2) value of 0.90 for the proposed equation, which was the highest R^2 value for all utilized correlations. The predicted tensile strength of the Cutler formation, however, best matched the correlation method proposed by Altindag & Guney (2010). Their study encompassed a wider range of lithologies, including weaker rocks (siltstones

and sandstones) with tensile strength values <10 MPa, which is likely why estimations of Cutler tensile strength were more accurate using this correlation equation.

Efforts to estimate fracture toughness values for sandstone lithologies best matched results of Whittaker et al. (1992). In their study, a variety of rock types were analyzed, including well-cemented sandstone. However, for estimations of fracture toughness for finer-grained and more porous samples from the Cutler Formation, no correlations were particularly well-suited. Model results from Missoula samples were invalid and therefore not considered here.

Utilizing these correlation values and predicting hypothetical values from analog UCS, strength parameters were overestimated in nearly all cases, particularly in the magnitude of fracture energy and resulting force at failure (Figure 3.7). For predicted models of Clinch and Chapman Ridge formations, the force at failure was overestimated by less than 10% and for the Cutler formation, force was overestimated by approximately 35%.

Application of property correlation to Gale crater lithologies

By applying correlation equations to data collected by the Curiosity rover at Gale crater, I estimated tensile strength and fracture toughness for mudstone and sandstone lithologies observed by the Curiosity rover. Estimated UCS for Stimson formation sandstone were considerably lower than any of the analog lithologies assessed in this study. By contrast, estimations of tensile strength and fracture toughness for mudstone of the Murray formation were higher than those derived for Missoula mudstone specimens. As a result, although our

analog lithologies do not match expected values for martian rocks, our choice of specimens helps constrain the potential variability of end-member lithologies expected in Gale crater.

I predicted both tensile strength and fracture toughness values for samples drilled by the Curiosity rover for which unconfined compressive strength values have previously been estimated (Peters et al., 2018). These values and predictions are listed in Table 3.8. To estimate tensile strength, I utilized the correlation derived from Nazir et al. (2013), and for fracture toughness predictions, I utilized correlations derived by Whittaker et al. (1992) and Zhang (2002) to constrain both minimum and maximum potential values.

Since UCS values between the Murray and Stimson formations consistently overlap and are <20 MPa, it is difficult to distinguish between predicted TS and K_{IC} values between the two formations. The UCS values of Murray formation drill holes at Pahrump Hills (denoted Telegraph Peak, Buckskin, and Mojave), the location of the Salsberry Peak caprock, represent some of the lowest estimated UCS (8 to 8.5 MPa) and thus exhibit fairly low values of estimated TS (1 MPa) and K_{IC} (<0.4 MPa*$m^{1/2}$). With the exception of the Okorusu site, Stimson formation drill holes (denoted Greenhorn, Lubango, and Big Sky) exhibit slightly higher UCS values (12 to 18 MPa) than the Murray formation at Pahrump Hills and thus higher values of TS (2 MPa) and K_{IC} (0.5 MPa*$m^{1/2}$).

Conclusions

In this study I utilized a multi-part approach to assess fracture growth and the conditions under which fractures propagate on Mars. First, analog rocks were selected to represent lithologies that occur in Gale crater, including very strong sandstone and extremely weak

Table 3.8 Predicted TS (from Nazir et al., 2013) and K_{IC} values (from Whittaker et al., 1992 and Zhang, 2002) for Murray and Stimson formation rocks drilled by the Curiosity rover.

Formation	Drill sample name	Estimated UCS (MPa) (Peters et al., 2017)	Predicted TS (MPa) (Nazir et al., 2013)	Predicted KIC (MPa*m^1/2) (Whittaker et al., 1992)	Predicted KIC (MPa*m^1/2) (Zhang, 2002)
Murray	Telegraph Peak	8	1.53 +/- 0.61	0.43 +/- 0.07	0.22 +/- 0.09
	Buckskin	8			
	Mojave	8.5			
	Quela	8.5-12			
	Oudam	12.0-18.0			
	Sebina	18			
	Marimba	18			
Stimson	Okorusu	8.5	1.78 +/- 0.53	0.46 +/- 0.06	0.26 +/- 0.08
	Greenhorn	12.0-18.0			
	Lubango	12.0-18.0			
	Big Sky	18			

siltstone. Through experimental testing, the mechanical properties of analog lithologies were determined. In this study, the properties of silt and sandstone samples were found to be within the range of previously tested terrestrial materials.

Second, XFEM techniques were used to simulate fracture propagation through analog lithologies. I utilize correlation efforts to estimate rock properties and demonstrate the ability to accurately predict fracture in light of limited mechanical property data from Mars rover missions. The best correlations observed for silt and sandstone lithologies in this study occurred when comparing analog carbonate-cemented sandstone to previously tested limestone lithologies. Sandstones encountered on Mars, however, rarely contain calcite, illustrating the need for additional testing in sandstone lithologies that lack a calcite component. I also show that porosity of materials may play a primary role in mechanical behavior, indicating the need for additional exploration. Finally, although I was unable to validate model results for our analog samples of poorly lithified mudstone, estimates of UCS from Curiosity rover drill data suggest that at least a subset of the materials on the martian surface exhibit similarly low strength, and highlights the need for additional testing of poorly lithified materials.

References

Abaqus Software 6.13 (2013). Abaqus analysis user's guide. Dassault Systemes Simulia Corp, Providence, RI.

Agustawijaya, D. S. (2007). The uniaxial compressive strength of soft rocks. *Civil Engineering Dimension*, 9(1), 9-14.

Ahern, A. A., Rogers, A. D., Macke, R. J., Thomson, B. J., Kronyak, R. E., & Kah, L. C. (2019). Thermal inertia and conductivity measurements of Mars analog rock samples. *Ninth International Conference on Mars.*

Altindag, R. & Guney, A. (2010). Predicting the relationship between brittleness and mechanical properties (UCS, TS, and SH) of rocks. *Scientific Research and Essays*, 5(16), 2107-2118.

Andersen, C. B., (1995). Provenance of mudstones from two Ordovician Foreland basins in the Appalachians. In Dorobek, S. L. and Ross, G. M. (Eds.), Stratigraphic evolution of foreland basins: Special Publication 52, Society of Economic Paleontologists and Mineralogists, 53-64.

Anderson, R. C., Jandura, L., Okon, A. B., Sunshine, D., Roumeliotis, C., Beegle, L. W., et al. (2012). Collecting samples in Gale crater, Mars; an overview of the Mars Science Laboratory sample acquisition, sample processing and handling system. *Space Science Reviews*, 170(1-4), 57-75. doi:10.1007/s11214-012-9898-9

Arvidson, R. E., DeGrosse Jr., P., Grotzinger, J. P., Heverly, M. C., Shechet, J., Moreland, S. J., et al. (2017). Relating geologic units and mobility system kinematics contributing to Curiosity wheel damage at Gale crater, Mars. *Journal of Terramechanics*, 73, 73-93. doi:10.1016/j.terra.2017.03.001

Ashby, M. F. (1992). *Materials Selection in Mechanical Design*. Pergamon Press: Oxford.

ASTM Standard C42 (2003). Standard test method for obtaining and testing drilled cores and sawed beams of concrete. *ASTM International*, West Conshohocken, PA.

ASTM Standard D2938-95 (1995). Standard test method for unconfined compressive strength of intact rock core specimens. *ASTM International*, West Conshohocken, PA.

ASTM Standard D3967-95a (1996). Standard test method for splitting tensile strength of intact rock core specimens. *ASTM International*, West Conshohocken, PA.

ASTM Standard D5731-95 (1995). Standard test method for determination of the point load strength index of rocks. *ASTM International*, West Conshohocken, PA.

ASTM Standard D7012-14 (2014). Standard test methods for compressive strength and elastic moduli of intact rock core specimens under varying states of stress and temperatures. *ASTM International*, West Conshohocken, PA.

Baker, V. R. & Bunker, R. C. (1985). Cataclysmic late Pleistocene flooding from glacial Lake Missoula: a review. *Quaternary Science Reviews*, 4, 1-41.

Banham, S. G., Gupta, S., Rubin, D. M., Watkins, J. A., Sumner, D. Y., Edgett, K. S., et al. (2018). Ancient Martian aeolian processes and palaeomorphology reconstructed from the Stimson formation on the lower slope of Aeolis Mons, Gale crater, Mars. *Sedimentology*, *65*(4), 993–1042. http://doi.org/10.1111/sed.12469

Baños, J. O., Amouric, M., de Fouquet, C., & Baronnet, A. (1983). Interlayering and interlayer slip in biotite as seen by HRTEM. *American Mineralogist*, 68, 754-758.

Belytschko, T. & and Black, T. (1999). Elastic crack growth in finite elements with minimal remeshing. *International Journal for Numerical Methods in Engineering*, 45(5), 601-620. https://doi.org/10.1002/(SICI)1097-0207(19990620)45:5<601::AID-NME598>3.0.CO;2-S

Bernabe, Y., Fryer, D. T., & Hayes, J. A. (1992). The effect of cement on the strength of granular rocks. *Geophysical Research Letters*, 19(14), 1511-1514.

Cargill, J. S. & Shakoor, A. (1990). Evaluation of empirical methods for measuring the uniaxial compressive strength of rock. *International Journal Rock Mechanics and Mining Sciences*, 27(6), 495-503.

Caswell, T. E., Milliken, R. E. (2017). Evidence for hydraulic fracturing at Gale crater, Mars: implications for burial depth of the Yellowknife Bay formation. *Earth and Planetary Science* Letters, 468, 72-84. http://dx.doi.org/10.1016/j.epsl.2017.03.033

Cattermole, J. M. (1955). Geology of the Shooks Gap quadrangle, Tennessee. U.S. Geological Survey GQ-76, scale 1:24,000.

Chambers, R.L. (1984). Sedimentary evidence for multiple glacial lakes Missoula. In: McBane, J. D., Garrison, P. B. (Eds.), Northwest Montana and Adjacent Canada. Montana Geological Society, Billings, MT, 189-199.

Dennison, J. M. & Boucot, A. J. (1974). Reference section for Silurian Clinch Sandstone and most nearly complete Devonian section in eastern Tennessee. *Southeastern Geology*, 16, 79-101.

Dorsch, J. & Driese, S. G. (1995). The Taconic foredeep as sediment sink and sediment exporter: implications of the origin of the white quartzarenite blanket (Upper Ordovician-Lower

Silurian) of the central and southern Appalachians. *American Journal of Science*, 295, 201-243.

Dunn, D. E., LaFountain, L. J., & Jackson, R. E. (1973). Porosity dependence and mechanism of brittle fracture in sandstones. Journal of Geophysical Research, 78(14), 2403-2417.

Durmekova, T., Holzer, R., & Wagner, P. (2003). Weak rocks in engineering practice. *Proceedings of the International Symposium of Geotechnical Measurements and Modeling*.

Edgett, K. S., Yingst, R. A., Ravine, M. A., Caplinger, M. A., Maki, J. M., Ghaemi, T, et al. (2012) Curiosity's Mars Hand Lens Imager (MAHLI) Investigation. *Space Science Reviews*, 170, 259-317. doi 10.1007/s11214-012-9910-4

Farah, R. (2011). Correlations between index properties and unconfined compressive strength of weathered Ocala Limestone. UNF Theses and Dissertations, Paper 142.

Gale, J. F., Laubach, S. E., Olson, J. E., Eichhubl, P., Fall, A. (2014). Natural fractures in shale: a review and new observations. *AAPG Bulletin*, 98, 2165-2216. doi: 10.1306/08121413151

Gorevan, S. P., Myrick, T., Davis, K., Chau, J. J., Bartlett, P., Mukherjee, S., et al. (2003). Rock Abrasion Tool: Mars Exploration Rover mission. *Journal of Geophysical Research*, 108(E12), 8068. doi:10.1029/2003JE002061

Grotzinger, J. P., Gupta, S., Malin, M. C., Rubin, D. M., Schieber, J., Siebach, K., et al. (2015). Deposition, exhumation, and paleoclimate of an ancient lake deposit, Gale crater, Mars. *Science*, 350(6257), aac7575. https://doi.org/10.1126/science.aac.7575

Gudmundsson, A., Fjeldskaar, I., Brenner, S.L. (2002). Propagation pathways and fluid transport of hydrofractures in jointed and layered rocks in geothermal fields. *Journal of Volcanology and Geothermal Research 116*, 257-278. https://doi.org/10.1016/S0377-0273(02)00225-1

Gudmundsson, A. (2011). *Rock Fractures in Geological Processes*. Cambridge University Press, New York.

Haberfield, M. M. & Johnston, I. W. (1990). Determination of the fracture toughness of a saturated soft rock. *Canadian Geotechnical Journal*, 27, 276-284. https://doi.org/10.1139/t90-038

Hanson, M. A., Enkin, R. J., Barendregt, R. W., & Clague, J. J. (2015). Provenance and deposition of glacial Lake Missoula lacustrine and flood sediments determined from rock magnetic properties *Quaternary Research*, 83(1), 166-177. doi:10.1016/j.yqres.2014.09.005

Hanson, M. A., Lian, O. B., & Clague, J. J. (2012). The sequence and timing of large late Pleistocene floods from glacial Lake Missoula. *Quaternary Science Reviews,* 31, 67-81.

Hatzor, Y. H., Zur, A., & Mimran, Y. (1997). Microstructure effects on microcracking and brittle fracture of dolomites. *Tectonophysics*, 281, 141-161.

Heidari, M., Khanlari, G. R., Torabi-Kaveh, M., Kargarian, S., & Saneie, S. (2014). Effect of porosity on rock brittleness. *Rock Mechanics and Rock Engineering*, 47, 785-790.

Hoek, E. & Brown, E. T. (1997). Practical estimates of rock mass strength. *International Journal of Rock Mechanics and Mining Sciences*, 34(8), 1165-1186. https://doi.org/10.1016/S1365-1609(97)80069-X

Jaeger, J. C. & Cook, N. G. W. (1979). *Fundamentals of Rock Mechanics*, 3rd edn. Chapman & Hill: London.

Johnson, R. B. & DeGraff, J. V. (1988). *Principles of Engineering Geology*, Wiley.

Kahraman, S., Fener, M., & Kozman, E. (2012). Predicting the compressive and tensile strength of rocks from indentation hardness index. *Journal of the South African Institute of Mining and Metallurgy*, 112(5), 331-339.

Kanji, M. A. (2014). Critical issues in soft rocks. *Journal of Rock Mechanics and Geotechnical Engineering*, 6, 186-195. https://doi.org/10.1016/j.jrmge.2014.04.002

Kataoka, M. & Obara, Y. (2015). Size effect in fracture toughness of sandstone. *13th International Congress of Rock Mechanics.*

Khoei, A. R. (2014). *Extended finite element method: theory and applications*. John Wiley & Sons: West Sussex. doi:10.1002/9781118869673

Kronenberg, A. K., Kirby, S. H., & Pinkston, J. C. (1990). Basal slip and mechanical anisotropy of biotite. *Journal of Geophysical Research*, 95, 19,257-19,278.

Kronyak, R. E., Kah, L. C., Edgett, K. S., VanBommel, S. J., Thompson, L. M., Wiens, R. C., et al. (2019). Mineral-filled fractures as indicators of multigenerational fluid flow in the Pahrump Hills member of the Murray formation, Gale crater, Mars. *Earth and Space Science*, 6, 238-265. https://doi.org/10.1029/2018EA000482

Kronyak, R. E., Kah, L. C., Fedo, C. M., Stack, K. M., Edgett, K. S., & Siebach, K. L. (2017). Capping units of the Murray formation, Gale crater, Mars: Salsberry Peak as a pre-Stimson formation caprock. *LPS XLVIII*, Abstract 1523.

Kuruppu, M. D., Obara, Y., Ayatollahi, M. R., Chong, K. P., & Funatsu, T. (2014) ISRM-suggested method for determining the mode I static fracture toughness using semi-circular bend specimen. *Rock Mechanics and Rock Engineering*, 47, 267-274. doi: 10.1007/s00603-013-0422-7

Langford, R. & Chan, M. A. (1988). Flood surfaces and deflation surfaces within the Cutler Formation and Cedar Mesa Sandstone (Permian), southeastern Utah. *Geological Society of America Bulletin*, 100, 1541-1549.

Li, C. & & Mahadevan, S. (2016). An efficient modularized sample-based method to estimate the first-order Sobol' index. *Reliability Engineering and System Safety*, 153, 110-121. doi:10.1016/j.ress.2016.04.012

Lim, I. L., Johnston, I. W., Chois, S. K. & Boland, J. N. (1994). Fracture testing of a soft rock with semi-circular specimens under three-point bending, part 1- mode 1. *International Journal of Rock Mechanics, Mining Science, & Geomechanics*, 31(3), 185-197. https://doi.org/10.1016/0148-9062(94)90464-2

Mangold, N., Thompson, L. M., Forni, O., Williams, A. J., Fabre, C., Le Deit, L., et al. (2016). Composition of conglomerates analyzed by the Curiosity rover: Implications for Gale crater crust and sediment sources. *Journal of Geophysical Research Planets*, 121, 353-387. doi:10.1002/2015JE004977.

Mares, V. M. & Kronenberg, A. K. (1993). Experimental deformation of muscovite. *Journal of Structural Geology*, 15(9-10), 1061-1075.

Marinescu, I. D. & Pruteanu, M. (2015). Deformation and fracture of ceramic materials, in *Handbook of Ceramics Grinding and Polishing (2nd Edition)*, 50-66. doi:10.1016/B978-1-4557-7858-4.00002-9

Mills, H. H. (2003). Inferring erosional resistance of bedrock units in the east Tennessee mountains from digital elevation data. *Geomorphology*, 55(104), 263-281. https://doi.org/10.1016/S0169-555X(03)00144-2

Moes, N., Dolbow, J., & Belytschko, T. (1999). A finite element method for crack growth without remeshing. *International Journal for Numerical Methods in Engineering*, 46, 131-150.

Nachon, M., Clegg, S. M., Mangold, N., Schröder, S., Kah, L. C., Dromart, G., et al. (2014). Calcium sulfate veins characterized by ChemCam/Curiosity at Gale crater, Mars. *Journal of Geophysical Research: Planets*, 119, 1991–2016. https://doi.org/10.1002/2013JE004588

Nachon, M., Mangold, N., Forni, O., Kah, L. C., Cousin, A., Wiens, R. C., et al. (2016). Chemistry of diagenetic features analyzed by ChemCam at Pahrump Hills, Gale crater, Mars. *Icarus*, 281, 121–136. https://doi.org/10.1016/j.icarus.2016.08.026

Natural Resources Conservation Service. (2012). Engineering Classification of Rock Materials, in *National Engineering Handbook.*

Nazir, R., Momeni, E., Armaghani, D. J., & Amin, M. (2013). Prediction of unconfined compressive strength of limestone rock samples using I-type schmidt hammer. *Journal of Geotechnical Engineering*, 18(1), 1767-1775.

Palchik, V. (1999). Influence of porosity and elastic modulus on uniaxial compressive strength in soft brittle porous sandstones. *Rock Mechanics and Rock Engineering*, 32(4), 303-309.

Peters, G. H., Carey, E. M., Anderson, R. C., Abbey, W. J., Kinnet, R., Watkins, J. W., et al. (2018). Uniaxial compressive strength of rocks drilled at Gale crater, Mars. *Geophysical Research Letters*, 45, 108-116.

Philipp, S. L. (2008). Geometry and formation of gypsum veins in mudstones at Watchet, Somerset, SW England. *Geological Magazine*, 145(6), 831-844. doi:10.1017/S0016756808005451.

Philipp, S. L., Asfar, F., Gudmundsson, A. (2013). Effects of mechanical layering on hydrofracture emplacement and fluid transport in reservoirs. *Frontiers in Earth Science*, 1(4). doi: 10.3389/feart.2013.0004.

Soreghan, G. S., Elmore, R. D., & Lewchuk, M. T. (2002). Sedimentologic-magnetic record of western Pangean climate in upper Paleozoic loessite (lower Cutler beds, Utah). *GSA Bulletin*, 114(8), 1019-1035

Stack, K. M., Grotzinger, J. P., Lamb, M. P., Gupta, S., Rubin, D. M., Kah, L. C., et al. (2018). Evidence for plunging river plume deposits in the Pahrump Hills member of the Murray formation, Gale crater, Mars. *Sedimentology*. https://doi.org/10.1111/sed.12558

Schieber, J., Bish, D., Coleman, M., Reed, M., Hausrath, E. M., Cosgrove, J., Gupta, S., et al., (2017). Encounters with an unearthly mudstone: Understanding the first mudstone found on Mars. *Sedimentology*, 64, 311–358. https://doi.org/10.1111/sed.12318

Schmidt, R. A. & Lutz, T. J. (1979). K_{IC} and J_{IC} of Westerly granite – effects of thickness and in-plane dimensions. *Fracture Mechanics Applied to Brittle Materials, ASTM STP 678*, 166-182.

Thomson, B. J., Bridges, N. T., Cohen, J., Hurowitz, J. A., Lennon, A., Paulsen, G., & Zacny, K. (2013). Estimating rock compressive strength from Rock Abrasion Tool (RAT) grinds. *Journal of Geophysical Research Planets*, 118, 1233-1244. doi:10.1002/jgre.20061

Villenueve, M., Diederichs, M. S., & Kaiser, P. K. (2012). Effects of grain scale heterogeneity on rock strength and the chipping process. *International Journal of Geomechanics*, 12, 632-647.

Walker, K. R., Shanmugam, G., & Ruppel, S. C. (1983). A model for carbonate to terrigenous clastic sequences: *Geological Society of America Bulletin*, 94, 700-712.

Watkins, J. A., Grotzinger, J., Stein, N., Banham, S. G., Gupta, S., Rubin, D., Stack, K., et al. (2016). Paleotopography of erosional unconformity, base of Stimson formation, Gale crater, Mars. *LPS XLVII,* Abstract 2939.

Whisner, S. C. (2005). The Middle Ordovician Tellico-Sevier Syncline: a stratigraphic, structural, and paleoseismic investigation. Doctoral Dissertation. University of Tennessee, Knoxville, TN.

Whittaker, B. N., Singh, R. N., Sun, G. (1992). *Rock fracture mechanics: principles, design and applications*. Elsevier: Amsterdam.

Zhang, Y. & Yu, D. (2019). Comparative study on the test method for tensile elastic modulus of rock materials. *Advances in Civil Engineering*, Article ID 3161953.

Zhang, Z. (2002). An empirical relation between mode I fracture toughness and the tensile strength of rock. *International Journal of Rock Mechanics and Mining Sciences*, 39, 401-406. doi:10.1016/S1365-1069(02)00032-1

Zhang, Z. X., Kou, S. Q., Lindqvist, P. A., & Yu, Y. (1998). The relationship between the fracture toughness and tensile strength of rock, in *Strength theories: applications, development & prospects for 21st century*, 215-219. Science Press: Beijing/NewYork.

Zi, G. & and Belytschko, T. (2003). New crack-tip elements for XFEM and applications to cohesive cracks. *International Journal for Numerical Methods in Engineering*, 57, 2221-2240. doi:10.1002/nme.849

CONCLUSIONS

The work outlined in the three chapters of this dissertation provides insight into the nature and formation mechanisms of fracture and vein systems in Gale crater, Mars. Mineralized fracture networks provide direct evidence of post-depositional fluid flow and indicate a protracted stability of liquid water at or near the martian surface. Such fractures represent unique targets for astrobiological investigation and potentially extend the window of habitability on Mars. Vein networks have been described in rover-scale images at multiple landing sites across the martian surface (Caswell & Milliken, 2017; Crumpler et al., 2014; Nachon et al., 2014; Squyres et al., 2012). In Gale crater, the orientation and intersection angles of isolated calcium sulfate veins at Yellowknife Bay has been used to infer hydrofracture as a potential formation mechanism (Caswell & Milliken, 2017; Nachon et al., 2014). At the Pahrump Hills (Mount Sharp group) locality in Gale crater, veins exhibit characteristically thicker, more complex morphologies than veins previously observed by the Curiosity rover. Evidence from the ChemCam (Nachon et al., 2014) and APXS (Van Bommel et al., 2016) instruments on the Curiosity rover indicate that chemically distinct fluid events deposited at least three distinct generations of veins at Pahrump Hills and include magnesium-rich gray veins, calcium-sulfate white veins, and iron, potassium, and fluorine-rich dark-toned veins. The multi-generational nature of veins is supported by a comprehensive analysis of vein morphology and microtextures based on Mastcam and high-resolution MAHLI images. Further analysis of vein size, complexity, and interactions between veins and host rock corroborate the interpretation of hydrofracture as the primary mode of vein formation at Pahrump Hills.

In addition to rover-scale vein networks present within the Mount Sharp group, erosionally resistant, potentially cemented, fractures have also been described at the orbital scale in Gale crater (Kerber et al., 2017; Milliken et al., 2014; Siebach & Grotzinger, 2013). Here I have described a regionally extensive network of polygonal fractures is present within strata of the Siccar Point group, a relatively young sequence of primarily aeolian deposits demonstrated to unconformably overlie the primary lacustrine deposits of northwest Gale crater (Banham et al., 2018; Fraeman et al., 2016; Watkins et al., 2016). Across the basal Siccar Point group, polygonal fractured are uniformly sized, laterally extensive, and exhibit bimodal fracture intersection angles. Polygon morphology indicates that fractures likely formed as a result of multiple cycles of wetting and desiccation. In addition, polygons exhibit erosional resistance, suggesting the potential for post-fracture interaction with diagenetic fluids. The presence of such fluid-related fractures within a dominantly aeolian (i.e. dry) system highlights the potential variability of the martian climate and further extends the history of fluid stability on Mars.

Finally, investigations into rock mechanics and engineering provide additional insight into better understanding the prediction of rock properties—critical to fracture modeling—in Gale crater. I utilized a multi-part approach to assess fracture growth and the conditions under which fractures propagate on Mars. First, analog rocks were selected to represent lithologies that occur in Gale crater, including very strong sandstone and extremely weak siltstone. Through experimental testing, the mechanical properties of analog lithologies were determined. In this study, the properties of silt and sandstone samples were found to be within the range of previously tested terrestrial materials and were validated by finite element models used to simulate fracture propagation through analog lithologies. I then utilized correlation between

different rock mechanical properties to predict fracture in light of limited mechanical property data from Mars rover missions. Results suggest that such efforts are promising, but that we currently lack sufficient testing of more unusual lithologies inferred for the martian surface.

References

Banham, S. G., Gupta, S., Rubin, D. M., Watkins, J. A., Sumner, D. Y., Edgett, K. S., et al. (2018). Ancient Martian aeolian processes and palaeomorphology reconstructed from the Stimson formation on the lower slope of Aeolis Mons, Gale crater, Mars. *Sedimentology*, 65(4),993–1042. https://doi.org/10.1111/sed.12469

Caswell, T. E., & Milliken, R. E. (2017). Evidence for hydraulic fracturing at Gale crater, Mars: Implications for burial depth of the Yellowknife Bay formation. *Earth and Planetary Science Letters*, 468, 72–84. https://doi.org/10.1016/j.epsl.2017.03.033

Crumpler, L. S., Arvidson, R. E., Bell, J., Clark, B. C., Cohen, B. A., Farrand, W. H., et al., (2014). Context of ancient aqueous environments on Mars from in situ geologic mapping at Endeavour crater. *Journal of Geophysical Research: Planets*, 120, 538-569. doi:10.1002/2014JE004699

Fraeman, A. A., Ehlmann, B. L., Arvidson, R. E., Edwards, C. S., Grotzinger, J. P., Milliken, R. E., et al. (2016). The stratigraphy and evolution of lower Mount Sharp from spectral, morphological, and thermophysical orbital data sets. *Journal of Geophysical Research: Planets,* 121, 1713–1736. https://doi.org/10.1002/2016JE005095

Gudmundsson, A., Kusumoto, S., Simmenes, T. H., Philipp, S. L., Larsen, B., & Lotveit, I. F. (2012). Effects of overpressure variations on fracture apertures and fluid transport. *Tectonophysics*, 581, 220–230. https://doi.org/10.1016/j.tecto.2012.05.003

Gudmundsson, A., & Brenner, S. L. (2001). How hydrofractures become arrested. *Terra Nova*, 13, 456–462. https://doi.org/10.1046/j.1365-3121.2001.00380.x

Kerber, L., Dickson, J. L., Head, J. W., & Grosfils, E. B. (2017). Polygonal ridge networks on Mars: Diversity of morphologies and the special case of the eastern Medusae Fossae Formation. *Icarus*, 281, 200–219. https://doi.org/10.1016/j.icarus.2016.08.020

Milliken, R. E., Ewing, R. C., Fischer, W. W., & Hurowitz, J. (2014). Wind-blown sandstones cemented by sulfate and clay minerals in Gale crater, Mars. *Geophysical Research Letters*, 41, 1149–1154. https://doi.org/10.1002/2013GL059097

Nachon, M., Clegg, S. M., Mangold, N., Schröder, S., Kah, L. C., Dromart, G., et al. (2014). Calcium sulfate veins characterized by ChemCam/Curiosity at Gale crater, Mars. *Journal of Geophysical Research: Planets*, 119, 1991–2016. https://doi.org/10.1002/2013JE004588

Peters, G. H., Carey, E. M., Anderson, R. C., Abbey, W. J., Kinnet, R., Watkins, J. W., et al. (2018). Uniaxial compressive strength of rocks drilled at Gale crater, Mars. *Geophysical Research Letters*, 45, 108-116.

Siebach, K. L., & Grotzinger, J. P. (2013). Volumetric estimates of ancient water on Mount Sharp based on boxwork deposits, Gale crater, Mars. *Journal of Geophysical Research: Planets*, 119, 189–198. https://doi.org/10.1002/2013JE004508

Squyres, S. W., Arvidson, R. E., Bell III, J. F., Calef III, F., Clark, B. C., Cohen, B. A., et al. (2012). Ancient impact and aqueous processes at Endeavour crater, Mars. *Science*, 336, 570-576. doi:10.1126/science.1220476

Thomson, B. J., Bridges, N. T., Milliken, R., Baldridge, A., Hook, S. J., Crowley, J. K., et al. (2011). Constraints on the origin and evolution of the layered mound in Gale crater, Mars using Mars Reconnaissance Orbiter data. *Icarus*, 214(2), 413–432. https://doi.org/10.1016/j.icarus.2011.05.002

VanBommel, S. J., Gellert, R., Berger, J. A., Campbell, J. L., Thompson, L. M., Edgett, K. S., et al. (2016). Deconvolution of distinct lithology chemistry through oversampling with the Mars Science Laboratory Alpha Particle X-ray Spectrometer. *X-Ray Spectrometry*, 45(3), 155–161. https://doi.org/10.1002/xrs.2681

Watkins, J. A., Grotzinger, J., Stein, N., Banham, S. G., Gupta, S., Rubin, D., Stack, K., et al. (2016). Paleotopography of erosional unconformity, base of Stimson formation, Gale crater, Mars. *LPS XLVII* 2939.

VITA

Rachel Emily Kronyak was born and raised in New Jersey. She attended Queen of Peace High School in North Arlington, NJ and graduated in 2010. After high school, she attended The Pennsylvania State University and graduated with a B.S. in Geobiology in 2014 with minors in Astrobiology and Marine Science. During her time at Penn State, Rachel gained undergraduate research experience under the supervision of Dr. Christopher House. This experience led Rachel to become a two-time summer intern at NASA Goddard Space Flight Center where she investigated the effects of Mars conditions on microbial growth working under Dr. Alexander Pavlov. After graduating from Penn State, Rachel began working towards her Ph.D. at the University of Tennessee in the fall of 2014 under the supervision of Dr. Linda Kah. During her first year at UT, Rachel became a team member of the Mars Science Laboratory Curiosity rover team and participated in weekly rover operations, serving in roles that include Mastcam Payload Uplink Lead, Keeper of the Plan, Documentarian, and mission blog writer. Throughout her time as a Ph.D. student, Rachel trained new rover team members on mission operations, mentored undergraduate research projects, participated in numerous NASA-related outreach events and lectures, co-chaired a session at the Geological Society of America annual meeting, first-authored 8 conference abstracts, presented at numerous Mars Science Laboratory team meetings and telecons, taught undergraduate-level labs, served as Executive Secretary on a NASA proposal review panel, attended a NASA-funded Planetary Volcanology workshop in Hawaii, initiated weekly department coffee and snack breaks, and helped organize and lead a lab group field trip to the western US.